Max-Planck-Institut für Meteorologie
Max Planck Institute for Meteorology

Examensarbeit Nr. 92

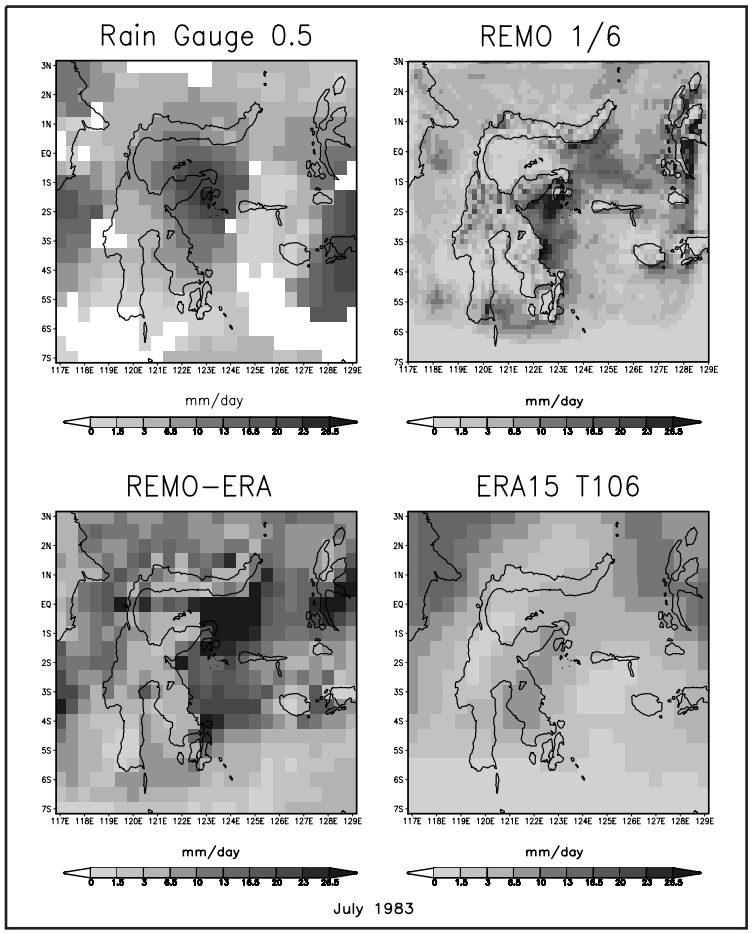

Simulations of Indonesian Rainfall with a Hierarchy of Climate Models

(Simulationen des Indonesischen Niederschlags mit einer Hierarchie von Klimamodellen)

von

Edvin Aldrian

Hamburg, Juli 2003

Dissertation zur Erlangung des Doktorgrades

Autor:

Edvin Aldrian Max-Planck-Institut für Meteorologie

Max-Planck-Institut für Meteorologie
Bundesstrasse 55
D - 20146 Hamburg
Germany

Tel.: +49-(0)40-4 11 73-0
Fax: +49-(0)40-4 11 73-298
e-mail: <name>@dkrz.de
Web: www.mpimet.mpg.de

Simulations of Indonesian Rainfall with a Hierarchy of Climate Models

(Simulationen des Indonesischen Niederschlags mit einer Hierarchie von Klimamodellen)

Dissertation
zur Erlangung des Doktorgrades
der Naturwissenschaften im Fachbereich
Geowissenschaften
der Universität Hamburg

vorgelegt von
Edvin Aldrian
aus Jakarta, Indonesien

Hamburg, Juli 2003

ISSN 0938-5177

Als Dissertation angenommen vom
Fachbereich Geowissenschaften der Universität Hamburg

auf Grund der Gutachten von Herrn Prof. Dr. Hartmut Graßl

und Frau Dr. Daniela Jacob

Hamburg, den 15 Juli 2003

Prof. Dr. H. Schleicher
Dekan des Fachbereichs Geowissenschaften

Gedruckt mit Unterstützung des Deutschen Akademischen Austauschdienstes

Abstract

This dissertation describes the analysis of the monthly, seasonal and interannual rainfall variabilities over the Maritime Continent and describes the potentials and limits of a wide range of climate models in simulating these variabilities. The study analyzes the simulated rainfall variability from two global reanalyses, an atmospheric general circulation model (AGCM), an atmospheric regional climate model (RCM) and an ocean general circulation model (OGCM). The two reanalyses and the AGCM output is available at T42 and T106 resolutions, while the RCM resolves 0.5° and $1/6^\circ$. The study explores the uncoupled as well as the coupled mode of RCM and OGCM and focuses mainly on the period 1979 to 1993.

With a regionalization method introduced in this study, the Maritime Continent is divided into three distinct climate regions, the south monsoonal, the northwest semi-monsoonal and the Molucca anti-monsoonal region. All three regions show different responses to monsoon and El Niño/Southern Oscillation (ENSO).

Two important rainfall variabilities ranging from monthly to interannualy time scale are the annual monsoon cycle and the irregular ENSO. The monsoon regulates local SST variability via ocean circulation, which in turn influences heat content of the upper ocean and eventually local rainfall. The study points to remote ENSO influences through SST forcing. Indeed, there is a local ocean circulation mechanism that drives the ENSO impact on Indonesian rainfall.

The rainfall climate of this region is potentially predictable on monthly and seasonal scales but only for limited and specific periods and regions. Despite such a potential, the study shows a consistent predictability barrier in spring as an intrinsic character of the Indonesian rainfall and a challenge to climate modeling in the region, because it limits model applications. The barrier is found by all models and at different resolutions.

The RCM and the OGCM have been especially tailored to the region and they produce realistic results. The global atmospheric model produces the large scale system well and the nested regional model shows a local phenomenon obscured in the global. A coupled atmosphere/ocean regional model shows improved dynamics through a better sea-air interaction and ocean/atmosphere feedback. However, also the uncoupled ocean and atmosphere models, separately, produce realistic results of rainfall and ocean variability albeit with some drawbacks. The quality of the RCM simulations is confined, in most cases, to the quality of the prescribed boundary forcings.

Contents

Table of Contents . . . . . .

1 Introduction **1**

2 Climatic Rainfall Patterns **4**

2.1 Introduction 5

2.2 Data and Methods 6

2.3 Results 7

2.3.1 The Covariance EOF and the VARIMAX Method 12

2.3.2 Spectral Analysis of the EOF and the Double Correlation Method . . . 14

2.3.3 Local SST Responses 16

2.3.4 Seasonal and Remote SST Responses 18

2.3.5 Ensemble ENSO Years 23

2.4 Discussion and Concluding Remarks 25

3 Rainfall Variability in ECHAM4 and Reanalyses **28**

3.1 Introduction 29

3.2 Data and Model 31

3.3 Regional Annual Cycle Analysis 32

3.4 Interannual Variability 38

3.5 Seasonal and Monthly Variability 42

3.6 Interannual Variability Related to ENSO 44
3.6.1 Spatial Patterns of the Rainfall Sensitivity to NINO3 SST 45
3.6.2 Seasonal and Monthly Variability Related to ENSO 47
3.7 Effects of Land-sea Mask Resolution 50
3.8 Concluding Remarks 51

4 Simulation with the MPI Regional Model 54

4.1 Introduction 55
4.2 Data and Model Setup 56
4.2.1 Data 56
4.2.2 REMO Model Descriptions 57
4.2.3 Model Setups 58
4.3 Results of REMO Simulations 59
4.3.1 The Five Major Islands 60
4.3.2 The Three Sea Regions 65
4.3.3 Improvement through Higher Resolution 68
4.3.4 Sensitivity Studies 71
4.4 Predictability of Rainfall Simulated by REMO 73
4.4.1 Intrinsic Errors 73
4.4.2 Internal and External Variances 78
4.5 Concluding Remarks 81

5 Monsoonal Character of Indonesian Waters 83

5.1 Introduction 84
5.2 Data and Model 85
5.2.1 Data 85

5.2.2 Model Descriptions 86
5.2.3 Experimental Setups 88
5.3 Ocean Circulation from MPI-OM Simulations 89
5.3.1 The Monsoonal Ocean Circulation 90
5.3.2 Monsoonal Character of the Indonesian Throughflow 93
5.3.3 Thermohaline Condition from Indonesian Water 95
5.4 The Three Monsoonal Climate Regions 97
5.4.1 The Monsoonal Region of South Indonesia 98
5.4.2 The Semi-monsoonal Region of Northwest Indonesia 98
5.4.3 The Anti-monsoonal Region of Molucca 99
5.4.4 How does Ocean Circulation Drives SST? 100
5.5 Subsurface Monsoonal Signatures 101
5.5.1 Monsoonal Transports Profile 103
5.5.2 Monsoonal Salinity Profile 106
5.5.3 Monsoonal Temperature Profile 108
5.6 Monsoonal Influence on ENSO Impact 108
5.7 Concluding Remarks 111

6 Modelling with a Coupled Regional Model 113

6.1 Introduction 113
6.2 Data and Model Setup 115
6.2.1 Data 115
6.2.2 Model Descriptions 115
6.2.3 Model Setups 117
6.3 Implication for the Atmosphere 119

6.3.1 The five major islands 119
6.3.2 The three sea regions 122
6.3.3 Precipitation Reduction over the Sea 123
6.4 Implication for the Ocean 125
6.4.1 Variability of Throughflow 125
6.4.2 SST Variability 126
6.4.3 Mean thermohaline condition 127
6.5 Concluding Remarks 130

7 Summary and Concluding Remarks 131

Acknowledgements 135

A Glossary 136

B Statistical tools 138

B.1 The Empirical Orthogonal Function (EOF) Analysis 138
B.2 The Rotated EOF Analysis 140

C Determination of the Liquid Water Content 142

D Atmospheric surface fluxes forcing 144

References 146

Chapter 1

Introduction

The rainfall climate of the Maritime Continent is very unique as it is located in the most active convective area of the world. This uniqueness has attracted scientists since the early 20^{th} century. Rainfall variability in this region is very complex and is considered as the *chaotic* part of the monsoon variability (*Ferranti* 1997). The complexity in land representation and incoherency of spatial and temporal rainfall patterns are quite a challenge for scientific investigations. Rainfall variability, indeed, influences the way of life for several hundred million people in the region. The economic and agricultural importance of rainfall variability, just mentioning two main sectors, is a strong motivation of the study. For example, the El Niño leads to devastating droughts with low crop yields, while too much rainfall in the peak of the wet season may produce devastating floods.

Regional climate study of rainfall in the region has so far been limited to smaller areas due to a limited amount of rain gauge station data. This study utilizes a maximum gauge data available to build a spatial and temporal rainfall data representation in this region. This is needed to work with a hierarchy of climate model. The climate modeling approach and comprehensive multi-resolution analyses of climate model rainfall variability in this region are relatively new. This study explores climate models from global to regional and from uncoupled to coupled ones. The study shall present the potentials and limitations of applying state of the art climate models for rainfall and climate studies in Indonesia.

Despite its flexibility to reach different spatial resolutions, the in-situ data set has limited temporal resolution, as it consists of monthly averages covering the period 1961 to 1993. However, most model analyses use the period 1979-1993 due to limited forcing data. Thus, analyses of the intra-seasonal or higher frequency rainfall variability are unattainable. On the other hand, the minimum possible low frequency analyses will be the 5 year variability.

Two main themes will be presented in this thesis. Firstly, studies and analyses of the monthly,

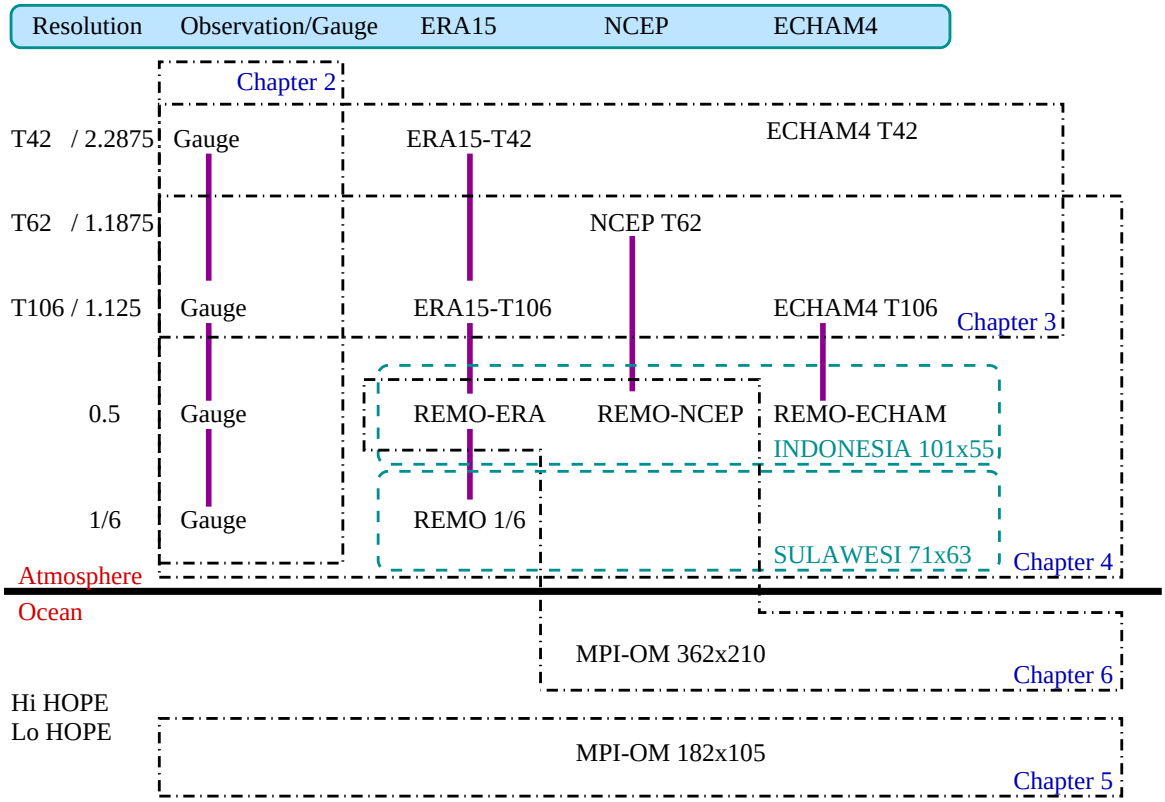

Figure 1.1: Schematic diagram of the structure and relationship among chapters in this thesis.

seasonal and interannual rainfall variability in the region, which focuses on the monsoonal and El Niño/Southern Oscillation patterns. Those two patterns are believed to be dominant factors in the region for such time periods. Secondly, studies on the performance and skill of state of the art climate models in representing rainfall variability in the region. The main question is whether we gain significant performance by going to higher resolution models. For this, we will utilize the results of a global climate model, reanalyses, a regional climate model, a global ocean model and a coupled ocean/atmosphere model.

Fig. 1.1 illustrates the structure and relationships among chapters in this thesis. In the remaining part of this introduction, brief descriptions of the chapters of this thesis are given. Each chapter, especially chapter 2 to 6, is designed to be an independent and full paper, thus some repetitions may inevitably occur in data and method descriptions.

Chapter 2 presents an overview of the main rainfall data used and the climatic characters of rainfall in the maritime continent, focusing on monsoonal and ENSO characteristics. This chapter discusses the monsoonal climatic regions that subdivide Indonesia into three climatic regions and the role of local and remote Sea Surface Temperature (SST) forcings.

In Chapter 3, the global representation of Indonesian rainfall in two reanalyses and a global climate model is analyzed together with their monthly and seasonal skills and their relation to

the three climate regions, the monsoon and ENSO. Also the sensitivity to spatial resolution will be addressed.

After the analysis of the global representation of rainfall, Chapter 4 presents the rainfall simulations of a Regional Climate Model that is driven by two reanalyses and a global climate model. This chapter presents the simulations at resolutions 0.5° and $1/6^\circ$ and the implication of resolution.

Since the Maritime Continent is mostly occupied by the sea, the ocean has important influences on atmospheric climate and its variability. In Chapter 5, the monsoonal character of the Indonesian waters is discussed in detail. The focus of the chapter is ocean variability that drives the different monsoonal regions and ocean variability simulated by a global ocean circulation model with detailed regional resolution. Also the implication of different resolutions will be addressed.

After having simulated the regional atmosphere with the Regional Climate Model and the regional ocean with a global ocean model, the result of the coupled model is presented in Chapter 6. The chapter focuses on the consequences of coupling a regional atmospheric model and a global ocean model for rainfall variability, ocean circulation and SST. The simulations were performed with forcings from two reanalyses and with two different resolutions of the ocean model.

A brief summary of the conclusions of all chapters, a discussion of some implications and outlooks are presented in the final Chapter 7.

Chapter 2

Characteristics of Climatic Rainfall Patterns in Indonesia

Abstract

The characteristics of climatic rainfall patterns in Indonesia are investigated using a new double correlation method, which is compared to the Empirical Orthogonal Function (EOF) and the rotated EOF methods. Also local and remote responses to Sea Surface Temperature (SST) are discussed. The result suggests three climatic regions in Indonesia with their distinct characteristics. Region A is located in southern Indonesia from south Sumatera to Timor island, part of Kalimantan, part of Sulawesi and part of Irian Jaya. Region B is located in northwest Indonesia and Region C encompasses Molucca and part of Sulawesi. All three regions show both strong annual and, except Region A, semi-annual precipitation signals. Region C shows the strongest El Niño Southern Oscillation (ENSO) influence followed by Region A. In Region B, the ENSO-related signal is suppressed. Except for Region B, there are significant correlations between SST and the rainfall variabilities indicating a good possibility for seasonal climate predictions. March to May is the most difficult season to predict. From June to November, there are significant responses of the rainfall pattern to ENSO in Regions A and C. A strong ENSO influence during this normally dry season (June to September) is hazardous in El Niño years, because the negative response means that higher SST in the NINO3 region of the Pacific will lower rainfall amount over the Indonesian region. Indonesian rainfall patterns reveal some sensitivities to SST variabilities in adjacent parts of the Indian and Pacific Oceans.

2.1 Introduction

There exist several studies on rainfall over Indonesia and its relation to large-scale climatic phenomena (*Braak*, 1921; *Wyrtki*, 1956; *Sukanto*, 1969; *Hackert and Hastenrath*, 1986; *McBride*, 1999; *Kirono et al.*, 1999; *Haylock and McBride*, 2001). The influence of large-scale climate phenomena varies across the region due to island topography and/or ocean-atmosphere fluxes, which are imposed by Sea Surface Temperature (SST) variability. To investigate the relationship of rainfall to the climatic phenomena, we need not only long-term rainfall time series but also more stations to better resolve the spatial variability over the entire Indonesian region. Better spatial and temporal resolutions of the climate over Indonesia allow a more quantitative understanding of the causal links of Indonesian rainfall to larger scale climate features. Hence, it is important to study the climatic rainfall pattern in the Indonesian region using more complete data sets and appropriate statistical tools. The results based on a new double correlation method, a covariance Empirical Orthogonal Function (EOF) and a rotated EOF will be discussed here.

Using monthly rainfall data from 33 stations over 48 years, *Kirono et al.* (1999) noted that during the El Niño 1997/1998, virtually the entire country had rainfall below the 10th percentile, with many stations recording the lowest rainfall on record. *Haylock and McBride* (2001) extended the studies using rainfall data from 63 stations from 1950 to 1998 to determine the spatial coherence of wet season anomalies.

It has been demonstrated that the SST anomalies in the region of Indonesia and northern Australia are closely related to the El Niño Southern Oscillation (ENSO; *Philander* 1983) phenomenon (*Newell et al.*, 1982; *Rasmusson and Carpenter*, 1982; *Nicholls*, 1983, 1984, 1985; *Gutman et al.*, 2000). The relationship of Indonesian SST to ENSO and the tendency for them to lead east Pacific SST suggests that they might provide forecasts of Indian monsoon with longer lead times than is possible using either Darwin pressure tendencies (*Shukla and Paolino*, 1983) or east Pacific SST (*Rasmusson and Carpenter*, 1982). Using global rainfall and SST data from 1979-1998, *Lau and Wu* (1999, 2001) indicated the importance of regional processes in affecting the Asian summer monsoon rainfall variability. On average, ENSO-related basin scale SSTs can account for 30% of the rainfall variability, and regional processes can account for an additional 20%. The results suggest that in order to improve seasonal-to-interannual predictability of the Asian monsoon, we need to investigate and exploit not only the relationship between monsoon and El Niño, but also intrinsic regional processes coupled with monsoon. Our study investigates the relation between SST in both the Pacific and Indian Oceans and its influence on the rainfall pattern in Indonesia.

Given the complexity of the region and many factors affecting the rainfall pattern, more complete data sets and a suitable statistical method are needed. In this chapter, we introduce a new regionalization method, the ”double correlation method” (DCM), based on the annual rainfall

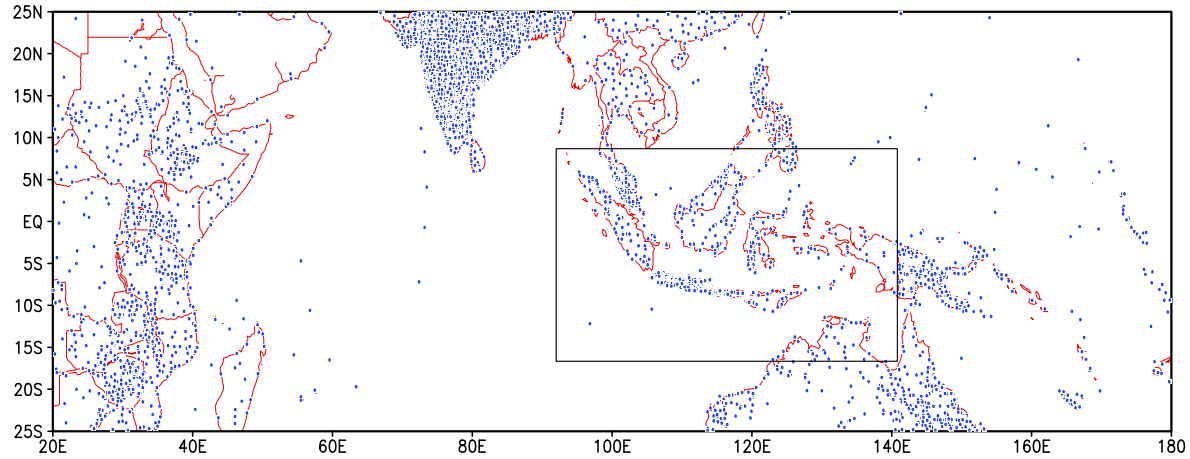

Figure 2.1: The distribution of rain gauges stations over 30 °S - 30 °N, 20 °E - 180 °E with 5419 stations and over the Indonesian archipelago over 15S- 8N, 90E - 140E (inside box) with 884 stations.

cycle. The first regionalization attempt for this region was done by *Wyrtki* (1956), when he divided the Indonesian waters into 9 subregions. The main objective of this chapter is to find an objective method for a division of Indonesian climate using DCM. In the next section we shall describe the data and the double correlation method. Section 3 discusses the result based on the double correlation method and its comparison with the covariance and rotated EOF and then evaluates the responses of each region to SST in local and surrounding seas. The section ends with an analysis of all ENSO years. Finally section 4 contains the overall discussion and conclusions.

2.2 Data and Methods

The study area covers the Indonesian archipelago or an area between 15 °S to 8 °N and 90 °E to 140 °E (Fig. 2.1). There are 884 rain gauges within the region. Among those are 526 stations of the Indonesian Meteorological & Geophysical Agency (BMG). The rest of stations comes from the World Meteorological Organization-National Oceanic and Atmospheric Administration (WMO-NOAA) project on the Global Historical Climatology Network (GHCN; *Vose et al.* 1992). We use monthly rainfall data from 1961 until 1993. Using the Cressman objective analysis (*Cressman*, 1959), these data are then gridded into the T106 resolution of the global models, which corresponds to a spatial resolution of 1.125 ° latitude by 1.125 ° longitude. Fig. 2.2 illustrates the rainfall climatology of the region using this data.

The gridded SST data from the Global Ice and Sea Surface Temperature dataset (GISST2; *Rayner et al.* 1996) version 2.3b are used in this study. This dataset is compiled from SST observations from 1871 - present, with a spatial resolution of 1 °. To have the same period as

the rainfall data, we use data from 1961 to 1993 only.

Due to the high spatial variability of the Indonesian rainfall, we need a statistical method that can reduce the bias error. It will be shown that the DCM provides comparable results in classifying the climate division to the EOF method. A region that consists of grid cells with similar annual cycles is likely to respond specifically and homogeneously to a climate phenomenon. The applied regions must be distinct (no overlap) from its neighbor and each should represent the dominant climate phenomenon acting on it. One could use a simple box with a definite longitudinal and latitudinal boundary to set a region. This approach is biased to some extent because many climatic factors, as previously mentioned, interplay over the region. The DCM could reduce this bias.

With the DCM, we look for a region, in which the annual cycles of its grid cells are correlated among themselves by more than a certain threshold value. To make it more efficient, rather than correlating all grid cells to each other, we first select some referenced cells. Secondly we correlate all other cells to these reference cells based on their annual cycles. Cells that are correlated above a certain threshold value are selected to belong to a region. Thirdly we correlate all grid cells again with the mean annual cycle of the resulting region using the same threshold value. The aim of the second correlation is to produce a region independent of the choice of the reference grid. The threshold value should be the highest correlation value, which produces no overlapping boundaries. In this paper, the threshold value chosen is 0.67, which statistically has above 99% significance level on our rainfall data set from only one correlation. Thus, with double correlations, the level of significance is much higher than a single correlation. With such a high degree of significance, the choice of reference cells is not difficult and not very relevant for the result.

To fulfill the above criteria, a simplified procedure has been carried out as follows. First, we selected 100 rain gauge stations with a high quality record and gridded them at the T42 resolution (2.8125 °). Those stations are distributed unevenly over Indonesia and cover 48 land grid areas. By visually comparing their mean annual cycles, they are attributed to 5 climatic regions. Then we selected our reference cells from these regions to start the double correlation method at the T106 resolution. All regions bounded by the same coordinates (15 °S - 8 °N, 90 °E - 141 °E).

2.3 Results

The result of the DCM is three climate regions as shown in Fig. 2.3. Region A (solid line) covers south Indonesia from south Sumatera to Timor Island, parts of Kalimantan, parts of Sulawesi, parts of Irian Jaya. Region B (short dashed line) is located in northwest Indonesia (close to the Asian continent) and Region C in Molucca and parts of Sulawesi (close to the

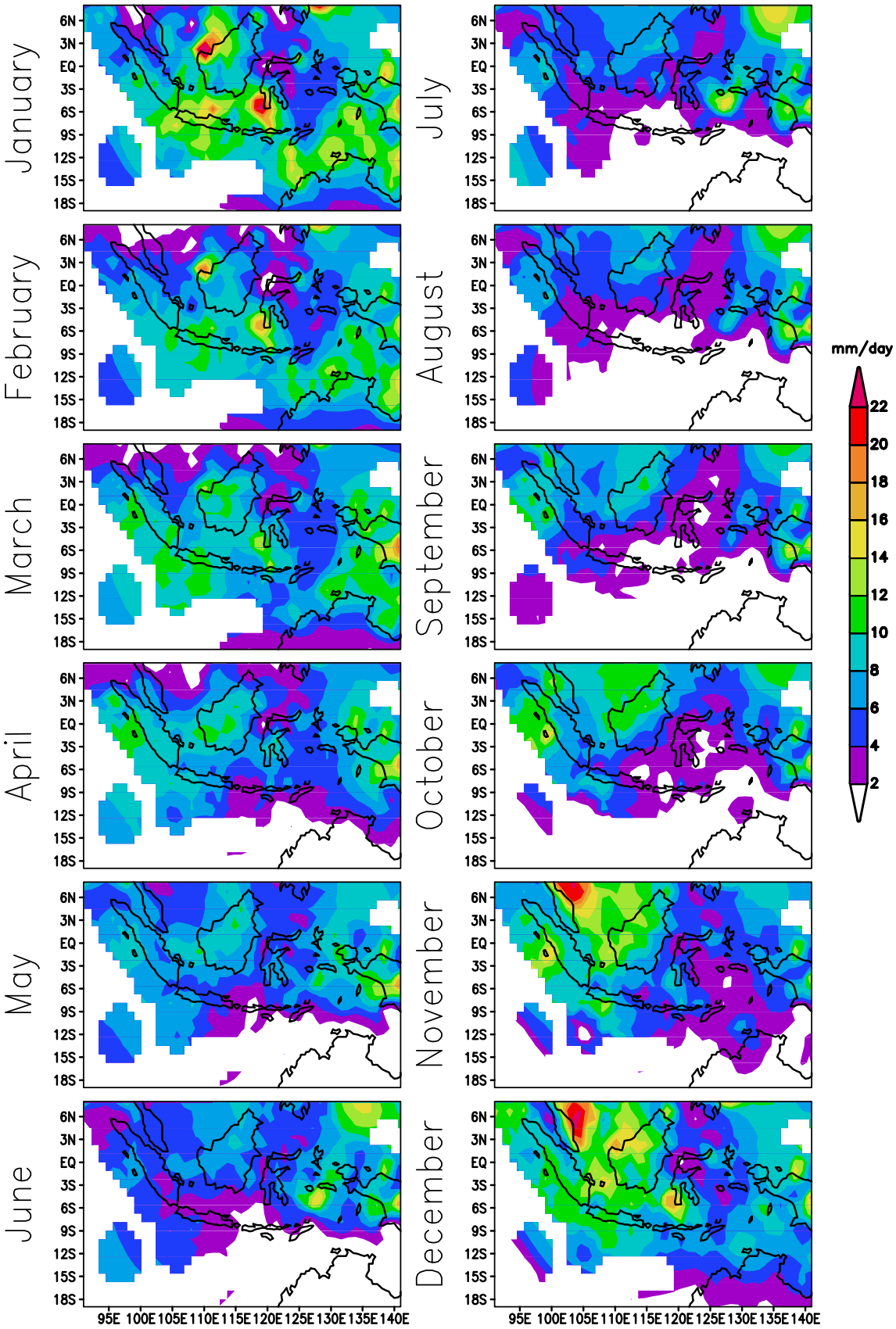

Figure 2.2: The 33 year (1961-1993) monthly rainfall average of the Maritime Continent.

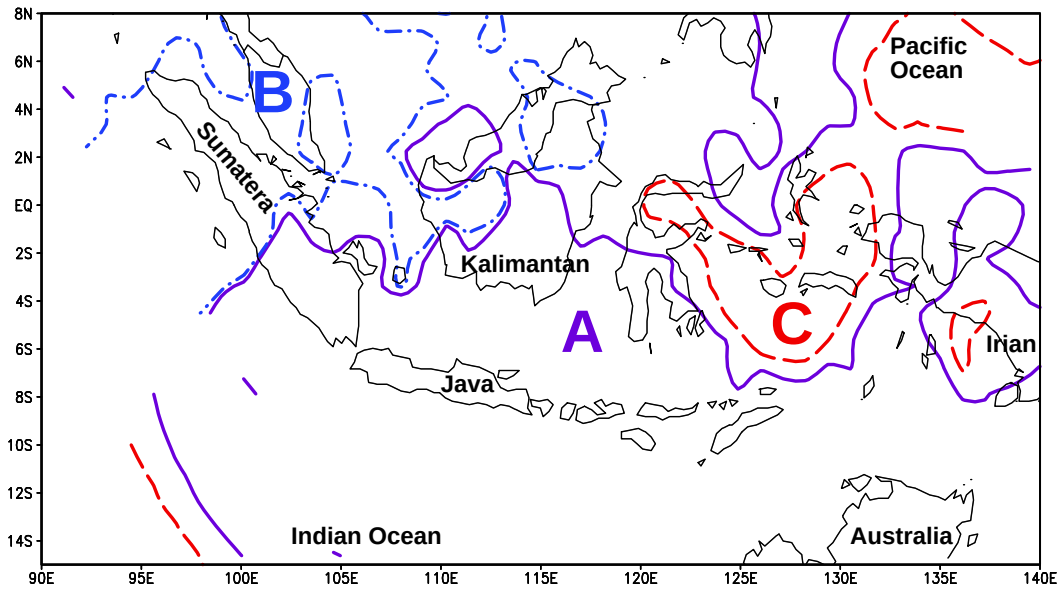

Figure 2.3: The three climate regions according to the mean annual patterns using a ”double correlation method”. Indonesia is divided into Region A in solid line (Australian monsoon), Region B in short dashed line (NE Passat monsoon) and Region C in long dashed line (Indonesian throughflow).

western Pacific Region). With the threshold value 0.67, we obtain a clear boundary among regions without overlapping, although there are some discontinuities (the intermediate region). Region A, which covers the largest area, is the dominant pattern over Indonesia. *Hamada et al.* (2002) classified Indonesia into four climatological regions. They found similar characters of the three regions we found and the intermediate region with no clear rainy and dry seasons.

The mean annual rainfall cycles of each region and their interannual standard deviations are described in Fig. 2.4. From this figure, each region has its own distinct feature. Region A has one peak and one minimum and experiences strong influences of two monsoons. Those are the wet northwest (NW) monsoon from November to March (NDJFM) and the dry SE monsoon from May to September (MJJAS). Region B has two peaks, in October November (ON) and in March to May (MAM). Those two peaks are associated with the southward and northward movement of the Inter Tropical Convergence Zone (ITCZ). There is no clear reason why the peak in ON is much higher than that of MAM. There is a possible influence of a cool surface current coming from the north out of the South China Sea during January - March (JFM) that suppresses the rainfall amount. Otherwise the annual cycle of Region B would be similar to that of Region A. Region C has one peak in June to July and one minimum (NDJF). The JJ peak in Region C is about 10 mm/day, while the peaks in Region A and B are 10.7 and 10.3 mm/day respectively. The minimum in Region A is the lowest and reaches a mean below 3.3 mm/day. Thus, Region A is the driest region during the dry season in JAS and the wettest region in December.

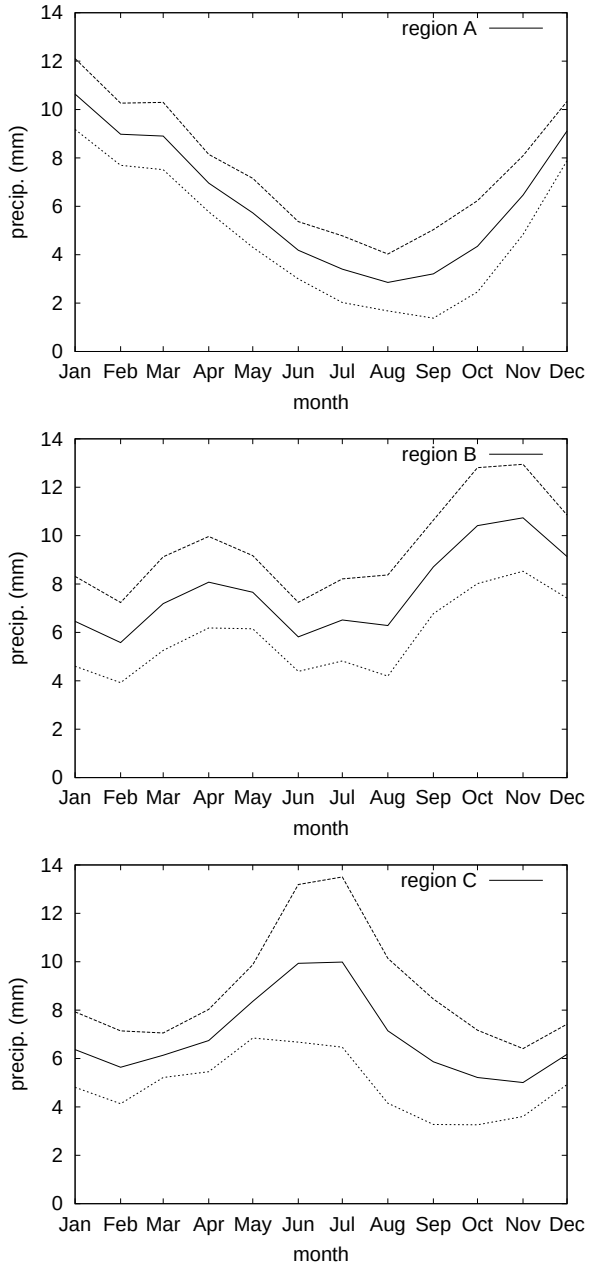

Figure 2.4: The annual cycles of the three climate regions (solid lines) using the ”double correlation method”. Dashed lines indicates 1 standard deviation (σ) above and below average.

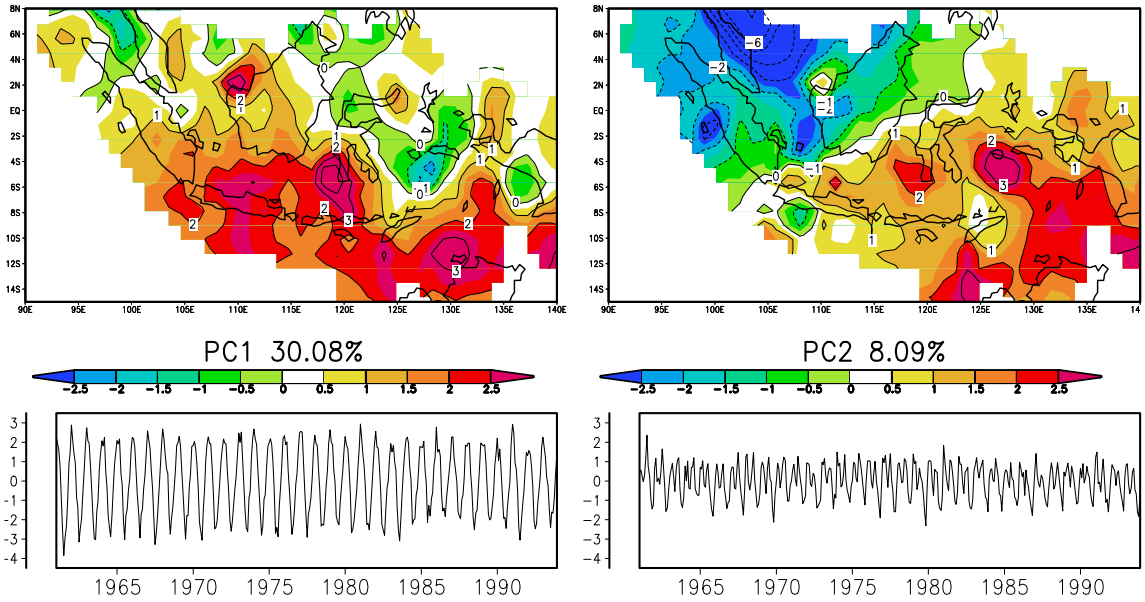

Figure 2.5: The first two principal components of the EOF method using the same data set as the double correlation method. Regions A and C in Fig. 2.3 are present in PC 1 and Region B (not obvious) in PC 2 with a broader intermediate region in east Indonesia between Region A and C. Below are the coefficient time series of each PC, which explain that PC 1 and PC 2 are the annual and the semi-annual patterns.

Region C, in comparison to the other two, has a unique annual cycle. The other two regions have their peaks near the end of the year, while the peak of Region C is in the middle. There is a strong evidence of the possibility of ocean influence in Region C. Region C or Molucca is along the eastern route of the Indonesian Throughflow (ITF) (*Gordon and Fine*, 1996). The ITF flows mainly through the Makassar Strait with a small part flowing through the Molucca Sea (*Gordon et al.*, 1999). The ITF in Molucca brings sea water from the warm pool area, which is located northeast of Irian Jaya Island (New Guinea). As suggested from the distribution of the region itself, there is some part of this region that lies north of Irian Jaya. Hence, the SST over Molucca is determined mainly by the condition over the warm pool. During the drier season of Region C (NDJFM) the sun position is in the southern hemisphere. The ITF brings cooler surface water from the warm pool to the Molucca Sea. This cooler SST inhibits the formation of a convective zone. On the other hand, during the wet season of Region C (MJJAS) the warm SST enhances the convective zone. Hence, we obtain the peak in MJJ and the minimum in ONDJ.

The standard deviation in Region A is smaller throughout the whole year, which indicates a strong coherent pattern. On the other hand, the other two regions have stronger interannual cycles than Region A. The homogeneous pattern in Region A indicates a wide extent of the dry season that reaches all Java and Lesser Sunda Islands, Sumatera and part of Kalimantan.

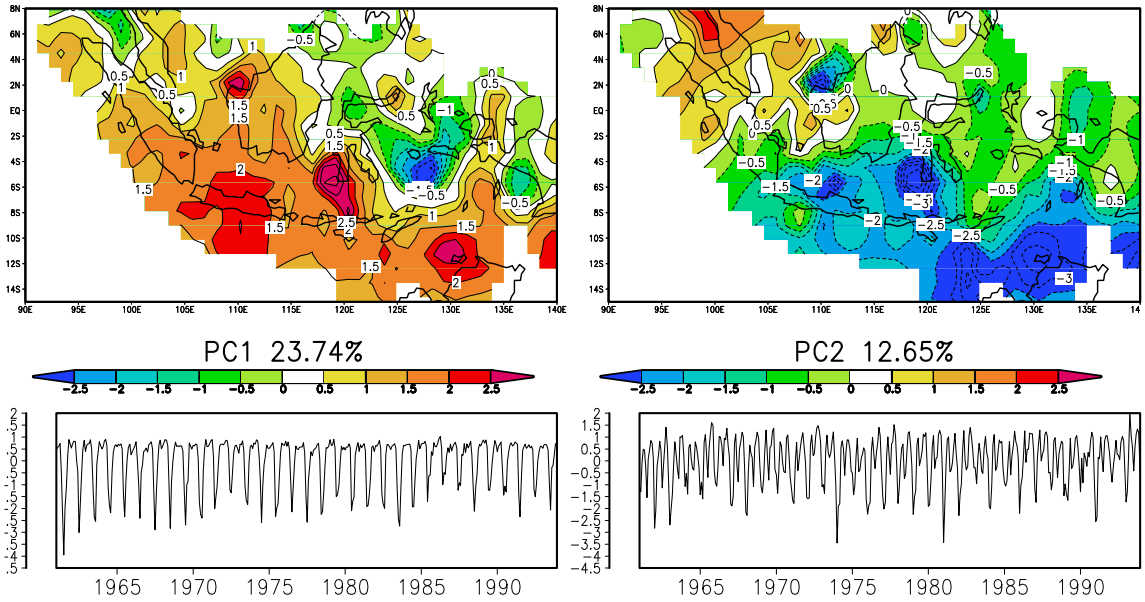

Figure 2.6: The first two principal components of the rotated EOF method using the first 100 PCs (explain 90.7% of all variances) from the unrotated EOF. Region A and C are indicated with boundaries > 0.5 and < 0.0 respectively in PC 1. While Region B is present in PC 2 with boundary > 0.5. Below are the coefficient time series of each PC, which explain that PC 1 and PC 2 are the annual and the semi-annual patterns.

2.3.1 The Covariance EOF and the VARIMAX Method

We compare the DCM with the covariance EOF method (*von Storch and Zwiers*, 1999) and the rotated EOF method. In this paper the VARIMAX rotation (*Kaiser*, 1958) was used as a way in rotating EOF. The EOF method is capable of extracting the principal components (PC) of patterns in a time series. Each of the PCs will be orthogonal to the others. The first PC (PC1) will be the most dominant pattern and explains most of the variance. Then PC2 will be the second most dominant PC followed by PC3, etc. There will be in total the same number of PCs as the number of data in the time series. The original data set will be the combination of all PCs multiplied by the time series of their respective coefficient time series.

The spatial pattern of PC1 and PC2 of the EOF method for the same data set is given in Fig. 2.5. PC1 and PC2 explain 30.08% and 8.09% of all variances and represent the annual and semi annual patterns. The distribution of apparent regions in PC1 resembles that of the DCM. Region A, B and C from the DCM are approximately represented in PC1 by the areas with values above 1.0, between 0 and 1.0 and negative values, respectively. The opposite sign of Regions A and B with respect to C for the EOF method implies the opposite annual cycle (as already seen in Fig. 2.4). The main differences between the results of both methods are the border of Region B, and the intermediate region in the east. The annual cycle of the intermediate region would be a mixture between pattern A and C with two peaks and minimums and a flat annual cycle.

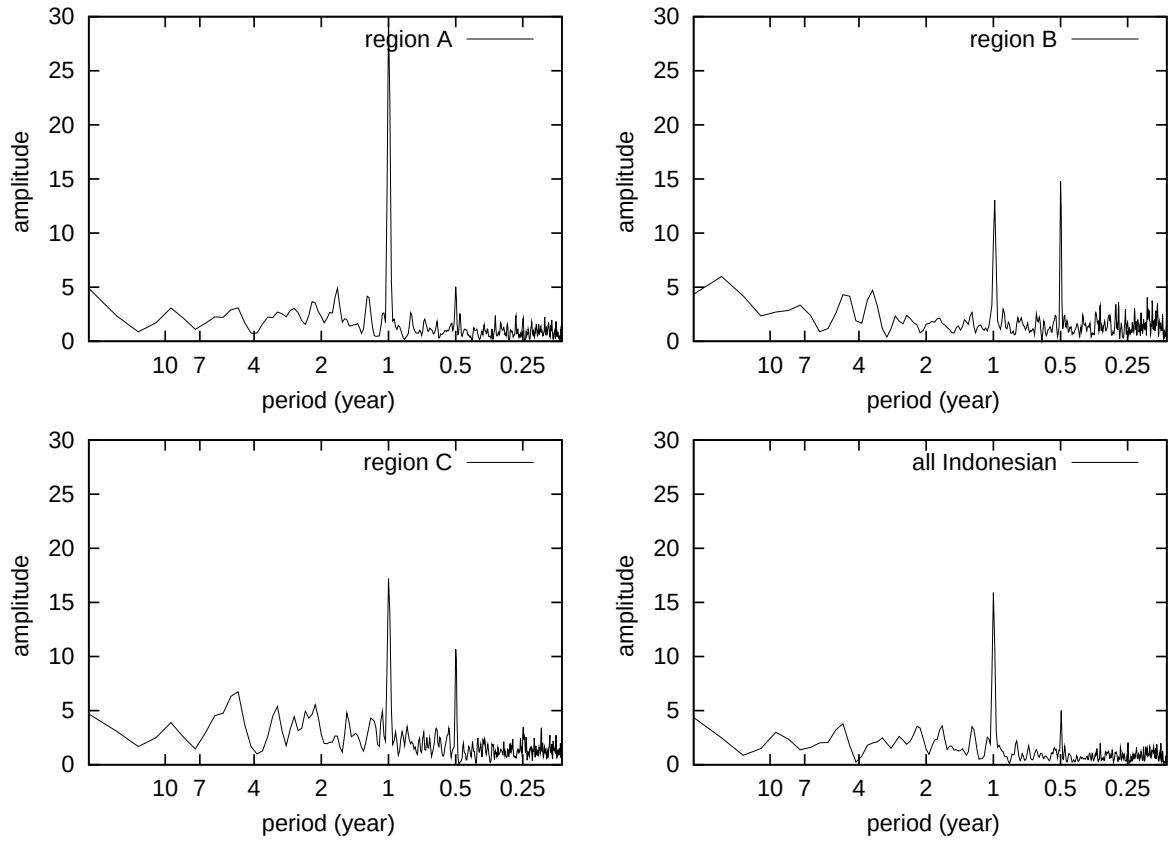

Figure 2.7: The frequency spectra of the three regions and the all indonesian region after smoothing with 1-2-1 convolution.

Figure 2.6 shows the first two principal components from the rotated EOF using the VARIMAX method. PC1 and PC2 explain 23.47% and 12.65% of all variances, respectively. Those PCs are calculated using the first 100 PCs (that explain 90.7% of all variances) of the EOF method. Again Region C corresponds to the negative valued region of PC1, while the border of Region A is obvious only in the eastern part. Region B has values above 0.5 of PC2. The presence of Region B in PC2 is understandable because Region B has similar semi annual characteristics as PC2.

In summary, it is difficult to judge whether the EOF or the VARIMAX methods give a better regionalization. With the EOF method, the boundaries of Region A and C exist in PC1, but not the boundary of Region B. While the boundaries of Regions B and C exist in PC1 and PC2 of the VARIMAX method, respectively, but not the western boundary of Region A. sometimes patterns derived from EOF analyses can be misleading and associated with very little physics (*Dommenget and Latif*, 2002).

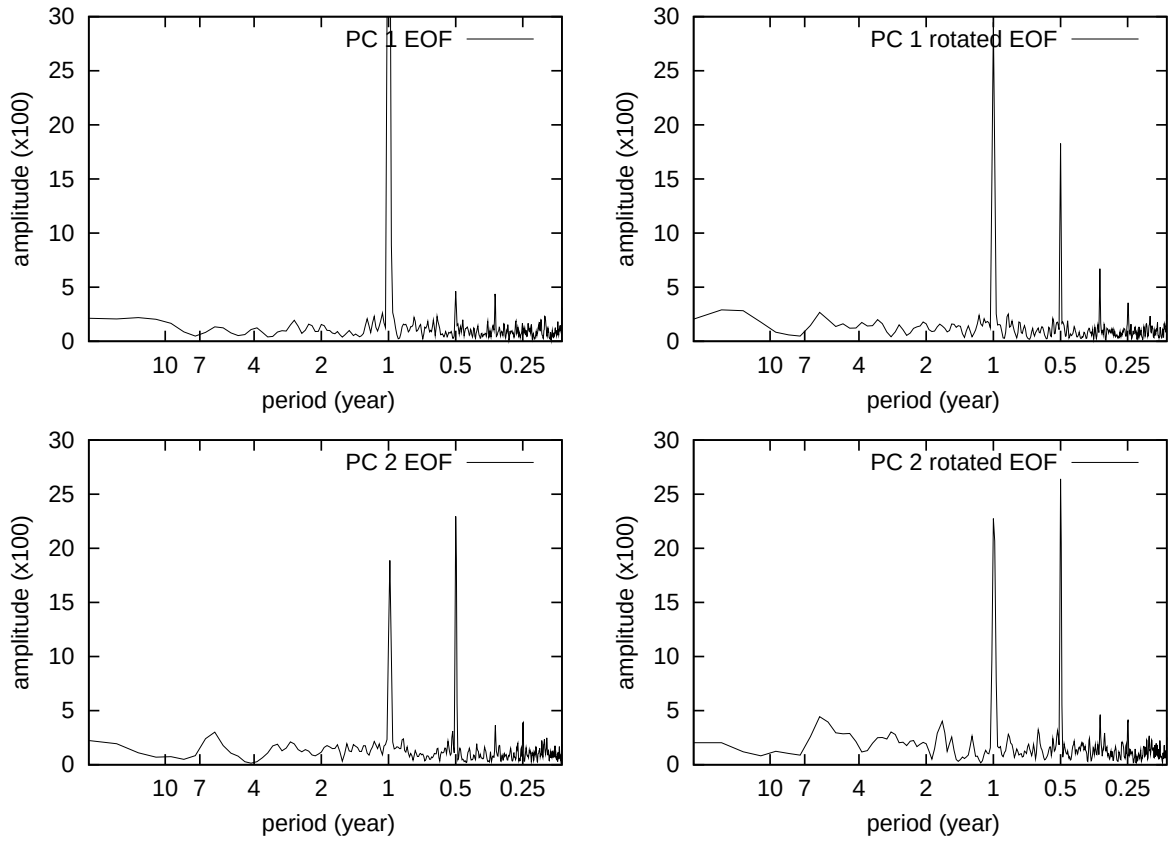

Figure 2.8: The frequency spectra of the first two PCs of the EOF method (left) and rotated EOF method (right) after smoothing with 1-2-1 convolution. PC 1 EOF has an overflow value of 64.9 in the period of one year.

2.3.2 Spectral Analysis of the EOF and the Double Correlation Method

To clarify which frequency dominates the rainfall pattern, we investigate the power spectra of each region from the DCM and each coefficient of the EOF and the VARIMAX methods. Figure 2.7 illustrates the power spectra of rainfall from the three regions and all-Indonesian (a box bounded by 15 °S, 8 °N, 90 °E and 140 °E). The spectra are shown with a logarithmic time scale for periods from 2 months to 30 years. Important time scales are indicated along the *x*-axis. Those important periods are 0.25, 0.5, 1, 2, 4 - 7 and 10 years, which represent three-monthly, semi annual, annual, biennial, ENSO related and decadal signals, respectively. Since the spectra are white noises or $AR(0)$ processes (a time series whose statistics (e.g., mean, variance, etc.) do not depend upon a fixed starting point, but only on time separation), all peaks are significant.

The spectrum of Region A has a strong annual signal. It dominates the overall pattern with a value more than six times any other maximum. The strongly prevailing annual signal of Region A suggests a strong homogeneous pattern as also shown by a small standard deviation of its annual cycle in Fig. 2.4.

The spectrum of Region B has strong annual and semi annual signals, with the semi annual one being slightly stronger than the annual. The strong semi annual signal is evident from the annual cycle, because of the presence of two peaks and two minimums (Fig. 2.4). Interestingly, there is a remarkable signal in a period of more than a decade. It is possibly due to decadal variability in the Indian Ocean.

The spectrum of Region C has two strong peaks and several weaker ones. The annual signal dominates the rainfall patterns of this region. The semi annual signal designates the presence of two peaks in the annual cycle. From the annual cycle, there is a peak in MJJ, and a smaller peak in NDJ. Other notable signals are the biennial and ENSO related signals (4 - 7 years) that contribute to the high standard deviations to the annual cycle of Region C. As shown in Fig. 2.4, Region C has large standard deviations from June to November.

Overall, the three regions show strong annual signals and, except Region A, semi annual signals. This is an indication that the DCM works well in isolating signals in a region based on its annual cycle. Region C shows the strongest ENSO signal, followed by Region A. In Region B, the ENSO related signal is suppressed, which is indicated by a minimum instead of a peak in the period range 4 - 7 years. The spectrum of all-Indonesian rainfall shows the dominance of annual and semi annual signals or monsoonal type of climate. The annual signal is three times stronger than the semi annual one. Low frequency signals (period more than one year) are stronger than high frequency signals (period less than one year). The strong decadal signals in all four spectra are in agreement with weak low frequency variabilities in EOF coefficients of PC1 (Fig. 2.5 and 2.6).

The spectra of the first two PC coefficients from both the EOF and VARIMAX methods are shown in Fig. 2.8. The units of *y*-axis are arbitrary. It is impossible to compare the amplitude values from both methods directly. Our interest is locations of significant peaks. The two spectra of EOF show strong annual and semi annual signals. Low frequency signals (period more than one year), semi annual signal and intraseasonal signal with a period of four-months in PC1 are overshadowed by the strong peak of the annual signal. Thus, compared to the result of the DCM, the EOF method gives a stronger annual signal. Although the three regions from the DCM are also obvious in PC1, the resulting spectra are different. The VARIMAX method shows both the annual and semi annual signals in the first two spectra. The signal strength is reduced from the annual, semi annual, and intra-monthly signals. The spectra of PC2 derived from both EOF and rotated EOF methods are comparable to the one of Region B, which shows annual and semi annual signals.

Hence DCM can be used to regionalize climate patterns based on the annual rainfall cycle. The DCM produces clear boundaries and indicates the dominance of the annual signal (to some extent the semi annual signal) in their spectra. If we compare the spectrum of the all-Indonesia with those of each PC, only PC1 from the VARIMAX method gives a comparable result. The

spectrum of all-Indonesia region exhibits particularly strong annual and semi annual signals. One may argue that the EOF analysis was done on the basis of monthly data, while our DCM was done on the basis of annual cycles. However, we utilized only the annual and semi annual components of the EOF and the VARIMAX methods. It is possible to do the DCM with the whole monthly data set, with the consequence of a lower threshold value for the same significance level. The results will differ according to the variability in each region. Regions with high variabilities such as Region C would not receive a comparable boundary as by the method applied here. The DCM is optimized in classifying regions according to their mean annual cycles. The high significance level of the threshold value contributes to regions with highly correlated grid cells. One major drawback of the method is the intermediate region. As stated before, the annual cycle of this region will be a flat annual one with two small peaks and two small minimums.

2.3.3 Local SST Responses

We are interested in semi annual and annual cycles of rainfall, the prominent time scales in this region. Therefore we also investigate the rainfall response to the ocean temperature in order to understand sea-air interaction locally and regionally. With regard to the local SST responses, we selected three ocean regions or boxes bounded by a certain longitude and latitude. The boxes chosen lie inside Regions A, B and C: South Molucca or Timor Sea (15 °S - 5 °S, 120 °E - 135 °E) for Region A, the South China Sea (1.5 °S - 8 °N, 102 °E - 110 °E) for Region B and Molucca Sea (6 °S - 2 °N, 122 °E - 135 °E) for Region C. In Fig. 2.9, the scatter plots of rainfall versus local SST are grouped by month for 33 years of monthly data (1961-1993).

In Region A, the rainfall is clustered by month in the temperature range from 25.6 °C to 30.3 °C and shows a SST-related function, as previously suggested by *Bony et al.* (1997a,b) and *Lau et al.* (1997). They showed that below 29 °C, the rainfall amount increases with SST, however the increase is not linear. Above 29.6 °C in contrast, the increase of local SST causes a decrease in the maximum rainfall amount. There is a clear distinction between the dry and the wet seasons. The dry season (MJJAS) has smaller SST than the wet one. Both SST and rainfall amount decrease from January to August and increase from August to December, as indicated by the mean annual cycle in Fig. 2.4. The rainfall in each month varies less in the dry season than especially in the wet season months in January and February. However, the majority of rainfall is distributed in narrow bands on both axes. This is in agreement with our previous result, which shows small standard deviations in the annual cycle of Region A all year long.

In Region B, there is no clear rainfall-SST relationship, especially from October to March. In DJF, high precipitation amount exists at low local SSTs, whereas in other regions SSTs are high in DJF. The rainfall is scattered from 25.5 °C to 30.5 °C and from as low as 1.27 mm/day

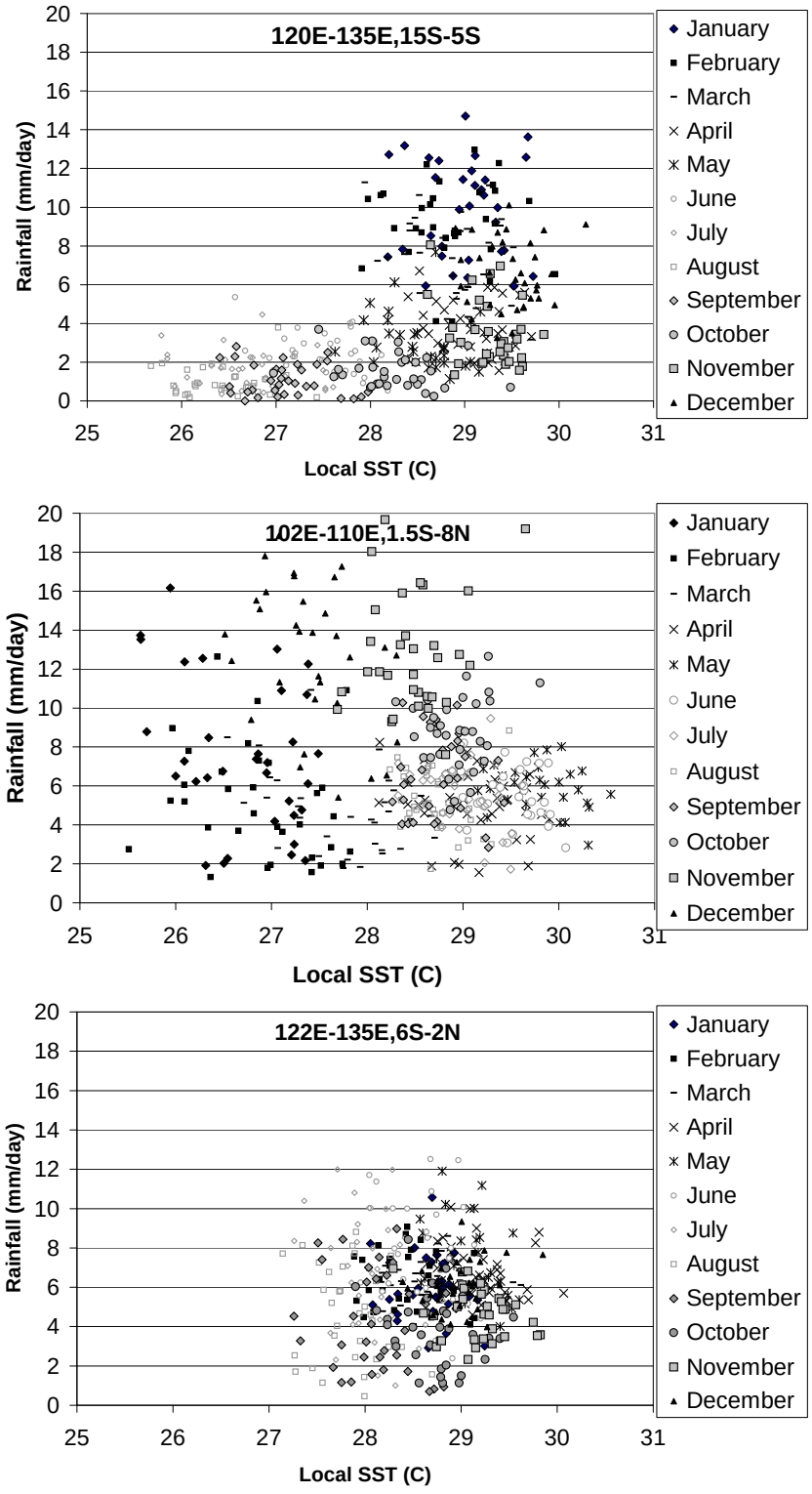

Figure 2.9: The monthly precipitation vs local SST patterns of the seas represent the three regions. Region A (top) is represented by the Timor Sea, Region B (middle) by the South China Sea and the Malaccan Strait and Region C (bottom) by the Molucca Sea.

to 24.7 mm/day. The range of SST in each month in this region is also high, reaching almost 3 °C (JFM) compared to 1.5 °C in Region A. From April to September, the data scatter less. The absence of a clear relationship between rainfall and SST in Region B suggests that the rainfall is independent of local ocean temperature and its variability. Possibly strong atmospheric forcing plays some role here.

Compared to two Regions A and B, Region C has the narrowest range in both axes especially in DJF. The rainfall is distributed from 27 °C to 30 °C and from 0.47 mm/day to 12.5 mm/day. There seems to be some weak relationship between SST and rainfall, but less obvious than in Region A. The scatter of rainfall amount is high from June to September as these months also show high standard deviations (Fig. 2.4).

In general, relationships between SST and rainfall appear in Region A and less obvious in C. It is important to investigate further other atmospheric factors that govern the rainfall pattern in Region B. This result is quite surprising because the area of our investigation is the maritime continent, which is surrounded by oceans. Since Region B is close to the Asian continent, the land ocean interaction may have impact on the rainfall pattern.

2.3.4 Seasonal and Remote SST Responses

In this subsection, we discuss rainfall responses to remote SST on a seasonal basis, i.e. for DJF, MAM, JJA and SON. This seasonal division does not exactly fit the local condition because in this region there are two monsoons in this region, the SE (MJJAS) and the NW monsoon (NDJFM), and two transitional months (April and October). Our analysis covers major oceans surrounding Indonesia up to the NINO3 region (5 °S - 5 °N, 150 °W - 90 °W) in order to see the ENSO response. The responses will be based on the correlation values between seasonal rainfall in each region and SST. Only correlation values above a certain significance level are presented.

For Region A, the rainfall responses to SST are given in Fig. 2.10. In DJF, there are significant negative correlations of rainfall to local SST (< -0.3) in the adjacent Indian Ocean and over Indonesia, from the South China Sea to the Banda Sea. The pattern indicates a relation to the Asian winter monsoon and the location of the ITCZ. Positive correlations exist for some parts in the central Pacific. In MAM, significant positive correlations exist east of Australia and in some parts of the northwestern Pacific. In JJA, the map shows two dipoles of correlation values. One is designated by opposite correlations between the maritime continent (positive) and the equatorial Indian Ocean (negative), while the other dipole is between again the maritime continent and the equatorial western Pacific. Positive correlations exist for the warm pool area, eastern Indonesia seas and the South Pacific Convergence Zone (SPCZ). Negative correlations exist for the NINO3 region and some parts of the Indian Ocean. In SON, these dipoles are

getting stronger with correlation values above $|0.7|$. In general, except in MAM, Region A experiences positive local SST influences on rainfall but also strong negative influences of ENSO and positive ones of SPCZ in JJA and SON. The responses to both phenomena are stronger in SON.

Region B, as shown in Fig. 2.11, exhibits only weak rainfall response to SST all year. There are only a few strongly positive responses in SON to SST in the West Pacific. Again, the weakest spatial pattern emerges for MAM. The result is consistent with the analysis to local SST (Fig. 2.9). Region B does not respond to ENSO at all, as already shown by a small amplitude in the rainfall spectrum for the ENSO time scale (Fig. 2.7).

Figure 2.12 shows the seasonal rainfall response in Region C to SST. In DJF significant signals exist in the western equatorial Pacific and the Indian Ocean. The response distribution in DJF is much wider and stronger than for Region A. The response in MAM is again the weakest, but stronger than for the other two regions. Strong signals appear in JJA and SON. In JJA, the spatial pattern shows smaller positive areas compared to Region A. However, the strongly negative western Pacific ENSO responses in JJA are stronger than in Region A. Thus Region C is more strongly influenced by ENSO in JJA than Region A. However, the response to Indian Ocean SST in JJA is smaller in Region C than in A. In spite of their opposite annual rainfall cycles, the SON responses in Region C and A are alike with two strong dipoles at the equator.

In general, MAM is the most unresponsive season with least significant correlation values in all three regions. The rainfall of Region A and C responds significantly negative (< -0.55) to ENSO events from June to November (an additional response exists in DJF for Region C). The confirmation of the seasonal or monthly variations of rainfall in all regions during ENSO events needs further investigations. High correlation from June to November in most parts of Indonesia suggests a good possibility for seasonal prediction using SST values. It may be possible to extend the prediction on a monthly basis, especially from June to November. *Haylock and McBride* (2001) showed that with regard to the relation of the all-Indonesian Rainfall index (63 stations) to the Southern Oscillation Index (SOI) during 1950-1998 the wet season (DJF) rainfall in Indonesia is inherently unpredictable. *Nicholls* (1981) presented evidence that interannual fluctuations of early wet season rainfall in the Indonesian Archipelago can be successfully predicted from prior observations of atmospheric pressure anomalies. It is shown that this predictability is related to SST anomalies.

Strong two dipoles in SON or boreal fall are associated to the atmospheric teleconnection between the Pacific and the Indian Oceans. *Arpe et al.* (1998) suggested that SSTs over the northern Indian Ocean are partly forced by SSTs over the tropical Pacific through ENSO related atmospheric forcing. The teleconnection strengthens during El Niño event and the teleconnection causes a dipole like variability in the Indian Ocean. In a non ENSO year, dipole like SST anomaly pattern exists in the boreal fall season, which can be explained by atmospheric forcing

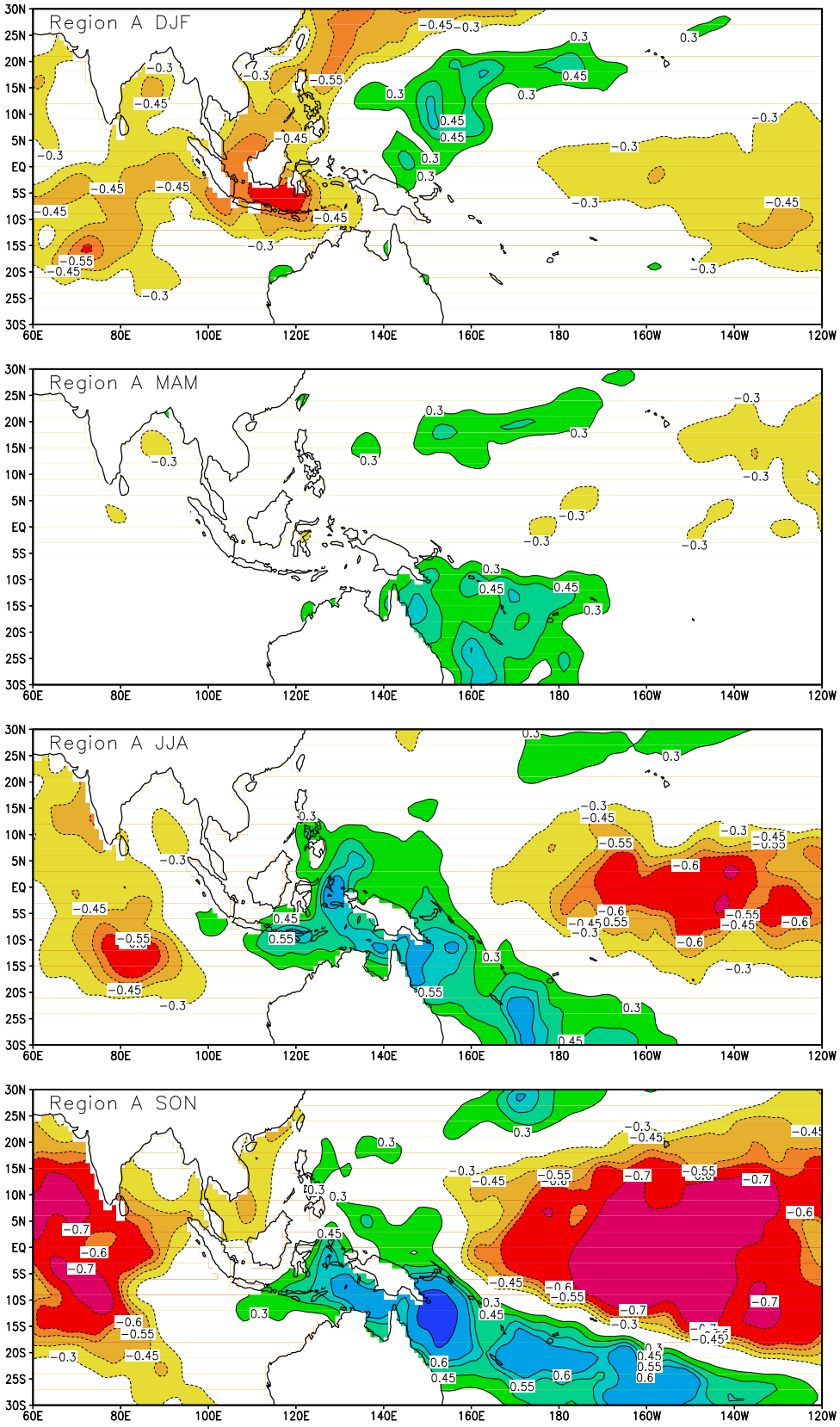

Figure 2.10: The seasonal correlation of rainfall in region A against SST. This figure shows correlation values |0.30|, |0.45|, |0.55|, |0.6| and |0.70|, which the first three correspond to 90%, 99% and 99.9% significant level for 33 years of the seasonal correlation.

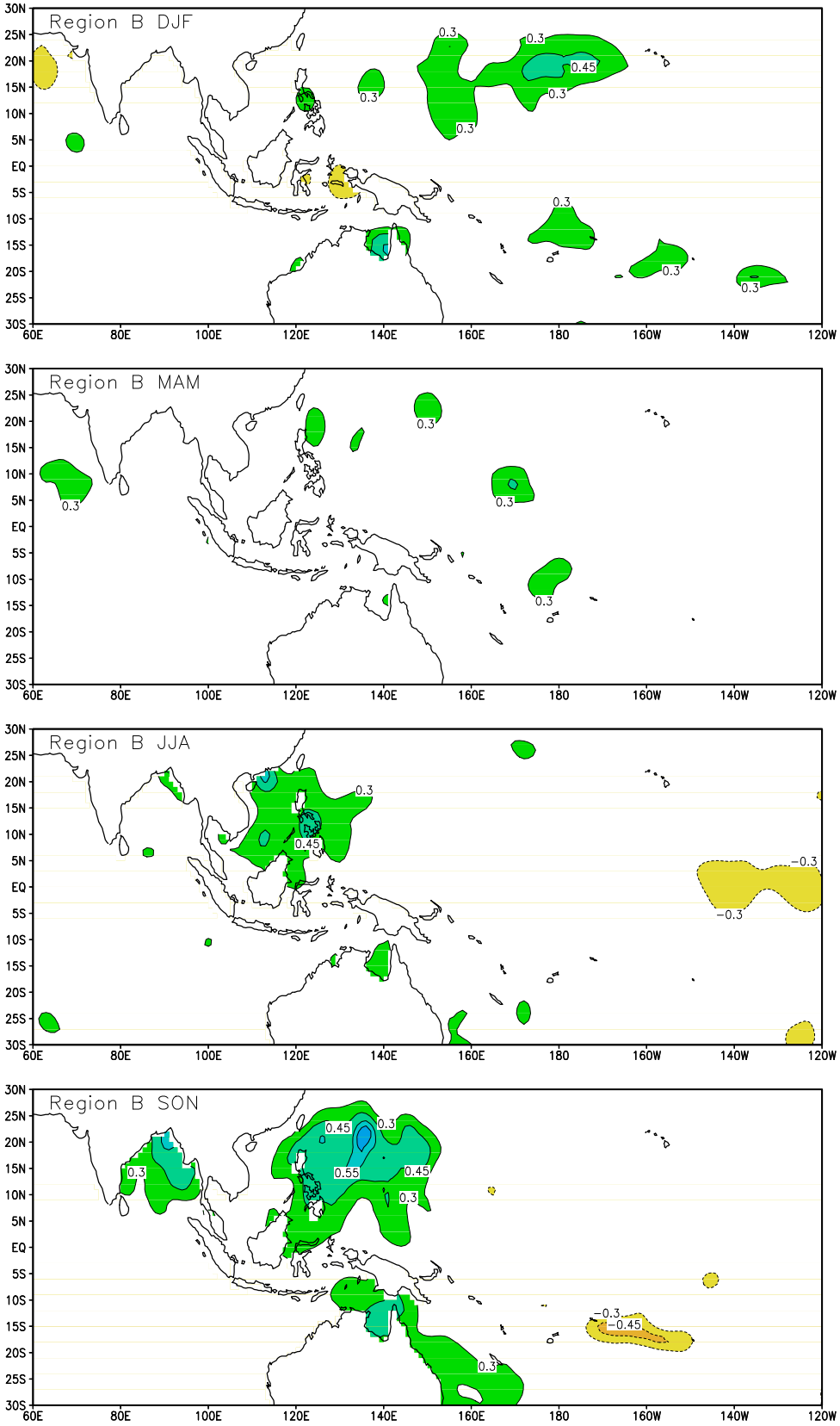

Figure 2.11: as Fig. 2.10, but for region B.

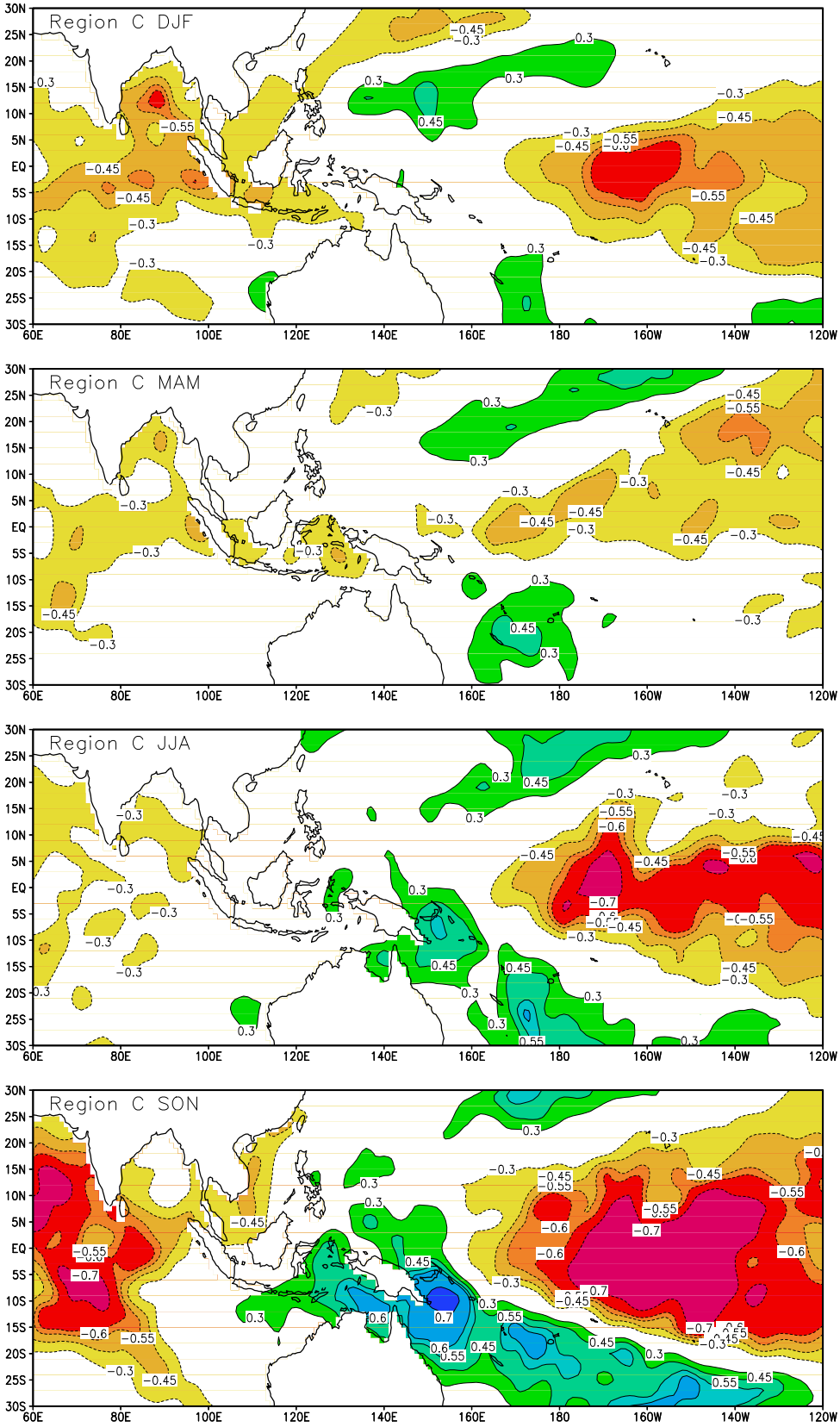

Figure 2.12: as Fig 2.10. but for region C.

(*Baquero-Bernal et al.*, 2002).

2.3.5 Ensemble ENSO Years

After seeing strong ENSO influence to Indonesian rainfall, we examine how the influence evolves on a monthly basis. With the definition of an ENSO year by *Roeckner et al.* (1996b), SST anomalies are classified as an ENSO event if they are greater than 1 °K in amplitude and persist for more than one year in the NINO3 region. As a result, the ENSO years from 1961 - 1993 are as follows:

El Niño year: 1965, 1969, 1972, 1982, 1987, and 1991

La Niña year: 1964, 1970, 1973, 1975, and 1988

After we have determined the ENSO years, we will divide the rainfall data into normal, El Niño and La Niña years and then we calculate an ensemble average of each classification above. The aim of this ensemble average is to give superimposed views of anomalies in each month. Using 46 stations data *Hamada et al.* (2002) analyzed rainfall anomaly during composite ENSO year in this region. The anomaly of each month is defined as

$$rain_{anom} = \frac{rain_{ENSO} - rain_{normal}}{rain_{normal}} \times 100 \tag{2.1}$$

From Fig. 2.13, the influence of El Niño is detected first in April with a sharp decrease of rainfall amount in northern Australia. In March there is no indication of El Niño, since there is no significant signal ($> |20\%|$) over Indonesia. There are some areas even with rainfall reductions up to 100%, i.e. totally dry. From May onward, the anomalies increase and diverge towards the Indonesian archipelago. The distribution of negative anomalies extends from southeast Indonesia westward and northward. By August the anomaly covers almost the whole country except North Sumatera and North Kalimantan or Region B. The distribution of highly dry areas varies among regions. However, most of the regions experience negative anomalies above 60%.

The maximum anomaly occurs in September. Anomalies of less than 60% cover the same areas as in August. Then from October onwards, the influence of El Niño decays and the influence disappears in December. In November, there is an indication of higher rainfall amounts coming from the north. November is the onset month of the Asian winter monsoon, as the ITCZ moves southward through this region. The significant positive anomaly of rainfall amount north of Indonesia suggests an El Niño - Asian monsoon interaction. The positive anomaly exists until February in the following year. There is a need of further investigations on this issue, which is beyond the scope of this paper.

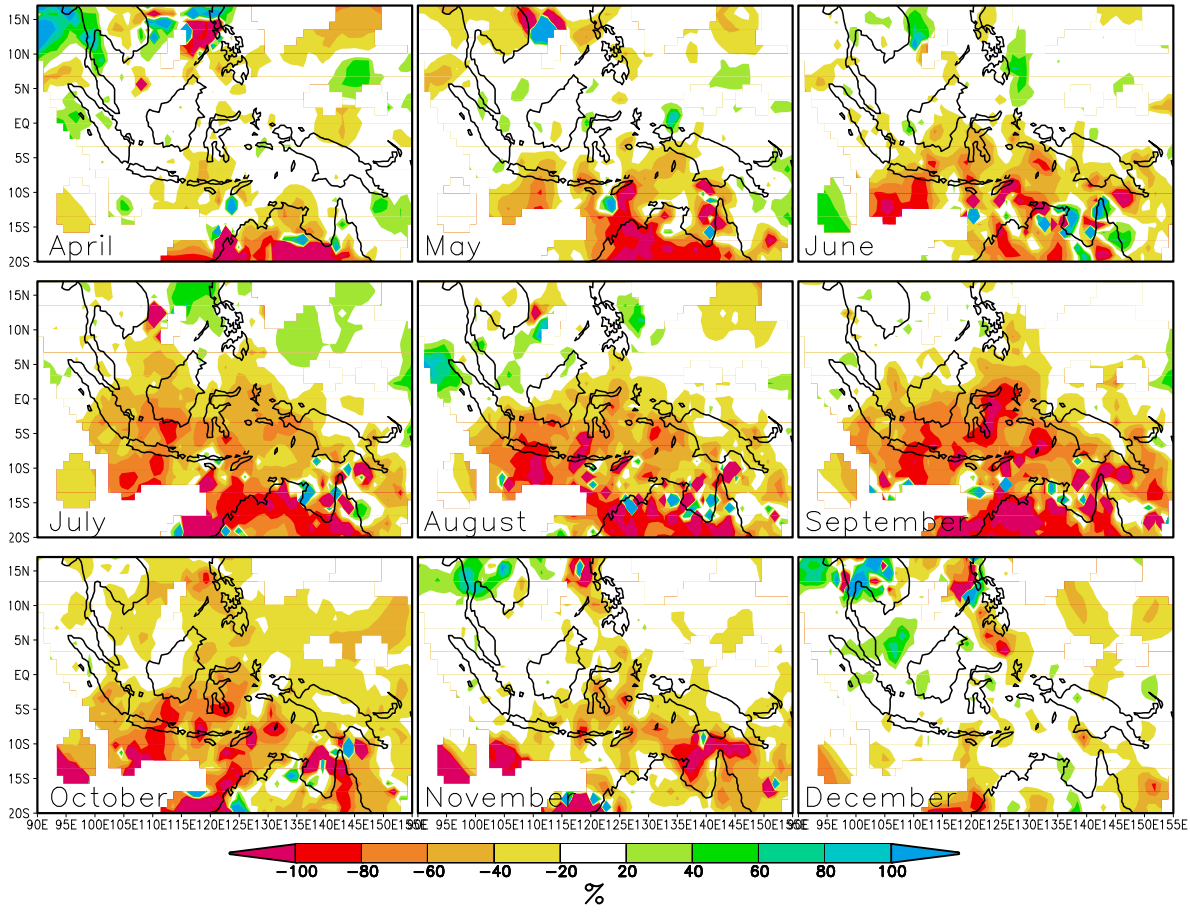

Figure 2.13: Percentage of rainfall anomaly during El Niño years.

Figure 2.14 shows that the situation in the ensemble La Niña year is the opposite of the ensemble El Niño year with a very similar spatial and temporal distribution. The La Niña signal or positive anomaly can be detected as soon as March, although these signals are not significant (mostly below 40% anomaly). Like in the El Niño year significant but now positive anomalies exist in north Australia in April. From that month onward, the positive anomalies increase spatially and in values, although some areas with unsignificant anomalies remain. The positive anomalies extend northward and westward from southeast Indonesia. There is an abnormity in July, where the rainfall in north Australia is negative, which reminds us of the similar case of July in the following El Niño year. That abnormity comes from La Niña years, which followed the El Niño years immediately (1970 and 1973). The difference between the pattern in July in this ensemble La Niña year and the July of the following El Niño year is a more positive anomaly in some other areas, which can be attributed to signals of the other three La Niña years.

The peak of the La Niña influence occurs like for El Niño in August and September, when the extension of highly correlated areas is largest. In September, most of the affected areas get more than double the rain. Like for El Niño, La Niña years do not affect rain in Region B. After September, the influence decay with time and the influence of La Niña has disappeared in

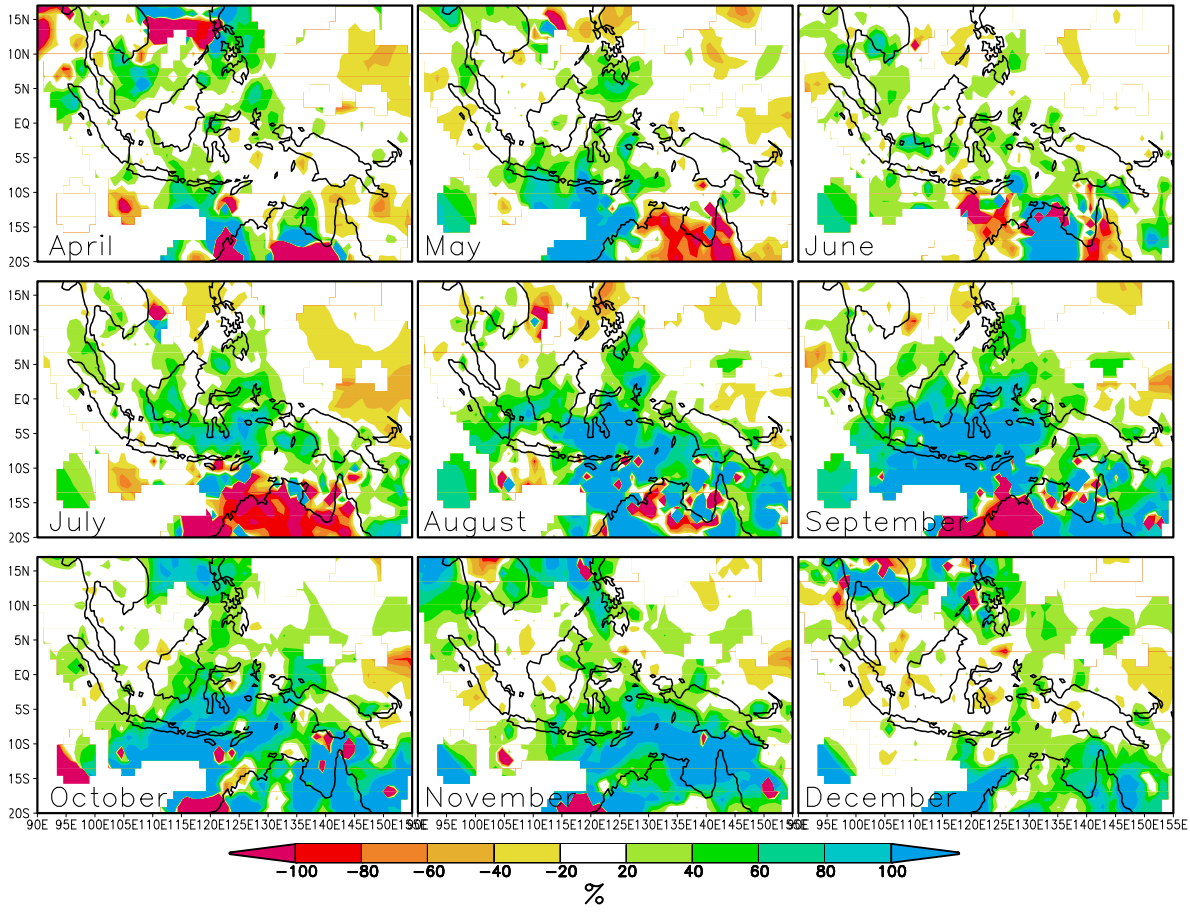

Figure 2.14: As Fig 2.13. but for La Niña years.

December. Interestingly, from October to December, the Asian winter monsoon is influenced by La Niña as in by El Niño but with opposite sign. Hence, areas, which receive more rain in winter during El Niño years, will receive less during October to December in La Niña years. This consistent feature indicates a possible negative influence of ENSO on the onset of Asian monsoon in the Southeast Asian region.

2.4 Discussion and Concluding Remarks

We have introduced a new regionalization method, the double correlation method (DCM). With DCM Indonesian rainfall climate can be divided into three clearly distinct regions. A comparison to the EOF and rotated EOF (VARIMAX) methods by analyzing their spatial patterns, and spectra has been done. Since the DCM gives strong annual and semiannual signals, the analysis of rainfall response to the ocean was also addressed. The analysis focused on monthly and seasonal response to the local and remote seas.

The DCM is reliable in isolating regions with a specific annual cycle of precipitation. The

method is simple and flexible. One can adjust the threshold correlation value to one's needs and use for other criteria. The resulting regions can have any shape. The spatial pattern of PC1 derived from the EOF and VARIMAX methods resembles, to some degree, regions found by DCM. Some limitations of the EOF method include patterns that are not dominant (they only explain 30.1% of all variance) and that have no clear boundaries. The DCM also provides a better spectrum in comparison to the other methods both for the spectrum of each region and all-Indonesian rainfall. The spectra from the DCM show strong annual and semiannual signals as the case of the spectrum for all-Indonesian rainfall. The VARIMAX method produces similar spectra to the all-Indonesian one and a similar boundary (PC2) for Region B to the DCM.

The DCM delineates three distinct regions of Indonesia with a characteristic annual cycle of precipitation. Region A, the southern part of Indonesia influenced by the SE (Australian) monsoon; Region B, the northwestern part of Indonesia with two precipitation peaks per year; and Region C, the Molucca region (western Pacific Region). Except Region C all other parts of Indonesia experience strong influences from the Asian monsoon or ITCZ.

Region B has remarkably small standard deviations and a strong annual and semiannual signal in its spectrum and does not respond to remote SST. From the diagram of monthly rainfall versus local SST and from the seasonal analysis, there is no consistent feature apparent in this region. The other two regions, however, respond strongly and thus promise capability for monthly to seasonal climate prediction. This capability is least in MAM or spring. This idea follows the lowest SST responses of each region in MAM compared to other seasons. This phenomenon is known as the spring predictability barrier. The spring predictability barrier refers to a lower skill generally observed for predictions that extend through boreal spring (see i.e. *Webster and Yang* 1992; *Balmaseda et al.* 1995; *Flügel and Chang* 1998; *Latif et al.* 1998; *Goddard et al.* 2000). *Latif and Graham* (1992) in a GCM experiment found that between April and June, the correlation coefficients between observed and predicted SST in the Pacific Ocean are much reduced in comparison to other periods, irrespective of when the prediction has been started. *Haylock and McBride* (2001) found that the correlation between all-Indonesian rainfall index (63 stations) and the SOI is lowest in DJF and MAM and higher for the other two seasons.

Local SST ranges for which rainfall occurs are from 25.7 °C to 30.5 °C. Region C has the narrowest range of SST and of rainfall variabilities. A narrow range of SST variability is susceptible to the effect of global climate change, which is presently estimated as an increase of the global surface temperature between 1.4 and 5.8 °C in the next hundred years (*Cubasch et al.*, 2001, Fig. 9.14). Whereas the rainfall in this archipelago occurs near the critical temperature of 29.6 °C, above which an increase in SST means a decrease of the rainfall amount. Thus seasonal and annual cycle changes of rainfall are highly possible in the future for Regions A and C.

Strong negative rainfall responses in Regions A and C to higher SST in the NINO3 area (the

warm phase of El Niño event) for northern hemisphere summer and autumn (JJASON) lower an already low rainfall and thus cause drought. On the other hand, during La Niña or the cold phase, the dry season gets considerable more rainfall. The ENSO influence to Indonesian rainfall lasts only until November, although some other parts of the world may still receive the impact later. Surprisingly, Region B does not experience any ENSO impact. If we look at Fig. 2.3, Regions A and C coincide with the ENSO affected parts from the result of the earlier assessment by *Ropelewski and Halpert* (1987). This paper advances further with the analysis of seasonal effects of ENSO.

Indonesian rainfall responds strongly to the remote ocean SST in the warm pool, the NINO3 and SPCZ area in regions A and C. The two dipoles in the rainfall SST response pattern indicate the Walker cell. The Walker cell is a tropical atmospheric phenomenon centered in the warm pool near Indonesia. The two dipoles show that with the Walker cell, the variability of precipitation from the Pacific and Indian oceans are important. Strong activities of this cell, which affect rainfall pattern in Indonesia, occur especially during the northern hemisphere summer (JJA) and autumn (SON). Moreover, that period is the period of intense influence of ENSO. Thus, there is a need for a further research on the interaction among ENSO, ITF, Walker cell and their influences on Indonesian rainfall, which is beyond the scope of this paper.

Chapter 3

Variability of Indonesian Rainfall and the Influence of ENSO and Resolution in ECHAM4 Simulations and in the Reanalyses

Abstract

A study on the skill of the atmospheric general circulation model ECHAM version 4 and two reanalyses in simulating the Indonesian rainfall is presented with comparisons to 30 years of rain gauge data. The reanalyses are those performed by the European Centre for Medium-Range Weather Forecasts and of the National Centers for Environmental Prediction jointly with National Center for Atmospheric Research. This study investigates the skill of the reanalyses and ECHAM4 with regard to regional, annual and interannual variability of rainfall and its responses to El Niño-Southern Oscillation (ENSO) events. The study is conducted at two resolutions, T42 and T106.

A new regionalization method called the double correlation method is introduced. With this method, the Maritime Continent is divided into three climate regions, the south monsoonal, the northwest semi-monsoonal and the Molucca anti-monsoonal region. Except over Molucca, the reanalyses and ECHAM4 simulate these annual rainfall patterns quite well.

The three regions are used to study the variability of Indonesian rainfall and to measure the skills of the reanalyses and ECHAM4. The skill of rainfall simulations in Indonesia depends on the region, month and season, and the distribution of land and sea. Higher simulation skills are confined to years with ENSO events. Except for the region of northwest Indonesia, the rainfall from June (Molucca) and July (south Indonesia) to November is influenced by ENSO, and it is

more sensitive to El Niño than La Niña events. The observations show that the Moluccan region is more sensitive to ENSO, receives a longer ENSO impact and receives the earliest ENSO impact in June. The ENSO impact will diminish in December. It is found that the reanalyses and the climate model simulate the seasonal variability better than the monthly one. The seasonal skill is the highest in June/July/August, followed by September/October/November, December/January/February and March/April/May. The correlations usually break down in April (for monthly analysis) or in spring (for seasonal analysis). In general the performance of ECHAM4 is poor, but in ENSO sensitive regions and during ENSO events, it is comparable to the reanalyses. The introduction of a higher resolution land-sea mask improves the model performance. Besides rainfall variability, signatures of the ENSO impact, the spring correlation breakdown and annual cycles are better represented by the higher resolution model.

3.1 Introduction

The Indonesian Maritime Continent is an interesting region for climate research. In atmospheric dynamics, this region is influenced by both the Hadley and Walker cells. The seasonal to interannual variabilities of Indonesian rainfall are characterized mainly by the monsoon (*Ramage*, 1971) and the El Niño-Southern Oscillation (ENSO; *Philander* 1989; *Ropelewski and Halpert* 1987, 1989; *Halpert and Ropelewski* 1992). Indonesia experiences two monsoons every year. They are the wet monsoon from November until March, which coincides with the presence of the Inter-Tropical Convergence Zone (ITCZ) in this region (*Asnani*, 1993), and the dry monsoon from May until September, when the dry southeasterly wind blows from Australia. *Ramage* (1971) and *Cheang* (1987) mentioned April and October as the transitional months. Annual and interannual climate variability in Indonesia is quite unique, as it is not homogenous over the whole region (*Wyrtki*, 1956) and the coherence of rainfall patterns varies with the season (*Haylock and McBride*, 2001). ENSO contributes to the rainfall pattern in this area and its influence is interconnected with the monsoons (*Lau and Nath*, 2000). During El Niño (La Nina) events or warm (cold) phases, this region experiences lower (higher) rainfall than in other years (*Gutman et al.*, 2000). So far, discussions of Indonesian rainfall variability in relation to ENSO have used the Southern Oscillation index (SOI). For example *Braak* (1919); *Berlage* (1927); *Schell* (1947); *Reesinck* (1952) and later *Nicholls* (1981) reported a good correlation between rainfall variations in Indonesia and the SOI. Here, we will use another ENSO predictor, the NINO3 sea surface temperature (SST), which has been used by many ENSO forecasting groups (*Barnston et al.*, 1999).

Recent analysis extends to include atmospheric general circulation model (AGCM) simulations. *Goddard et al.* (2000) gave a comprehensive review of the seasonal and inter-annual skill of climate simulations over recent decades, including the performance of AGCMs in general. *Barnett*

et al. (1997) did a predictability analysis of mid-latitude climate on ensembles of simulations with the ECHAM4 (*Roeckner et al.*, 1996a) and the NCEP atmospheric model and found that the models' skill is higher by about 50% during strong SST events in the tropical Pacific. *Moron et al.* (1998) examined the skill and reproducibility of seasonal rainfall in the tropics for the ECHAM4 model at resolution T30. They found that with regard to the June to September interannual variability over southeast Asia from Pakistan to Taiwan (including Indonesia), the skill of ECHAM4 is mainly confined to years of strong tropical Pacific SST variability. Nonetheless there is yet no specific study addressing the influence of higher resolution on the skill of a GCM in the region.

There have been many studies on the quality of the simulated rainfall for the National Centers for Environmental Prediction and National Center for Atmospheric Research (NCEP-NCAR) reanalysis (*Kalnay et al.*, 1996) and the ERA15 (*Gibson et al.*, 1997) from the European Centre for Medium-Range Weather Forecasts (ECMWF). *Janowiak et al.* (1998) found good agreement with regard to large scale features and substantial differences in regional precipitation between the NCEP reanalysis and observation from the Global Precipitation Climatology Project (GPCP; *WCRP* 1990). *Stendel and Arpe* (1997) found that ERA15 precipitation fields were superior in the extra tropics to other reanalyses when compared with GPCP data. *Annamalai et al.* (1999) found the ERA15 to be better than other reanalyses in describing the Asian summer monsoon, while *Newman et al.* (2000) point to a substantial problem with the precipitation in the warm pool area near the Maritime Continent by all reanalyses.

The purpose of this chapter is an assessment of the performance or skill of the two reanalyses and the Max-Planck-Institute's atmospheric model ECHAM4 in simulating the variability of Indonesian rainfall as documented by gauge observation and how their performances vary in regard to the monsoon, ENSO, ITCZ and model resolution. The study will focus on monthly and seasonal means, but will examine interannual aspects of rainfall. One of the problems in simulating the Indonesian rainfall is the land-sea representation. Most of the areas are highly complex with oceans and chains of islands, which are difficult to represent even by a high-resolution model. Thus, it is important to study the role of the model resolution. Due to the high level of heterogeneity in the region, it has to be speculated that the typical horizontal resolution used in GCMs cannot adequately represent the complex interactions of mountains, air and sea. We have therefore included a higher resolution simulation with the same model in order to determine the ECHAM resolution required to make useful simulations in the region and classified regions according to major climate controls using rain gauge data.

The outline of this chapter is as follows. Section 2 discusses data and the ECHAM4 model, section 3 regional and annual climate cycle analyses, section 4 inter-annual variability and section 5 seasonal and monthly variability. In section 6 the relation of rainfall variability to ENSO is investigated while section 7 discusses the land-sea mask effect at different resolutions. Finally, section 8 presents conclusions.

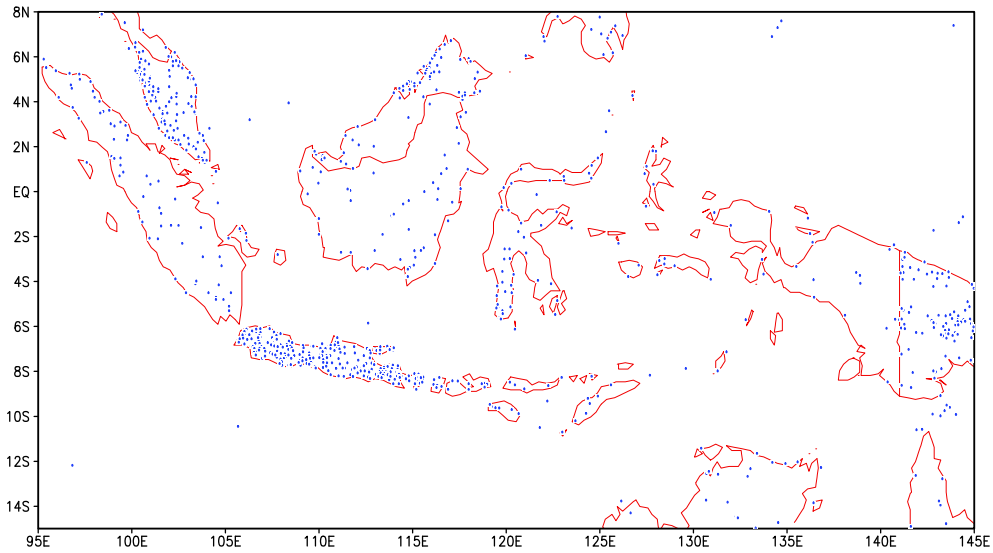

Figure 3.1: The distribution of rain gauge stations over the Indonesian archipelago or over 15S-8N, 95E - 145E with 884 stations.

3.2 Data and Model

The data used in this study are monthly rainfall data collected by the Indonesian Meteorological & Geophysical Agency (BMG) at 526 stations all over Indonesia, and monthly mean rainfall data from the WMO-NOAA project on The Global Historical Climatology Network (GHCN; *Vose et al.* 1992) from 1961 to 1993. In our area of interest (15 °S - 8 °N and 95 °E - 145 °E), there are 884 rain gauges (Fig. 3.1). These data are gridded to match the other datasets at T42 and T106 resolutions.

This study uses two reanalysis data sets. The first is ERA15 (*Gibson et al.*, 1997), which is available at the horizontal resolutions of T42 and T106 (the original calculation) or equivalent to 2.8125 ° and 1.125 ° in the tropics, respectively, from 1979 until 1993. The second one is the 40 year NCEP reanalysis (NRA; *Kalnay et al.* 1996), from which the time period from 1961 to 1993 with a fixed spatial resolution of T62 (equivalent to 2.5 ° in the tropics) is used. For comparisons with other T42 products, a regridding procedure is applied to change the NRA grid format from T62 into T42.

The ECHAM4 (*Roeckner et al.*, 1996a) model is a spectral model with a triangular truncation at the wavenumbers 42 (T42) and 106 (T106). For the vertical representation a 19 level hybrid sigma-pressure coordinate system is used. The time integration is carried out using a semi-implicit ”leap-frog” method. The orography and the land-sea mask are calculated from a high resolution (1 km) US Navy data set. Unfortunately, due to limited computer resources, the T106 output is available only for 10 years from 1979 - 1988, while the coarser resolution (T42) is available from 1979 - 1993 (see Table 3.1). The ECHAM4 model was driven by interannu-

Table 3.1: Resolutions and time span of data sets used

	Resolution	Time span
Rain gauge data	T42 / T106	1961 1993
ERA15	T42 / T106	1979 1993
NRA	T42 (regridded from T62)	1961 1993
ECHAM4	T42 / T106	T42: 1979 1993; T106: 1979 1988

ally varying SSTs from the Atmospheric Model Intercomparison Project 2 (*Gates*, 1992; *Gates et al.*, 1999) at both resolutions.

In addition, SST data from the GISST2 (Global Ice and Sea Surface Temperature) dataset (*Rayner et al.*, 1996) are used. This dataset is compiled from SST observations from 1903 - 1994 with a spatial resolution of 2.50, and is used to determine the ENSO years. The resolution of this data set is not of main concern here, because only an area average on NINO3 (5 °S - 5 °N, 150 °W - 90 °W) is taken into account. With the definition of an ENSO year by (*Roeckner et al.*, 1996b), SST anomalies are classified as an ENSO event if they are larger than 1 °K in amplitude and persist for more than one year in the NINO3 region. As a result, the ENSO years from 1961 - 1993 are as follows:

El Niño year: 1965, 1969, 1972, 1982, 1987, and 1991

La Niña year: 1964, 1970, 1973, 1975, and 1988

3.3 Regional Annual Cycle Analysis

Due to a high horizontal variability in this region (*Haylock and McBride*, 2001), there is a need to classify regions according to their annual rainfall cycles. The first regionalization attempt was made by *Wyrtki* (1956), when he divided the Indonesian waters into nine subregions. Here we introduce the double correlation method in which it is noted that grid cells with similar annual cycles are likely to respond similarly and homogeneously to a climate phenomenon and shall belong to a region. Each of the regions must be distinct from the others and each is influenced by the specific dominant climate phenomenon acting on it. To establish a strong climate pattern, this section utilizes long term observations from 1961-1993.

With the double correlation method, we look for a region, in which the annual cycles of its grid cells are correlated among themselves above a certain threshold value. For higher efficiency,

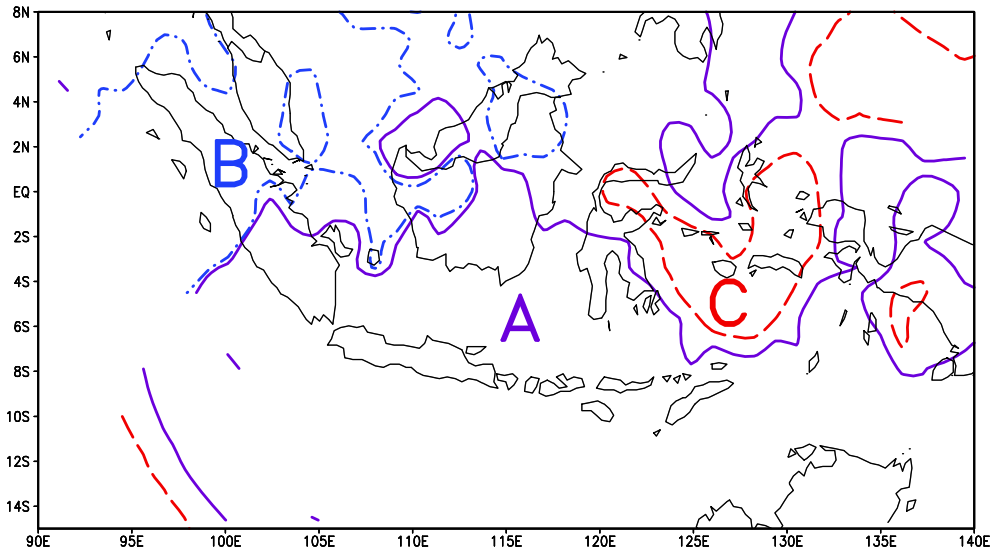

Figure 3.2: Three climate regions using the double correlation method, which divides Indonesia into region A (solid curve); the southern monsoonal region, region B (dashed-dotted curve); the semi-monsoonal region and region C (long dashed curve); the anti monsoonal region.

rather than correlating all grid cells to each other, we first select some reference cells. Secondly we correlate all other cells to these reference cells based on their annual cycles. Cells that are correlated above a certain threshold value are belonging to a region. Thirdly we correlate all grid cells again with the mean annual cycle of the resulting region using the same threshold value. The aim of the second correlation is to produce a region independent of the choice of the reference grid. The threshold value should be the highest correlation value that produces no overlapping boundaries. In this paper the threshold value chosen is 0.67, which is the 99% significance level in our data from only one correlation. Thus, with double correlations, the level of significance is much higher. The result of this method is illustrated in Fig. 3.2, where the Maritime Continent is divided into three climate regions, the southern Region A, the north-western Region B and the Moluccan Region C. From now on, all analysis will use these three regions.

In order to show the similarity of the approaches, the first two Principal Components (PC) of Empirical Orthogonal Function (EOF) analysis from monthly rainfall over 25 °S - 25 °N and 20 °E - 180 °E were also calculated (not shown). PC 1, which represents the annual pattern, has 30.08% of all the variances and shows Region C over Molucca. The areal extent of this region is similar to Region C of the present method. Additionally, PC 1 shows Regions A and B (the positive part). PC 2 with 8.09% of total variance also shows Region B and represents the semi-annual patterns such as the double peaks of Region B. Those two PCs only explain less than half of the total variance because we took the whole dataset of 33 years. Other PCs explain non-annual patterns, while we are aiming only at the annual patterns for our regionalization.

The annual cycle given by observed data at T106 resolution in Region A is shown in

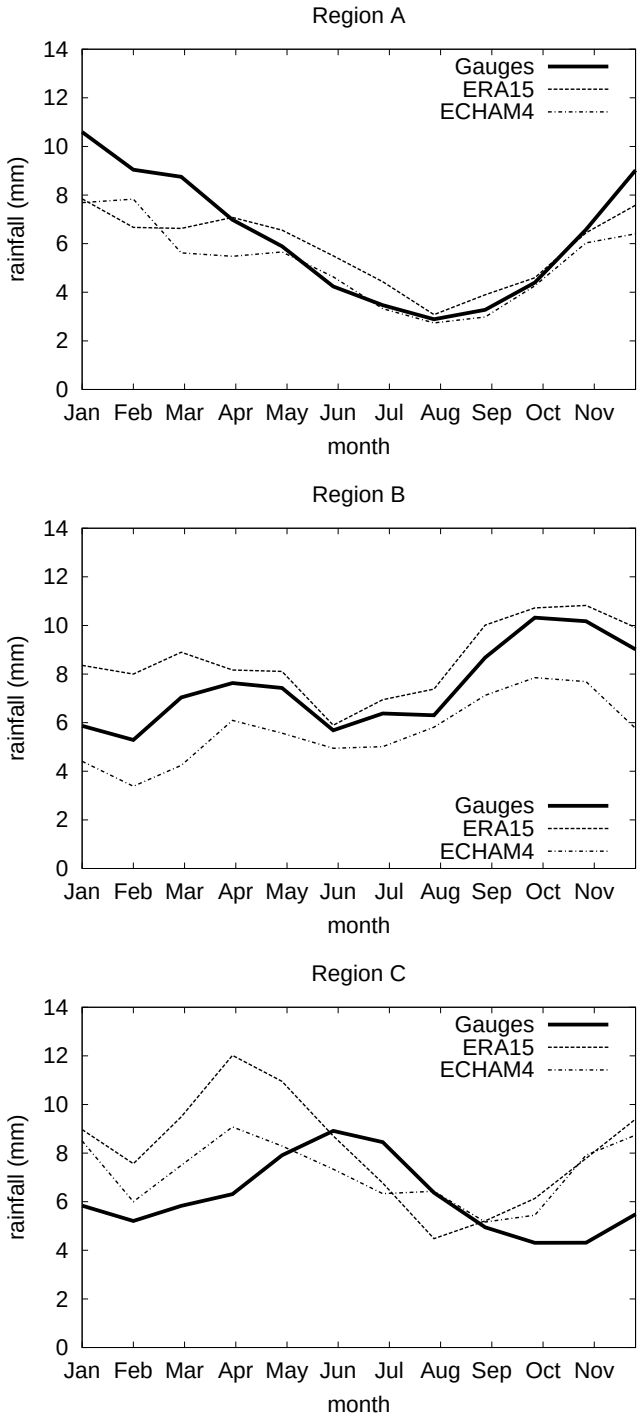

Figure 3.3: The annual rainfall cycle (mm/day) of each region at T106 resolution for observation with rain gauge (bold), ERA15 (thin dashed) and the ECHAM4 simulation (thin dot-dashed).

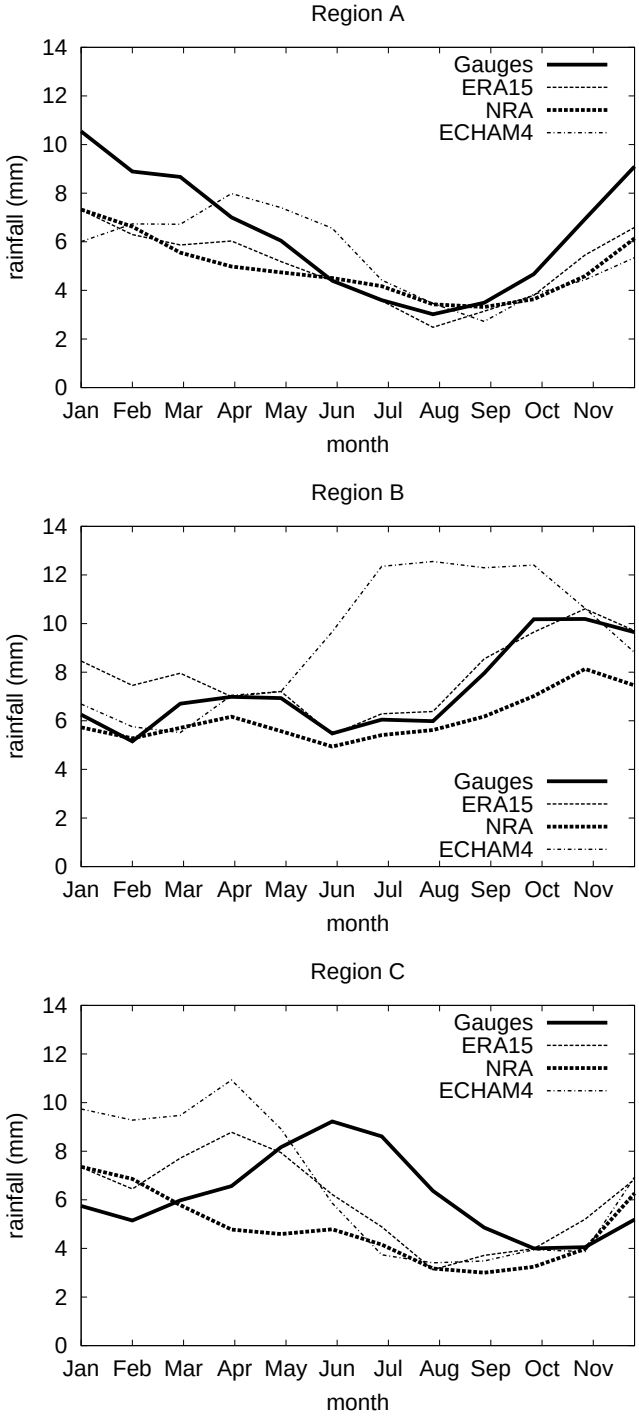

Figure 3.4: As Fig. 3.3, but for the T42 resolution, and NRA (bold dashed).

Fig. 3.3. We observe maximum in December/January/February (DJF) and a minimum in July/August/September (JAS). This illustrates two monsoon regimes: the wet northeast monsoon from November to March (NDJFM) and the dry southeast monsoon from May to September (MJJAS). With a strong monsoonal cycle and the southern location, we refer to this region as the southern monsoonal region. The annual cycle of Region B has two peaks, in October/November/December (OND) and March/April/May (MAM). The peaks in OND and in MAM represent the southward and northward movements of the ITCZ respectively. *Davidson et al.* (1984) and *Davidson* (1984) described in detail the ITCZ movement in this region in boreal winter. We thus call Region B the northwest semi-monsoonal region. We also note in Fig. 3.3 that Region C is quite different from the others and has a peak in May/June/July (MJJ), and we therefore refer to this region as the Molucca anti-monsoonal region.

Along with the annual cycle from observations, Fig. 3.3 shows the annual cycle of ERA15 and ECHAM4 at T106 resolution over corresponding regions of Fig. 3.2. Patterns in Region A of ECHAM4 and ERA15 agree well with observations although the peaks of the wet season are less than observed. It is interesting to note that in Region A ERA15 and ECHAM4 show a very similar annual march. In Region B, ERA15 produces more rainfall than observations throughout the year in contrast to less rainfall given by ECHAM4. However, their correlations with regard to time with observations are above 0.80, which means that the representation of the annual cycle is excellent. In Region C, the performances differ considerably. There the annual peak of ERA15 and ECHAM4 is found in MAM instead of in MJJ, and there is a strong overestimation of December rainfall. It is possible that these peaks represent an erroneous movement of the ITCZ.

At T42 resolution (Fig. 3.4) the reanalyses and model behave differently. In Region A, the reanalyses agree well and follow the observed annual cycle and they are particularly good in JAS, but again underestimate the wet DJF. ECHAM4 has a peak in MAM instead of NDJ and extends the wet season far too long into May and June. In Region B, ECHAM4 considerably overestimates rainfall from June to October i.e. during the dry period. In this region ERA shows an almost perfect annual cycle. NRA has a similar annual cycle as ERA15 but underestimates the peak in OND. In Region C, ECHAM4 and ERA15 again misplace the peak observed in June and July. The worst correlation in Region C is that of NRA, which is considerably different from to observations. In fact, NRA's annual cycle is similar to that in Region A. Table 3.2 summarizes the reanalyses and model skills with regard to their annual cycles. The reanalyses simulate temporal patterns of Region A and B quite well, while ECHAM4 shows large errors in Region B. However, neither reanalyses nor model show good agreement in Region C.

In summary of Fig. 3.3 and 3.4, NRA has a poorly pronounced annual cycle with no clear peak. NRA was produced at T62 and was truncated to T42, so should have the benefit of a higher resolution land-sea mask. Obviously, this information is not passed on to the atmosphere. In Region C ERA15 has a clear peak at both resolutions, but it occurs too early in the year. ERA15

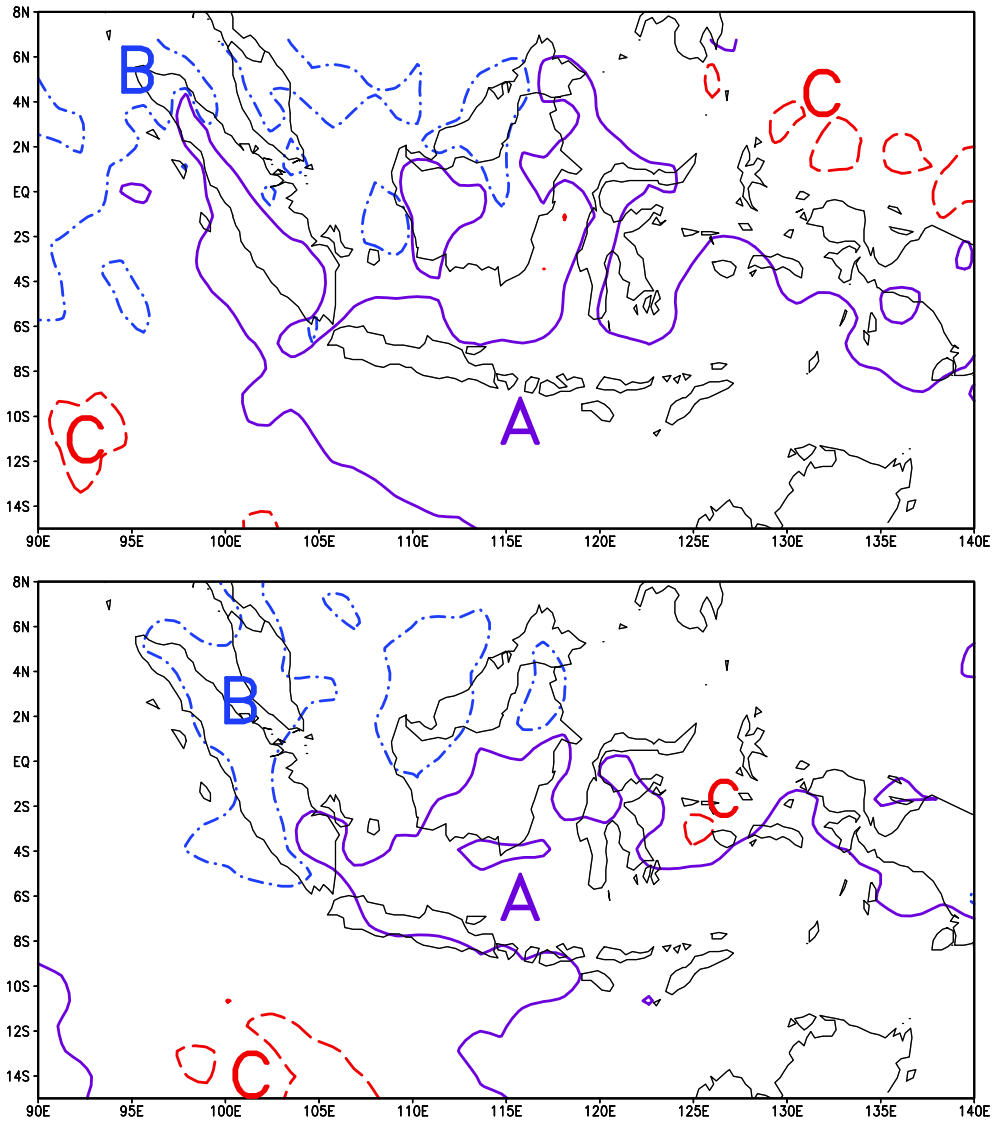

Figure 3.5: As Fig. 3.2, the climate regions at the T106 resolution as simulated by ERA15 (above) and ECHAM4 (bottom) using annual rainfall patterns of gauges as shown in Fig. 3.3.

at a coarser resolution has a less pronounced annual cycle. The performance of ECHAM4 at higher resolution resembles that of ERA15, although less pronounced, while ECHAM4 at lower T42 resolution disagrees with observations in all three regions.

This analysis can be used to explain correlation values in Table 3.2 or the deviations of their annual cycles in Fig. 3.3. Fig. 3.5 shows the regionalization that would result from ERA15 and ECHAM4 at T106 using the corresponding annual cycle procedure as in observations (Fig. 3.3). In Fig. 3.5 for both ERA15 and ECHAM4 Region A and B, as expected, are located in southern and northwestern Indonesia, respectively. Meanwhile the climate of Region C is not in the proper location in the ERA15 results. ECHAM4 represents Region C climate only for one grid cell in central Molucca plus some areas south of Indonesia. These results show that ERA15 and ECHAM4 cannot perform well with regard to Region C in the previous analysis. ECHAM4

Table 3.2: Correlations of ERA15, NRA and ECHAM4 in three regions with the observed annual cycles. One, two and three asterisks indicate correlations at 90%, 99% and 99.9% significance levels, respectively.

	Region A			Region B			Region C		
	Obs - ERA15	Obs - NRA	Obs - ECHAM	Obs - ERA15	Obs - NRA	Obs - ECHAM	Obs - ERA15	Obs - NRA	Obs - ECHAM
T42	0.97***	0.94***	0.56**	0.86***	0.97***	0.32*	0.27	0.01	0.13
T106	0.91***	-	0.93***	0.88***	-	0.88***	0.27	-	0.2

gives a broader Region B while ERA15 gives a broader Region A, the latter indicating a wider dry area or area affected by the southeast monsoon and the former indicating a longer period of wet northeast monsoon. Another feature are broader intermediate regions in both cases. The expected annual cycle of the intermediate region will be a flat one with two small peaks. Similar analysis at T42 resolution (not shown here) can be used in explaining values in Table 3.2 and patterns in Fig. 3.4.

3.4 Interannual Variability

The analysis of interannual variability in this study is based on monthly and seasonal (three-monthly) averages for the three climate regions. Fig. 3.6 to 3.8 show interannual variations of seasonal means of rainfall for different seasons from observations from 1961 to 1993, two reanalyses and ECHAM4 at T42. Values represent the interannual variations of the rainfall after removing their averages and trends in units of a standard deviation (σ). In Fig. 3.6 for Region A there are good correlations between observations and NRA in JJA and SON. Except for a weak El Niño of 1969, El Niño years coincide with rainfall below $-\sigma$ in JJA and SON. In general, the two reanalyses and the model simulation have the worst skill in MAM and the best in JJA. During extreme El Niño events such as in 1982, all show good skills from JJA and simulate this event quite well ($< -\sigma$) as it extends to DJF, except ECHAM4 in DJF. In the case of the weak 1987 El Niño, all simulate the event only in JJA and SON. The impact of La Niña is not as clear as El Niño's and occurs only in SON. The La Niña events of 1964, 1970, 1973 and 1975 have clear signals in SON. In general, the impact of El Niño on Region A is greater than the impact of La Niña. *Chen and van den Dool* (1997) indicated significantly higher predictability during El Niño phases than during La Niña.

Fig. 3.7 shows similar information for Region B. Agreement between observed precipitation and reanalyses or ECHAM4 is low in all seasons. This region seems to show no El Niño effects

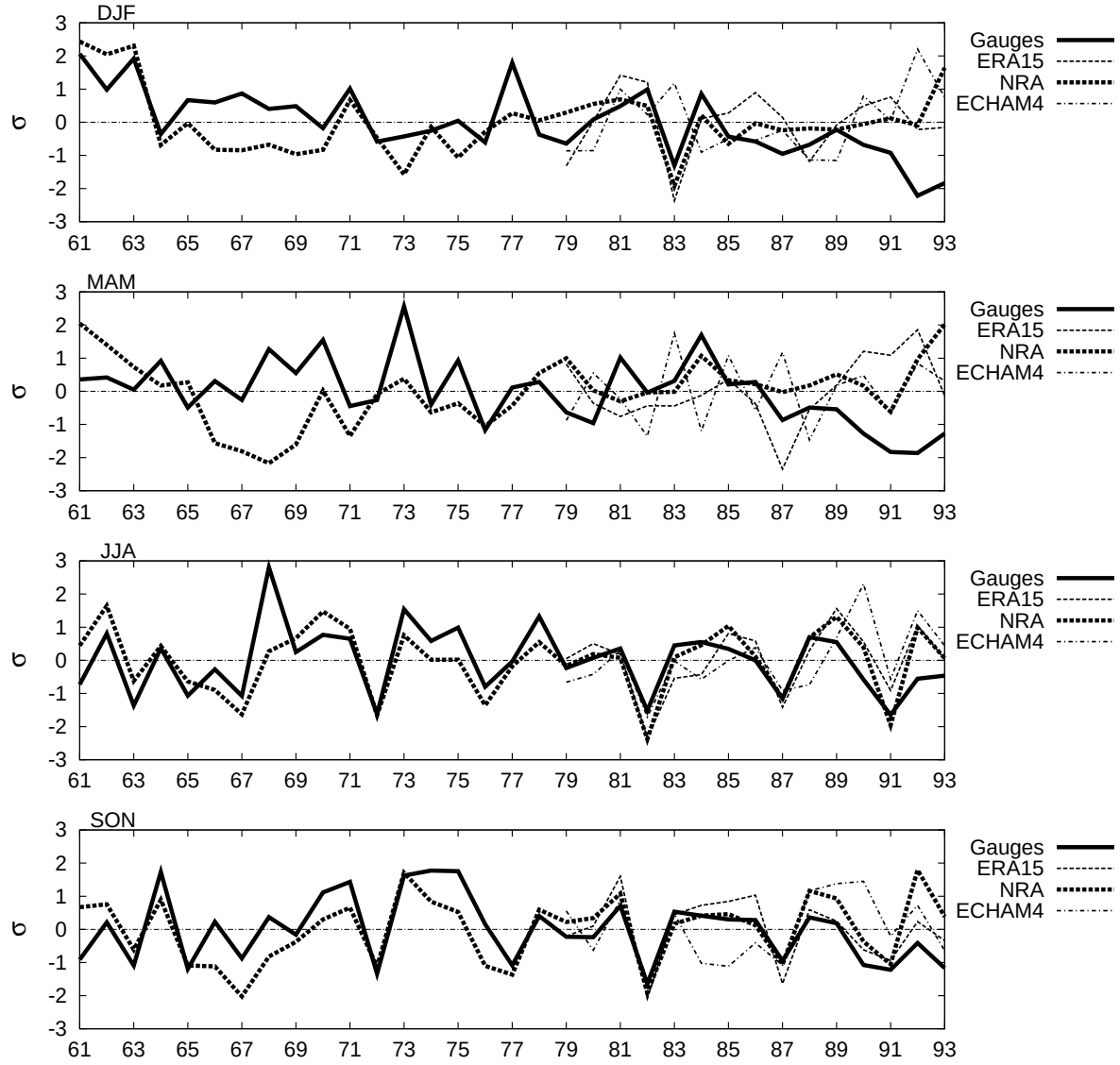

Figure 3.6: The inter-annual variation indices of seasonal rainfall in region A at T42 resolution for observation (bold solid), ERA15 (thin dashed), NRA (bold dashed) and ECHAM4 (thin dot-dashed). The ordinates are the variation of rainfall in units of standard deviation (σ).

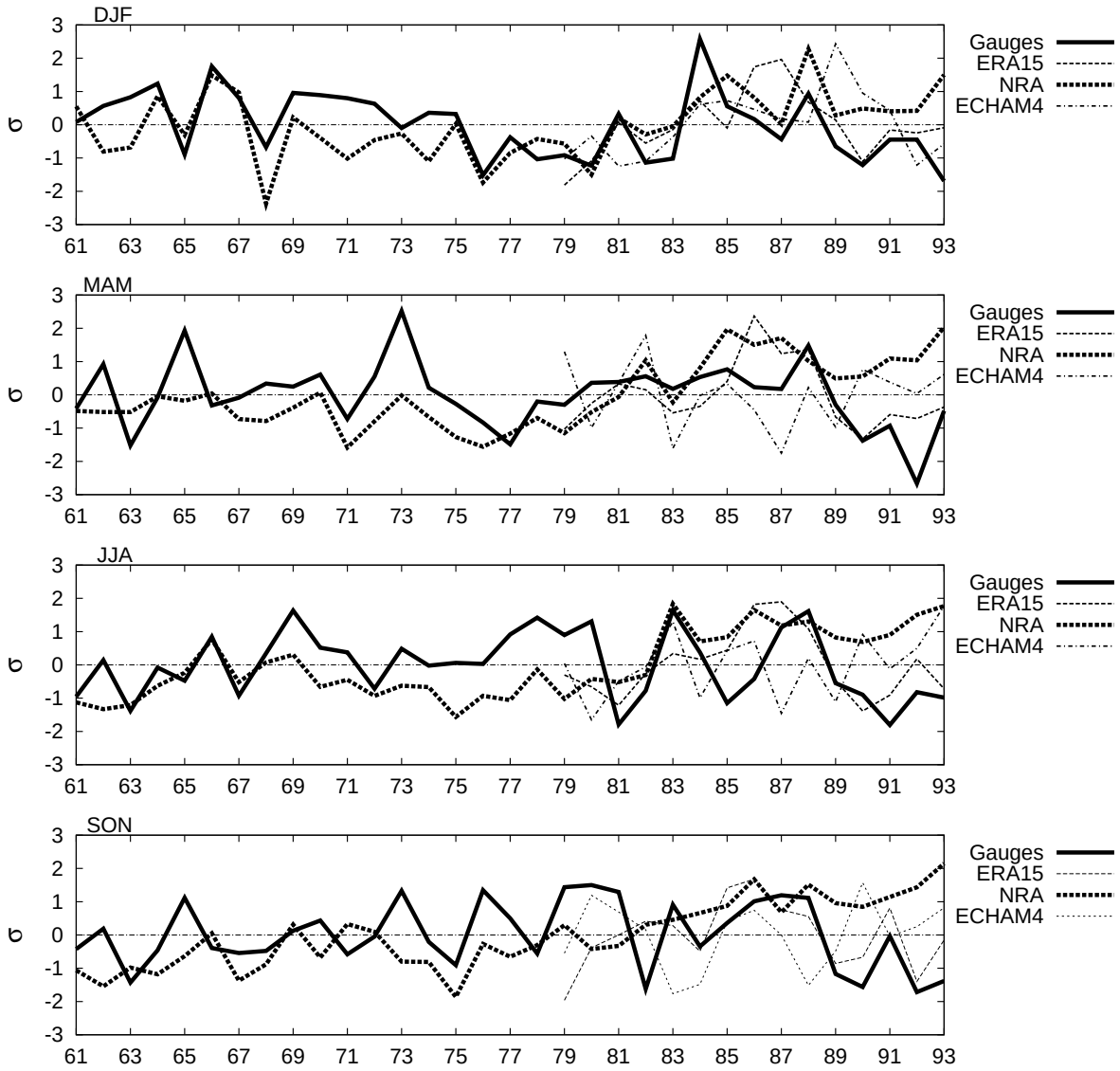

Figure 3.7: As Fig. 3.6, but for region B.

on rainfall (*Ropelewski and Halpert*, 1987), unlike in Region A. Surprisingly, the peaks from observations in the spring (MAM) of El Niño year 1965 and La Niña years 1973 and 1988 are high. They may be connected to strong monsoon activities, as the ITCZ is leaving Indonesia during this time of year.

Fig. 3.8 illustrates the interannual variations for Region C. SON has the highest skill for reanalyses and ECHAM4. Like Region A, all have the worst skill in MAM. In SON, the variations during the El Niño events of 1982, 1987 and 1992 are well simulated by the reanalyses and the model. Like Region A, Region C receives strong El Niño impacts that last from JJA to DJF with smaller magnitudes. Smaller magnitudes imply that Region A is more sensitive to El Niño than Region C. Since the El Niño impact or rainfall reduction occurs during the peak of the rainy season, the impact will be less devastating than that of Region A, which receives the impact

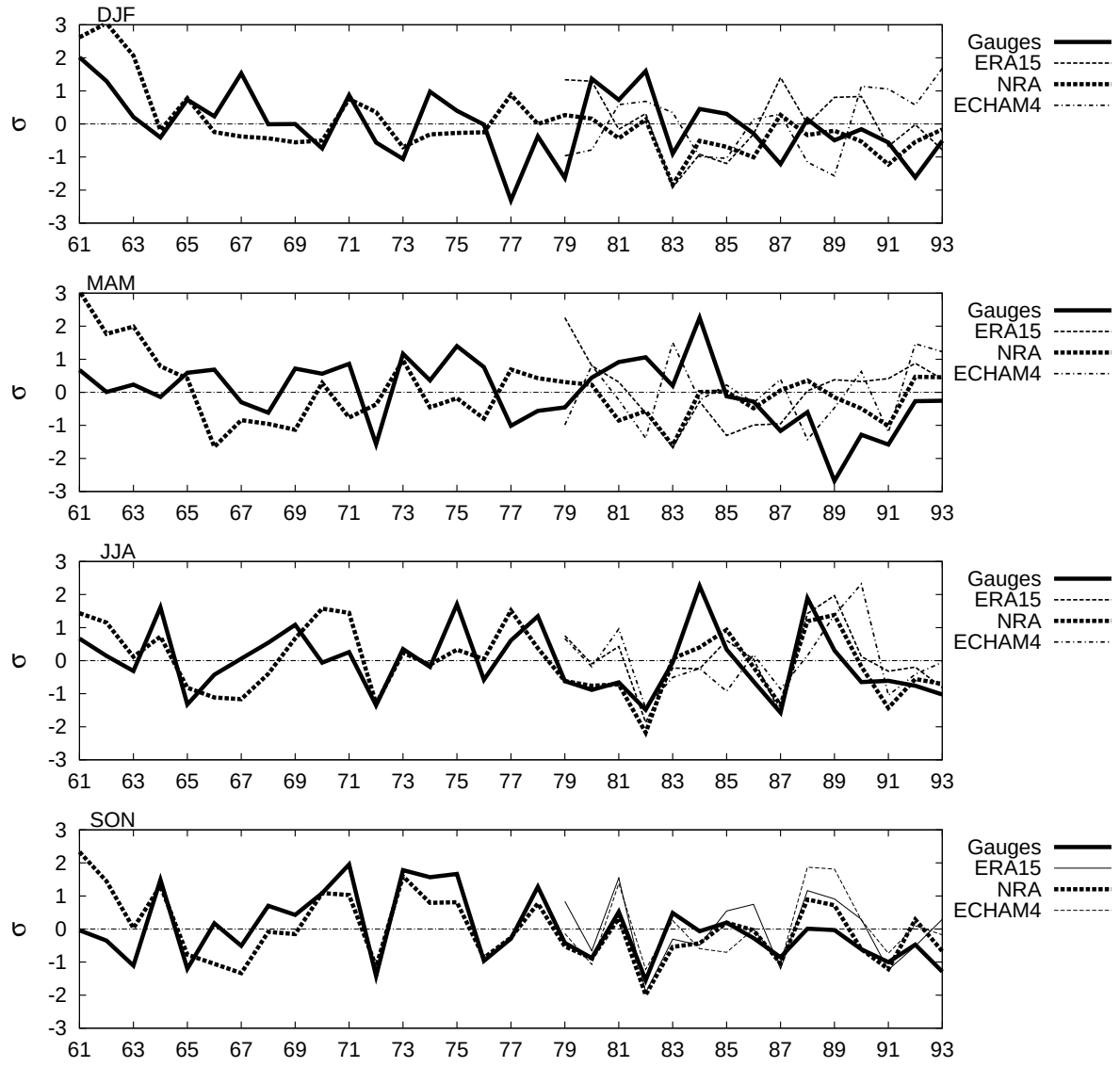

Figure 3.8: As Fig. 3.6, but for region C.

during the dry season.

In the case of La Niña years there is no consistent feature among models and observations. In La Niña years 1964 and 1970, Region A has larger values in SON than in JJA. However, in JJA of the same year the index is higher in Region C. In La Niña year 1970, the variation index of Region C is higher in SON. All models show the La Niña of 1988 (JJA and SON) quite well. Reanalyses show the decreases of this La Niña activity in SON over Region A and C. In summary, reanalyses and ECHAM4 behave in accordance with observations only during extreme ENSO events. This agrees with the results of analysis of seasonal climate forecasts, which was found to be minimal in non-ENSO years (*Barnston et al.*, 1994; *Landman and Mason*, 1999). An example of a non-ENSO year, when the rainfall index is high in Regions A (JJA) and C (MAM and JJA) is 1984. The models do not simulate this well. The high rainfall index in this

year is associated with a strong monsoon. Thus, models simulate variations due to ENSO events better than those due to monsoons.

3.5 Seasonal and Monthly Variability

In Fig. 3.9 the seasonal mean correlations between observations and reanalyses and the model simulations, respectively, are compared for resolutions T42 and T106. Except for ECHAM4 at T106, which uses data from 1979-1988, correlations are calculated for data from 1979-1993. The measure of significant correlation is the 95% significance level.

Correlations show a distinct variation during the annual cycle. In Region A at T42, ECHAM4 has the same annual cycle variation as NRA. Only ERA15 shows a good correlation in DJF. Except for ECHAM4 in JJA in Region C, the correlations are significant in Region A and C for JJA and SON. In Region C the NRA reanalysis performs best. In Region A and C, the least insignificant correlation is in MAM and the highly significant one in JJA. There is a consistent breakdown of correlations in spring in Regions A and C. In Region B NRA and ECHAM4 do not agree with the positive correlation of ERA15.

At the T106 resolution, the seasonal correlations of ERA15 and ECHAM4 in Region A are higher than those at T42. As at T42, the correlation breaks down in Regions A and C in the spring. Except for a low skill in DJF of ERA15 in Region C, the skill in Region A and C in general is similar to that at T42. In Region B, ERA15 at T106 has a similar feature and a better skill than at T42. As in the case of the annual cycle, the ECHAM4 performance in Region B is better for JJA at T106 than at T42. In Fig. 3.4 and 3.5, we saw that the annual cycle of ECHAM4 at T42 deviates significantly in JASO and higher resolution improves the annual cycle. Furthermore, there is a considerable improvement for ECHAM4 in the higher resolution in Region A and C in these seasons. In fact in JJA, ECHAM4 outperforms ERA15 in all regions. The inconsistent features in Region B in both resolutions suggest weak skill and low forcing by reanalyses and the ECHAM4 model.

Fig. 3.10 shows the monthly correlations of the T42 (left) and T106 (right) resolutions for the three regions. The variations from month to month are very high and do not retain the skill suggested before in seasonal mean analysis. In Region A at T42, the correlations of ECHAM4 are not in accordance with those of ERA15 and NRA, while the correlation of NRA agrees well with that of ERA15. In Region B at T42, again the correlation of NRA and ERA15 vary during the annual cycle in a similar way, but NRA has much smaller values. ECHAM4, on the other hand does not agree with either of them. In Region C at T42 the annual cycle of the correlations of the three are alike with the exception of ECHAM4 in August. NRA shows higher positive values while ERA and ECHAM4 agree at lower values most of the year. In Region A at T106

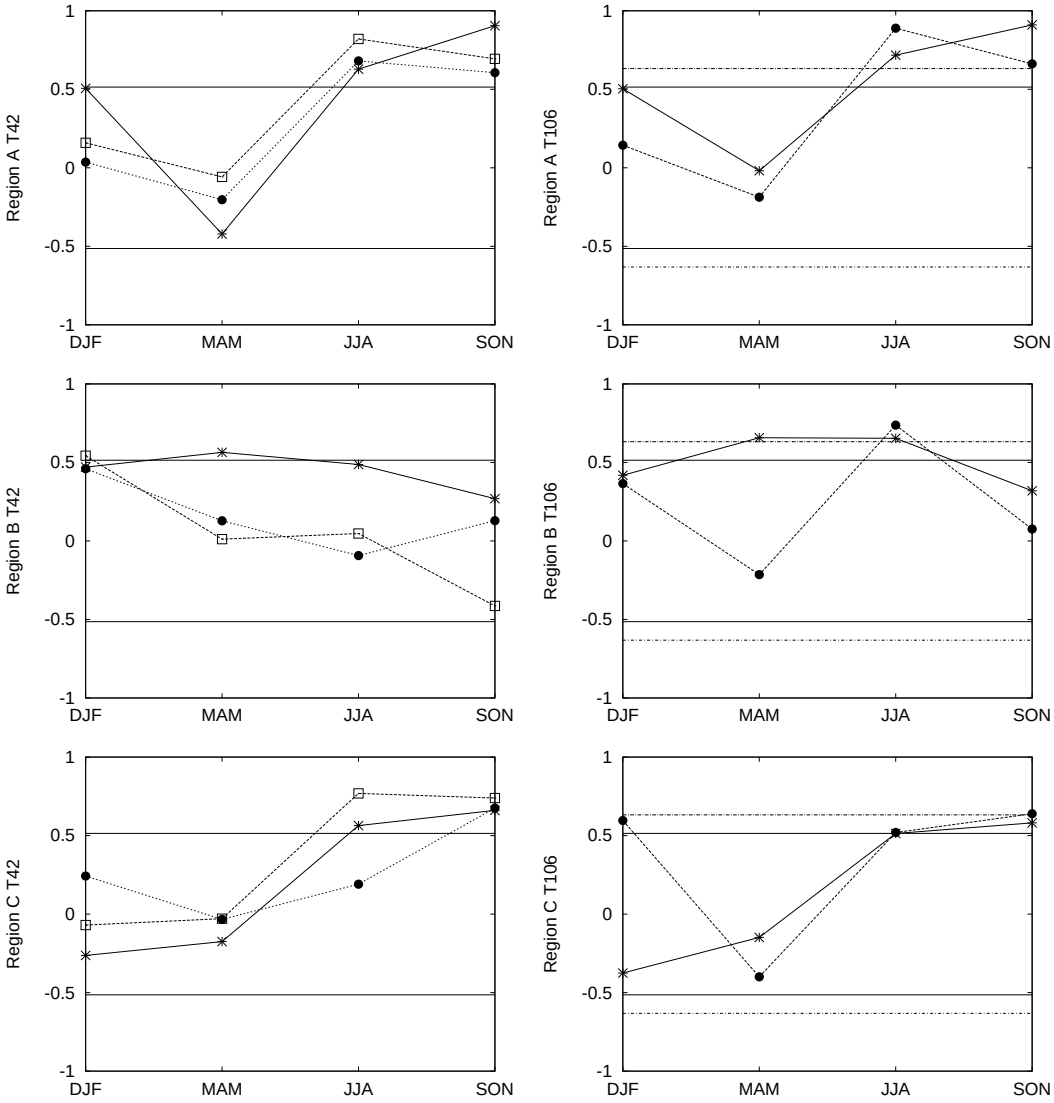

Figure 3.9: The average seasonal correlation in region A (above), region B (middle) and region C (bottom) at T42 resolution (left) and at T106 resolution (right) between observation and ERA15 (∗), NRA (□) and ECHAM4 (●). Solid horizontal lines represent 95% significance levels on two sides for all data except ECHAM4 at T106; dashed horizontal lines represent 95% significance levels on two sides of ECHAM4 at T106.

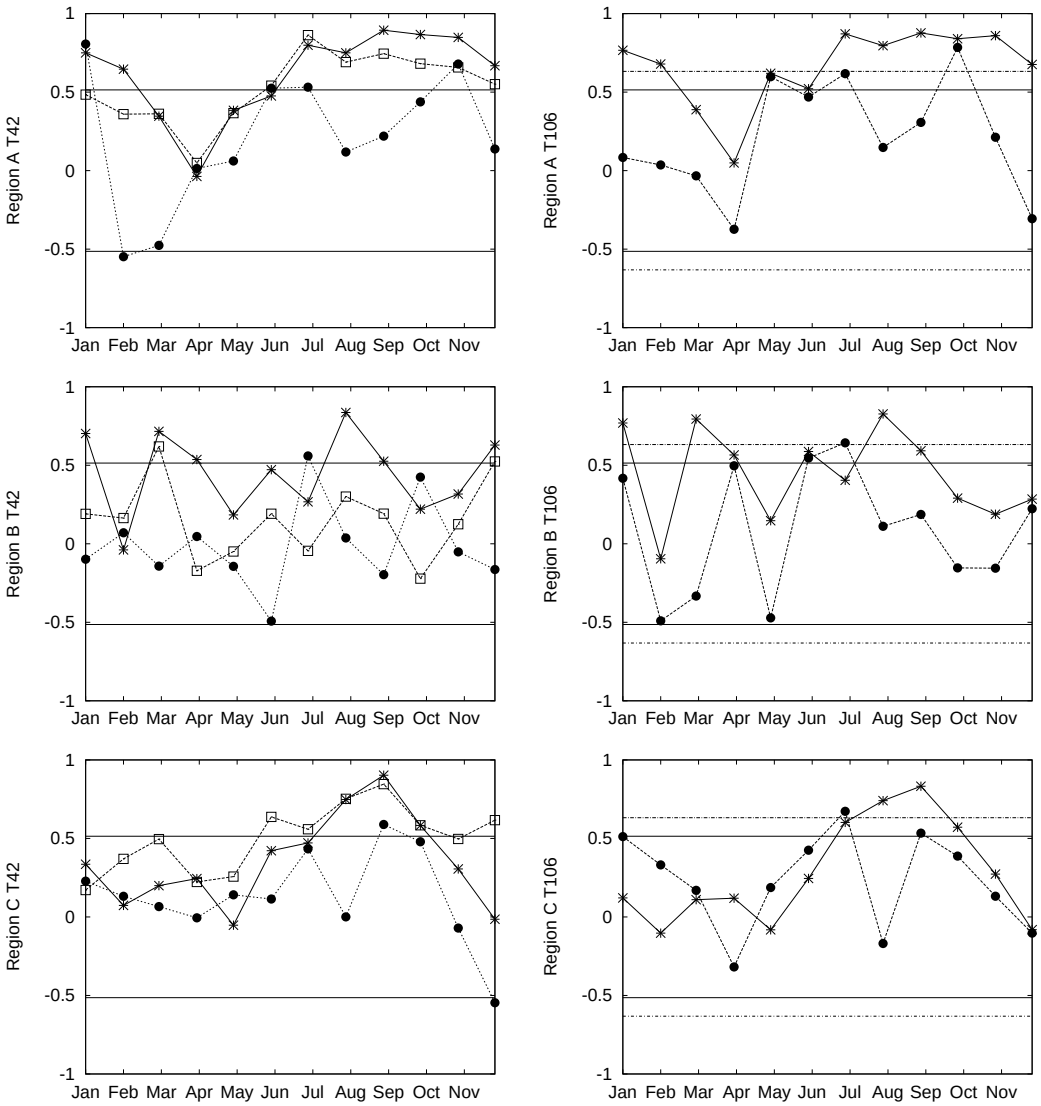

Figure 3.10: As Fig. 3.9, but for the average monthly correlation.

ECHAM4 agrees well with the monthly correlation of ERA15 except in JA and ON and with lower values. In Region B at T106 ECHAM4 resembles ERA15, but with smaller values. Again in Region C ECHAM4 is in phase with the variation of ERA15 except in August. The model shows yet again, as detected in the seasonal analysis of Regions A and C, the spring breakdown with the lowest correlations from February to April.

3.6 Interannual Variability Related to ENSO

From the above discussions, the impact of ENSO events is prominent in Regions A and C, that is, over most of Indonesia. *Nicholls* (1984) showed strong seasonal relations between SST in Indonesian waters and over the Pacific. Before that, *Nicholls* (1981) showed evidence

of air sea interactions in Indonesia and that Indonesian rainfall is related to SST anomalies. Using the Southern Oscillation Index (SOI), an index based on the difference of mean sea level (MSL) pressure over Darwin and Tahiti, *Ropelewski and Halpert* (1989) showed that in an ensemble ENSO year annual variations of rainfall patterns in Indonesia (except in northwest Indonesia) are 89% in coherence with SOI from 1885-1983, and that annual rainfall variations over Indonesia are associated with SST anomalies at 91% coherence during July of ENSO event years until June of the following year. *Ropelewski and Halpert* (1987) calculated that in Indonesia (except the northwestern part) during the period of June - November there is a coherence of interannual variation of rainfall with SOI of 82%.

ENSO events characterize the seasonal and monthly skills of the reanalyses and the ECHAM4 simulation. During ENSO years, reanalyses, the model simulation and observations show good agreement, especially in JJA and SON. Our results confirm that ENSO is the main driving force of high skill, which is in agreement with *Barnston et al.* (1994) and *Landman and Mason* (1999). From Fig. 3.6 and 3.8, ECHAM4 variability agrees with observations strongly only during ENSO events. However, the high predictive skill of ENSO impact is lost when the correlations in Region A and C break down in spring.

3.6.1 Spatial Patterns of the Rainfall Sensitivity to NINO3 SST

Fig. 3.11 depicts the sensitivity of the Indonesian rainfall to NINO3 SST forcing during the dry monsoon (MJJAS) and the wet monsoon (NDJFM) (*Ramage*, 1971; *Cheang*, 1987). The sensitivity is indicated by the correlation between rainfall and NINO3 SST. This figure considers only correlation values with significance levels above 95%, 99% and 99.9%.

The impact of ENSO as defined by the observations is more prominent during MJJAS with a significant coherent area of negative signals in most parts of Indonesia. In NDJFM the observed rainfall data show significant negative responses to SST in south Indonesia, Molucca, northeast of Australia and a part of north Borneo. Some areas have good correlation values above 99% significance level in both seasons over 33 years (1961-1993). Region B does not have responses to NINO3 SST at all as shown by *Ropelewski and Halpert* (1987).

The ERA15 response in MJJAS is too weak and covers only a small area. In NDJFM, ERA15 shows good response over Kalimantan, north of the warm pool and south of New Guinea. ERA15 also gives a significant positive response in west Sumatera in NDJFM. ECHAM4 shows too strong response in MJJAS east of 125 °E. In NDJFM, ECHAM4 gives a good response over Kalimantan, northern Molucca and north of the warm pool. For the remaining area, precipitation in ECHAM4 does not show a significant correlation to observations.

The exact period of ENSO impact on each region varies and needs further research on a seasonal

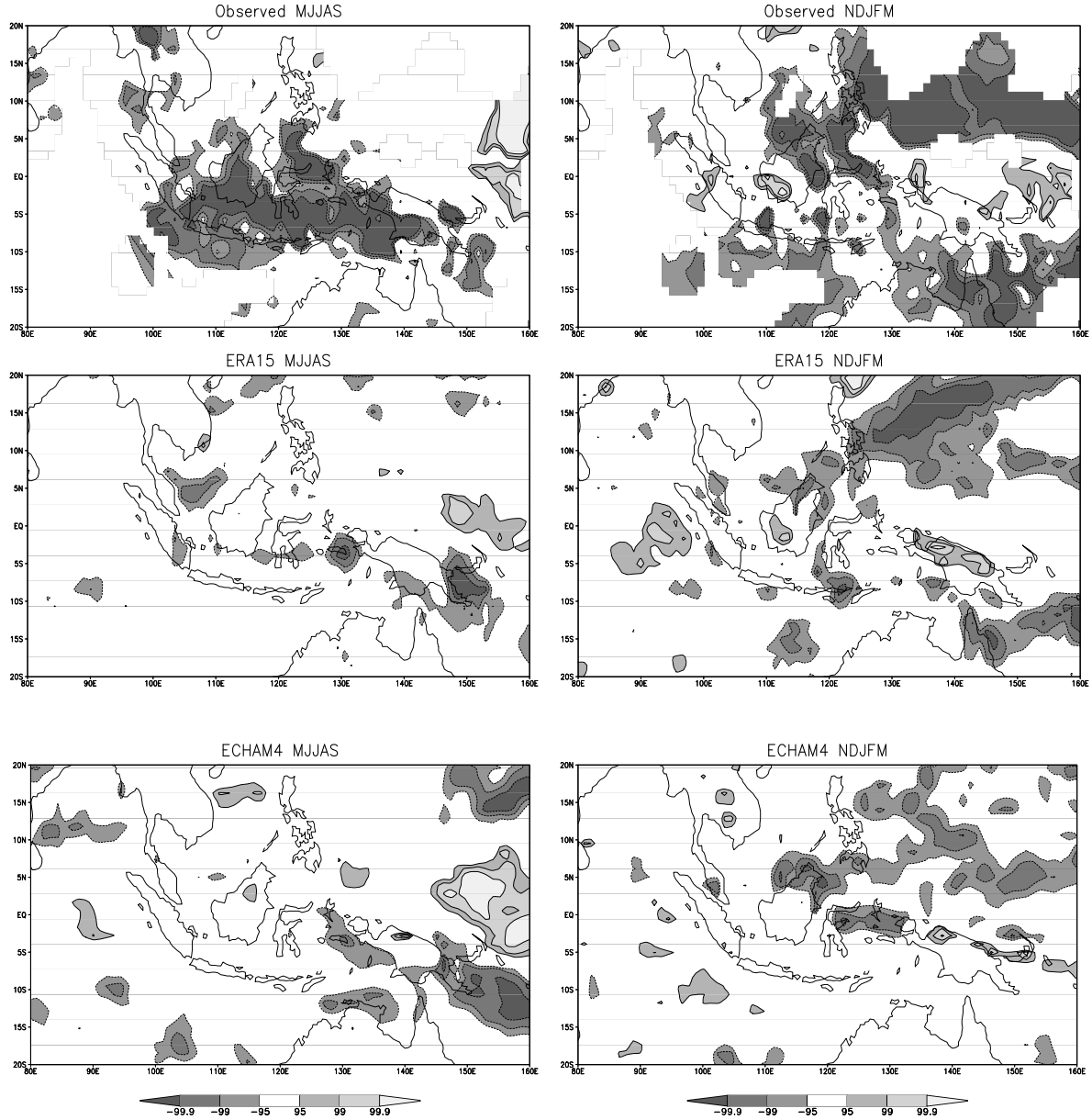

Figure 3.11: Spatial patterns of rainfall - NINO3 SST correlations for observations (top), ERA15 (middle) and ECHAM4 (bottom) during MJJAS (left) and NDJFM (right) at T106 resolution. All are shown with their statistically significant correlation level, where the solid (dashed) lines represent positive (negative) correlation. The three level of gray scales on both sides represent 95%, 99% and 99.9% significance levels. For example, for observed data (1961 - 1993), these significant levels correspond to correlation values $|0.33|$, $|0.42|$ and $|0.52|$ respectively.

or monthly basis. *Chen and van den Dool* (1997) and *Haylock and McBride* (2001) showed that the ENSO cycle predictability has a large seasonal dependence.

3.6.2 Seasonal and Monthly Variability Related to ENSO

Fig. 3.12 illustrates the negative seasonal mean correlation between rainfall and NINO3 SST for the three regions. A high correlation is indicated for T42 only in JJA for Region C for observations and in JJA and SON for Region A and C for ERA15. The two reanalyses follow the pattern for observations, especially in DJF, but are reduced to almost zero in MAM. In both these seasons, ECHAM4 gives erroneous positive correlations. The correlations between SST and precipitation for reanalyses and ECHAM4 follow highly observations in Regions A and C with strong negative values in JJA and SON. For ECHAM4, there are significant (above 99% correlation level) SST responses in SON (-0.51) in Region A, MAM (-0.52) in Region B and JJA (-0.47) and SON (-0.59) in Region C. In Region B correlations are insignificant indicating ENSO effect.

At T106 resolution, the positive role of a higher resolution becomes very clear in seasonal mean correlations of observations, ECHAM4 and ERA15. At this resolution, significant improvements of negative responses in JJA and SON, in agreement with observations, are seen for Regions A and C. ECHAM4 performance is improved and the breakdown of correlations in spring is even clearer with lower positive MAM values in Region C. Only in DJF and MAM for Region A are the deviations of ECHAM4 responses higher than observations and reanalyses. No significant values in Region B again confirm that this region shows no ENSO influence at all. In Region B, ECHAM4 is very close to ERA15 and both have large errors compared to observations in SON and DJF. Higher resolution only improves the model simulation in MAM. A summary of seasonal rainfall response to SST variations at two different resolutions is given in Table 3.3.

The correlations for monthly means similar to Fig. 3.12 are shown in Fig. 3.13. At T42, the

Table 3.3: The seasonal correlation of rainfall with. NINO3 SST. One, two and three asterisks indicate the correlations at the 90%, 95% and 99% significance levels, respectively.

	Region A			Region B			Region C		
	Obs - ERA15	Obs - NRA	Obs - ECHAM	Obs - ERA15	Obs - NRA	Obs - ECHAM	Obs - ERA15	Obs - NRA	Obs - ECHAM
T42	0.16	0.26	-0.08	0.98***	0.19	0.97***	0.64*	0.90***	0.45
T106	0.81**	-	0.99***	-0.17	-	-0.22	0.82**	-	0.89***

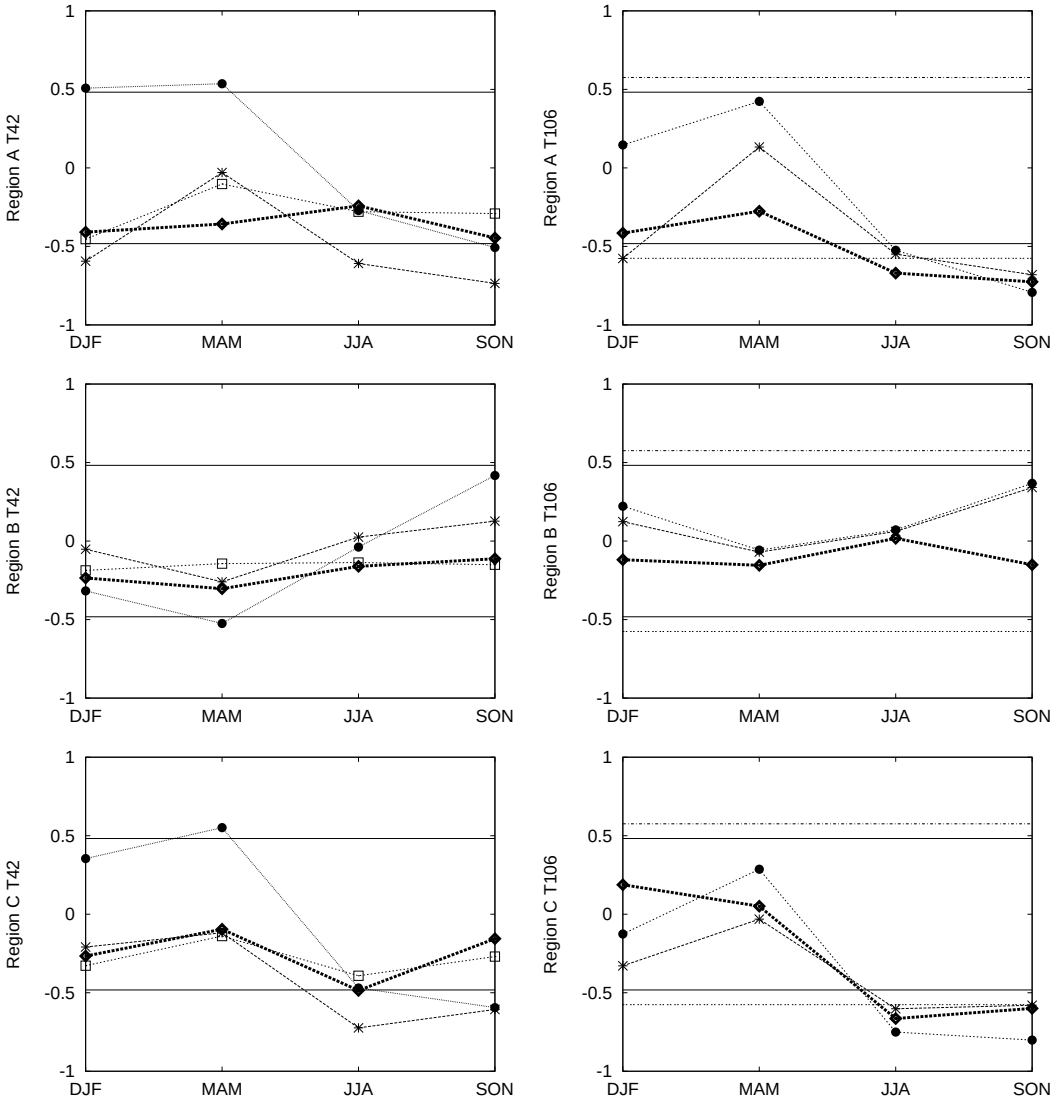

Figure 3.12: The seasonal mean values of correlations between NINO3 SST and average rainfall in region A (above), region B (middle) and region C (bottom) at the T42 resolution (left) and the T106 resolution (right) of observed data (⋄), ERA15 (∗), NRA (□) and ECHAM4 (●). Solid horizontal lines represent 95% significant levels on two sides of all data except ECHAM4 at T106, while dashed horizontal lines represent 95% significant levels on two sides of ECHAM4 at T106.

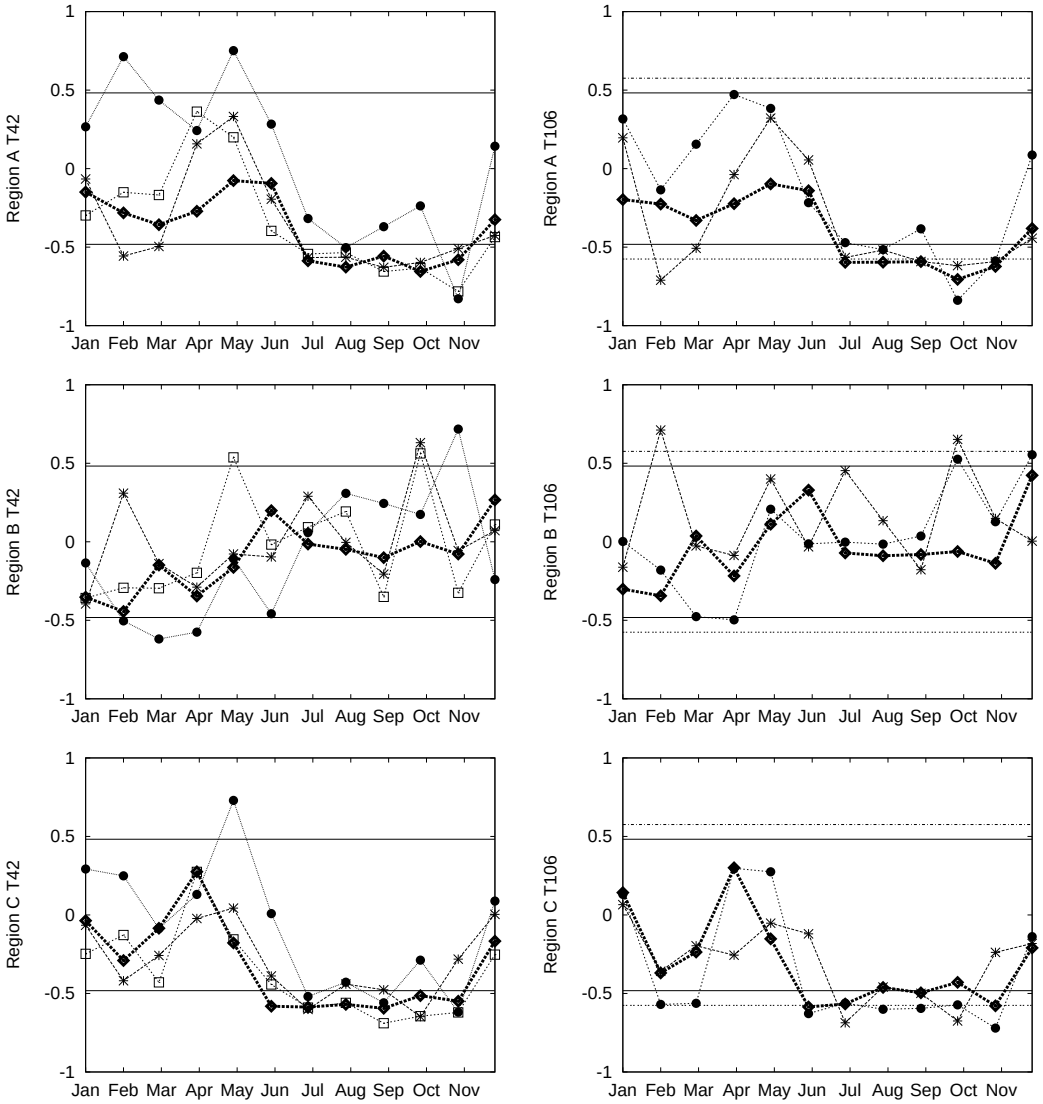

Figure 3.13: As Fig. 3.12, but for the monthly mean correlations.

observations show more complicated structures and more significant correlations compared to the seasonal analysis in Fig. 3.12. Correlations between observations are significant from July to November in Region A and from June to November in Region C. In other words, the ENSO impact is significant in the dry period and the transition period to the wet period and ENSO has no impact on the peak of the wet northeast monsoon in DJF (Fig. 3.3). A significant response of rainfall in Region C on Nino3 SST in June indicates that this region receives an ENSO impact earlier than Region A, and the rainfall in June foreshadows the ENSO event. However, there is no clear improvement at the higher resolution. In both resolutions, the reanalyses and the model follow quite well the observed response between June and December in Regions A and C. The observed data show that the correlations at T42 are higher than at T106 in Region C. In spring, the correlation breaks down in Region A and C as before. The correlation values of ECHAM4 for both resolutions exhibit erroneously high values in Regions A and C in the

Table 3.4: The monthly correlation of rainfall vs NINO3 SST. One, two and three asterisks indicate correlation at the 95%, 99% and 99.9% significance levels, respectively.

	Region A			Region B			Region C		
	Obs - ERA15	Obs - NRA	Obs - ECHAM	Obs - ERA15	Obs - NRA	Obs - ECHAM	Obs - ERA15	Obs - NRA	Obs - ECHAM
T42	0.78***	0.69***	0.83***	0.24	0.42**	0.22	0.78***	0.88***	0.66**
T106	0.76***	-	0.84***	-0.21	-	0.44**	0.53**	-	0.89***

spring. As before, the performance of ECHAM4 improves considerably for higher resolution. NRA and ECHAM in Region C have the best responses all year long, with correlation values of 0.88 with observations. In Region B, there is yet again no indication of an ENSO impact.

3.7 Effects of Land-sea Mask Resolution

The correlation analysis at two different resolutions raises the question of the role of the land-sea mask. Does a higher resolution land mask contribute to higher model skill ? At the T106 resolution there are some additional land areas that do not appear at the T42 resolution. This section focuses on the effect of these additional land grid cells on rainfall errors. The analysis below is restricted to ECHAM4 results, since only ECHAM4 has two independent simulations at two resolutions.

Fig. 3.14 illustrates the land-sea distribution at both resolutions. Even at the T106 resolution, the model cannot represent some small islands or even the correct shape of a big island such as Sulawesi. The rainfall for those additional land points will be compared to observations at T106, and then the differences will be analyzed. The following section describes as an example the rainfall error at two resolutions in January 1979 for the additional grid cells. We study the statistics of the errors by a scatter plot and frequency distribution diagram.

Fig. 3.15 shows a scatter plot of errors at both resolutions from ECHAM4. This plot indicates the difference between the newly introduced land points at T106 and the corresponding grid points at T42. Although there is no significant shift of peaks or medians between the two curves, the frequency distribution at T42 is broader than that at T106. Thus, there are more underestimations at T42 than at T106 and a more coherent result at T106. Other statistical measures are the mean error and the root mean square (RMS) error values. A greater RMS error at T42 is seen in Fig. 3.15, where the frequency distribution of T42 is skewed toward the negative side. Overall, the introduction of a new land-sea mask at the higher resolution improves the

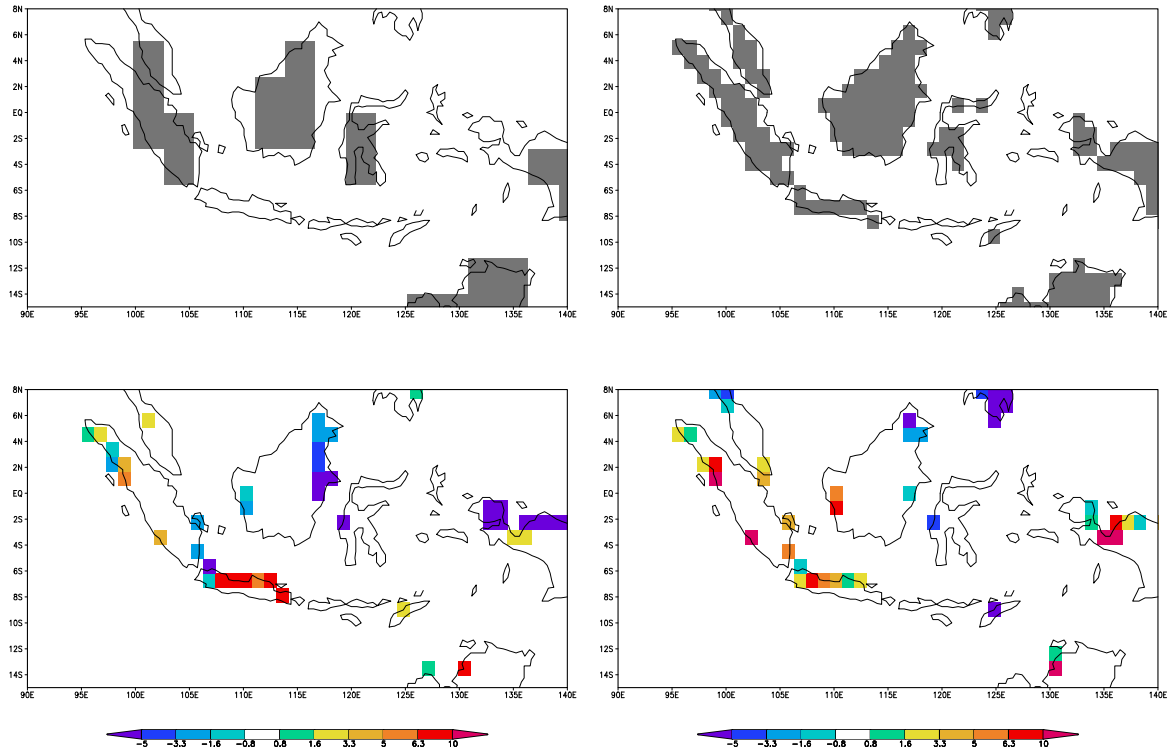

Figure 3.14: The land sea mask of the T42 (top left) the T106 (top right) and two examples of calculated errors (mm/day) of newly introduced land grids (top right minus top left figures) by higher resolutions in Jannuary 1979. The bottom left shows errors in T42 and the bottom right in T106.

model performance. *Lal et al.* (1997) found that ECHAM simulation at T106 captures both the spatial and temporal characteristics of the Indian monsoon climatology better than the T42 and produces less erroneous diurnal and seasonal cycles of area-averaged surface air temperature. *Stendel and Roeckner* (1998) studied the influence of horizontal resolutions on ECHAM4 model simulations, and found a more vigorous tropical convection at higher resolution and that a higher resolution model has a positive impact on regional rainfall patterns, which are affected by the orography. With regard to the rainfall simulated by ECHAM, *May and Roeckner* (2001) found that the resolution effect is particularly strong over the tropical oceans with sharper gradients between wet and dry areas as a result of enhanced convection at T106 in comparison to T42.

3.8 Concluding Remarks

We have examined the performance of two reanalyses and the ECHAM4 model with regard to rainfall over Indonesia at two different horizontal resolutions. We have introduced a new regionalization method in order to separate climate zones. The analysis focuses on regional,

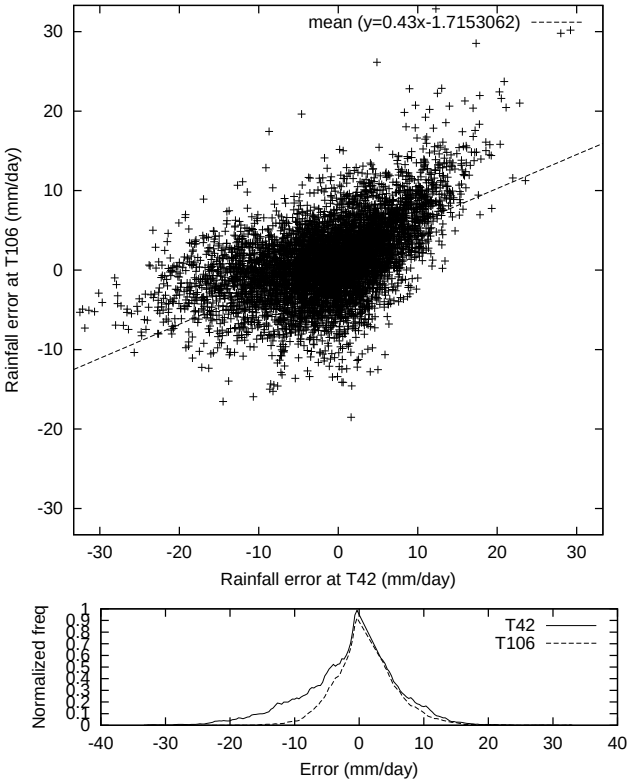

Figure 3.15: Scatter plots of error distributions by ECHAM4 in two different resolutions of newly introduced land grids. The plots show cases of all errors in 120 months (1979-1988). The bottom part illustrates the normalized frequency distributions of those errors.

monthly and seasonal means as well as the annual cycle and interannual variability for three such climate regions. The correlation of rainfall to SST variations in the NINO3 region has also been investigated. In addition, the resolution dependence by a changed land sea mask representation at two different resolutions has been addressed.

With the new double correlation method, we have identified three main climate regions each with its own characteristic annual precipitation cycle. These regions simplify the previous regionalization by *Wyrtki* (1956). Many authors use a simple box with definite latitudes and longitudes to designate a climate region. The method presented here is more flexible because the resulting region can have any shape. The regionalization method produces three main climate regions; the southern monsoonal, the northwestern semi-monsoonal and the Moluccan anti-monsoonal.

The simulated rainfall has a seasonal dependence and an ENSO cycle dependence. From the interannual analysis of Region A and C (Fig. 3.6 and 3.8), El Niño (La Niña) years are indicated by rainfall index below $-\sigma$ (above $-\sigma$) in SON, except the very weak 1969 El Niño. Thus, the rainfall in SON in either region can be used as an ENSO index. The observation shows that Region A is more sensitive to ENSO (section 4), while Region C has the same length of ENSO impact as Region A and receives the earliest significant ENSO impact (section 6) and there is

no ENSO impact in the peak of the wet southeast monsoon. The reanalyses and ECHAM4 simulate variability during ENSO years better when coherent signals appear especially during El Niño years. The study shows better seasonal than monthly model skills. The highest skill occurs in JJA, followed by SON, DJF and MAM. *Haylock and McBride* (2001) showed better predictability of Indonesian rainfall in SON than in DJF. Good skills in JJA promise good ENSO forecast, since the most severe environmental and socio-economic impact of ENSO on Indonesia occurs in SON (*Kirono et al.*, 1999). The study shows the breakdown of the correlation in spring (MAM). Observed SSTs are used as lower boundaries for the reanalyses and very likely the same observed SSTs are used to run the ECHAM4 simulation. Nonetheless the combination of meteorological data and SST yields only a very small correlation for reanalyses in spring (MAM). The observed SST applied to the model even yields an erroneous positive correlation. *Trenberth and Caron* (2000) showed a northward shift of a high correlation area between rainfall over Indonesia and SOI in MAM, whereas in other seasons the Maritime Continent is covered by strong correlations.

Indonesia, except Region B experiences consistent ENSO related rainfall anomalies. These results are in agreement with the results of *Ropelewski and Halpert* (1987, 1989); *Halpert and Ropelewski* (1992). The present study not only gives similar rainfall-anomaly maps as shown by these authors, but also the seasonal march of impact received in each region. Southern Indonesia or Region A is the most El Niño sensitive region. While Region C, which is located in the Indonesian throughflow region, is also an ENSO sensitive region, where the throughflow variation itself is also affected by ENSO (*Meyers*, 1996). This study could be extended with ERA40 (*Simmons and Gibson*, 2000) and the whole NRA40.

Chapter 4

Long Term Simulation of the Indonesian Rainfall with the MPI Regional Model

Abstract

Simulations of the Indonesian rainfall variability using the Max Planck Institute regional climate model (RCM) REMO have been performed using three different lateral boundary forcings: Reanalyses from the European Centre for Medium-Range Weather Forecasts (ERA15), the National Centers for Environmental Prediction and National Center for Atmospheric Research (NRA) as well as from ECHAM4 climate model simulation. REMO simulations were performed at 0.5° horizontal resolution for the whole archipelago and at 1/6° for the Sulawesi Island. REMO could, in general, reproduce the spatial pattern of monthly and seasonal rainfall over land areas but overestimated the rainfall over sea. Superiority of REMO over the land is due to much improved orography, while over the ocean REMO suffers from surface flux and the coupling to an ocean model seems to be needed. REMO reproduces variability during ENSO years but fails to show a good monsoon contrast. Despite the strong influence of the lateral boundary fields, REMO shows a realistic improvement of a climatic local phenomenon over Molucca. Significant improvement for the step from global to 0.5° resolution are notable, but not from 0.5° into 1/6°. The REMO simulation driven by ERA15 has the best quality, followed by NRA and ECHAM4 driven simulations. The quality of ERA15 is the main factor determining the quality of REMO simulations. A predictability study shows small internal variability among ensemble members. However there are systematic intrinsic climatological errors as shown in the predictability analysis. These intrinsic errors have monthly, seasonal and regional dependences and the one over Java is significantly large. The intrinsic error study suggests the presence of the spring predictability barrier and a high level of predictability in summer.

4.1 Introduction

The Indonesian part of the Asian monsoon has received less attention in comparison to other Asian monsoon areas like India and China. Studies of the monsoon over the region using global and regional climate models are rare. This study is motivated by the inadequate results of the high resolution global circulation model (GCM) over Indonesia at the T106 resolution. Due to the presence of complex topography and insufficient model resolution in the region, current GCMs shows a mediocre performance in simulating the rainfall variability in the region. Furthermore, previous studies showed significant improvements of rainfall representation when a moderate resolution was replaced by a higher GCM (*Stendel and Roeckner* 1998, *Jha et al.* 2000). In addition, there is no study yet using a regional climate model (RCM) in the region. The complexity of the region especially the land sea representation requires a high resolution model.

One possibility for downscaling GCM results to the regional scale is to apply a nested RCM. For reviews of RCM, the readers are referred to *Mesinger* (1997) and *Staniforth* (1997). The Max Planck Institute (MPI) RCM or REMO (*Jacob* 2001 and *Jacob et al.* 2001) is suitable for this purpose because REMO provides detailed forecasts of weather parameters close to the ground and an improved simulation of clouds and rainfall compared to GCM. The regional model is, however, dependent upon the lateral boundary prescription (*Warner et al.*, 1997), which limits their capability in studying long-term climate behavior. The purposes of the study are to show REMO capabilities in simulating the monthly to interannual rainfall variability, to see the downscaling effect at two different resolutions (0.5° and $1/6^\circ$), to compare the variability with three different lateral boundary conditions from the European Centre for Medium-range Weather Forecast (ECMWF) Reanalyses (ERA15; *Gibson et al.* 1997), the National Centers for Environmental Prediction and National Center for Atmospheric Research (NCEP-NCAR) Reanalyses (NRA; *Kalnay et al.* 1996) and the MPI ECHAM4 (*Roeckner et al.*, 1996a) simulation at the resolution T106 and to explore the rainfall predictability with different initial conditions.

This chapter focuses on the rainfall simulated by REMO. The regional model produces large-scale and convective type precipitation, however due to limited observations, the study focuses mainly on the total rainfall. The time scale is limited to monthly, seasonal and interannual from 1979 - 1993 (except ECHAM4, which is only available from 1979 - 1988). The outline of this chapter is as follows. Section 2 discusses the data and model setup, section 3 the results of REMO simulations in five major islands and three sea regions with three different boundary forcings, the results of some sensitivity studies conducted to improve the rainfall simulation over the sea and the results of the down scaling effects. Section 4 discusses the REMO predictability. Finally, section 5 summarizes some highlights of the findings.

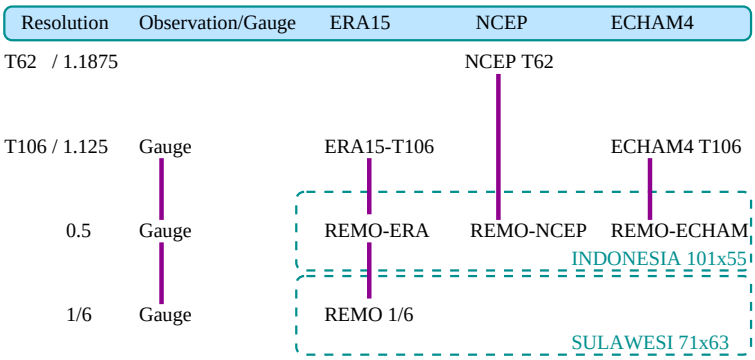

Figure 4.1: The experiment setups with three lateral boundaries and two different resolutions.

4.2 Data and Model Setup

4.2.1 Data

The data used in this study are monthly rainfall data collected by the Indonesian Meteorological & Geophysical Agency (BMG) at 167 stations all over Indonesia, and monthly mean rainfall data from the WMO-NOAA project on The Global Historical Climatology Network (GHCN; *Vose et al.* 1992) from 1979 to 1993. In our area of interest (19 °S - 8 °N and 95 °E - 145 °E), there are 545 rain gauges. These data are gridded to match the other datasets at T106 and 0.50 resolutions using the *Cressman* (1959) method. As the second observation data set, a combination of gauge observations with satellite estimates from the Global Precipitation Climatology Project (GPCP; *Huffman et al.* 1997) at the 1 ° spatial resolution is used. The data has been interpolated into the REMO grid.

The simulations were driven by lateral boundary conditions interpolated from two reanalyses. The first one is ERA15, at the horizontal resolutions T106 or equivalent to 1.125 ° in the tropics and the second one is the 40 year NCEP reanalysis (NRA) with a fixed spatial resolution of T62 (equivalent to 2.5 ° in the tropics). The reanalyses data are used from 1979 until 1993 every 6 hours.

The third lateral boundary data set is the product of the ECHAM4 climate simulation for a resolution sensitivity study (*Stendel and Roeckner*, 1998). The ECHAM4 model is a spectral model with a triangular truncation at the wavenumbers 106 (T106). For the vertical representation a 19 level hybrid sigma-pressure coordinate system is used. The time integration is carried out using a semi-implicit ”leap-frog” method. The orography and the land-sea mask are calculated from a high resolution (1 km) US Navy data set. This simulation is part of the Atmospheric Model Intercomparison Project (AMIP; *Gates* 1992), in which several global atmospheric models participated in simulating climate over 1979 - 1988. The ECHAM4 model was driven by interannually varying SSTs from the AMIP 2 (*Gates et al.*, 1999) at T106 resolution.

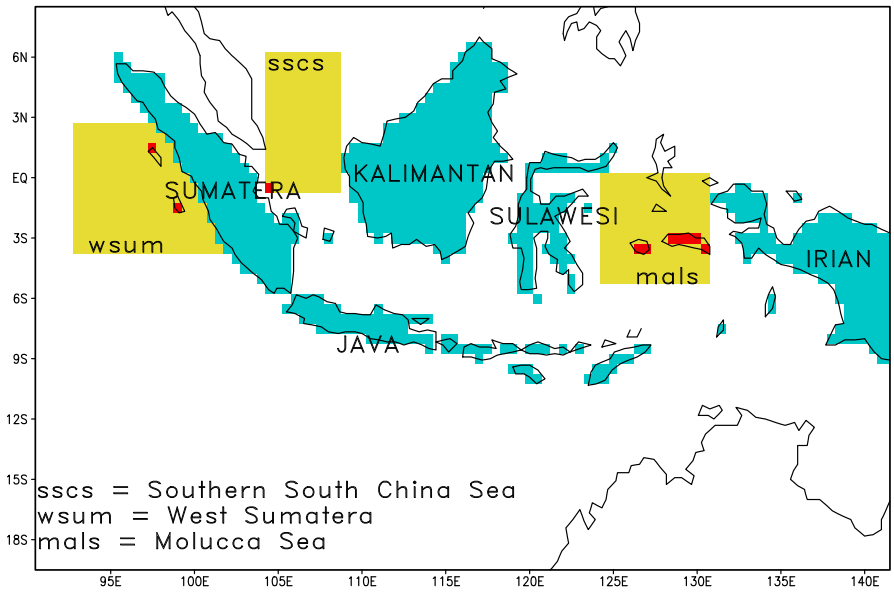

Figure 4.2: The five major islands and three sea areas examined in this study.

The gridded SST data from the Global Ice and Sea Surface Temperature dataset (GISST2; *Rayner et al.* 1996) version 2.3b are used in this study to validate other SST data. This dataset is compiled from SST observations from 1903 - present, with a spatial resolution of 1 °. To have the same period as the rainfall data, we use data from 1979 to 1993 only.

4.2.2 REMO Model Descriptions

REMO is capable to run with the European Model/Deutschland Model (EM/DM; *Jacob and Podzun* 1997) or the ECHAM4 parameterizations (e.g., *Jacob* 2001). In this study, the physical parameterizations of the Max-Planck Institute climate model ECHAM4 have been used. The dynamical core of the model as well as the discretisation in space and time are based on the Europa-Modell. However, in REMO with ECHAM-4 physics not enthalpy and total water content but temperature, water vapour and liquid water are prognostic variables. In addition to temperature, water vapour and liquid water the horizontal wind components and surface pressure are prognostic variables in REMO. The model uses the Arakawa-C grid for the horizontal representation and a hybrid system of p and η using 20 levels of vertical coordinates. Vertical discretization follows *Simmons and Burridge* (1981). The time discretization uses a semi-implicit leapfrog scheme and an explicit advection scheme. The lateral boundary interpolation uses the method of *Davies* (1976), where the lateral boundary relaxation zones extend to 8 grid rows. The lateral boundary consists of all prognostic variables except some parameter described in Table 4.1. At the upper boundary a radiative upper boundary condition according to *Klemp and Durran* (1983) and *Bougeault* (1983) is applied.

The radiation parameterization is adopted from the European Centre for Medium Range Forecasts' model (*Fouquart and Bonnel*, 1980; *Morcrette and Fouquart*, 1986) with only few changes described in *Roeckner et al.* (1996a). The grid scale parameterization of cloud microphysics is based on the solution of budget equations with the bulk schemes from *Kesler* (1969) and the sub grid-scale precipitation processes follow *Tiedtke* (1989), with deep convection adjustments due to *Nordeng* (1994). Condensation follows *Sundqvist* (1978).

Clouds are divided into stratiform and convective clouds. The liquid water content of stratiform clouds is determined by the corresponding budget equation including sources and sinks due to phase changes and precipitation. An empirical, temperature dependent, function is used to determine the cloud ice content, thus influences on the radiation are included. The parameterisation of the convective clouds is based on the mass flux concept from *Tiedtke* (1989) with changes in the deep convection.

REMO has three types of convection: penetrative, shallow and mid-level convection. Only one scheme is allowed in a grid cell and no different layers of convection. Penetrative convection is considered when the cloud base is in the planetary boundary layer and large-scale convergence prevails in the lower troposphere. In shallow convection, the cloud is formed in conditions of a slightly divergent flow and is often driven by evaporation at the surface or over water. In mid-level convection, the cloud has its cloud base in the free atmosphere and occurs together with large-scale lifting in the vicinity of fronts with regions of thermal instability. Penetrative convection is assumed if the dynamic fraction due to advective humidity transport predominates, while shallow convection is assumed if evaporation from the surface (land or ocean) is of larger importance.

In REMO, soil temperatures on land are calculated from diffusion equations solved in five different layers covering the uppermost 10 m of the soil. The global data set of fields of land surfaces is constructed from the major ecosystem complexes of *Hagemann et al.* (1999), for which the new improved version is also available (*Hagemann*, 2002). Surface mean orography and variances are calculated from the USGS GTOPO30 data with a spatial resolution of 1 km x 1 km. All surface parameters are constant in time, i.e., do not vary monthly or seasonally. The land surface scheme follows *Dümenil and Todini* (1992). The non partial REMO is used in this study, where only one type of surface cover is present on each grid cell (land, water or ice).

4.2.3 Model Setups

The model was run in the climate mode at the resolution 0.5° with lateral boundaries from ERA15 (REMO-ERA), NRA (REMO-NRA) and an ECHAM4 simulation (REMO-ECHAM). The lateral boundaries have a temporal resolution of 6 hours and are interpolated for a 5 minute time step. A simulation of 15 years (1979 - 1993) was performed for each reanalysis and a

Table 4.1: The quality of the three different lateral boundaries

Forcings	Days	Time span	Liquid water content	Specifi c humidity	Original resolution
ERA15	365	1979-1993	yes	all layers	1.125
NRA	365	1979-1993	no	not upper 9 layers	1.875
ECHAM4	360 (Julian)	1979-1988	yes	all layers	1.125

simulation of 10 years (1979 - 1988) for the ECHAM4 model. Table 4.1 points out major differences among the three lateral boundary fields.

A regional model has to be initialised and supplied with lower and lateral boundary values during the whole simulation. Initialisation is done once for all prognostic variables in all model levels. In addition, surface temperature, soil temperatures for five soil layers down to a depth of 10 m, soil moisture, snow depth and temperature as well as the skin reservoir content (water stored by the skin of the vegetation) must be supplied.

The study was conducted at two resolutions. At the resolution 0.5° (55 km), the model is formulated in a finite difference grid with 101 points in longitude, 55 points in latitude and 20 hybrid vertical layers with a bottom left corner at 91°E/19°S. This grid system covers the whole archipelago. At the resolution $1/6^\circ$ (18km) the model has 63 grid points in longitude and 71 points in latitude and 20 hybrid vertical layers with a bottom left corner at 117°E/7°S. The latter grid system covers the Sulawesi Island. The Sulawesi simulation (REMO-1/6) was driven by the lateral boundary from REMO-ERA outputs. Fig. 4.1 illustrates the structure of REMO simulations at two resolutions.

In the predictability analysis, those simulations become the control runs and six other simulations were performed for REMO-ERA and REMO-ECHAM, which make up two ensemble simulations. Thus each ensemble consists of a control run and ensemble members, whose initial condition differs from the control run by 12 to 72 hours, and each is integrated for 15 years.

4.3 Results of REMO Simulations

The annual and interannual climate over the region is characterized mainly by the monsoons and ENSO events. The region is divided into three types of climate patterns, the monsoonal, the semi-monsoonal and the anti-monsoonal type of climates. According to rain gauge measurements, the monsoonal pattern exhibits a precipitation maximum in May/June/July and a dry period in December/January/February, while the semi-monsoonal pattern shows two peaks, a larger one in November/December and a smaller one in March/April. The anti-monsoonal pattern has almost the opposite pattern of the monsoonal pattern. In the forthcoming analysis, we will examine the long term rainfall variability simulated by REMO in comparison with ob-

servation. Then we will look at the improvement by using a resolution hierarchy from T106, REMO 0.5 ° and 1/6 ° resolutions and will perform some the sensitivity studies. The analysis will focus on the five major islands and the three sea regions as shown in Fig. 4.2.

4.3.1 The Five Major Islands

Figure 4.3 illustrates the results of REMO simulations with three different lateral boundaries over five major islands. Java is a unique island with a homogenous strong monsoonal pattern, while the others have mixed patterns between monsoonal, semi-monsoonal and anti-monsoonal. REMO-ERA produces Java's pattern quite well. However there are some overestimations during the peak of the wet season and REMO-ERA produces a longer dry period with underestimated rain amount. Whereas REMO-NRA overestimates the wet season and REMO-ECHAM does not show a good contrast between the wet and the dry seasons. From a previous analysis with the ERA15 data (Chapter 3), the dry monsoon region (region A) has spatial extent covering most of the Sumatera Island and this indicates a dryer Java or longer dry period for Java. While in the analysis with ECHAM4 data, the spatial extent of the wet season region (region B) reaches Java Island and indicates a longer wet season. The analyses of the rain gauge (Chapter 3) shows that the rain gauge, the border between the dry and wet regions lies in the third portion of southern Sumatera. REMO is a hydrostatic climate model which suffers from weaker vertical movements near steep orography. Under dry conditions, the limitation is even worse, when the supply of water vapor is lacking and the remaining convection is initiated from orographic uplifting. The orographic convection is barely present in REMO because the 0.5 ° grid system does not resolve the orography over the region well. A similar finding with a 1 ° grid RCM for the Indian monsoon region has been reported by *Bhowmik and Prasad* (2001). Thus, there are large discrepancies between observations and REMO, when REMO-ERA underestimates rainfall in the dry period. Over the other islands, the problem does not appear as strong as over Java because the contrast between dry and wet season is not so strong. During two ENSO events in 1982 and 1991, the variability of the reanalyses driven REMO simulations agrees with observation. Even REMO-ECHAM4, which usually shows an overestimated dry period, has a significant drop at the beginning of the dry period.

Over the other islands, REMO simulations do mostly underestimate rain amount. All simulations over Irian, agreements in correlation over land areas with observation are high. The quality of the simulated variability of REMO-ERA15 decreases consequently from Java to Kalimantan, Sumatera, Sulawesi and Irian Island. During a strong El Nino year of 1982 the variability of the model results for major islands with different model boundaries are consistent, including REMO-1/6. The correlation between REMO-ERA and REMO-1/6 is high (0.946) in all years. The correlation values in Irian are low because the island is located at the lateral boundary zone of the RCM. The prognostic variables on the entire outer boundary of REMO are identical to

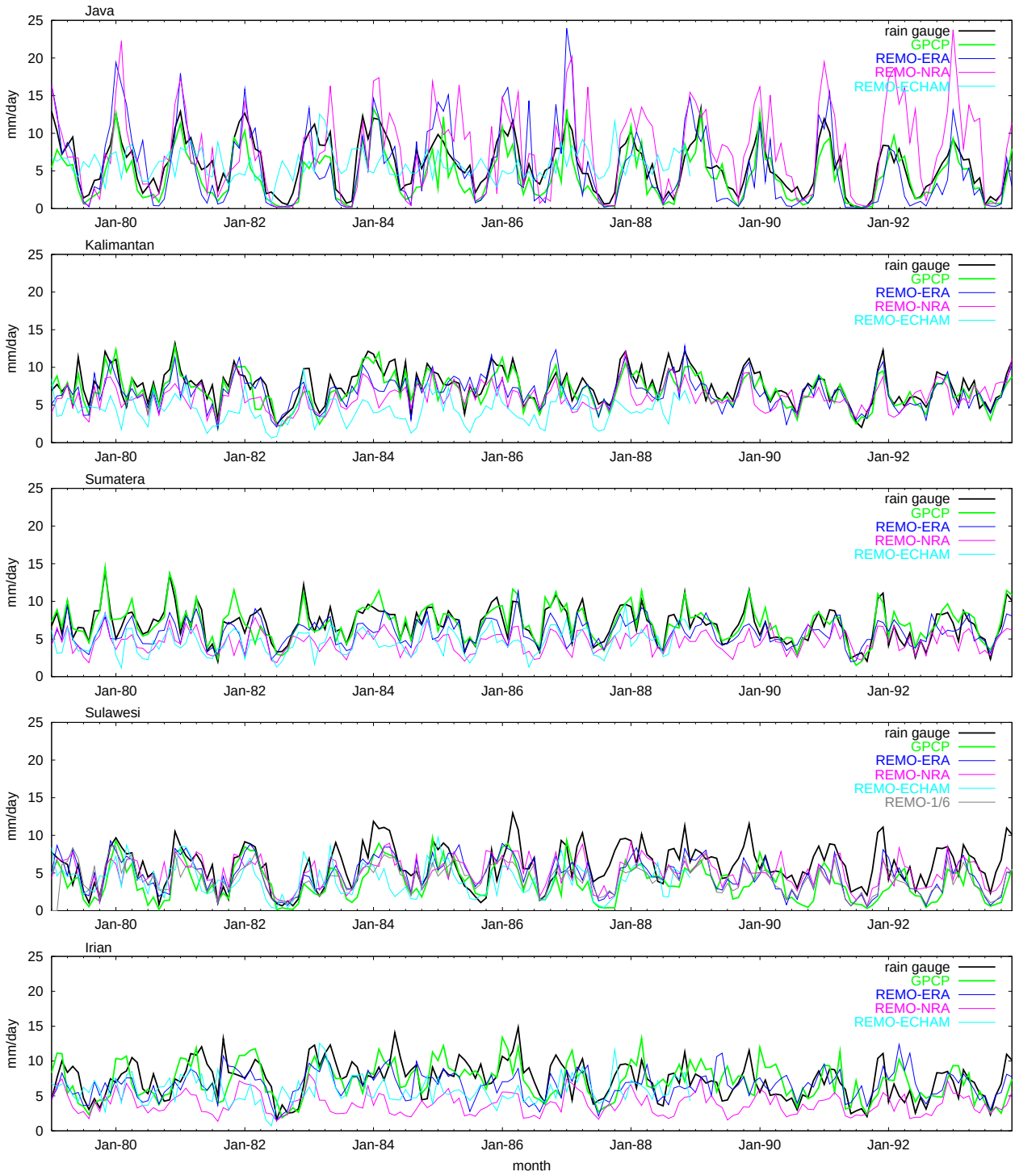

Figure 4.3: Variability of simulated and observed rainfall for the five major islands.

the values of the corresponding driving model. The prognostics equations are only solved for the interior model grid points. Spurious precipitation values appear in the outermost part of the interior domain. Beside that, Irian has the lowest number density of rain gauges, which contributes to a poor quality of observed rainfall area averages.

REMO-ERA performances are always better than those of REMO-NRA and REMO-ECHAM. REMO-ERA has a better monsoon representation than the others. ERA15 has the best forcing fields among the three. NRA has originally lower resolution than ERA15, no specific humidity in the upper 9 levels and no information on the liquid water content. Although having such quality limits, REMO-NRA could produce good simulations because we are dealing with the lower atmosphere and the NRA quality in the lower level is good. Unlike the other simulations, REMO-NRA fails to improve the representation of the local phenomenon over eastern Sulawesi (Table 4.2).

At T106 ECHAM4 exhibits considerably less variability than the two REMO simulations and, the monsoons are not well simulated. However, during strong ENSO years its quality is better. Similar characteristics appeared in REMO-ECHAM at 0.5 ° resolution. Furthermore, ECHAM4 has different time quality, which is using Julian days instead of real calendar year. As monthly averages in ECHAM4 are based on 30 days (see Table 4.1), there might be accuracy issues related to that date discrepancy. In spite of this, REMO-ECHAM produces good results over Kalimantan, Sulawesi and especially over Sumatera. Moreover, there are stronger improvements during the ENSO years of 1982 and 1991.

Over Sulawesi Island, there is also a REMO simulation at 1/6 ° resolution available. The REMO simulation at 1/6 ° has a correlation value to observations similar to that of 0.5 ° simulation. In fact in the last ten years, the higher resolution simulation is a reproduction of the coarser one. Thus, in comparison to the observations at the 0.5 ° resolution, there is not much improvement by going into a higher resolution for Sulawesi. Limited data quality in 0.5 ° degree may not be suitable for that comparison.

Despite all of this, the quality of each REMO simulation is highly comparable to its original lateral boundary counterpart. A high correlation result, as shown in Table 4.2, corresponds to a high correlation at the GCM resolution and so do most low correlation results. Exceptions to these are the results for REMO-ERA and REMO-ECHAM over Sulawesi and REMO-ERA over Irian, where there are significant improvements by REMO simulations. Both Sulawesi and Irian are nearby the missing anti-monsoonal climate pattern over Molucca Sea, thus improvements in both areas are understandable. At 0.5 ° the rest of land correlations show merely the down scaling implication of a limited area modeling. As a note all correlations are made at the 0.5 ° resolution.

Although REMO uses similar parameterizations as ECHAM4, the quality of REMO-ECHAM

Table 4.2: Correlations between rainfall simulations in REMO and global models and observations for the five major islands

Island	REMO			Global		
	ERA	NRA	ECHAM4	ERA	NRA	ECHAM4
Java	0.798	0.716	0.173	0.815	0.691	0.533
Kalimantan	0.780	0.668	0.422	0.780	0.761	0.417
Sumatera	0.708	0.682	0.637	0.764	0.639	0.472
Sulawesi	0.645	0.577	0.541	0.450	0.680	0.506
Irian	0.434	0.350	0.143	0.399	0.443	0.223

is not better than the others. The quality of REMO simulations tends to follow the quality of the original forcing field at the coarser resolution. Thus, the quality of the REMO output is determined more by the quality of the boundary forcing than by the physical parameterizations. ECHAM4 at T106 is driven by AMIP2 SST, which is presumably as good as the other observed SST in reanalyses, however the quality of atmospheric circulation is lower due to inadequate orography representation and the uncoupled atmospheric simulations. REMO may inherit many of the systematic errors from the global model.

Beside correlation to observations, another measure of REMO performance is the mean difference between REMO simulations and observations. The mean error is useful in calculating the mean bias from a two-sided distribution and is calculated using the following formula:

$$\overline{err} = \overline{(x - x_{obs})} \tag{4.1}$$

Fig. 4.4 shows the mean errors in REMO rainfall simulations for the five major islands using three different lateral boundaries and of the original simulation at the GCM resolution. For the ERA driven simulation, there are considerable improvements of correlation or reduction of errors except for some months over Java. Over Sulawesi, ERA15 has large errors in April/May/June due to the missing anti-monsoonal rainfall pattern. With NRA, notable error reduction exists over Sulawesi only. From Table 4.2, REMO-NRA fails to show improvements of correlations over Sulawesi. But when using mean error analysis, an improvement becomes apparent. For ECHAM4 there is no significant improvement over all five major islands. Interestingly the error over Irian Island in the REMO-ECHAM result is similar to that of the ECHAM4 result or follows the lateral boundary. The other two REMO simulations over Irian, however, do not exhibit similar features. In fact, except over Java, the mean errors over other islands by REMO-ECHAM resemble those of ECHAM4 but are larger. Similar parameterizations at both resolutions may be responsible for this feature. The mean errors over Java are the largest for the different lateral boundary forcings. This island has a strong monsoon contrast between the dry

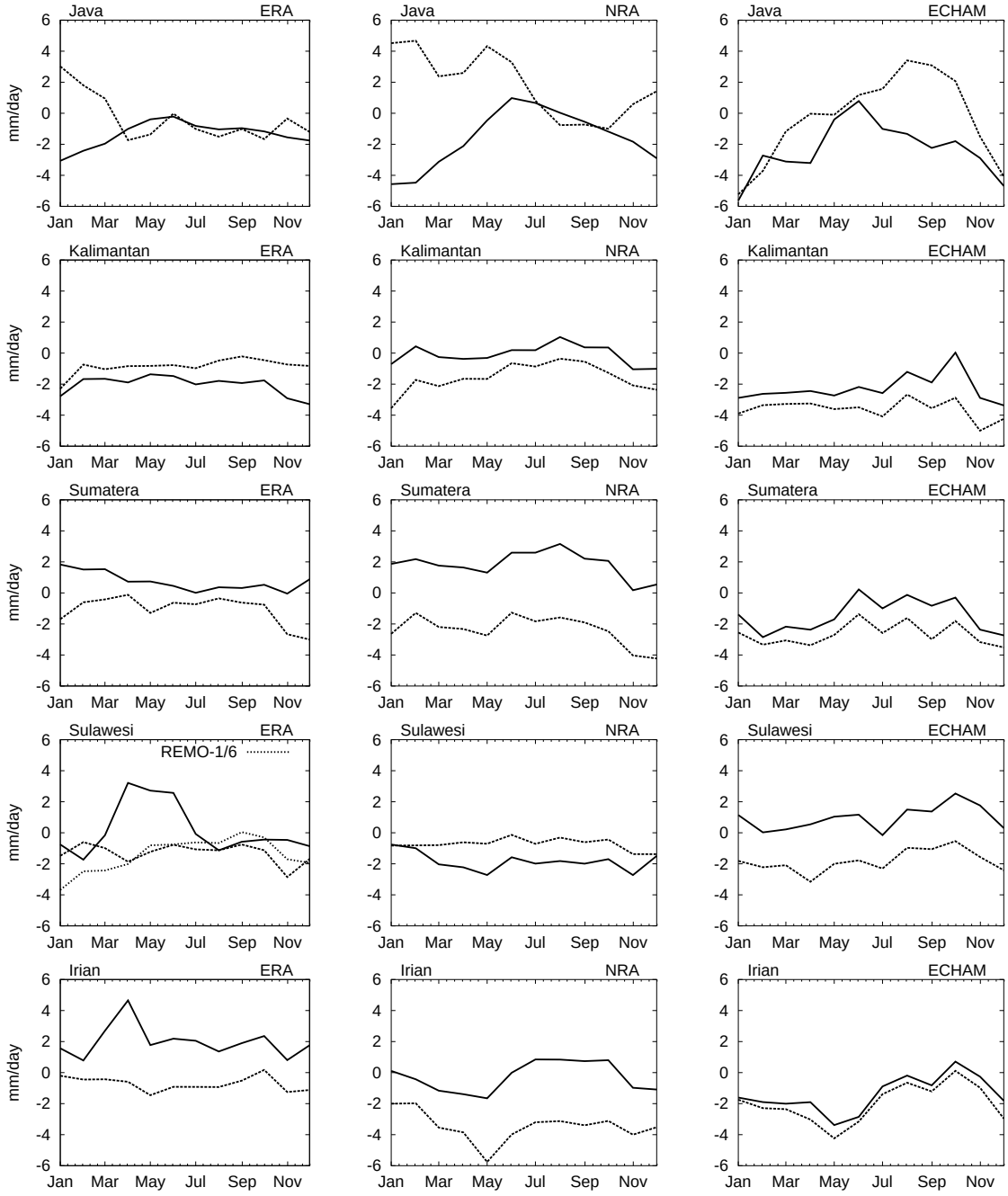

Figure 4.4: Monthly mean errors of rainfall simulations (mm/day) for five major islands with three different lateral boundary forcings from ERA (left) NRA (middle) and ECHAM4 (right) at the GCM resolution (solid lines) and the REMO 0.5 ° resolution (dashed lines).

and wet periods and REMO fails to simulate this.

4.3.2 The Three Sea Regions

The three sea regions (see Fig. 4.1) are West Sumatera (WSUM), the Molucca Sea (MOLS) and the southern part of the South China Sea (SSCS). The WSUM region has above average rainfall all year long. The MOLS has the anti monsoonal type climate and is much affected by ENSO events. The SSCS has the semi-monsoonal character with a double rainfall peaks in SON and MAM. It is difficult to verify the results over the ocean because there are no observed ocean rainfall data with comparable resolution in this region and the precipitation climatology tends to lack observations over the oceans and should be treated with caution. Here, we use the secondary ocean data from GPCP. Before looking at the rainfall variability, we will discuss the quality of the SST data used by REMO.

Table 4.3 summarizes the quality of the SST data sets from the three lateral boundary fields in comparison to an independent GISST2.2 data set through the root mean square error (RMSE). The RMSE is useful in calculating the absolute mean error regardless of the distribution type and is defined as follow:

$$RMSE = \sqrt{\overline{(x - x_{obs})^2}} \tag{4.2}$$

The SST in SSCS has the least error in comparison with other regions, while MOLS has the largest error, where the RMSE reaches more than 0.5 °C. Another quality measurement is the monthly mean errors as shown in Fig. 4.5. Both reanalyses have large negative biases over MOLS, but the smallest bias in the other two regions. From both RMS and mean errors, both reanalyses have similar SST data quality since they may have been derived from the same source. For example over MOLS, the correlation value between the two SST is high (0.993) and the RMS error is very low (0.09 °C). Over SSCS, agreements among SST are high, except for ECHAM in DJF.

The results of the three REMO simulations over sea are shown in Fig. 4.6. Like in the case of the simulations over Sulawesi, the simulations over the Molucca Sea show a significant improve-

Table 4.3: REMO root mean square errors (°C) of SST for the three sea regions (in comparison to GISST2.2 SST).

	Southern South China Sea	Molucca Sea	West Sumatera
REMO-ERA	0.153084	0.577285	0.330395
REMO-NRA	0.145185	0.554426	0.316757
REMO-ECHAM	0.277618	0.338743	0.342254

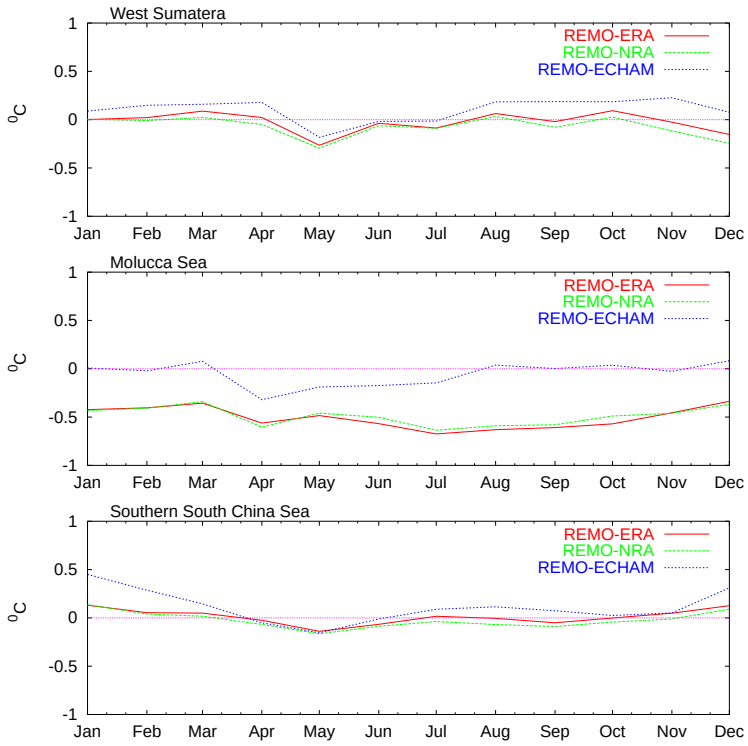

Figure 4.5: Monthly mean SST errors (°C) in the three sea regions.

ment for REMO-ERA, a small improvement for REMO-ECHAM and deterioration for REMO-NRA when compared to the global driving fields, both land (Sulawesi) and sea (Molucca) correlations decrease by 20% from original NRA to REMO-NRA. NRA has a coarser resolution than the other two. NRA and ERA have very similar SST and both have similar negative biases in relation to the other SST data. However, REMO-NRA fails to show improvement over Molucca. In addition the quality of the atmospheric representation, either the resolution or lack of some parameter fields by NRA such as the liquid water content and upper air specific humidity in higher levels, contributes to this discrepancy. Interestingly, REMO-ECHAM shows a small improvement over this region, although a bias of 0.5 °C is observed between ERA and ECHAM4.

With ERA15 as lateral boundary, REMO overestimates generally rainfall over the ocean. However, over the SSCS where the SST has the smallest difference to GISST2.3 SST, REMO-ERA gives a realistic rainfall amount. Thus, in the least error prone region (SSCS), the agreement is rather high and the time series are better correlated than for the other regions. However, as shown in Table 4.4, these high correlations depend on the quality of the lateral boundaries. Over SSCS the quality of the rainfall variabilities of the driving fields is also high. In the case of ECHAM4, large errors in this region will cause large errors REMO simulations as well. The situation over SSCS shows that realistic SST values lead to high quality rainfall simulation both at GCM and REMO resolution, underlining the importance of correct SST forcing. The occurrence of local precipitation maxima over the sea (i.e., at the grid point scale) might be linked to a

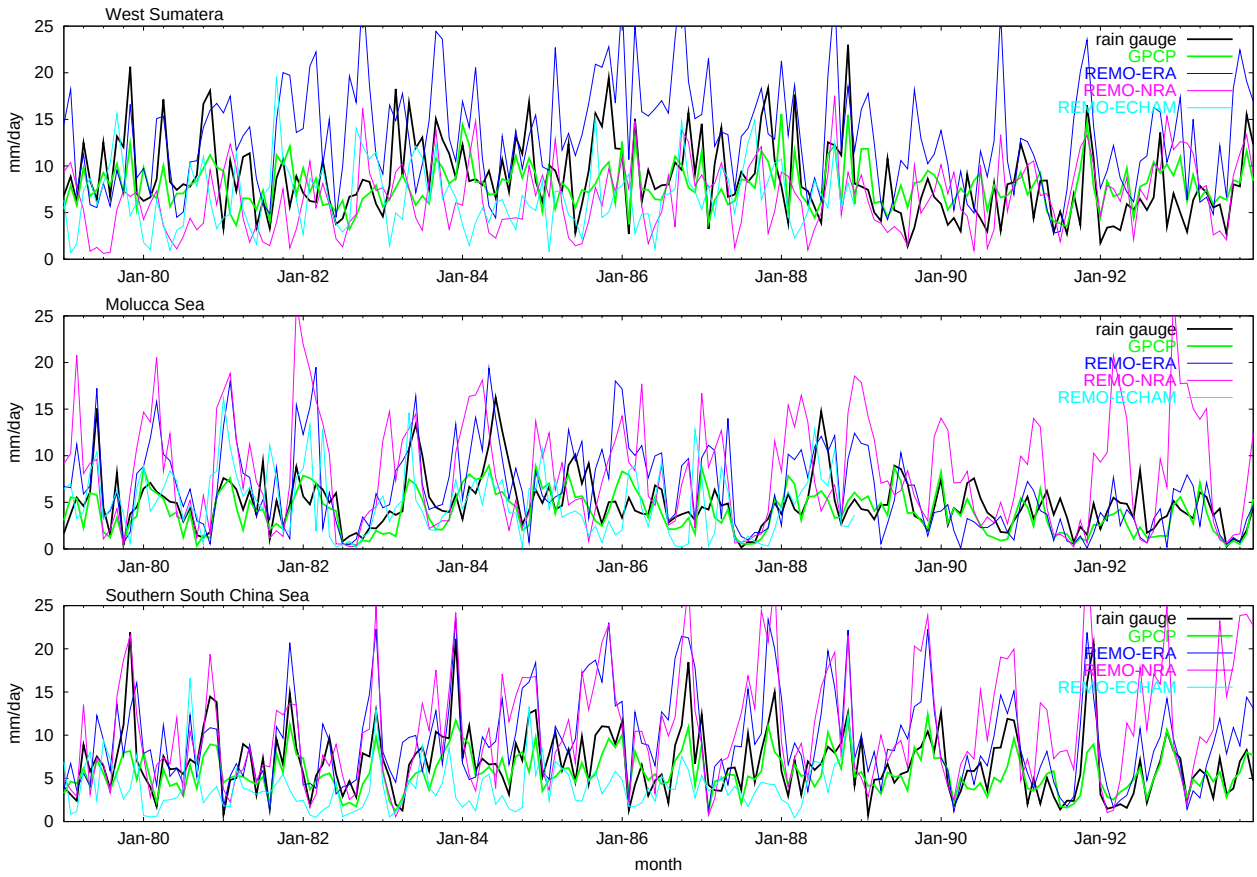

Figure 4.6: Variability of simulated and observed rainfall for the three sea regions.

feedback between local circulation (enhanced low level convergence) and release of latent heat of condensation, producing local warming and subsequent enhanced convergence and vertical motions. This feature has been previously discussed in *Giorgi* (1991).

Over WSUM, REMO performances resemble the quality of the corresponding lateral boundary forcing. Moderate SST agreement and low observed rainfall quality may also be responsible for the discrepancies. Due to the lack of rainfall data over the sea, monthly mean errors such as in Fig. 4.4 for simulations over land cannot be analysed.

Table 4.4: Correlations between rainfall simulations in REMO and global models and observations for the three sea regions.

Sea region	REMO			Global		
	ERA	NRA	CHAM4	ERA	NRA	ECHAM4
West Sumatera	0.390	0.191	0.118	0.370	0.055	0.052
Molucca Sea	0.570	0.290	0.391	0.222	0.517	0.345
Southern South China Sea	0.680	0.641	0.283	0.748	0.638	0.320

4.3.3 Improvement through Higher Resolution

Figures 4.7 and 4.8 present the improvement by REMO simulation over Sulawesi in a hierarchy of model resolutions from T106 or 1.125 ° (bottom right) to 0.5 ° (bottom left) and to 1/6 ° (upper right) in comparison to the observed rainfall at resolution 0.5 ° (upper left). These examples are taken from a normal year (a non-ENSO year) and from peaks of the wet season (January) and the dry season (July). Sulawesi has two climate systems (bimodal system). They are the regular monsoonal system in the south, part of central and north Sulawesi Island and the anti monsoonal system in the eastern and northern part of central Sulawesi Island. The monsoonal system has the annual rainfall maximum in DJF, while the anti monsoonal system reaches it in JJA.

During the dry season, as shown in Fig. 4.7, observations show maximum rainfall in the middle and eastern parts of Sulawesi. ERA15 does not show the corresponding maxima, but REMO in both resolutions show the correct locations and magnitudes of the maxima. Similar results are also indicated for the peak of the wet season in Fig. 4.8, when the maximum lies in south Sulawesi. REMO-ERA improves correlation with observation compared to ERA15 over Sulawesi. The improved correlation indicates a more realistic model climate in REMO for this area and reveals a formerly obscured local phenomenon.

Higher resolution (at 1/6 °) also gives more vigorous orographic rainfall over Sulawesi than for coarser resolution. There is a general tendency of RCMs to overpredict precipitation amounts over high topography (see *McGregor* 1997 for a review), presumably because of incorrect handling of the gradients along steep sigma surfaces. Similar findings have been reported by *Menendez et al.* (2001) and *Nobre et al.* (2001) over South America and *McGregor and Walsh* (1994) over Australia.

The representation of the anti monsoonal climate over the Moluccan archipelago is not as good as that for eastern Sulawesi because the Moluccan archipelago is close to the boundary the REMO domain. If it would be extended further east at high resolution, we expect a better representation of the anti monsoonal system. A remaining deficiency is the common problem overestimated rainfall over the ocean at both REMO resolutions.

In summary the downscaling by REMO with three spatial resolutions shows a better rainfall representation over the Molucca region and part of Sulawesi. The anti monsoonal system was missing in the T106 analysis. Although, the boundary forcing does not contain it REMO could produce this bimodal system at higher spatial resolution, indicating that the anti monsoonal circulation over Molucca and east of central Sulawesi is a local phenomenon which can not be resolved with a low resolution global model at T106.

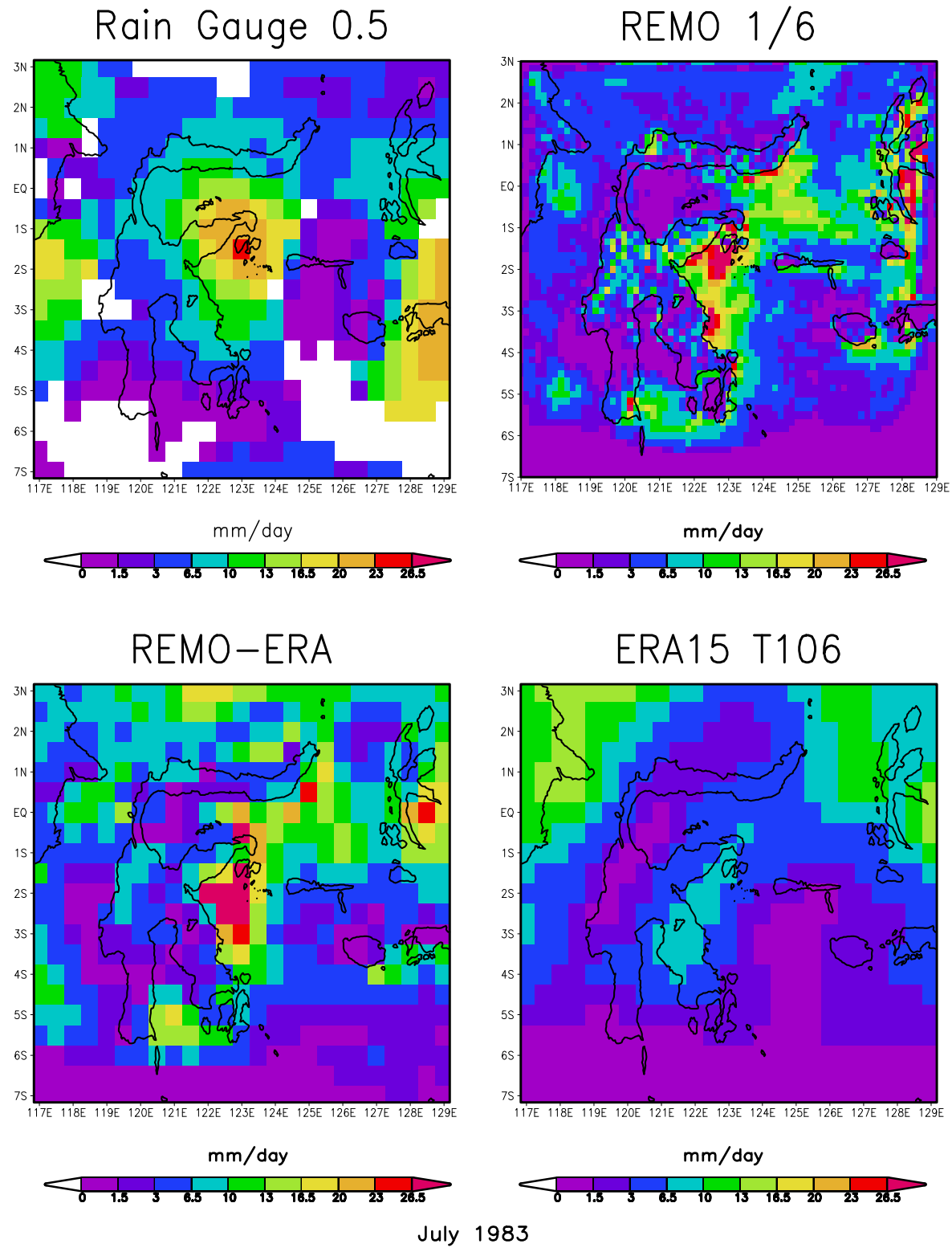

Figure 4.7: An example of the effect of resolution in a hierarchy of climate models for rainfall simulation in ERA15 reanalysis, REMO-ERA at 0.5 ° and REMO-1/6 in comparison to observations at 0.5 ° resolution. The example is taken from July of a normal year 1983.

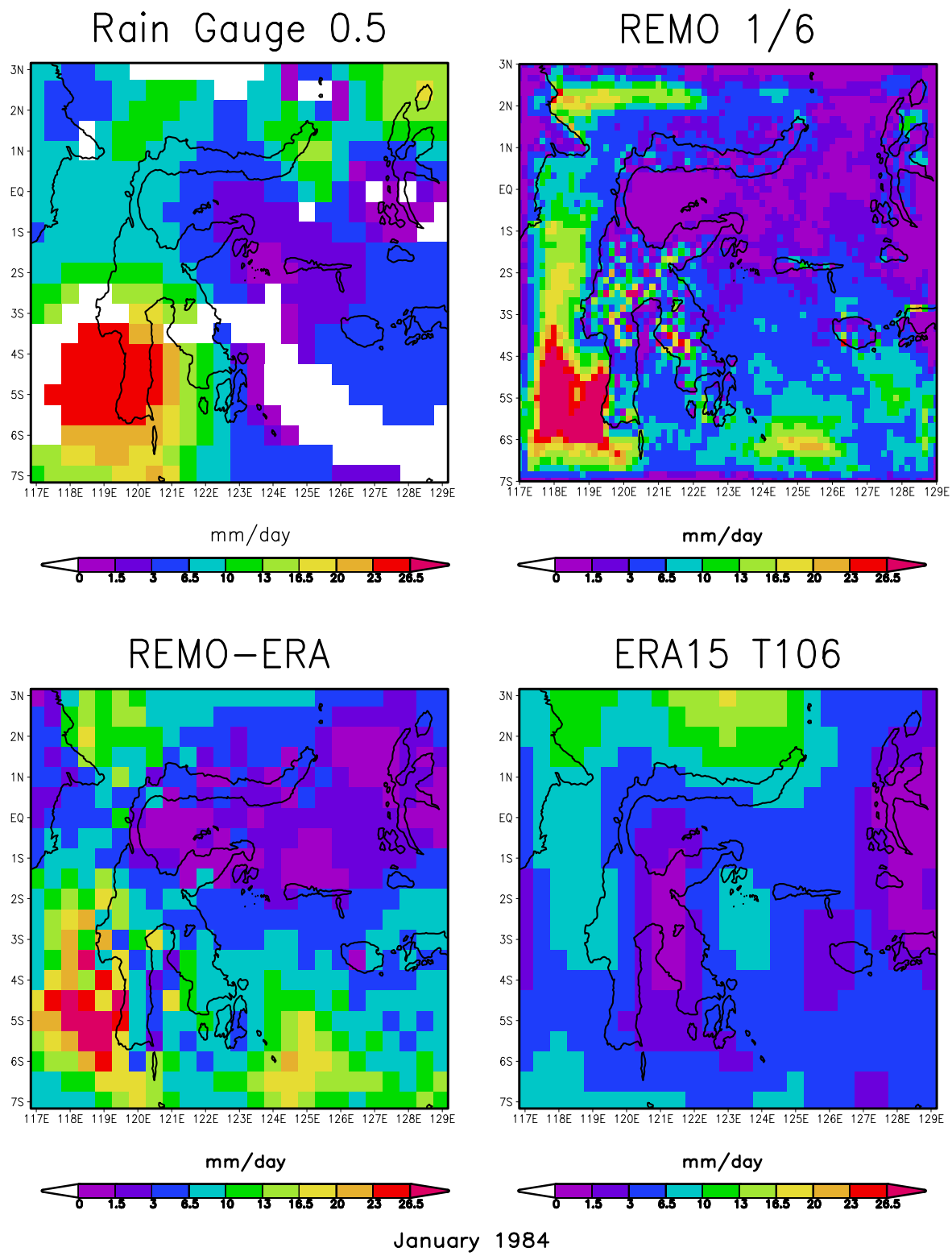

Figure 4.8: As Fig. 4.7, but for January 1984.

4.3.4 Sensitivity Studies

REMO produces overestimates rainfall over the ocean. Although the area averages are comparable, peak values over the ocean are too high. In order to understand the possible background of this overestimation, we adjusted some parameters, which eventually would reduce the precipitation over the ocean with minimal changes over land. In doing so, we changed the minimum cloud thickness over land (ZL) and ocean (ZO), the minimum humidity level for the condensation to start (ZRTC) and of the large-scale cloud system (ZRTL), SST and the Charnock constant (CCHAR). The sensitivity study was performed with REMO-ERA, which shows the best results so far. The REMO-ERA with changed parameters was rerun for the first 4 years between 1979 - 1982 to allow all simulations to use the same starting point and compare the results to the control run. Fig. 4.9 illustrates two examples from the sensitivity study over Kalimantan and Southern South China Sea in comparison to REMO-ERA or the control run.

The minimum cloud thickness for the start of the precipitation process over land (ZL) and over sea (ZO) are set to 1500 m in REMO, but in the original ECHAM4 parameterization they ranged from 3000 to 5000 m. We changed them to 2000 m or 3000 m, or varied them between 3000 m and 5000 m and looked for effects upon rainfall over land and sea. The result shows no significant influence on rainfall over the sea. Over land, however, a reduction of the average rainfall by 1.28 mm/day over Kalimantan occurs when adopting a flexible threshold between 3000 and 5000 m.

The second approach was to apply a constant SST reduction by 1.0 °C. This reduction lowered rainfall over land and sea. However the reduction over land was less than over sea and the latter is unrealistically large (5 mm/day). This kind of sensitivity study shows the importance of SST for climate modeling over the region. Furthermore, with only a little more than 21% of land area and small islands all over the place, the mean climate of the region is oceanic or ocean affected.

Another sensitivity test is to change the minimum relative humidity threshold for the condensation to start in a grid volume. This parameter involves two precipitation processes, the convective and large-scale precipitation. In the original formulation both parameters (ZRTC and ZRTL) were set to 60%. Changing them to 80% causes significant changes over land and sea. Interestingly, the rainfall over land increases somewhat, while the rainfall over sea decreases significantly.

Evaporation is a key process for atmospheric water cycle and thus precipitation processes. The Charnock constant is a measure for the rate of evaporation or the evaporation flux into the atmosphere from the ocean. In the original ECHAM4 parameterization, this parameter is set to 0.032. REMO also uses this value but only for a grid cell size above 0.5 °, while for finer resolution a value of 0.0123 is used. In this sensitivity study, the original ECHAM4 parameterization

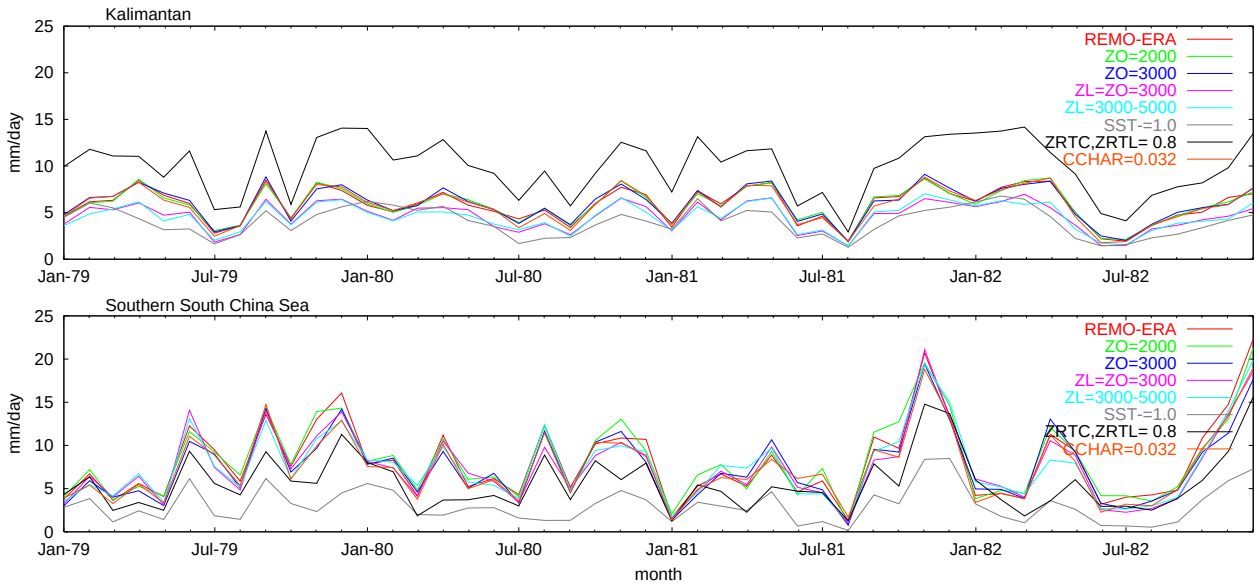

Figure 4.9: Two examples of the results from the sensitivity study over Kalimantan and the Southern South China Sea.

is used. The result shows only a slight precipitation decrease between the sensitivity and the control run. Like in the case of changing SST, the decrease of rainfall over the sea is a bit larger than over land. This fact marks this constant as the next good candidate of the solution for the problem of rainfall overestimation over sea.

Table 4.5 summarizes the seven sensitivity studies. From the above presented analysis, there are three possible candidates for the solution of the problem of rain overestimation over the sea. These are the reduction of SST, changed ZRTC and ZRTL and a changed Charnock constant. Drastic reduction takes place when the REMO SST is reduced by 1.0 °C and ZRTC and ZRTL are set to 80%. But the reduction takes place also over land, while we intend to have reductions over sea only. Furthermore, when we compare the result with observations, this reduction does

Table 4.5: Mean difference (mm/day) between sensitivity studies and control run (REMO-ERA).

Sensitivity type	Land					Sea		
	Java	Kalimantan	Sumatera	Sulawesi	Irian	Wsum	Mols	SSCS
ZO=2000	0.003	0.034	-0.018	0.051	0.078	-0.092	0.037	0.178
ZO=3000	0.413	0.114	0.678	0.508	0.443	-1.241	-0.224	-0.569
ZL,ZO=3000	-0.471	-1.243	-0.757	-0.857	-0.617	-1.093	-0.659	-0.568
$3000 < (ZL, ZO) < 5000$	-0.460	-1.289	-0.781	-0.831	-0.583	-1.049	-0.415	-0.497
SST-=1.0 °C	-1.782	-1.788	-1.634	-2.266	-0.789	-4.657	-4.866	-5.068
ZRTC,ZRTL=80%	2.569	4.135	5.675	2.655	3.888	-1.336	-3.307	-2.459
CCHAR=0.032	-0.046	-0.057	-0.014	-0.191	0.148	-0.351	-0.425	-0.673

not always bring the rainfall amount close to observations. It may be a combination of several possibilities, which have been discussed above, that are responsible for the discrepancies of rainfall between REMO and observations. From the three sea regions, the least error prone region (SSCS) has the least bias. In conclusion, the combination of prescribed SST and parameterization errors may be key contributors and a coupled ocean atmospheric model is needed for further investigation.

4.4 Predictability of Rainfall Simulated by REMO

Lorenz (1969) found that each scale of motion possesses an intrinsic finite range of predictability. A small error in the initial state of a nonlinear system will grow and will render a forecast useless after some time, regardless of the model error. For this study we performed ensemble simulations by changing initial land and atmospheric states to measure the internal variability of the model. *Ji and Vernekar* (1997) applied a similar technique for a RCM, but for a shorter term. The simulation was setup by varying the initial condition by 12 hours from 0 to 72 hr and making a control run at 0 hr and six ensemble members. With this setup we change all lateral boundaries at the initial condition and the exact length of the first month of simulation will be slightly different among ensemble members. There are two ensemble simulations using boundary forcings from ERA15 and ECHAM4 to represent reanalyses and GCM model simulations. This predictability study refers to the predictability of the initial condition or the predictability of the first kind. We will look how strong the initial condition affects the short and long-term simulation.

From long term simulations with ERA15 and ECAHM4 lateral boundary forcings as shown in Fig. 4.10, there are only small internal variabilities among control run and other ensemble members. All ensemble members follow strongly the variability prescribed by the control run. This characteristic appears in all seasons and regions (not shown). The variability of ensemble members follows the control run right after the first month. Thus, after a while, there is no effect left from changing the initial condition or, in other words, the boundary condition controls strongly the variability of each ensemble member. In comparison to land, the variability over sea is larger in both types of REMO experiments. The internal variability does not grow or decay with time but establishes itself as an intrinsic finite range of REMO predictability.

4.4.1 Intrinsic Errors

A more cautious investigation employs monthly root mean square errors (RMSE) of the internal variability. By looking at this, we exclude other external errors and examine solely the intrinsic

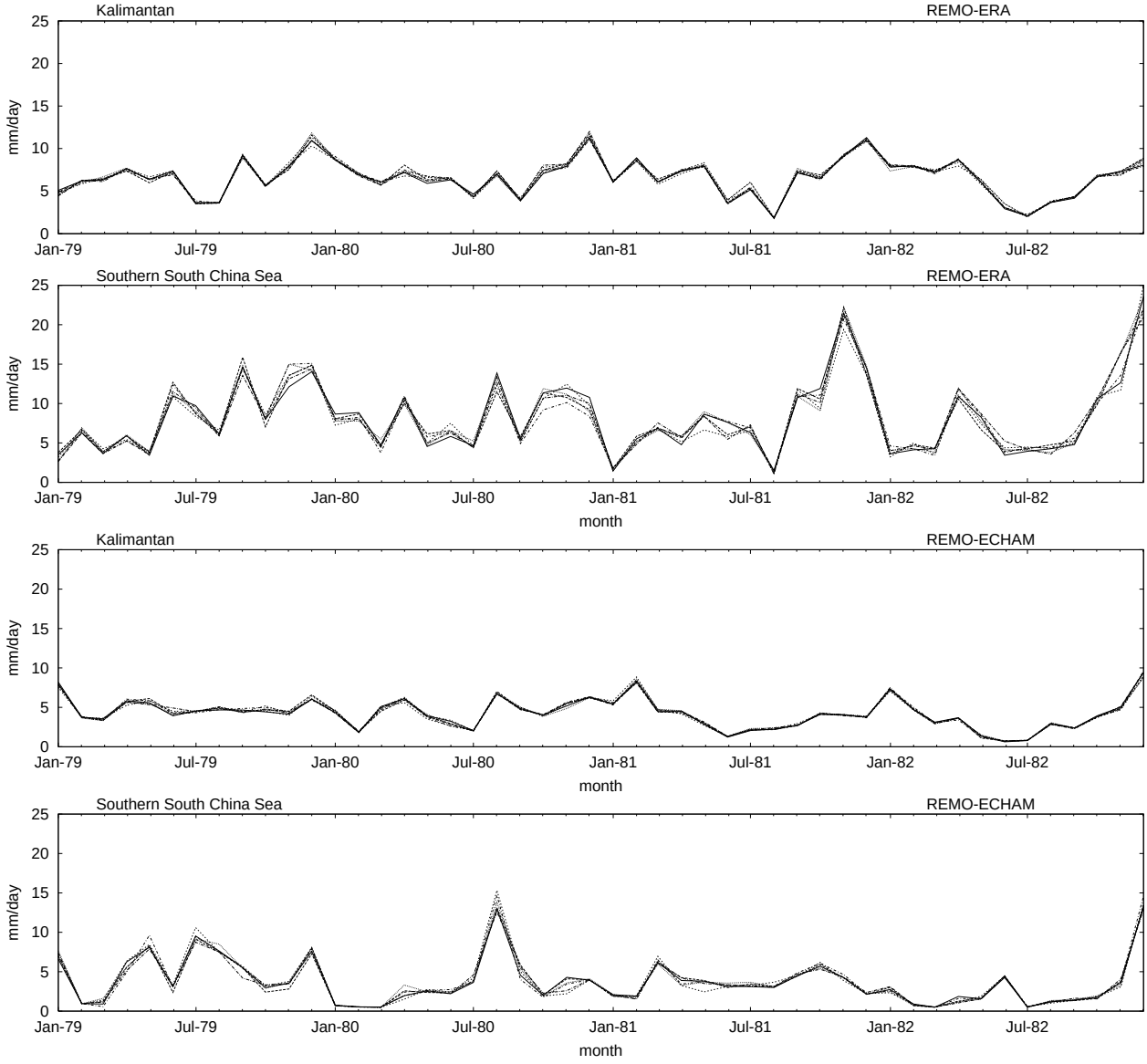

Figure 4.10: Examples of the results from the long term predictability study over Kalimantan and the Southern South China Sea from REMO-ERA and REMO-ECHAM. Each graph consists of a control run and 6 ensemble member simulations. For the sake of clarity only the first 4 years are shown.

climatological error due to different initial conditions, since we maintained all model parameters and lateral boundaries. Any errors will be due to the initial condition as a possible source of errors in REMO simulations over the region. The intrinsic climatological error over the five major islands and the three sea regions are shown in Figs. 4.11 and 4.12.

Interestingly, each island has a unique and a coherent annual pattern. Java has the largest error especially in REMO-ERA, whose RMSE reaches almost 3 mm/day in April. This RMSE is significantly large considering the average value of REMO-ERA and REMO-NRA in April of 4.87 and 9.20 mm/day respectively. Other islands have less than a third of Java's error. From both types of REMO experiments, there are considerably large errors during Northern Hemisphere spring (March/April/May) than during other seasons. Indonesia experiences at this time of the year the transition between the wet and the dry monsoon periods. On the other hand, there is also a systematic pattern of the lowest error during the Northern Hemisphere summer (June/July/August), when most of Indonesia experiences the peak of the dry period. Furthermore, this lowest error period is the most coherent period. Thus we expect that simulations of rainfall over Indonesia have the highest predictability in this time of the year. In other words, this season is the best period to examine other predictabilities beside internal predictability due to initial conditions. The other two seasons (December/January/February and September/October/November) have errors in between the two seasons as discussed earlier.

Over sea, the variability of the intrinsic climatological error due to initial condition is less coherent and has magnitudes higher than those over the lands. Moreover, there is no common pattern as those over major island areas. The highest spring and lowest summer errors are detected over the Molucca Sea. REMO simulations often produce overestimations of rainfall over the sea. The internal climatological error is also responsible to such discrepancies. Thus, from the result of this predictability study alone, higher error over the sea is expected from REMO simulations over Indonesia.

Consistent and large intrinsic errors in spring for a large part of Indonesia contribute to lower predictability skill in this season and may be related to the spring predictability barrier. The spring predictability barrier refers to a lower skill generally observed for predictions that extend through boreal spring (*Blumenthal,* 1991; *Goswami and Shukla,* 2000; *Latif and Flügel,* 1991; *Latif and Graham,* 1992; *Webster and Yang,* 1992; *Balmaseda et al.,* 1995; *Davey et al.,* 1996; *Moore and Kleeman,* 1996; *Chen and van den Dool,* 1997; *Yu et al.,* 1997; *Flügel and Chang,* 1998; *Latif et al.,* 1998; *Weiss and Weiss,* 1999; *Goddard et al.,* 2000; *Thompson and Battisti,* 2001).

The predictability study suggests a monthly or seasonal variability of the intrinsic RMSE error of REMO over Indonesia. It has been demonstrated previously (e.g. *Errico and Baumhefner* 1987; *Vukicevic and Errico* 1990; *Paegle et al.* 1997; *Laprise et al.* 2000) that the predictability of regional climate models is distinct from that of global models. The RMSE among ensemble

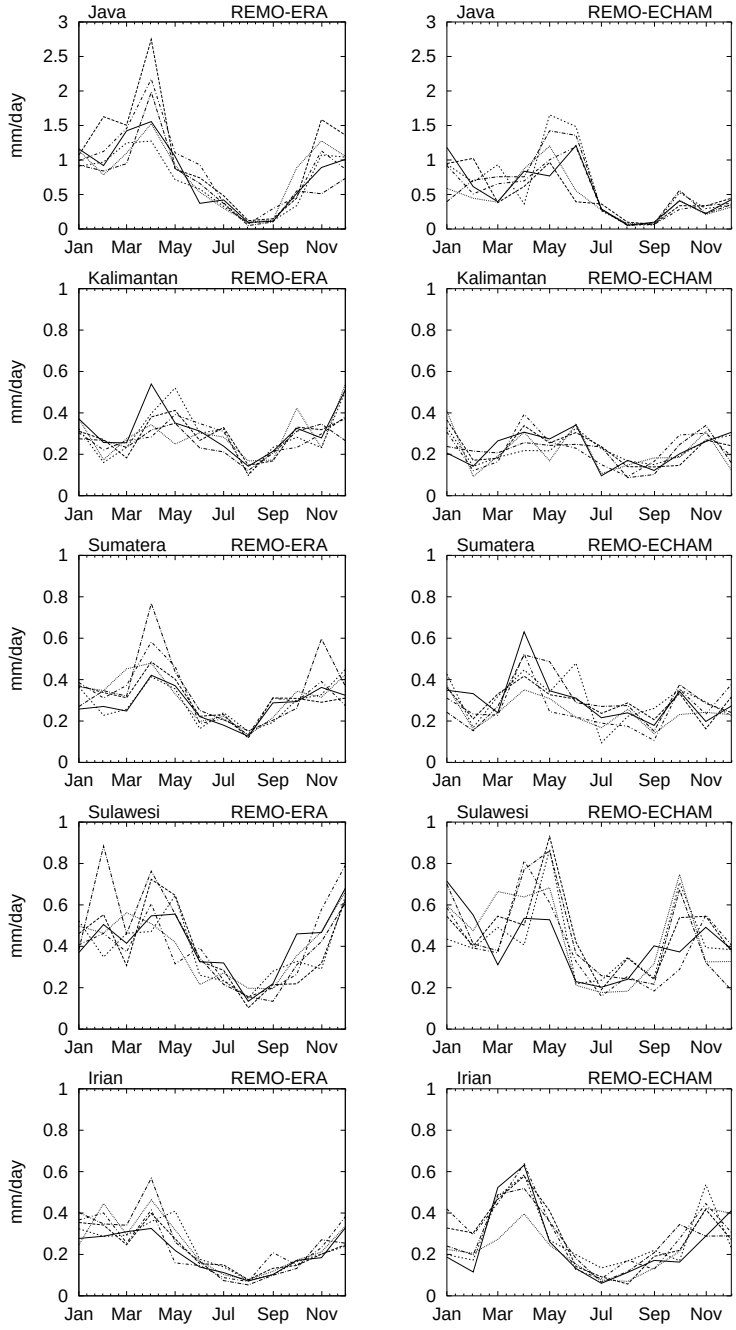

Figure 4.11: Monthly root mean square difference (mm/day) of ensemble members to control run for five major islands as a measure of the internal predictability of six ensemble members caused by the initial values. Note that Java has magnitudes three time larger than the other islands.

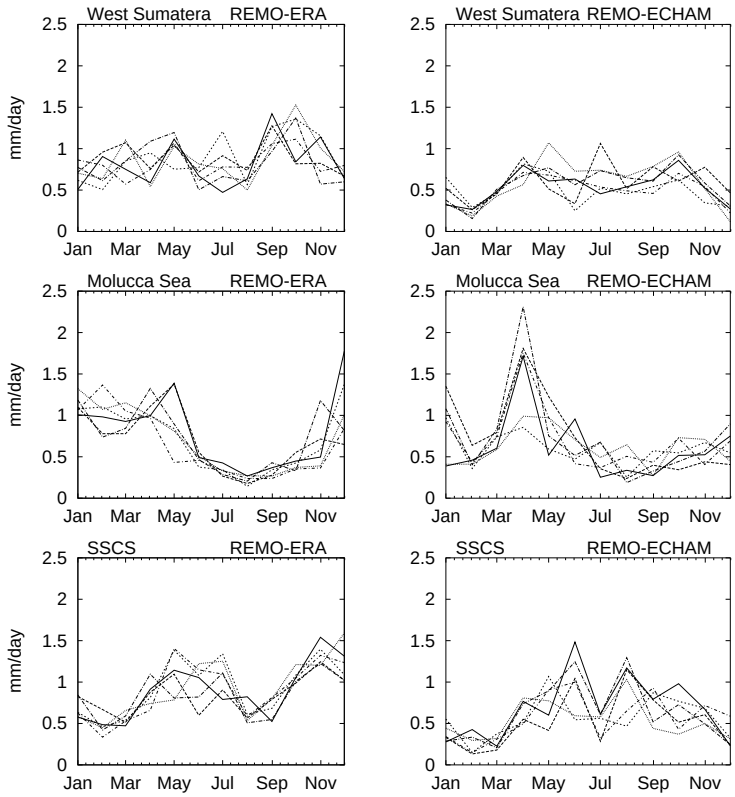

Figure 4.12: As Fig. 4.11, but for three sea regions.

members, unlike for global models, asymptotes to a value much smaller than the variance due to natural variability. While these studies concentrated mainly on other parameters such as geopotential, temperature or wind field, the present study examines the rainfall. In this study the value of RMSE of rainfall among ensemble members does not asymptote to a single value, but rather follows the intrinsic natural variability, which varies by region and season.

This predictability study shows that the lateral boundary plays a key role. However, the above analysis also showed a possibility that a local phenomenon, such as in Molucca, could appear in regional simulation that has no counterpart in the original simulation at T106. This local phenomenon appears in all ensemble members (not shown) with a high predictability or low internal variability like in other areas. Thus REMO enhances the ”just in time” local phenomenon independent of errors caused by different initial conditions. This characteristic is very important and useful for some REMO applications. For example, the regional model simulation can be used in a future climate scenario as a down scaling tool. It is not necessary to run the climate simulation for a longer period. We may proceed directly into the intended period without having to worry about the initial conditions. This is only true for local convective phenomena or in a small land area such in maritime continent, otherwise we need to wait until the soil reaches its equilibrium and restart the simulation using that equilibrium soil.

The lateral boundary condition, which is updated every 6 hours, is responsible for the high

predictability level. REMO cannot keep the memory of an initial condition after some consecutive changes of the lateral boundaries, which eventually limits the degree of freedom of REMO. There are ways to increase the degree of freedom in REMO simulations. For example, we could supply SST from a different time period for each ensemble member. This kind of study would refer to the second kind of predictability (boundary value problem). Another possibility is to supply the ocean surface boundary condition from a stand alone ocean simulation and couple that with REMO. Rather than changing the initial condition once, the ocean model could supply different SST information every 6 hour and hence give more degrees of freedom to REMO.

The result indicates that REMO has a small internal variability, which indicates that the corresponding simulations are strongly constrained by lateral boundary conditions. A RCM should be sufficiently free to develop internal mesoscale processes in order to be useful for sensitivity studies. In this study REMO has shown its ability to enhance regional features over Sulawesi and the Molucca Sea. The strong boundary influence may also be due to the small domain size used in this study. *Jones et al.* (1995) concluded that the regional climate model domain should be sufficiently small that the synoptic circulation does not depart far from that of the driving GCM. However, *Podzun et al.* (1995) found that the domain should also be sufficiently large to allow development in the regional climate model of features having a finer scale than those skillfully resolved by the GCM. Furthermore, *Bhaskaran et al.* (1996) found that the tropical monsoon simulation with a RCM is relatively insensitive to model domain size, which contrasts strongly with simulation results from Europe by *Jones et al.* (1995).

4.4.2 Internal and External Variances

Another measure of the predictability of an ensemble simulation is the internal and external variances or variability. The predictability is determined by the summation of those variances. In this study the internal variance is defined as

$$var(x_i, < x >) = \langle \overline{(x_i - < x >)^2} \rangle \tag{4.3}$$

and the external variance as

$$var(< x >) = \overline{(< x > - \overline{< x >})^2} \tag{4.4}$$

where x_i is the i-th ensemble member, the "$< x >$" operator denotes the ensemble average and the " $\overline{x}$ " operator denotes the time average. The method employed here is comparable to the Analysis of Variance (ANOVA) method. The internal variance measures the degree of freedom of a domain and measures how high the quality with one simulation (without ensemble) will be. In this case low internal variability indicates an expected good performance by just a single

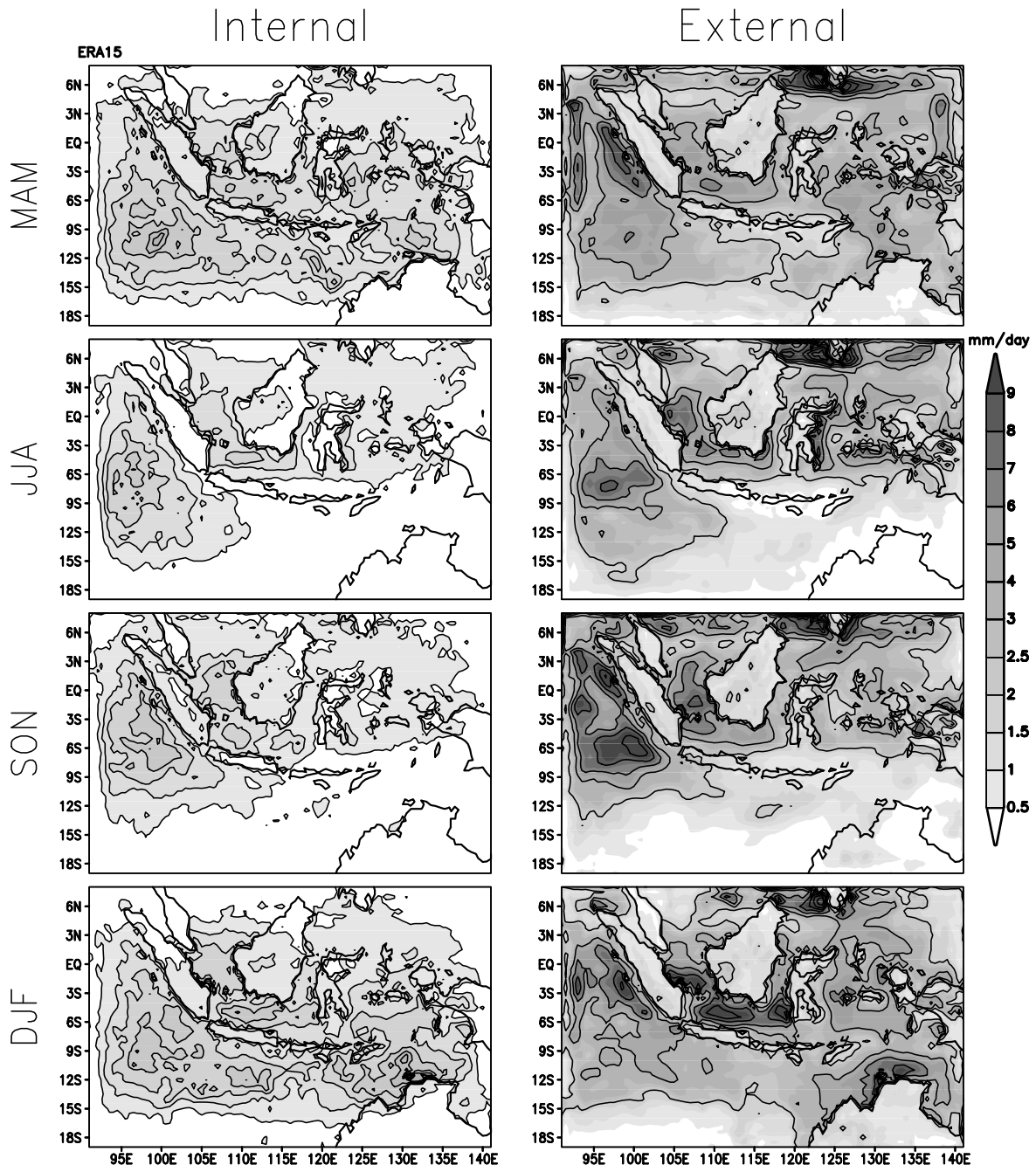

Figure 4.13: The internal and external variances of the ensemble REMO-ERA simulation.

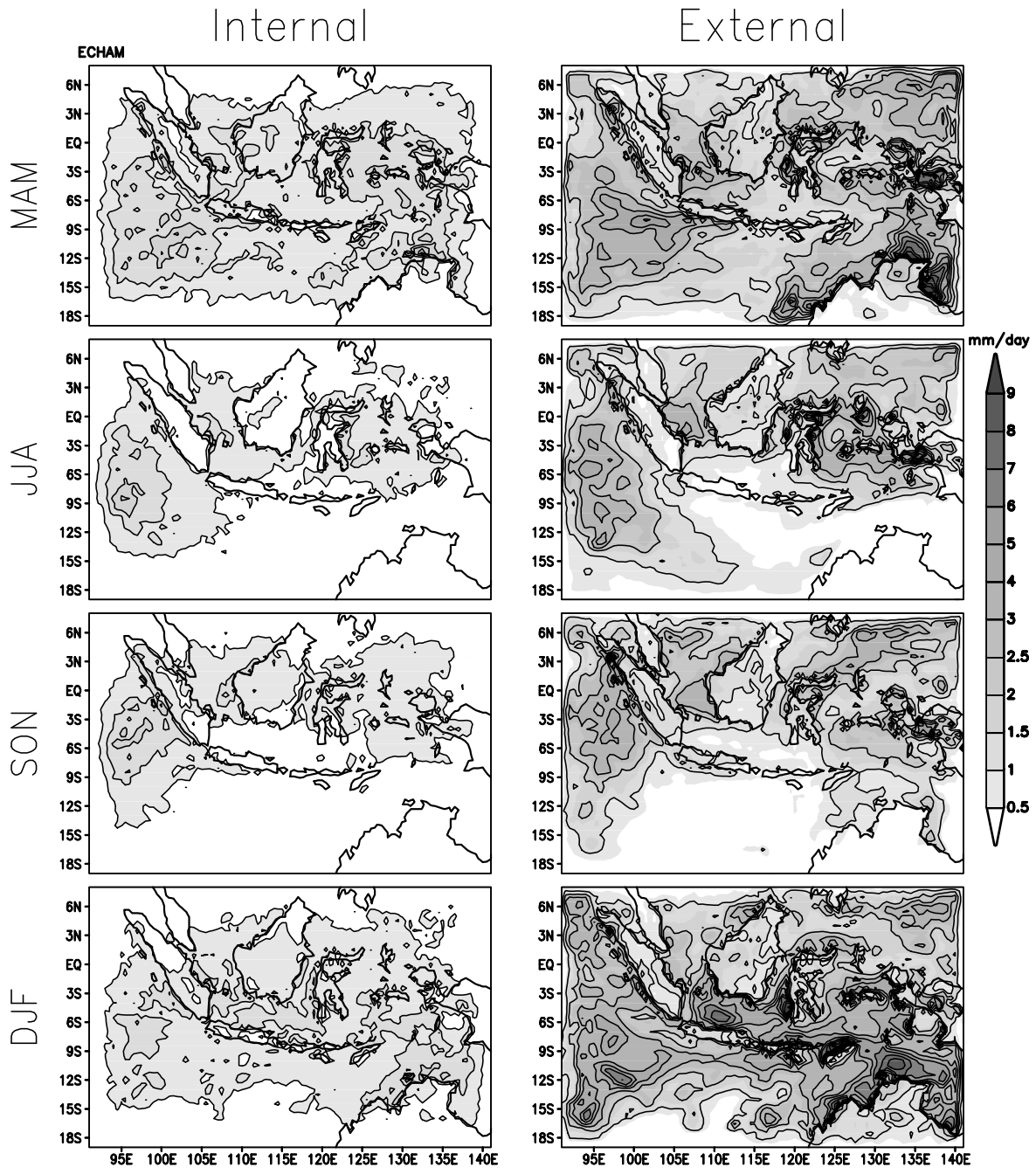

Figure 4.14: As Fig. 4.13, but for REMO-ECHAM.

simulation. Low degree of freedom may also mean too strong boundary condition control, while, the external variance measures the contribution of large scale phenomena surrounding the domain. Hence the predictability is high when the external variance is low.

Figures 4.13 and 4.14 show the seasonal internal and external variances of ensemble simulations from REMO-ERA and REMO-ECHAM, respectively. From both figures, the seasonal internal variances are only about a quarter the external variances. Thus, variability among ensemble members is mainly due to external climate phenomena. Low internal variability may also be due to too strong lateral boundaries. The lateral boundary extends up to 8 grid cells as shown in internal variances on both figures. Within the inner region, the model is capable to develop variability independent on lateral boundaries. The inner region shows variances according to climate activity, whereas higher variances exist in wetter regions or areas with higher precipitation activity. Consequently, the internal variance has a seasonal dependency according to wet and dry seasons, when JJA and SON have less variance than the other seasons. The latter condition is also true for the external condition, where higher variances are related to major seasonal disturbances in the region, such as high precipitation in west of Sumatera in all seasons, tropical storm tracks near Mindanao (not clear in REMO-ECHAM), tropical disturbances in northern Australia in DJF and a high precipitation area over Java sea. Another persistent contrast exists between variances over land and sea with variances over land or higher predictability over land than over the sea. The persistence is highest west of Sumatera, which has all year long high precipitation or nearly no seasonal dependence.

Although the measure of variance presented here is able to show sources of discrepancies among ensemble members, this variance measurement is limited to REMO only. There is a need of more ensemble quality measurements from other regional models operating in the area to determine the real quality of REMO simulation. The only comparison made here is between two different lateral boundaries; ERA15 and ECHAM, where ECHAM boundary gives lower variances than ERA15 does. Hence, the quality of a single simulation by REMO-ECHAM is closer to its ensemble mean than for REMO-ERA. The present study shows that high predictability is achievable over land in JJA followed by SON. The latter result is consistent with the findings in previous subsection.

4.5 Concluding Remarks

We have described the performance of rainfall simulations over Indonesia with REMO driven by three lateral boundary conditions coming from two reanalyses and an ECHAM4 simulation at two different horizontal resolutions. We analyzed the results for the five major islands and three selected sea regions. Also sensitivity and REMO predictability studies for different initial condition have been performed. The analysis focuses on monthly, seasonal and interannual

variability of rainfall simulations as well as the annual cycle.

The model, in general, is able to reproduce the spatial pattern of monthly and seasonal rainfall prescribed by the lateral boundaries. It produces correct variability for ENSO years but fails to show a good monsoon contrast. The simulations over land are better in this respect than over sea. The high quality of REMO over land is due to resolved orography, while over the ocean REMO suffers from surface fluxes problems and overestimates the rainfall. The model's dependence on various sub grid parameterizations is a very complex issue and is not fully understood at present. Analyses of a sensitivity study to reduce too strong precipitation over sea are still leaving some possibilities. Beside the lateral atmospheric boundary, SST is the major factor determining the quality of simulations where the least error prone region (SSCS) has the least bias.

The results suggest the important role of lateral boundary conditions. REMO-ERA, which has the best lateral boundary fields supplied by ERA15, produces the closest simulation to observations except over Java. Despite the strong influence of the lateral boundary, REMO shows realistic improvement of a local climate phenomenon over Molucca through higher correlation (REMO-ERA and REMO-ECHAM) and mean errors (REMO-NRA).

Improvement with higher resolution is obvious from T106 to 0.5 $^\circ$ but not to 1/6 $^\circ$. There is no need to go for higher resolution of 1/6 $^\circ$, where there are more vigorous orographic rainfalls over the Sulawesi Island. However, it has to be investigated later with higher quality rainfall data. It may be that the parameterization we are using over this region is most suitable for the 0.5 $^\circ$ resolution. Moreover, RCM parameterization schemes are normally tuned to the GCM resolution (*Nouger et al.*, 1998). For this island, it might be needed to use a non-hydrostatic model. Steep orography as well as the temperature gradients associated with the strong orographic convection can only be adequately simulated with non-hydrostatic models

The predictability study shows small internal variability among ensemble members. This means that the model can be used in any place in time without worrying much about spin up. However the intrinsic climatological errors as shown in the predictability analysis are worth to be considered. Those intrinsic errors have monthly, seasonal and regional dependences and the one over Java is significantly large. The intrinsic error study suggests the presence of the spring predictability barrier and a high level of predictability in summer.

Here are some suggestions for improvement of the current study. The REMO-ERA could be extended to include the whole new ERA40 as the lateral boundary. REMO simulations with 1/6 $^\circ$ resolution over other islands, simulations with the partial REMO or a complex grid cell definition and simulations with a better annual cycle of vegetation are worth to try.

Chapter 5

Monsoonal Character of Indonesian Waters Simulated by an Ocean Global Circulation Model

Abstract

A regional model study on the monsoonal characters of Indonesian water using the Max Planck Institute ocean global circulation model, MPI-OM1, has been done with two different surface boundary forcings and two different resolutions. The lateral boundary conditions are determined by the reanalyses from the European Centre for Medium-Range Weather Forecasts (ERA15) and the National Centers for Environmental Prediction and National Center for Atmospheric Research (NRA). The simulation with NRA was performed from the period 1948 to 1999 and with ERA from the period 1979 to 1993. However most of the analyses are done for the period 1979-1993. Beside real time simulation, the result of a climatological run with a forcing from the German Ocean Model Intercomparison Project (OMIP) is also presented. This study uses a special conformal grid from a bipolar orthogonal spherical coordinate system, which allows irregular positions of the poles. The resolution plays a more important role than different surface boundary forcing in determining the result of the simulation. A higher resolution model gives higher frequency variability and better variabilites than the coarser one. The model could simulate the variability of ocean circulation quite well, but with the sea surface temperature (SST) variabilities, the model shows warmer biases due to the static surface boundary. The simulated variability of the total transport by the Indonesian throughflow during the strongest El Niño 1997/1998 has a correlation value of 0.83 with the in-situ observations. The SST variability, which is regulated by the ocean circulation, clarifies the monsoonal character of precipitation pattern in the three monsoonal regions. We found the mechanism of ocean circulation that regulates SST variability in a way that the horizontal advection influences the

heat energy content variability after 3 to 4 months and the heat energy influences the SST a month later. The monsoonal signatures are clearly seen in all ocean parameters and ocean transport exhibits the most coherent monsoonal character. The monsoonal depth varies among different seas in the area. The study suggests a possible mechanism of the El Niño Southern Oscillation (ENSO) impact on Indonesian rainfall through the ocean and an important role of the monsoonal property of the ocean circulation in that mechanism.

5.1 Introduction

The term ”monsoon” refers to a seasonally reversing circulation with a period of one year. The main driving force for the monsoon circulation is the contrast in thermal properties of land and sea. Since land has a smaller heat conduction than the ocean, the absorption of solar radiation increases the surface temperature over land much more rapidly than over the ocean (*Ferranti*, 1997). In Indonesia, the monsoonal activity is mainly related to the meridional movement of the Inter Tropical Convergence Zone (ITCZ). Although the monsoon has such a strong influence also on the sea, studies on the monsoonal properties of Indonesian waters have been very rare in comparison to similar atmospheric studies. *Quadfasel and Cresswell* (1992) found for example that the changes of monsoonal wind and the variations of the freshwater flux from the Indonesian archipelago are responsible for the annual cycle of the ocean flow. As the region is covered mostly by ocean (79%) and less by land (21%), the study of the regional land climate cannot disregard the ocean. In fact, most land climate of the region is ocean climate, where intense air sea interaction occurs around major islands. For example, *Susanto et al.* (2001) found a monsoon generated upwelling along the coasts of Java and Sumatera. Since the position of the maritime continent as the action center of the Hadley and Walker cells and the Indonesian throughflow, one has to study the local ocean atmospheric interaction. Moreover, as a previous study with a regional climate model (Chapter 4) has found large variances in ocean climate and an important role of the ocean Sea Surface Temperature (SST). This study is motivated by the finding of three distinct monsoonal climate types in the archipelago: the southern monsoonal, the northwestern semi-monsoonal and the Moluccan anti-monsoonal climate. There is a need to establish the ocean aspects that also drive the climatology of all three regions.

In order to achieve that goal, we applied the Max Planck Institute ocean global circulation model (OGCM), the MPI-OM1 (*Marsland et al.*, 2003). MPI-OM is the latest development of the Hamburg Ocean Primitive Equation (HOPE) model (*Wolff et al.*, 1997). A major improvement is the transition from a staggered E-grid to an orthogonal curvilinear Arakawa C-grid (*Arakawa and Lamb*, 1977), which allows arbitrary placement of the poles in a bipolar orthogonal spherical coordinate system. HOPE previously has been used for global climate studies (for example *Drijfhout et al.* 1996 and *Rodgers et al.* 2000) and regional studies (*Marsland and*

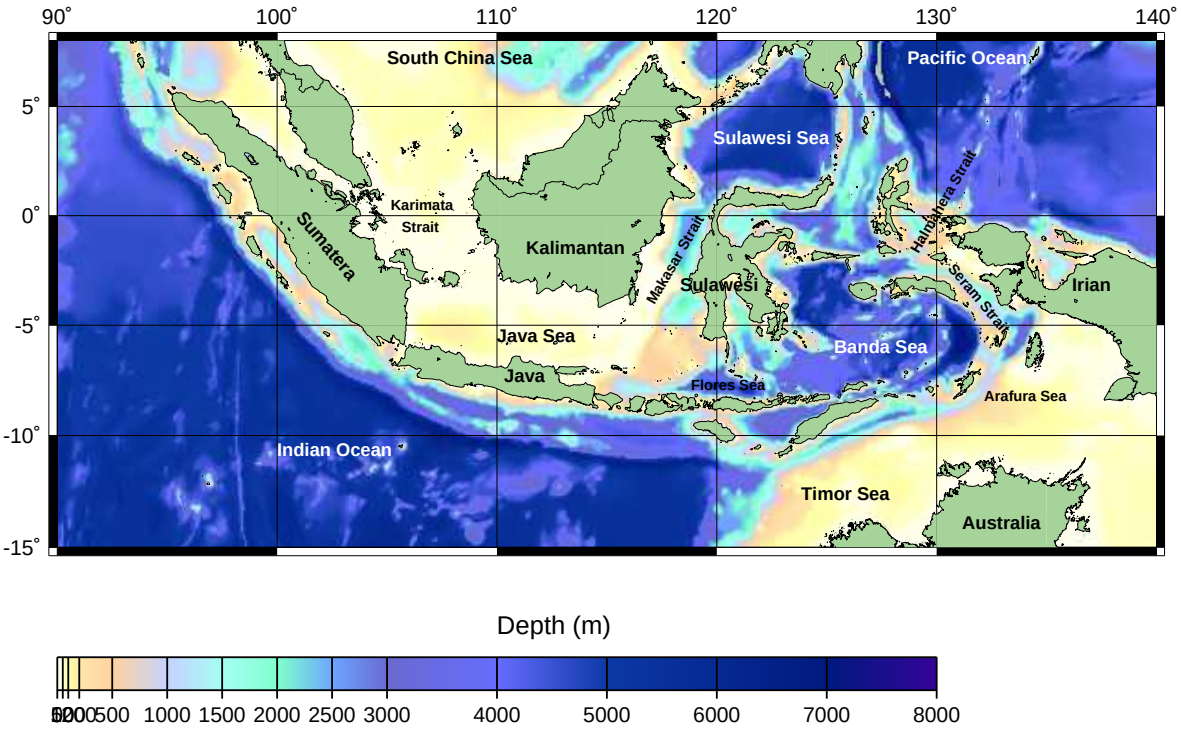

Figure 5.1: The ocean topography of the study area.

Wolff, 1998, 2001). In this study MPI-OM will be used for a regional study with a special grid.

The chapter focuses on the monsoonal variability of the ocean circulation in the three regions and surrounding seas. In addition, the variability of the Indonesian throughflow and the impact of El Niño Southern Oscillation (ENSO) on the monsoon as well as the sensitivity of the model results to spatial resolution will be investigated. The time scale is limited to monthly, seasonal and interannnual variability from 1979 - 1993. The outline of this chapter is as follows. Section 2 discusses the data and model setup, section 3 the general results for ocean circulation and section 4 specific circulations in each of the three regions simulated by the MPI-OM. Section 5 describes subsurface monsoonal signatures and section 6 the ENSO impact. Finally, section 7 summarizes major findings.

5.2 Data and Model

5.2.1 Data

This study uses surface forcing fields from two reanalyses: the ECMWF reanalysis (ERA15; *Gibson et al.* 1997), which is available at the horizontal resolution of T106 (equivalent to 1.125 °

in the tropics), from 1979 until 1993, and the more than 50 years NCEP reanalysis (NRA; *Kalnay et al.* 1996), for the time period from 1948 to 1999 available at the horizontal resolution of T62 or 2.5 $^\circ$ in the tropics. The forcing data have been interpolated to the model geometry. For climatological runs, the German Ocean Model Inter-comparison Project (OMIP; *Röske* 2001) forcing was used. SST data from the GISST2 (Global Ice and Sea Surface Temperature) dataset (*Rayner et al.*, 1996) are used for comparison.

5.2.2 Model Descriptions

The model uses the ocean bottom topography from a 5 minute global ocean bathymetry, corresponding to about 9 km resolution at the equator. Fig. 5.1 shows the bathymetry around the maritime continent, which lies between two continental shelves (Asia and Australian), two large oceans and is surrounded by deep oceans basins. Since the focus of the study is monsoon circulation, most attention will be given to the circulation variability of the upper 500 m, where the monsoon has considerable influence. In this study, the contribution of river runoff is minimized by using a limited number of rivers, whereas only 52 major rivers are used (*Dümenil et al.*, 1993).

We use a special conformal grid where the north (south) pole is located in China (Australia), which is herein named the BANDA-HOPE setup. This pole placement offers two major advantages over regular latitude-longitude grids. Firstly, the placement of the poles over land removes the numerical singularity associated with the convergence of meridians at the geographical north pole. Secondly, the choice of nondiametric poles allows the construction of regionally high resolution in a global domain and thus avoids the problems associated with either open or closed boundaries. However, it should be noted that this approach has the disadvantage of globally constraining the model time step to one small enough to be appropriate for the highest resolution region. This limitation will be analyzed with different resolutions in the present study. Fig. 5.2 illustrates this conformal grid with a global and a regional view. The minimum cell size is located near the poles. In table 5.1, selected information on the model setup is presented. The higher resolution grid is characterized by a double horizontal resolution and 30 vertical levels (as opposed to 20 levels in the coarse resolution) with increasing level thickness from surface to bottom. MPI-OM is a hydrostatic ocean model, which uses z-coordinates for vertical discretisation. For a detailed description of MPI-OM, the readers are referred to *Marsland et al.* (2003).

Several parameterisations of sub-gridscale processes have been incorporated into the model. Firstly, a bottom boundary layer (BBL) slope convection scheme has been included that allows for a better representation of the flow of statically unstable dense water masses over sills and off shelves. Secondly, harmonic horizontal diffusion of the tracer fields has been replaced by

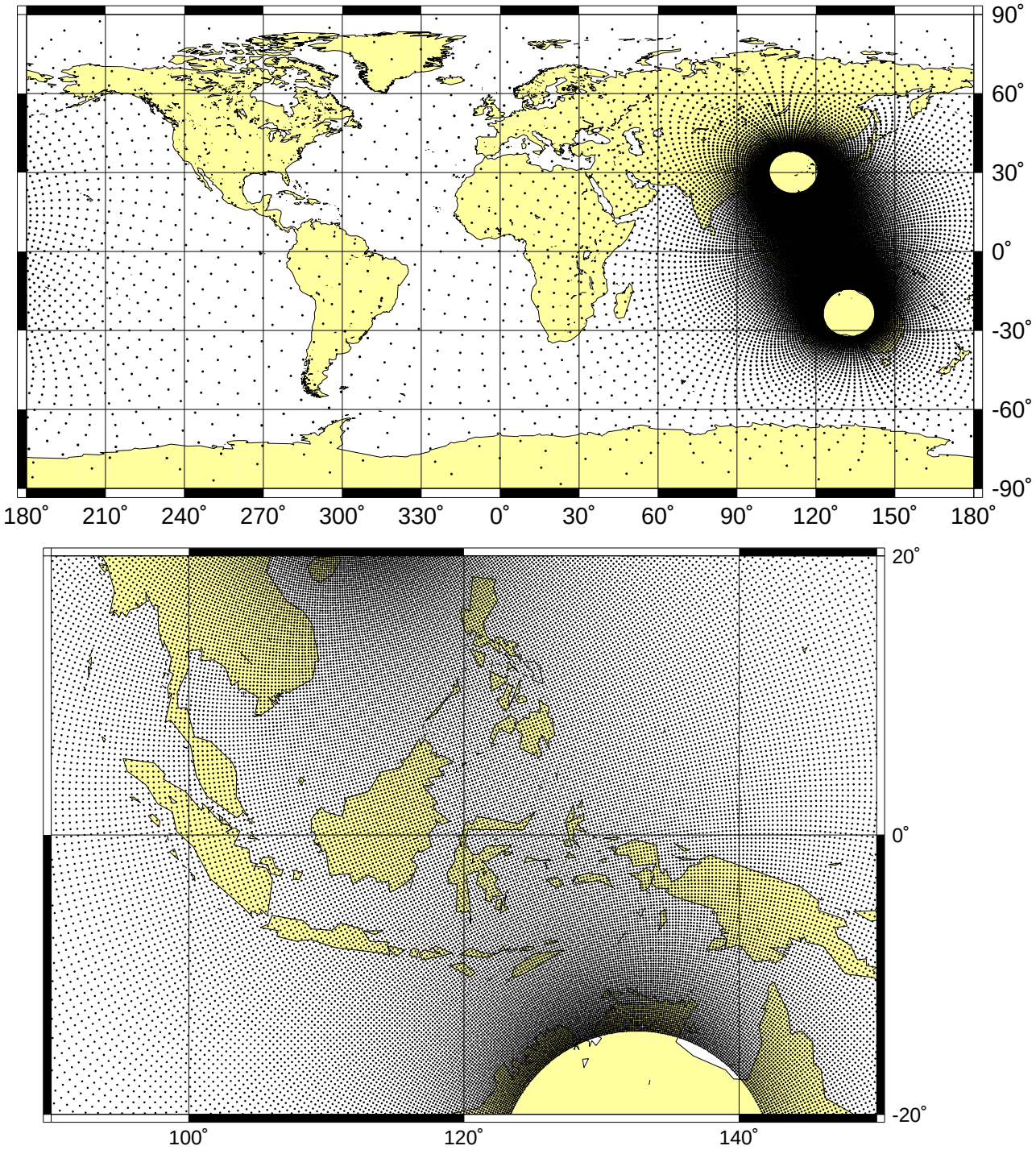

Figure 5.2: The global view of the low resolution MPI-OM orthogonal curvilinear grid (above) and the regional view of the high resolution grid system of the MPI-OM ocean model (below) with 362×210 grid cells.

Table 5.1: MPI-OM ocean model descriptions

	Low Resolution	High Resolution
Meridional grid points	105	210
Zonal grid points	182	362
Layers	20	30
Mid of layer level (m)	10,30,50,75,110,155,215,295,400, 535,700,895,1125,1400,1750, 2200,2750,3400,4200,5350	6,17,27,37,47,57,69,83,100,123,150, 183,220,265,320,385,460,550,660, 795,970,1220,1570,1995,2470,2970, 3470,4020,4670,5520
North Pole	112 °E 29 °N	
South Pole	132 °E 22 °S	
Time step	3200 s	1440 s
Input / Output	6 hourly / monthly	
Cell size (Banda Sea)	0.391 ° (40km)	0.202 ° (20km)
Max. cell size (west equatorial Atlantic)	8.20 ° (800km)	3.88 ° (370km)
Input forcing (OMIP climatology, NCEP/NCAR and ERA15 reanalyses)	2 m air temperature short wave radiation forcing precipitation rate cloud cover dew point temperature zonal (u) momentum surface flux meridional (v) momentum surface flux 10 m wind velocity	

an isopycnal scheme (*Griffies*, 1998). Isopycnal diffusion is preferable since it accounts for the observation that tracers are basically mixed along isopycnals. Thirdly, eddy-induced tracer transport has been included by the implementation of a Gent and McWilliams (*Gent et al.*, 1995) style parameterisation. Fourthly, the so-called convective adjustment has been replaced by a parameterisation using enhanced vertical diffusion. This allows for the introduction of a time dependent oceanic response to static instability.

5.2.3 Experimental Setups

The model was initialized with the annual mean data from the gridded World Ocean Atlas 1998 (*Levitus et al.*, 1998). Then the model was run for the first initial year, during which three-dimensional Newtonian (linear) relaxation of the thermohaline fields (temperature and salinity) was applied to all wet grid cells below the fourth model layer. In the later simulation years, the model uses surface boundary forcings from two different reanalyses, NRA for a period from

Table 5.2: Major Seas and Straits.

No.	Area or section	Start position	End position	Remarks
1.	South China Sea	112.0E 8.0N	106.1E 1.8N	
2.	Karimata Strait	106.1E 1.8N	109.2E 5.0S	between Sumatera and Kalimantan
3.	Java Sea	109.2E 5.0S	116.1E 5.8S	ocean depth 50m
4.	Makasar Strait	116.1E 5.8S	120.2E 4.0N	between Kalimantan and Sulawesi
5.	Sulawesi Sea	120.2E 4.0N	131.0E 2.9N	between Sulawesi and Mindanao
6.	Halmahera Strait	131.0E 2.9N	129.1E 2.1S	between Halmahera and Irian
7.	Seram Strait	129.1E 2.1S	131.5E 4.7S	between Seram and Irian
8.	Banda Sea, Timor Sea	131.5E 4.7S	124.0E 14.S	between Australia and Timor

1948 to 1999 and ERA for the ERA15 period from 1979 to 1993. MPI-OM receives at specified frequency (forcing time step) the global, predefined atmospheric fields, from which heat, freshwater and momentum fluxes are calculated using bulk formulae. The first 31 years from the MPI-OM-NRA run were skipped due to spin-up. MPI-OM-ERA was initiated using the restart forcing from MPI-OM-NRA 1979 and was integrated for 15 years from 1979 - 1993. During integration, we applied the surface boundary forcing every 6 hours and produced monthly average outputs. The same configuration is applied for the low and high resolutions. In total there are 132 years of climate integration using different resolutions and surface boundary forcings.

Beside these real time simulations, this study includes a climatological run, which was set up using the German OMIP climatology data set as the surface forcing and was rerun for at least 10 years, which was skipped later due to spin-up. The OMIP forcing was derived from the ECMWF reanalysis 15 year averages. Contrary to six-hourly forcing in the real simulation, the climatology run is integrated with daily resolution and atmospheric synoptic scale variability was used. The climatology run uses in the low resolution grid only and it served mostly for model tuning and sensitivity studies.

5.3 Ocean Circulation from MPI-OM Simulations

In the following subsections, we will examine the products of the MPI-OM simulations applying two different surface boundary forcings and resolutions. The analyses will focus on ocean surface circulation, the Indonesian throughflow and the thermohaline circulation of major seas. There are eight major ocean sections in and around Indonesia that will be used in each vertical profile analysis, where the inset figure in each contour map represents all 8 sections of Table 5.2 starting in the South China Sea.

5.3.1 The Monsoonal Ocean Circulation

The result of the high resolution MPI-OM-NRA (Fig. 5.3 and 5.4) shows the anatomy of the surface ocean current in the Indonesian region. The model simulation results in figures 5.3 and 5.4 agree well with a detailed description of the ocean circulation in Indonesian seas by *Wyrtki* (1961). Only major ocean circulations are described here. Two important eddies in eastern Indonesia are the Mindanao Eddy (127 °E, 8 °N) in December/January and the Halmahera Eddy (130 °E, 3 °N) from July to November and a minor Sulawesi Sea eddy in December/January (119 °E, 2.5 °N). The latter eddy has also been modeled by an OGCM from *Masumoto et al.* (2001). Figure 5.3 illustrates the annual march of the surface flow around the eastern islands. The flow is everywhere monsoonal, being mainly driven by the monsoonal surface wind, which reverses direction in every half year.

The Indonesian throughflow is the major circulation feature around the eastern islands. Most of the throughflow passes through the Makasar Strait originating in the north Pacific, as found before (*Godfrey et al.*, 1993; *Godfrey*, 1996). Some of the flow passes through Lombok Strait (116 °E, 8.2 °S) and some makes a detour to the east and then flows through the Ombai Strait between Flores and Timor Islands (124 °E, 9.5 °S) before reaching the Indian Ocean. The flow through Makasar Strait from the North Pacific is most intense from April to October. The reversal flow in December and January is very weak. *Inoue and Welsh* (1993) and *Masumoto and Yamagata* (1993) proposed a strong role of the southeast trade winds along the southern edge of Indonesia in lowering sea levels in August and thus leading to maximum throughflow at this time. Furthermore, the *Wyrtki* (1973) jets impose a strong semiannual modulation on the seasonal cycle, with minor sea level maxima in May and November. We notice that the high resolution model in this study produces a coherent semi annual variability.

In North Molucca, there is an intrusion through the Halmahera Strait from the West Pacific and the water masses flow first to north Molucca (the Halmahera Strait, the Lifamatola Strait, then the Molucca Sea) before they are collected at the north end of the Makasar Strait. This surface water comes from the south Pacific and circulates at the eastern edge of New Guinea (Irian) to the north of Irian before entering the Halmahera Strait (*Godfrey*, 1996). *Morey et al.* (1999) found that Halmahera prevents a flow from the South Pacific into the Sulawesi Sea and diverts some South Pacific water southward through the Seram and Banda Seas. The monsoonal character of the flow within this strait is very important for the understanding of the anti-monsoonal precipitation pattern of the north Molucca region. The peak of the water intrusion into the north Molucca area coincides with the peak of the wet season of the anti-monsoonal region in June/July/August. To the north of Irian, there is another important monsoonal surface flow from and to the Warm Pool, because the Warm Pool shows direct impact of ENSO. The flow is in direction toward Molucca from March to October and the other half of the year in the direction toward the Warm Pool.

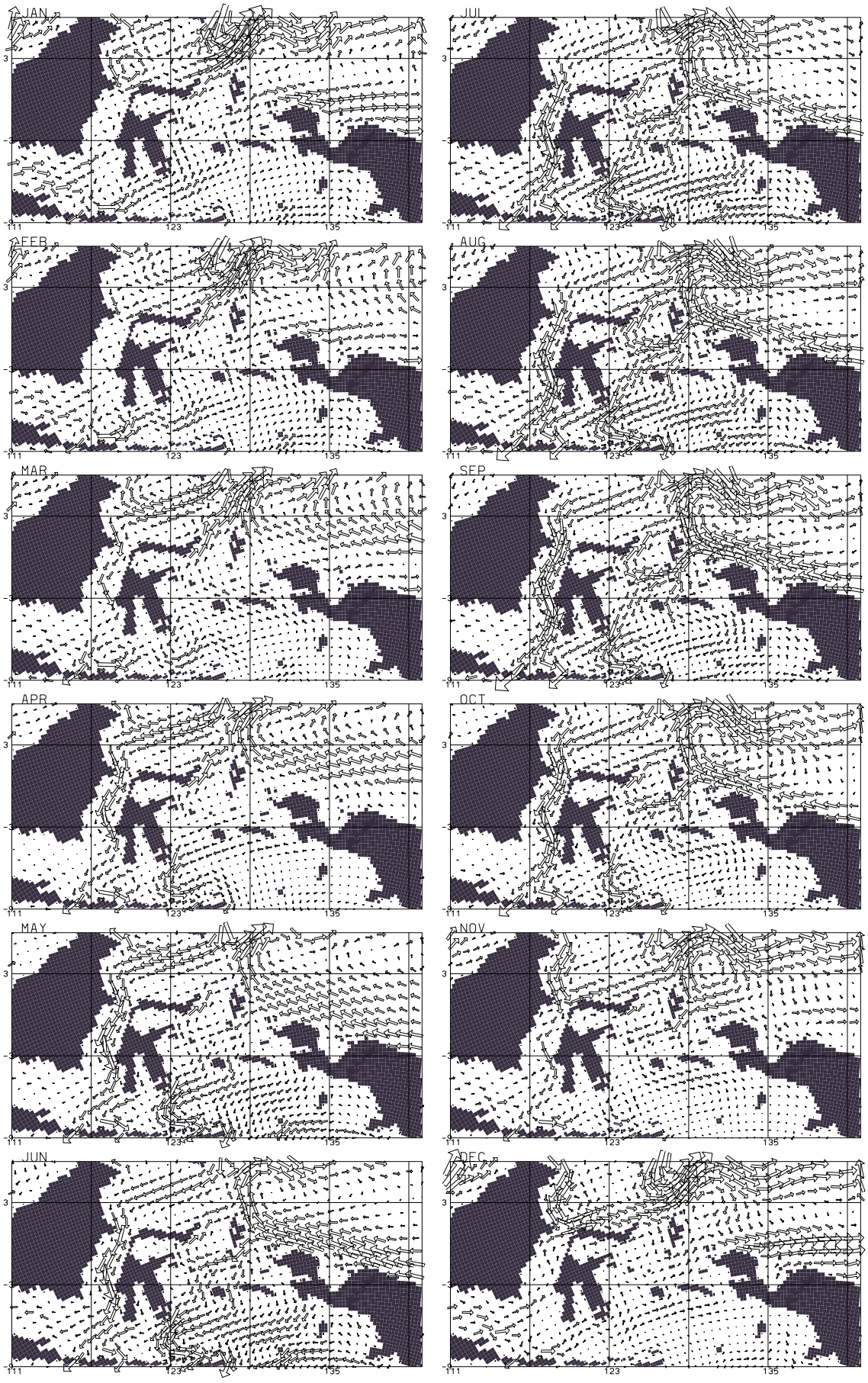

Figure 5.3: Monthly average (1979-1993) of near surface flow (17 m depth) of the high resolution MPI-OM simulation of the eastern part of Indonesia.

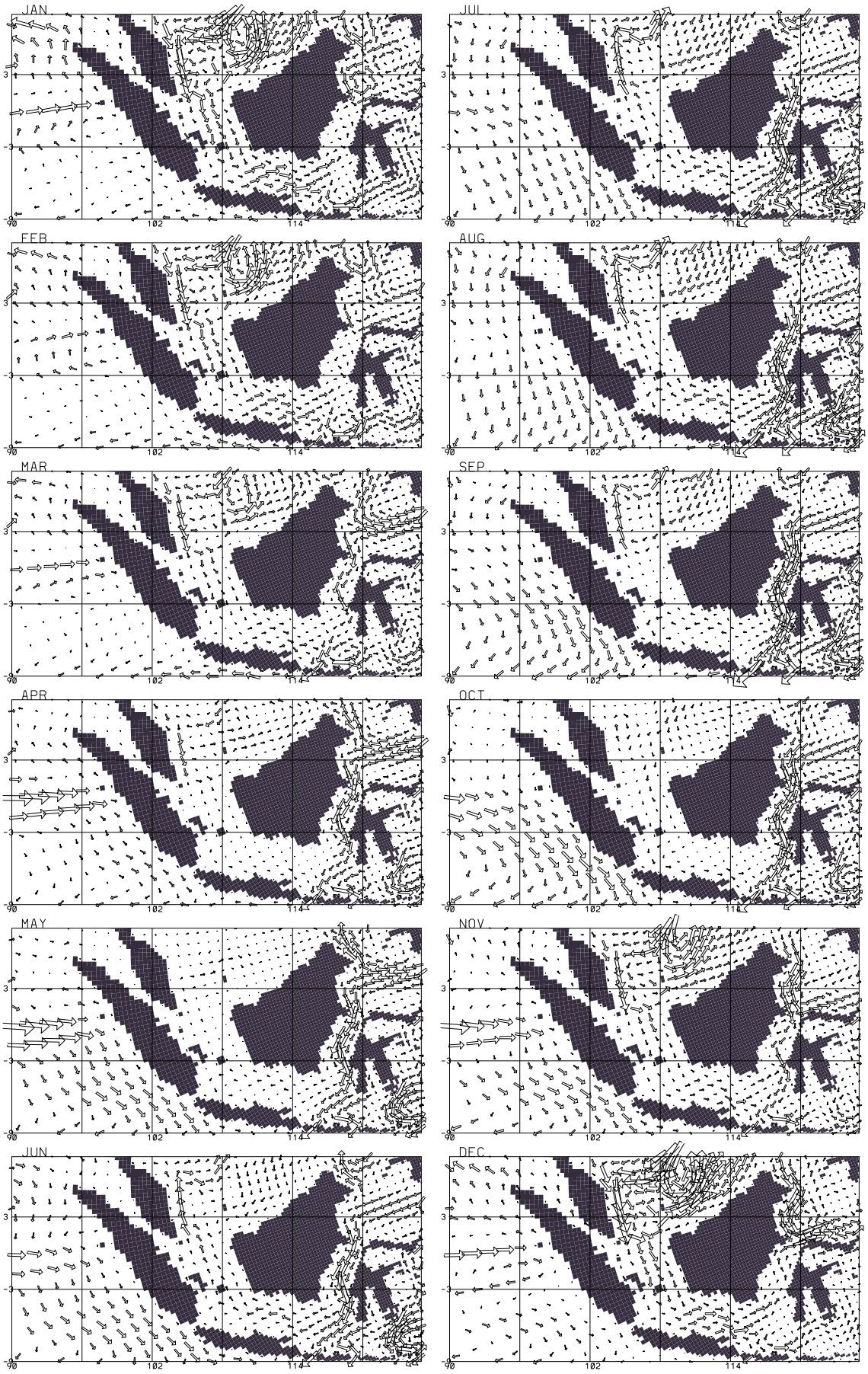

Figure 5.4: As Fig. 5.3, but for western Indonesia.

The annual march of the surface flow in the seas around western Indonesia is given in Fig. 5.4. Intense flow occurs in the South China Sea from November to March or during the Northern Hemisphere winter. This intense flow in the South China Sea brings a cold current surge. The next section will show that the cold surge will reduce the SST by almost 3 °C in the northwestern region. Another interesting flow occurs in the Indian Ocean west of Sumatera. There is no reversal flow but the intensity of the flow shows seasonal periodicity. Thus the climate in west Sumatera will be determined considerably by the condition in the Indian Ocean.

5.3.2 Monsoonal Character of the Indonesian Throughflow

The Indonesian throughflow provides a warm water connection between the tropical Pacific and the Indian Ocean (*WCRP*, 1998). According to *Wyrtki* (1987) the air pressure difference between the Pacific and the Indian Ocean is the main driving force for it. This flow passes the Indonesian archipelago mostly through the Makasar Strait (*Hirst and Godfrey*, 1993; *Godfrey et al.*, 1993) and Molucca (*Rodgers et al.*, 2000). Fig. 5.5 illustrates the variability of two major pathways of the Indonesian throughflow in Makasar Strait (major path) and Halmahera Strait (minor path) in model simulation using two different forcings and two resolutions. The transport is calculated as the monthly mean vertical barotropic stream function at the southern end of the Makasar Strait and the northern tip of the Halmahera Strait.

The monsoonal character of the throughflow within the Makasar Strait is well simulated. In section 5, we will analyze how deep the monsoonal character of this throughflow is. The high resolution model exhibits some higher frequency signal of the flow and the difference between the high and low resolution product is obvious. The average maximum and minimum between the two resolutions differ by about 5 Sv. The difference between the different forcings is not obvious for the two resolutions, except after 1989, when the high resolution ERA forcing deviates from the high resolution NRA and follows the variability of the low resolution.

The middle panel in figure 5.5 shows the comparison between the model results and observations by *Gordon et al.* (1999), who measured the vertically integrated profile of the flow at 2.87 °S, 118.45 °E. There is a clear improvement of the model results for higher resolution. The correlation to the observation increases from 0.285 to 0.83. While the high resolution model simulates the variability quite well, it does not pick up the very low transport between September 1997 and February 1998. Interestingly, the model is able to simulate the low transports in the early phase of El Niño in April 1997. Such low variability, from the long simulation above, is present every year and is not a specific property of an El Niño year. The monsoonal characters of the flow in this period is not very clear but the observations show an extremely small total flow from October to January, which is consistent with the long period simulation in this strait (top panel). However, the minimum flow at the end of 1996 is not as clear as that of 1997.

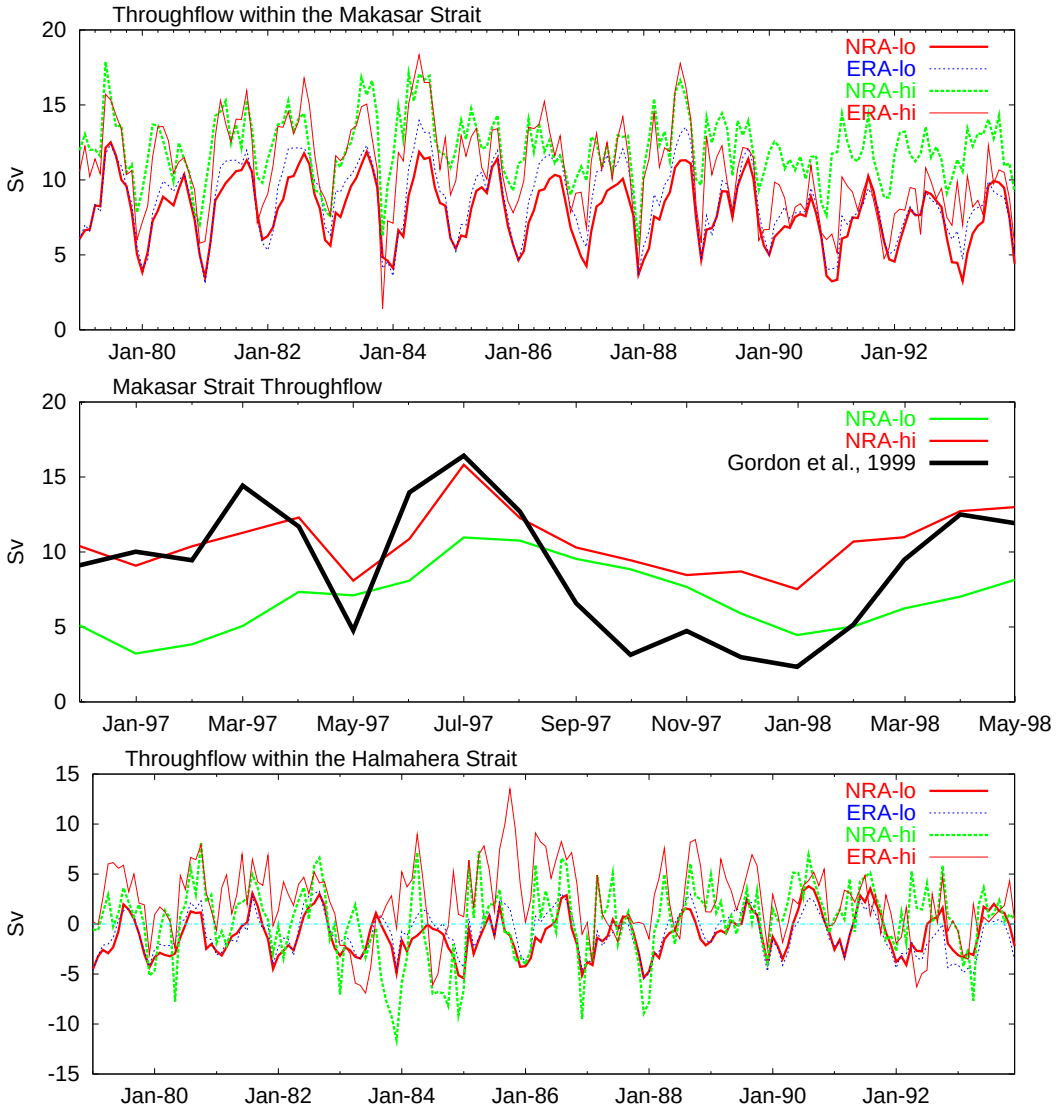

Figure 5.5: Flow through Makasar Strait (above) from 1979 - 1993, from November 1996 - June 1998 (middle) in comparison to recalculate monthly observed data from Gordon, et al. (1999) and through Halmahera Strait (bottom), modelled at two resolutions. Positive sign denotes southward flow. The correlation between NRA-hi and observed flow is 0.83.

Many observational and model studies suggest that the Indonesian throughflow is modulated by ENSO with larger (smaller) volume transport prevails during La Niña (El Niño) (*Kindle et al.*, 1989; *Meyers*, 1996; *Bray et al.*, 1996; *Fieux et al.*, 1996; *Gordon and Fine*, 1996; *Potemra et al.*, 1997; *Gordon and McClean*, 1999). The latter refer to the May condition 1997 during El Niño and 1998 during La Niña and between December 1996 (La Niña) and December 1997 (El Niño), when the ocean model could produce the same variability with less magnitude. In the long simulation from 1979 - 1993 at high resolution with NRA forcing, we notice that in December 1982, 1987 and 1991 (El Niño) the transport is about 7 Sv, 5 Sv and 9 Sv, respectively, while the only La Niña case of December 1988 shows 9.5 Sv. Thus the variability of the present model agrees with the findings of the above mentioned authors.

The simulation of the minor pathway of the Indonesian throughflow is given in the bottom figure. Again, like the flow through Makasar Strait, the high resolution model exhibits higher frequency and more vigorous variability, which does not exist in the lower resolution results. The result of different forcings is more coherent for lower than at higher resolution. The monsoonal character of the flow is also obvious and the whole vertically integrated column shows reversed flow, as the flow changes sign periodically. Thus, we expect a deeper monsoonal depth in this strait than in Makasar Strait.

5.3.3 Thermohaline Condition from Indonesian Water

Fig. 5.6 illustrates the average vertical temperature profiles of eight sections in major Indonesian seas in January and July, the peak of the wet and the peak dry season. The monsoonal changes are noticeable in the upper layer. In the Java Sea the temperature change is minimal in comparison to the deeper sea in the east. In the eastern seas the annual temperature change reaches more than 2.5 °C in the Seram Strait. The 20 °C thermocline is located at around 150 m depth in both seasons. In the Sulawesi Sea there is a thermal front (around 125 °E) in January, which is weaker in July. We will look at this phenomenon in the salinity profile and in the section on subsurface monsoonal signatures. The southern South China Sea also exhibits significant temperature changes of almost 3 °C at the northern edge of section 1. The 20 °C thermocline is about 10 m shallower in January than in July there. The temperature change in this region is opposite to the changes in the eastern part. If we analyze the monthly march of the vertical temperature profile (not shown), there is a zonal propagation of temperature changes.

The salinity profile of the Indonesian waters at the peak of the wet season (January) and the dry season (July) is shown in Fig. 5.7. There are sharp gradients of the pycnocline in both seasons over the first 100 m especially in the southern South China Sea, but not in the shallow Karimata Strait and the Java Sea. Note also that the pycnocline in both seasons changes in those layers. In January vertical mixing exists in the Sulawesi Sea and is associated with the thermal front in

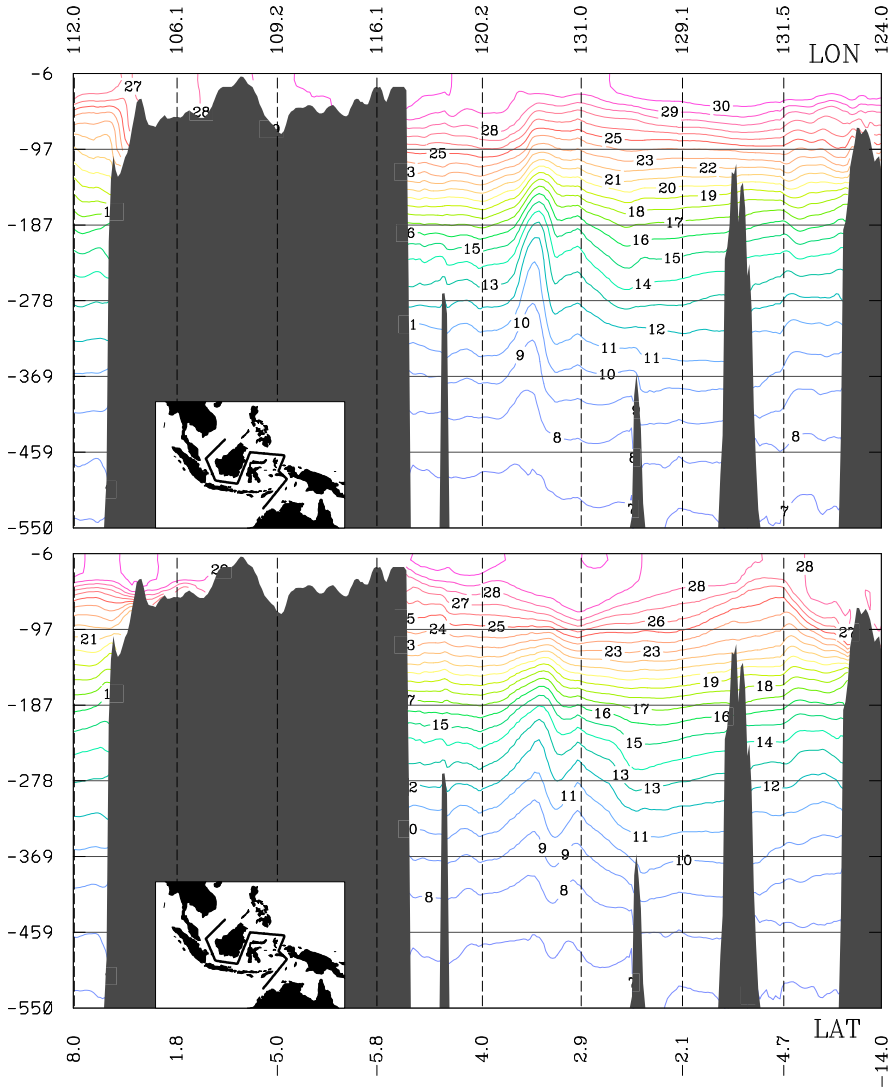

Figure 5.6: Mean vertical temperature profile down to 550 m depth (contour intervals is 1 °C) in January (above) and July (bottom) between 1979 and 1993 from MPI-OM-NRA at high resolution. The abscissa represents the 8 sections through the various ocean regions as defined in Table 5.2 and illustrated in the inset. For each section the start and end latitude (longitude) is given at the bottom (top) abscissa scale. Note that equal section lengths in this figure corresponds to different geographical distances.

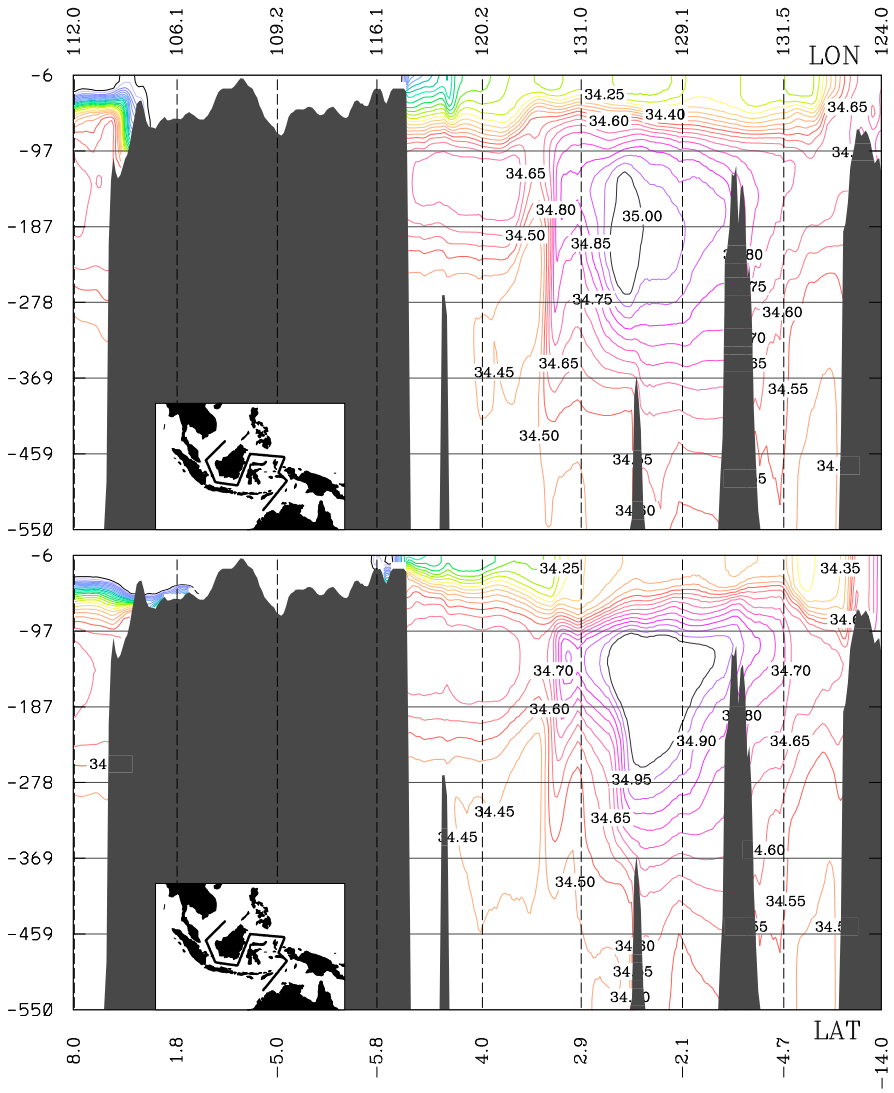

Figure 5.7: As Fig. 5.6, but for salinity. Contour interval is 0.05 psu.

the temperature profile. In the northern edge of the southern South China Sea, there is a deeper pycnocline in July than January, which indicates less salinity in the surface layer due to the presence of the ITCZ. However in most places salinity changes are smaller than 0.5 psu in both seasons. Changes below 180 m depth are not significant in most sections.

5.4 The Three Monsoonal Climate Regions

From previous chapters, Indonesia can be divided into three main climate regions: the south monsoonal (from south Sumatera to Timor Island, parts of Kalimantan, parts of Sulawesi and parts of Irian), the northwest semi-monsoonal and the Molucca anti-monsoonal region. The monsoonal region has a rainfall maximum in December/January/February (DJF) and a mini-

mum in July/August/September (JAS). The semi-monsoonal region has two peaks, in OND and MAM, while the anti-monsoonal has a peak in MJJ. In this section we will examine the ocean variability that leads to the climate condition in all three regions as shown in Fig. 5.8.

5.4.1 The Monsoonal Region of South Indonesia

The annual temperature cycle in southern Indonesia from the GISST data has annual peaks in December and April (above 29 °C) and a minimum in August (around 26.5 °C). That pattern follows the meridional movement of the ITCZ, which leads to higher SST and higher precipitation amount. From *Bony et al.* (1997a,b) and *Lau et al.* (1997) it is known that the SST range between 28 °C and 29.6 °C is favorable for high precipitation amount and the range below is related to the dry season from May to September. Thus, the wet monsoon takes place from November to March. MPI-OM simulates the annual cycle quite well but with a warm bias all year long. The largest bias occurs in December with almost 2 °C. The MPI-OM simulations with NRA and ERA forcing in two resolutions are very consistent to each other. The climatological run with the OMIP forcing, on the other hand, gives SST closer to observation in the dry season and a somewhat less warm bias in the wet season. The OMIP simulation shows even a slightly colder bias in the peak of the dry season. According to the empirical relation between SST and rainfall by *Bony et al.* (1997a) and others, the warm bias could change the monsoonal pattern of rainfall, since SST above 29.6 °C is no longer favorable for precipitation.

5.4.2 The Semi-monsoonal Region of Northwest Indonesia

The model simulates the annual cycle of SST in this area quite well with a warm bias above 1 °C. The largest bias is simulated with ERA forcing especially during May to November. The OMIP simulation has a strong bias from October to December. The maximum SST is observed in May and the minimum in December/January/February, which coincides with the incoming cold surge from the South China Sea. The cold surge reduces the SST by 3 °C, which eventually reduces the precipitation amount in the area. The semi-monsoonal region has two annual rainfall peaks in October/November and April/May when the SST is within a favorable range. From June to October, the region experiences another precipitation minimum, which is not as low as during the dry season in southern Indonesia. In fact, the average rainfall in the ”dry” season of this region is above the annual average of the southern monsoonal region (5 mm/day).

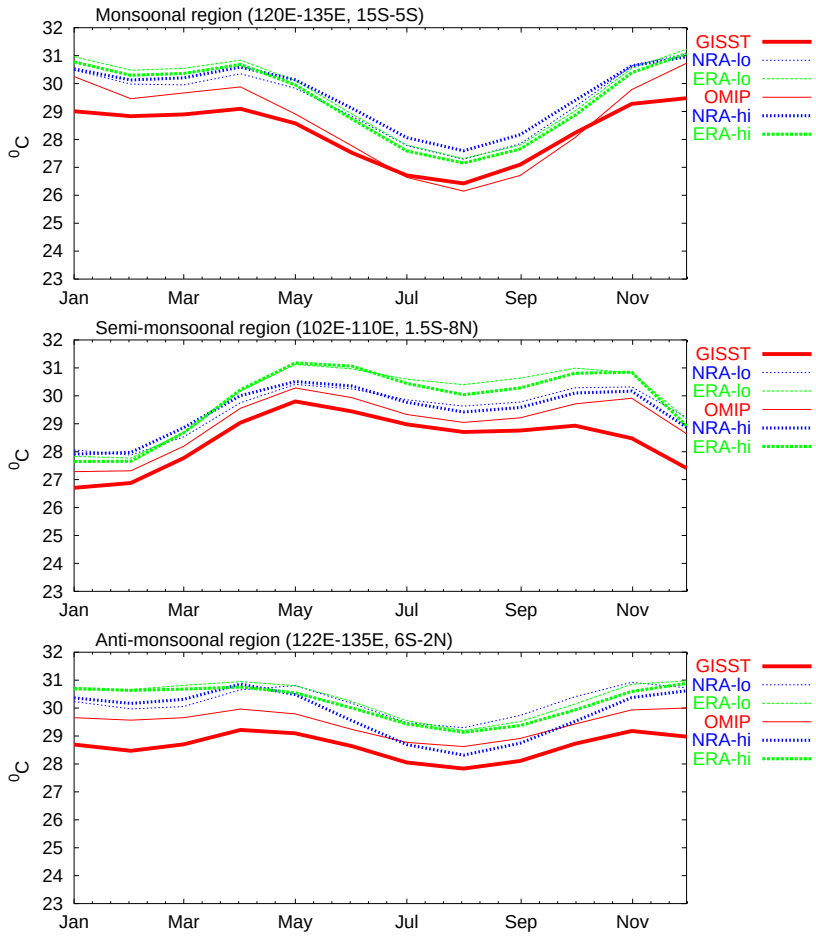

Figure 5.8: Monthly average (1979 - 1993) SST for the three monsoonal regions, from observation (GISST) and model simulations.

5.4.3 The Anti-monsoonal Region of Molucca

In this region, the model simulates the variability well but with 2 °C warm bias. The model produces a coherent pattern except for the low resolution NRA forcing from June to October. The GISST annual cycles are represented with a narrower SST range in north Molucca. Furthermore, Fig. 5.3 shows surface current intrusion from the Warm Pool that supports a warmer SST in north Molucca during June/July/August. The intrusion reaches south to Seram Island or circulates only in north Molucca, and small parts reach further south to the Flores Sea. Although there is no certainty about how much the presence of this intrusion is responsible for high SST values, it is held possible that without the intrusion SST would drop below 28 °C during the mid of the year with lower rainfall. In this case the shape of the annual cycle would look like that of the monsoonal region. In the next section, we will look at the depth of the monsoonal current intrusion reaching northern Molucca.

Thus the anti monsoonal climate of Molucca is a result of:

- the presence of an intrusion from the tropical Warm Pool in the mid of the year, which brings high SST values and distinguishes the SST of the area from that just a few degrees south of it,
- higher rainfall amount in MJJ due to an SST drop into the favorable range of precipitation between 28 °C and 29.4 °C,
- high annual SST values that contribute to average high rainfall all year round.

5.4.4 How does Ocean Circulation Drives SST?

We argued that the ocean circulation regulates SST variability. One way to show this is by using a simple water column and calculating its heat budget. Assuming a column of ocean water as given in Fig. 5.9, the total energy inside the column is given by

$$E_T = \int\int\int cT_t(x,y,z)\rho dxdydz, \tag{5.1}$$

where $T(x,y,z)$, c and ρ are the temperature profile, specific heat capacity of sea water ($4.0 \times 103 Jkg^{-1}K^{-1}$) and density of sea water ($1025 kgm^{-3}$). The total monthly energy change must equal the atmospheric fluxes and the net horizontal advection from the ocean current. The total energy change within one month is given by

$$\frac{dE_T}{dt} = \frac{\int\int\int cT_t(x,y,z)\rho dxdydz}{dt} = Q_{surf}dxdy + c\rho\left(\int\int UTdydz + \int\int VTdxdz\right) \tag{5.2}$$

where Q_{surf}, U and V are the residual atmospheric energy fluxes, zonal fluxes and meridional fluxes. The latter two components are the horizontal advection components.

The heat budget of the anti-monsoonal region north Molucca (3 °S – 2 °N, 122 °E – 135 °E) is given in Fig 5.10. In the top panel, there are three parameters: the atmospheric fluxes ($Q_{surf}dxdy$), total heat change of the water column (total $dTdV/dt$) and the heat content of the upper 12 layers or 200 m depth. The upper 200 m heat exchange accounts for, in average, 68% of the total heat exchange in the column. On the other hand the surface fluxes contribute, on average, 17% to the heat exchange. In some cases, the surface fluxes dominate the heat exchange. Hence, the contribution of the surface fluxes is on average small in comparison to the horizontal advection.

The middle panel shows the variability of horizontal advection, i.e. the zonal inflow from the Pacific region, the heat content three month later and the SST from GISST observation four month later. Here, the zonal flow from the Pacific is considered, as it accounts for more than

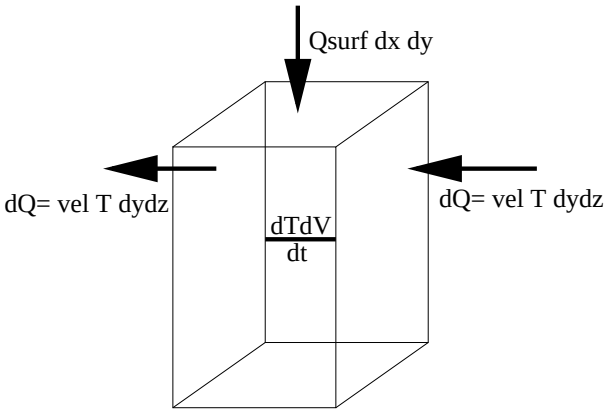

Figure 5.9: Energy budget exchange within a water column.

90% of total horizontal advection. The three month time lag between zonal inflow fluxes and heat energy content is due to the accumulation process (integration) of a harmonic function. The zonal flow is monsoonal with a period of a year. Thus the integral of a harmonic function with one year period will be out of phase 90 ° or 3 month. The time lag between heat content and the SST is due to the ocean surface response time. The correlation between the heat content of the upper layers (3 months lag) and SST (4 months lag) is 0.394, between zonal flow and heat content (3 months lag) is 0.207 and between zonal flow and SST (4 months lag) is 0.194. All correlations are calculated from 15 year simulations. Possible sources of error are the imperfect column boundary, which considers only the major zonal input from the Pacific and only the upper 200 m and does not account for upwelling and atmospheric fluxes. From Fig. 5.10 (top panel), there is a considerable contribution by atmospheric fluxes. In summary, the role of the ocean circulation for SST variability is due to the build up of additional heat over 3 month in the upper 200 m layer.

The bottom panel shows the same parameters for the semi-monsoonal region in the southern South China Sea. Unlike for the case of the anti-monsoonal region, here the meridional flow from the north is used instead. The results show a time lag of 4 months from the horizontal advection to the heat content and another month to be in-phase with the SST variability. The correlation between the heat content (4 months lag) and SST (5 months lag) is 0.711, between zonal flow and heat content (4 months lag) 0.613 and between zonal flow and SST (5 months lag) 0.842.

5.5 Subsurface Monsoonal Signatures

We will now investigate how deep the monsoonal influence ocean parameters in Indonesian waters via a subsurface monsoonal index. The monsoonal index is a measure of how large the ratio of the monsoonal component of the spectra is compared to total variance. The ratio has

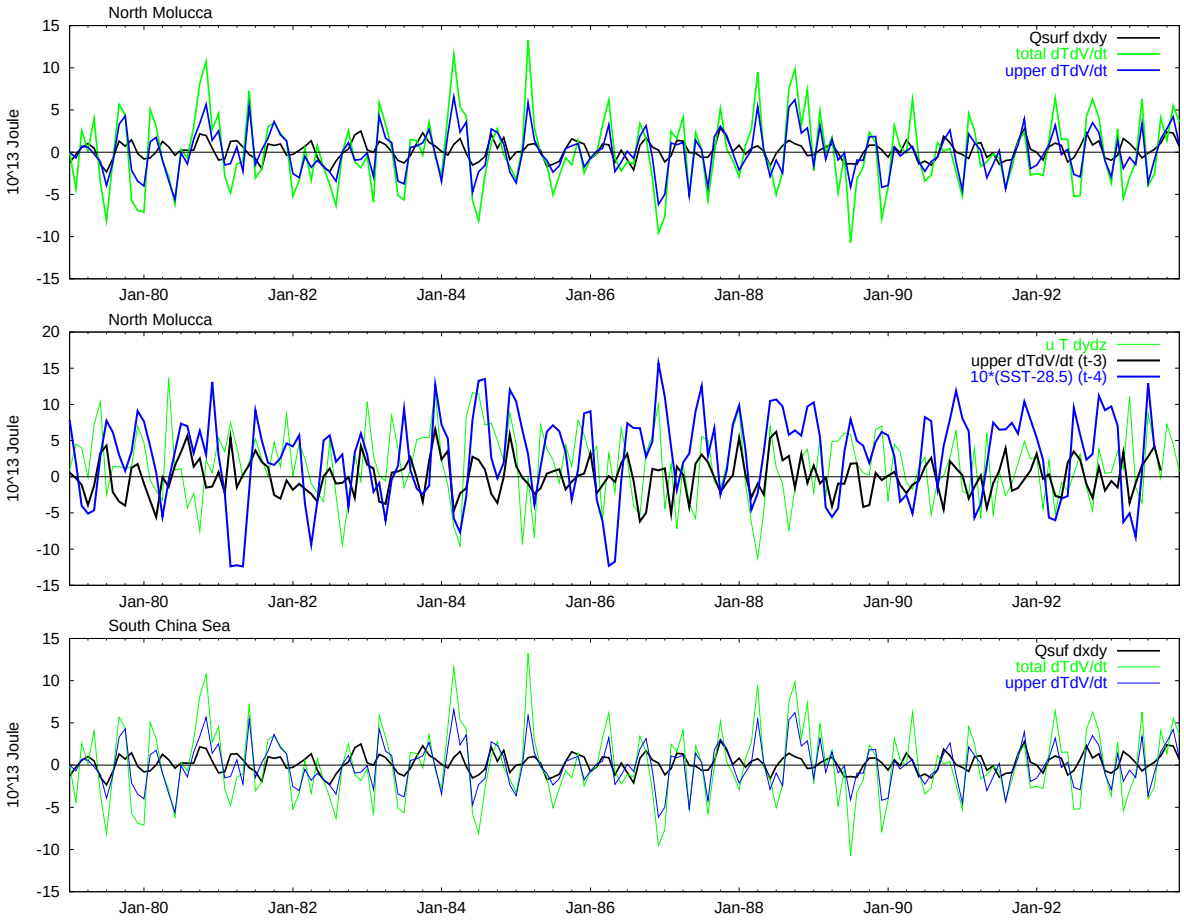

Figure 5.10: The ocean heat budget for the anti-monsoonal region. The upper panel shows the Q_{surf}, total heat content change $dTdV/dt$ and the heat budget of 12 layers (183 m). The middle panel shows zonal heat advection within the upper 200 m ($uTdydz$), the heat content of the upper 12 layers and the rescaled SST. Notice that in the bottom panel the heat content (SST) is lagging by 3 months (4 months) to the zonal advection. The correlation between the heat content(t-3) and SST(t-4) is 0.394, between zonal fluxes and heat content(t-3) 0.207 and between zonal flow and SST(t-4) 0.194. The bottom part shows the middle panel parameters for the semi-monsoonal region.

a range between 0 and 1 and the larger the index, the more dominant the monsoon is. The monsoon index M is calculated as

$$M = \frac{a^2_{annual} + b^2_{annual}}{w \cdot var_0} \tag{5.3}$$

where a, b, w and var_0 are the real and imaginary annual components of the Fourier transform, the normalization factor and total variance, respectively. The Fourier transform is calculated as follows:

$$f(t+1,x) = \frac{1}{\sqrt{n}} \sum_{j=0}^{n-1} i(j+1,x) e^{2\pi jt}, \tag{5.4}$$

$$f(t) = \sum_{t=0}^{n} a_j \sin\left(\frac{2\pi jt}{n}\right) + i \sum_{t=0}^{n} b_j \cos\left(\frac{2\pi jt}{n}\right), \tag{5.5}$$

where the first and the second parts of Eq. 5.5 denote the real and imaginary components of the transform, respectively. In our calculation, we consider only the annual component and the normalization factor, w, is defined as $2\pi\sqrt{n}$. Then, the variance is defined as

$$var_0 = \frac{\sum_{i=1}^{N} (x_i - \overline{x})^2}{N} \tag{5.6}$$

Figures 5.11, 5.12, 5.13 and 5.14 illustrate vertical profiles of the monsoonal indices in the eight sections for zonal and meridional transports, salinity and temperature. The spectra are calculated from a 15-year band from 1979 - 1993 on all levels of the high resolution MPI-OM-NRA simulation. The monsoonal depth is defined here as the layer with a monsoonal index > 0.2 and the transport is called monsoonal with reversing flow every 6 months.

5.5.1 Monsoonal Transports Profile

The monsoonal transport profile has a relative direction following the grid system. The terms zonal and meridional, thus, do not exactly follow the east-west and north-south direction, but follow each grid cell's direction. The zonal transport profile of Fig. 5.11 shows intense monsoonal transport near the surface. In Karimata Strait, Java Sea and Seram Strait, the monsoonal transport explains more than 90% of the variance. In Sulawesi Sea and Halmahera Strait, the monsoonal signature reaches the bottom. In the Halmahera Sea the monsoon index of more than 50% variance dominates the whole column, although the deeper the location, the smaller the variance and the flow are. The Makasar Strait and western Sulawesi Sea have no deep monsoon signature. The deep flow in Makasar Strait and Sulawesi Sea is a continuous Indonesian

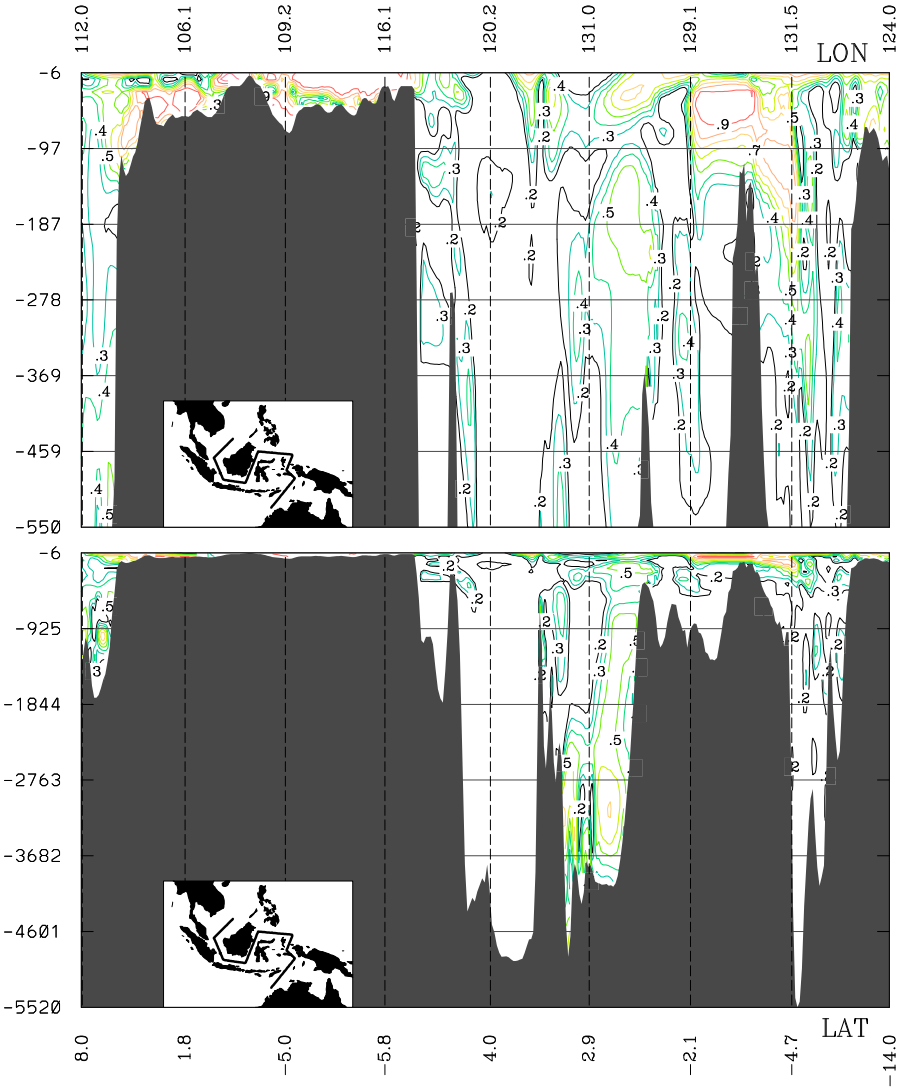

Figure 5.11: Monsoon indices or the ratio of the monsoonal component to total variance of the zonal transport for 1979-1993 in the MPI-OM-NRA model simulation at high resolution. Labels and inset follow Fig. 5.6. Minimum threshold level is 0.2 and contour interval is 0.1. The top figure shows the upper 550 m and the lower figure the whole ocean.

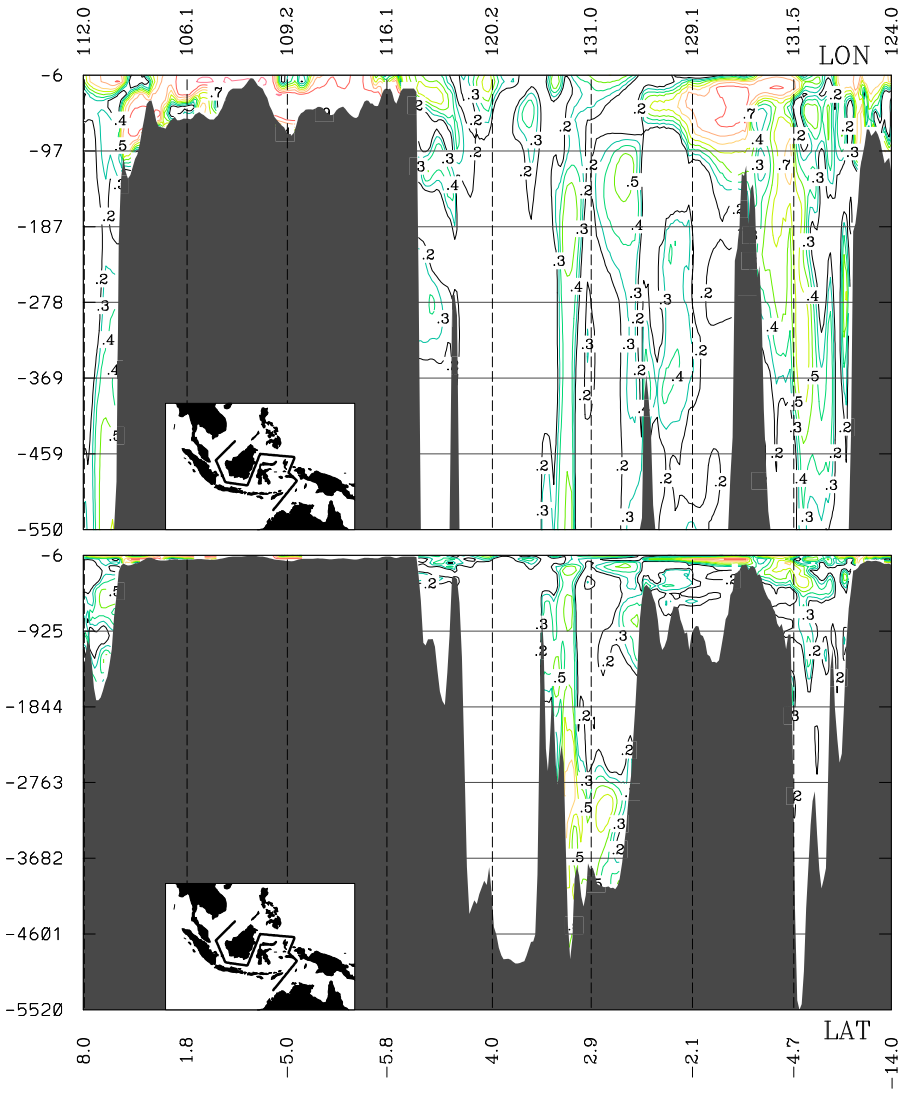

Figure 5.12: As Fig. 5.9, but for the meridional transport.

throughflow. Interestingly, there is a monsoon index < 0.2 at the surface in the eastern and western edge of the Sulawesi Sea.

The meridional transport profile in Fig. 5.12 exhibits a similar character as the zonal profile. Most monsoonal transports exist near the surface and deeper monsoonal flow is found on the eastern side of the Sulawesi Sea down to the bottom of Halmahera Strait. The empty zonal profile at the surface in the eastern and western edge of the Sulawesi Sea has meridional monsoonal transport. On the other hand, there is no meridional monsoonal flow in the middle of Sulawesi Sea and the middle of Halmahera Strait. The complementary zonal and meridional transports at the surface are associated with the west Sulawesi and Halmahera eddies, as discussed previously.

From figures 5.11 and 5.12, it is clear that the Java Sea is the most monsoonal region, followed by Seram Strait, whose highest monsoonal index occurs around 30 to 60 m depth. The

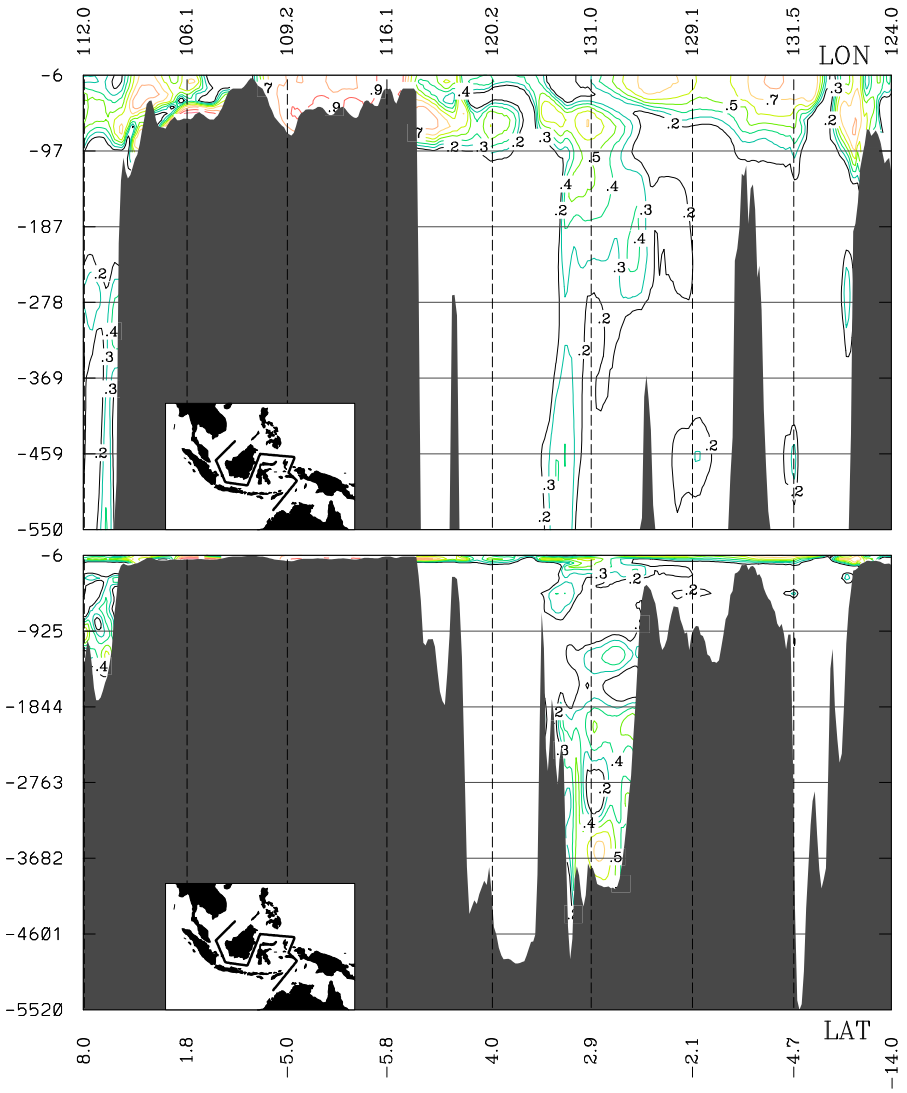

Figure 5.13: As Fig. 5.9, but for the salinity profile.

deep north Molucca water intrusion is found around 250 m with $M > 0.5$ in section 6 of the vertical profile of Fig. 5.11. *Morey et al.* (1999) found that the presence of Halmahera Island only changes the throughflow composition in the surface layer but not the throughflow in the undercurrent. The monsoonal depth of the flow through within the Makasar Strait is found to be 110 m. From the throughflow analysis (Fig. 5.5), the flow remains southward as indicated by positive flows. Thus there is an intense persistent southward undercurrent (below 110 m) through Makasar Strait.

5.5.2 Monsoonal Salinity Profile

Unlike the transport profiles of the previous two figures, the salinity profile in Fig. 5.13 shows a much simpler pattern, in which the monsoonal salinity depth was found to be 100 m with

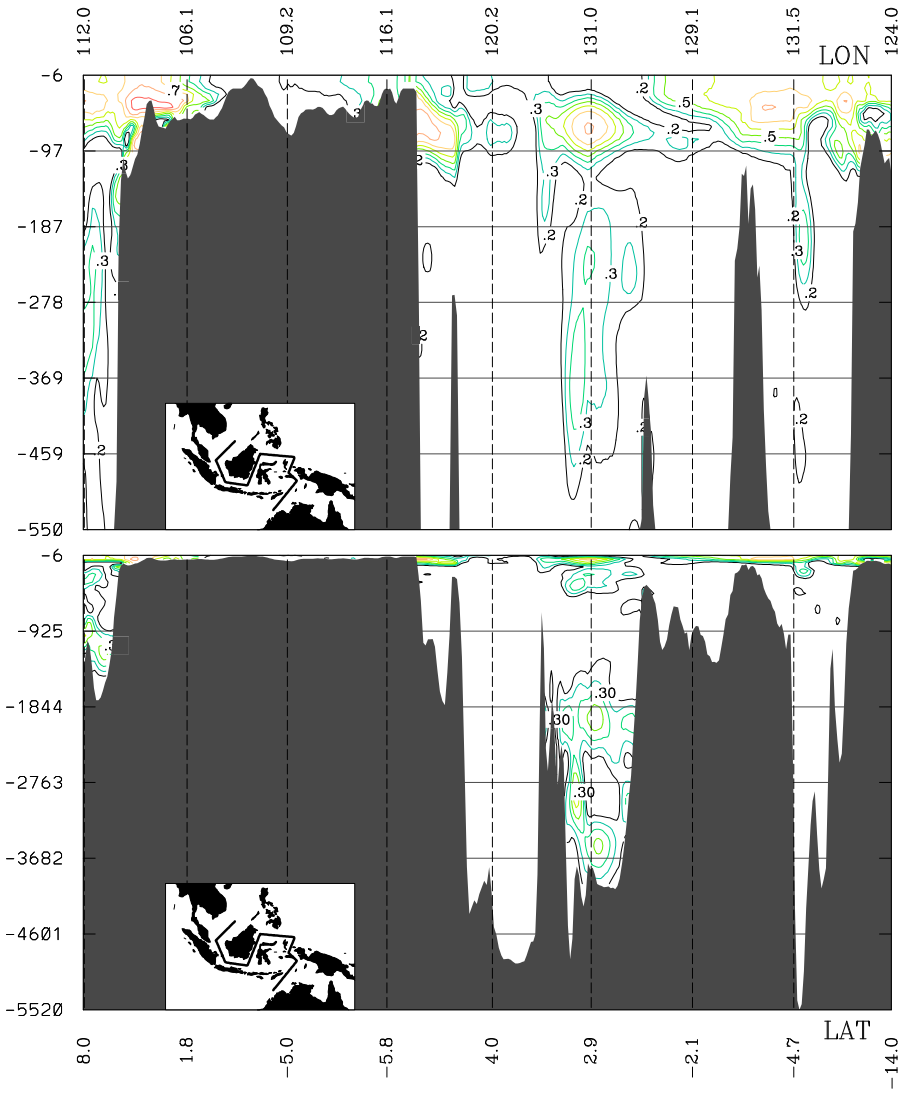

Figure 5.14: As Fig. 5.9, but for the temperature profile.

the most intense layer at around 50 m. Interestingly, following the salinity profile of Fig. 5.7, there is a vertical intrusion in the Sulawesi Sea and the Halmahera Strait down to 550 m. The vertical salinity profile change in the Sulawesi Sea is consistent with the transport profile. Like the transport profiles, there is a deep monsoonal activity to the bottom of Sulawesi Sea and Halmahera Strait. Unlike the transport profile, this deep monsoonal signature is not connected to the surface profile. Salinity profile is usually associated with the density profile and our result is comparable to Fig. 4 from *Gordon and Susanto* (2001), who reported the mid-depth of the pycnocline in the Banda Sea at 150 m, whereas the model simulation show a 120 m depth in the northern edge of the Banda Sea.

5.5.3 Monsoonal Temperature Profile

The monsoonal temperature profile in Fig. 5.14 show similar patterns as the salinity profiles. Most monsoonal activity occurs in the upper 100 m and the most intense change is found at 70 m depth. Like for the salinity profile, there is a monsoonal pattern in the eastern edge of Sulawesi Sea associated with the temperature front at 129 °E. Other deep monsoon structures exist in the South China Sea, Banda Sea and down to the bottom of Halmahera Strait.

The monsoonal front in the Sulawesi Sea occurs from November to February (see. Fig 5.3, 5.6, 5.7, 5.13 and 5.14), when there is an intense flow from the western Sulawesi Sea. On the eastern edge of Sulawesi Sea there is shallow water and a chain of small islands from northern Sulawesi to Mindanao Island in the Philippines. When the surface water reaches this edge, this warm and light (lower salinity) water mass sinks to the deep ocean (around 125 °E). This vertical water intrusion does not occur on the other time of the year. The signature of the vertical flow in the Sulawesi Sea is consistent from Figures 5.3, 5.7, 5.11 and 5.12). *Masumoto et al.* (2001) found an intraseasonal eddy in the Sulawesi Sea (125 °E) leading to a similar problem in their study with another OGCM. The vertical section of meridional velocity and temperature in January along 3 °N shows similar vertical transport at 125 °E as we found here. The vertical transport in their model reaches 110 m depth.

5.6 Monsoonal Influence on ENSO Impact

The Indonesian climate is a directly and strongly influenced by ENSO events (for example *Gutman et al.* 2000). In this section, we will look at the ENSO impact as a function of the monsoon phase by studying at the SST anomaly during composite ENSO events. For this analysis the long term SST data of more than 30 years will be separated into normal, El Niño and La Niña years. Then we calculate an ensemble average of each classification above. The aim of this these composites is to give superimposed views of anomalies in each month. El Niño (La Niña) years are defined for a SST anomaly in the NINO3 region (5 °S - 5 °N, 150 °W - 90 °W) above (below) 1 °C that persists for one year. As a result, the ENSO years from 1961 - 1993 are as follows:

El Niño year: 1965, 1969, 1972, 1982, 1987, and 1991

La Niña year: 1964, 1970, 1973, 1975, and 1988

The SST for such composite ENSO events in the Molucca region, which is believed to be the most affected region, is given in Fig. 5.15, both for observations (GISST) and model results. MPI-OM simulates the SST deviation from the normal year well but with a warm bias of 1.5 °C,

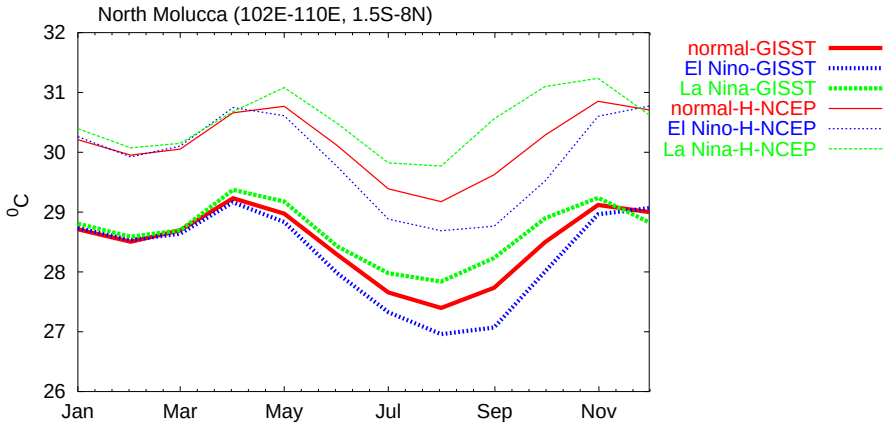

Figure 5.15: SST anomaly over Molucca from GISST (thick lines) and the low resolution MPI-OM-NRA (thin lines) simulation during composite El Niño, La Niña and normal years.

which results from the boundary forcing. The different SST range for observation and models has a consequence for the annual rainfall cycle. After *Bony et al.* (1997a) and others, such higher SSTs lie in the upper unfavorable range and will reduce the precipitation. There is a need to investigate this case with a coupled model.

In the anti-monsoonal region, the SST over Molucca changes during ENSO events but with opposite sign for El Niño and La Niña. In both cases, the anomaly starts in April, reaches its peak around August and September and decreases afterward until December. As a consequence, an initially warmer SST will bring SST up to a favorable precipitation range and induce more rainfall. While on the other hand the cooler SST will lower the SST even further and inhibit rainfall. The deviation pattern from a normal year agrees with *Gordon and Susanto* (2001), who investigated the Banda Sea (3.5 °S - 7.5 °S and 123.5 °E - 134.5 °E) for ENSO events between 1982 and 2000 also by using GISST SST. They found that the ENSO impact is largest in September and ceases in January of the following year. However, no attention was given to the possible cause for the decease. When we apply the Banda Sea SST data for the different period 1961-1993, the ENSO impact still deceases in December. This indicates that in different decades there is a one-month shift of the end of the impact.

The ocean surface circulation in Fig. 5.3 revealed that the surface ocean current has a monsoonal pattern, which is driven mainly by the monsoonal surface wind. This monsoonal surface pattern regulates the SST over the region. From May until October, sea water from the Warm Pool area (northeast Irian Island) to the archipelago cools (heats) the local SST during El Niño (La Niña) events, which eventually reduces (increases) the rainfall amount. The latter flow does not persist throughout the year. From November until February there is a reverse current from the archipelago outward to the warm pool area. This mechanism helps diminish the ENSO impact as stated above. The monsoonal or reversal surface current is also responsible for the prompt responses the archipelago received in May or during the early stage of ENSO. The

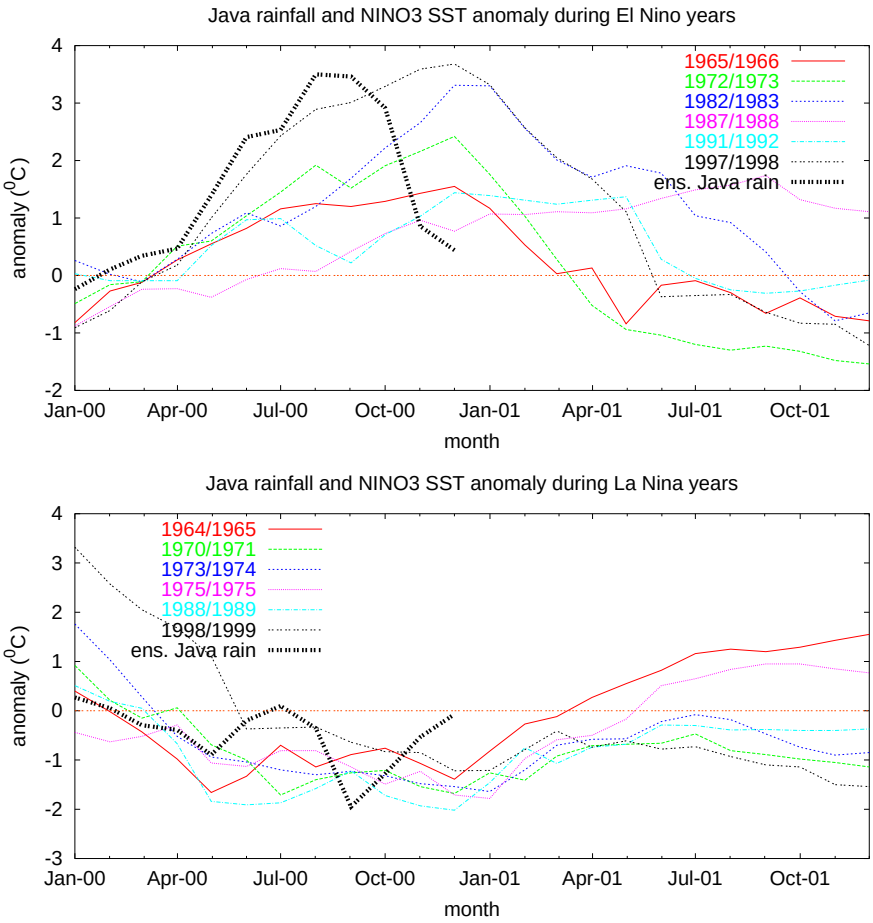

Figure 5.16: Ensemble Java rainfall anomaly in comparison to the NINO3 SST anomalies during El Niño (top) and La Niña (bottom) years from the start of ENSO event until the end of next year. The ensemble Java rainfall is scaled to fit the corresponding SST anomaly scale.

zonal propagation of the ENSO impact is regulated by the ocean surface circulation in the archipelago, which itself is driven by the monsoon. The ocean model clarifies that the surface ocean circulation drives this mechanism. Hence, we found no ENSO impact in December, January and February, the peak wet season of southern Indonesia. Some prolonged ENSO events beyond April may give an impact on rainfall afterwards.

In order to strengthen that hypothesis, we look at the ensemble of all Java rainfall data from the combined sources GHCN (*Vose et al.*, 1992) and the Indonesian Bureau of Meteorology. With regard to the ensemble Java rainfall anomaly (Fig. 5.16), the ENSO impact is similar to the SST case. The anomaly starts in April, reaches its peak in August and September, and deceases afterward. The impact on Java rainfall for La Niña is not exactly oposite to that of El Niño, as the impact is found to diminish temporarily during the peak of the dry season around June. Interestingly, in December either El Niño or La Niña events is still growing and most of them reach their peaks around January-February, when there is no more ENSO impact in Indonesia. Some events that persist beyond April may have considerable impact on the Indonesian rainfall

afterward, as suggested by the ocean circulation. In summary, El Niño has no impact on the peak of the wet season, while La Niña has no impact on the peak of the dry season.

5.7 Concluding Remarks

The study on the monsoonal properties of Indonesian waters with the Max Planck Institute global ocean model MPI-OM used the results of model simulations from two different horizontal and vertical resolutions and two different surface boundary forcings. We analyzed the three monsoonal climate regions and eight sections of the Indonesian seas, with a focus on the upper 500 m of the ocean.

The MPI-OM model is able to simulate the Indonesian throughflow and SST variability quite well with certain biases. An inappropriate representation of the bulk formula for air-sea heat and water exchange in the region may cause this discrepancy. One way to prove the latter hypothesis is by simulating the regional climate in a coupled ocean and atmosphere climate model. In the coupled model, instead of calculating fluxes with the bulk formula, the fluxes are supplied from the atmospheric model.

The simulation of the Indonesian throughflow has improved significantly for higher spatial resolution. The higher resolution simulations give some higher frequency variabilities, while the coarse one seems to picks up the monsoonal property only. Resolution plays a more important role than surface boundary forcing. In fact, MPI-OM produced the variability of the total Indonesian throughflow transport during the strongest El Niño 1997/1998 with a correlation value of 0.83 to the in-situ observation. Unfortunately due to limited resources, the Indonesian throughflow analysis is only available for the MPI-OM-NCEP simulations. For the SST simulations, there is not much difference between the variability for both resolutions as well as different boundary forcings. The warm bias is related to the static supply of the surface boundary forcing. SST as the upper-most ocean property is directly influenced by atmospheric forcing. One way to reduce the bias is by coupled ocean atmosphere simulations.

The near surface flow in Indonesian seas is influenced by the monsoon and reaches to a depth of about 100 m. The depth varies in different seas and affects the transport and thermohaline circulations. Ocean transport has the deeper monsoonal signatures than other quantities. The most intense transport occurs at 50 m depth, not at the surface. The zonal flow characterizes the monsoonal propagation in the atmosphere and the sea. The SST variability, for example, propagates zonally and the wet season starts in the northwest at the end of September and propagates to the east. The dry season comes from the southeast and propagates westward.

Most of the rainfall variability and the monsoonal character of the three regions can be explained by SST variability and an empirical relation proposed by *Bony et al.* (1997a) and others. This

empirical relation shows the importance of sea-air interaction in the region and the importance of a correct SST pattern for climate modelling of the maritime continent. The SST variability is largely regulated by the ocean circulations. Horizontal advection changes the heat content for 3 to 4 months when SST reaches its maximum or minimum.

In the last section, we discuss a possible mechanism of the ENSO impact on Indonesian rainfall, which is driven mainly by the ocean circulation. The archipelago receives an ENSO impact only over parts of the year. This limited impact is due to the monsoonal ocean circulation. The zonally dominated flow suggests a zonal propagation of the impact and an important role of the surface current intrusion in north Molucca. A detailed explanation of the ENSO mechanism requires a comprehensive ocean atmosphere climate analysis from the region such as the real propagation of rainfall anomaly (see Chapter 2), while the focus of this study was more on the ocean variability.

Chapter 6

Modelling of Indonesian Rainfall with a Coupled Regional Model

Abstract

Long term high resolution coupled climate model simulations using the Max Planck Institute Regional Climate Model and the Max Planck Institute Ocean Model has been performed with boundary forcings from two reanalyses, firstly from the European Centre for Medium-Range Weather Forecasts and secondly from the joint reanalysis of the National Centers for Environmental Prediction and the National Center for Atmospheric Research. The coupled model was run without flux correction and at two different ocean resolutions. The results show improved performance after coupling: A remarkable reduction of overestimated rainfall over the sea for the atmospheric model and of warm SST biases for the ocean model. There is no significant change in rainfall variability at higher ocean model resolution, but ocean circulation shows less transport variability within Makasar Strait in comparison to observations.

6.1 Introduction

A problem in simulating the Indonesian rainfall is the appropriate land-sea representation. The area is highly complex with large ocean coverage and chains of islands. Intense ocean atmosphere interactions take place in this most convective region of the world at the ocean surface. Due to large ocean areas, such processes will be important in modeling the climate of the region. With a stand alone (uncoupled) atmospheric or ocean model, such processes cannot be simulated adequately. The uncoupled atmospheric model uses the spatially and temporally prescribed and interpolated Sea Surface Temperature (SST). An integrated or coupled ocean/atmosphere model gives more realistic dynamics close to the ocean surface. The ocean

atmospheric exchange takes place at higher frequency determined by the coupling setup. Regional climate studies using a coupled ocean/atmosphere model for the maritime continent are relatively new.

Our study is motivated by the unsatisfactory result of some rainfall patterns in the uncoupled climate model for this region (Chapter 4 and 5). The uncoupled atmospheric model had a major drawback in overestimated rainfall over the sea. The uncoupled ocean model, on the other hand, had a problem with the bulk formulae for heat fluxes, which consequently lead to a warm SST bias over the region. The coupled climate model hopefully reduces these problems. With a coupled model, we give more degree of freedom to both models. In the uncoupled ocean model, the forcing is prescribed from the atmospheric reanalyses and recalculated to provide surface water and heat fluxes for the model using an empirical bulk formulae. Such an approach suffers from a large effect in an archipelago, since the bulk formulae are applied globally and may not be suitable for local and regional. This deficiency might be reduced in a coupled model, because the Regional Climate Model (RCM) improves the coarse resolution of the reanalyses and thus provides a high resolution atmosphere in the coupled region.

Our approach is to use a very high resolution regional atmospheric model coupled to an ocean model with an adjusted special conformal grid that both have a comparable high resolution in the region. A nested RCM could downscale GCM results to a regional scale. The Max Planck Institute (MPI) RCM or REMO (*Jacob*, 2001; *Jacob et al.*, 2001) is suitable for this purpose, because REMO provides detailed forecasts of weather parameters close to the ground and an improved simulation of clouds and rainfall compared to a GCM. On the other hand, the Max Planck Institute Ocean Global Circulation Model (OGCM), the MPI-OM1 (*Marsland et al.*, 2003) can also be used for a regional climate study (*Marsland and Wolff*, 1998, 2001). MPI-OM1 is the latest development of the Hamburg Ocean Primitive Equation (HOPE) ocean model (*Wolff et al.*, 1997). A major improvement is the transition from a staggered E-grid to an orthogonal curvilinear Arakawa C-grid (*Arakawa and Lamb*, 1977) and arbitrary placement of the poles from a bipolar orthogonal spherical coordinate system. This coupling method, to the authors' knowledge, is relatively new to the region.

The purposes of this chapter are to analyze the performance of a very high resolution coupled climate model, to compare the result with the stand alone (uncoupled) mode and to see the importance of different ocean model resolutions. The study focuses on rainfall and ocean circulation from the monthly to the interannual time scale. Limitations are the domain size and the period of analyses from 1979 to 1993. The outline of this paper is as follows. Section 2 presents the data and model setup, section 3 discusses the implication of coupling for the atmosphere and section 4 the implication for the ocean. Finally, section 5 summarizes the highlights of the findings.

6.2 Data and Model Setup

6.2.1 Data

The data used in this study are monthly rainfall data collected by the Indonesian Meteorological & Geophysical Agency (BMG) at 167 stations all over Indonesia, and monthly mean rainfall data from the WMO-NOAA project on The Global Historical Climatology Network (GHCN; *Vose et al.* 1992) from 1979 to 1993. In our area of interest (19 °S - 8 °N and 95 °E - 145 °E), there are 545 rain gauges. These data are gridded to match the other datasets at T106 and 0.50 resolutions using the *Cressman* (1959) method. As the second observation data set, a combination of gauge observations with satellite estimates from the Global Precipitation Climatology Project (GPCP; *Huffman et al.* 1997) at the 1 ° spatial resolution is used. The data has been interpolated into the REMO grid.

This study uses surface ocean forcings from two reanalyses, one from ECMWF reanalysis (ERA) or ERA15 (*Gibson et al.*, 1997), which is available at the horizontal resolutions T106, equivalent to 1.125 ° in the tropics, from 1979 until 1993, and NCEP reanalysis (NRA; *Kalnay et al.* 1996), from the time period 1948 to 1999. The forcings have been interpolated to the model geometry.

For climatological runs, the German Ocean Model Inter-comparison Project (OMIP; *Röske* 2001) forcing was used. This study also made a climatological run, which was setup using the German OMIP climatology dataset as the surface forcing and was rerun for at least 10 years, which was skipped later due to spin-up. The OMIP forcing was derived from the ECMWF reanalysis 15 year averages.

6.2.2 Model Descriptions

Both REMO and MPI-OM are hydrostatic models working on the Arakawa-C grid for the horizontal representation. REMO requires a lateral boundary forcing at the sea surface and in each vertical layer at the boundary, while MPI-OM requires sea surface conditions from the atmosphere.

The Regional Atmospheric Model (REMO)

The REgional atmosphere MOdel (REMO) is based on the 'Europa-Modell' of the German Weather service (*Majewski*, 1991). It can be alternatively used with the physical parameterisations of the Europa-Modell or with the parameterisations of the global climate model ECHAM-4 (*Roeckner et al.*, 1996a), which have been implemented at the MPI. The dynamical core of the

model as well as the discretisation in space and time are based on the Europa-Modell. However, in REMO with ECHAM-4 physics not enthalpy and total water content but temperature, water vapor and liquid water are prognostic variables. In the present study REMO with ECHAM-4 physics is applied. A more detailed description of the REMO can be found in Chapter 4.

The Ocean Model (MPI-OM)

The Max-Planck-Institute Ocean Model (MPI-OM, formerly C-HOPE) is the ocean/sea ice component of the Max-Planck-Institute climate model ECHAM/MPI-OM. MPI-OM is a primitive equation model (z-level, free surface) with the Boussinesq and incompressibility assumptions, formulated on an orthogonal curvilinear Arakawa C-grid. This study uses a special conformal grid where the north pole is located in China and the south pole in Australia. A more detailed description of the MPI-OM is given in Chapter 5.

Coupling

REMO/MPI-OM coupling was carried out using the OASIS coupler developed by CERFACS (*Valcke et al.*, 2000). The coupling procedure is similar to the one used in the MPI climate models ECHO-G (*Legutke and Voss*, 1999) and ECHAM-5/MPI-OM. In this study the main task of the coupler is to synchronize time for coupling or data exchange, because both models are running at different time steps.

The regional climate model (REMO) covers only a part of the MPI-OM area and divides the global Ocean Global Circulation Model into two sub-domains: coupled and non-coupled. This peculiarity provides a requirement to run MPI-OM both in coupled and stand-alone modes simultaneously using additional atmospheric forcing defined in the non-coupled domain. The coupled domain is the REMO domain covering the whole archipelago (19 °S – 8 °N, 91 °E – 141 °E).

In the coupled domain, the ocean model receives, at a specified frequency (coupled time step), heat, freshwater and momentum fluxes which are calculated in REMO (F_{remo}) and passes back the sea surface parameters to the atmospheric model. Outside the coupled domain, the ocean model receives, at specified frequency (forcing time step), the global, predefined atmospheric fields, which are recalculated in heat, freshwater and momentum fluxes (F_{bulk}) using a bulk formulae. Note, that the coupled time step and the forcing time step can be different. The fluxes, which are to be used as an ocean model forcing (F), are then the result of the following mixing scheme:

$$F = I \cdot F_{remo} + (1 - I) F_{bulk} \tag{6.1}$$

where I is defined as follow

$$I = \begin{cases} 1, & \text{inside coupling/REMO region} \\ 0, & \text{outside coupling/REMO region} \end{cases} \tag{6.2}$$

In a normal condition, REMO-MPI-OM coupling also includes ice parameters. Since the coupled domain is located in a tropical region, the ice component is omitted. Thus the ocean only passes the sea surface temperature to the atmosphere. Fig. 6.1 illustrates the coupling processes between reanalyses, REMO and MPI-OM in coupled and uncoupled domains.

Interpolation from the atmospheric grid to the ocean's grid and vice versa is achieved in the ocean model using the so-called mosaic interpolation. Thus the OASIS coupler sees both the models on the same computational grid, i.e. the REMO grid, because it represents also the coupled domain. The interpolation scheme from MPI-OM to REMO is as follow

$$F_{ij}^{M} = \frac{\sum_{lm} F_{lm}^{R} \cdot A_{ijlm}}{\sum_{lm} A_{ijlm}} \tag{6.3}$$

and from REMO to MPI-OM using the formula

$$F_{lm}^{R} = \frac{\sum_{ij} F_{ij}^{M} \cdot A_{ijlm}}{\sum_{lm} A_{ijlm}} \tag{6.4}$$

where F_{ij}^{M}, F_{lm}^{R} are the fields defined on MPI-OM and REMO grid, respectively. A_{ijlm} is the interpolation matrix.

Usually an ocean model has a much finer resolution than an atmosphere model. To take into account small-scale variability, a subscale correction of the atmospheric heat fluxes is used. As these fluxes are strongly dependent on the sea surface temperature this correction is assumed to be proportional to the difference between the SST calculated in MPI-OM and the same SST interpolated onto the atmospheric grid and backward. The proportionality constant which is actually equal to dQ/dT, where Q is a heat flux and T is a surface temperature, was set according to *Röske* (2001) from 50 to 60 W/(m^2K)

6.2.3 Model Setups

REMO setup

REMO was run in the climate mode at the resolution 0.5 ° or about 55 km horizontal resolution and 20 hybrid vertical levels. The REMO domain is formulated in a finite difference grid with

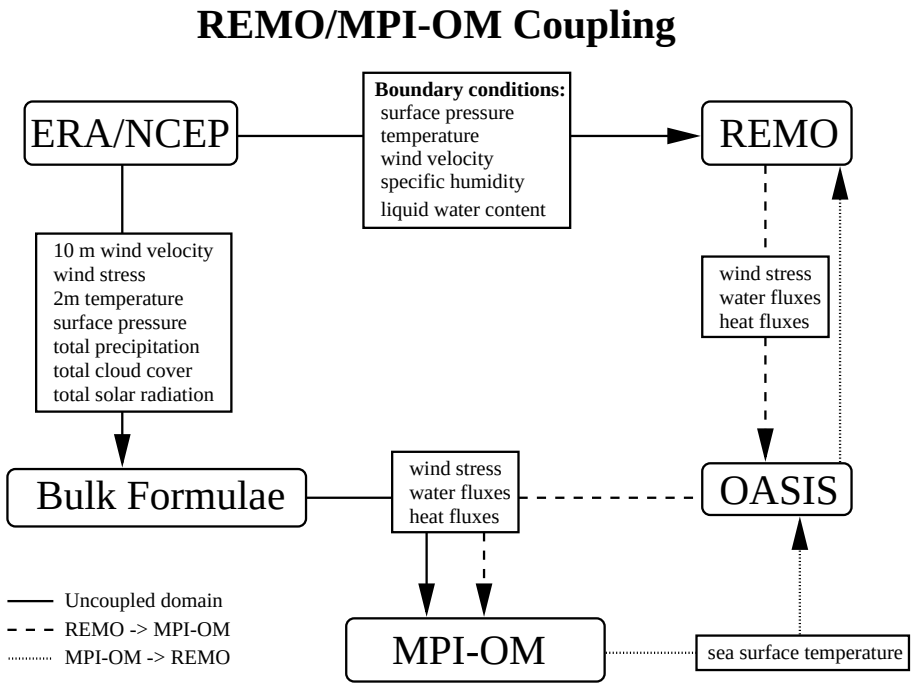

Figure 6.1: A schematic view of the processes in the coupled and uncoupled domain for the ocean/atmosphere coupling of the atmospheric regional climate model REMO and the global ocean model MPI-OM, using a coupler (OASIS).

101 points in longitude, 55 points in latitude with a bottom left corner at 91 °E/19 °S or a region between 15 °S - 8 °N and 91 °E - 141 °E. This grid system has 21% land coverage. The model was forced with lateral boundaries from ERA15 and NRA. The lateral boundaries have a temporal resolution of 6 hours and are interpolated into a 5 minutes time step. REMO obtains the lower boundary conditions over the sea surface from MPI-OM through the OASIS coupler at every coupling time step (6 hours) and, at the same time, passes the atmospheric momentum, heat and water fluxes to the ocean model. In the uncoupled mode, REMO has its own prescribed SST from the corresponding reanalyses. The REMO used in this study allows only one type of land cover, either land, sea or ice.

A RCM has to be initialized and supplied with lower and lateral boundary values during the whole simulation. Initialization is done for all prognostic variables in all model levels. In addition, surface temperature, soil temperatures for five soil layers down to a depth of 10 m, soil moisture, snow depth and temperature as well as the skin reservoir content (water stored by the skin of the vegetation) must be supplied.

MPI-OM setup

The MPI-OM is a global model, which uses a bipolar orthogonal spherical coordinate system with a special conformal grid where the north (south) pole is located in China (Australia). The horizontal resolution gradually varies between a minimum of about 15 km near the poles and

a maximum of 370 km in the western edge of equatorial Atlantic. The model has 30 vertical levels with increasing level thickness from top to the bottom. This study used two resolutions of MPI-OM as described in Table 5.1.

The MPI-OM is started from the stand alone mode and it is initialized by climatological temperature and salinity data (*Levitus et al.*, 1998). It is then integrated for 31 years from 1948-1978 using 6 hourly NCEP reanalysis data as forcing. The period of this integration is used as spin-up. In the coupled mode, the model is started from the state obtained by the stand-alone runs after the spin-up. The initial date is 01.01.1979 and it is integrated until 31.12.1993. In the uncoupled mode the model continues the integration until 1999. Atmospheric forcing, calculated from NCEP reanalysis data is applied every 6 hours. At that same time the ocean model gets atmospheric fluxes calculated in REMO and passes sea surface temperature to REMO.

Coupling Experiments

The coupled REMO/MPI-OM experiments covered the period from 1979 to 1993. One simulation was performed for each reanalysis and two resolutions of MPI-OM. In total, for two reanalyses and two resolutions there are 60 years of integration. During the whole experiment, instead of the salinity relaxation procedure only the constant freshwater flux correction was used. No heat and momentum flux corrections were applied during the entire coupling experiments.

The model output consists of two parts: the atmospheric and oceanic. REMO output is based on the REMO's rotated Arakawa C-grid with 20 vertical hybrid levels and has been stored with 6 hours time interval. The ocean dataset, omitting the sea-ice parameter output, is written on the MPI-OM orthogonal curvilinear Arakawa C-grid with 20 (low resolution) and 30 (high resolution) vertical levels as monthly mean values.

6.3 Implication for the Atmosphere

This section presents results from the coupled model integrations and their comparisons to the uncoupled REMO model described in Chapter 4. The stand alone model results will not be covered in detail here. We will look at the variabilities for the five major islands and three sea regions as illustrated in Fig. 4.2.

6.3.1 The five major islands

Fig. 6.2 shows variabilities of rainfall from the coupled REMO-MPI-OM simulations from two reanalyses with two different ocean resolutions. There are no notable differences between simulations with different ocean resolutions or, in other words, the lateral boundary and reanal-

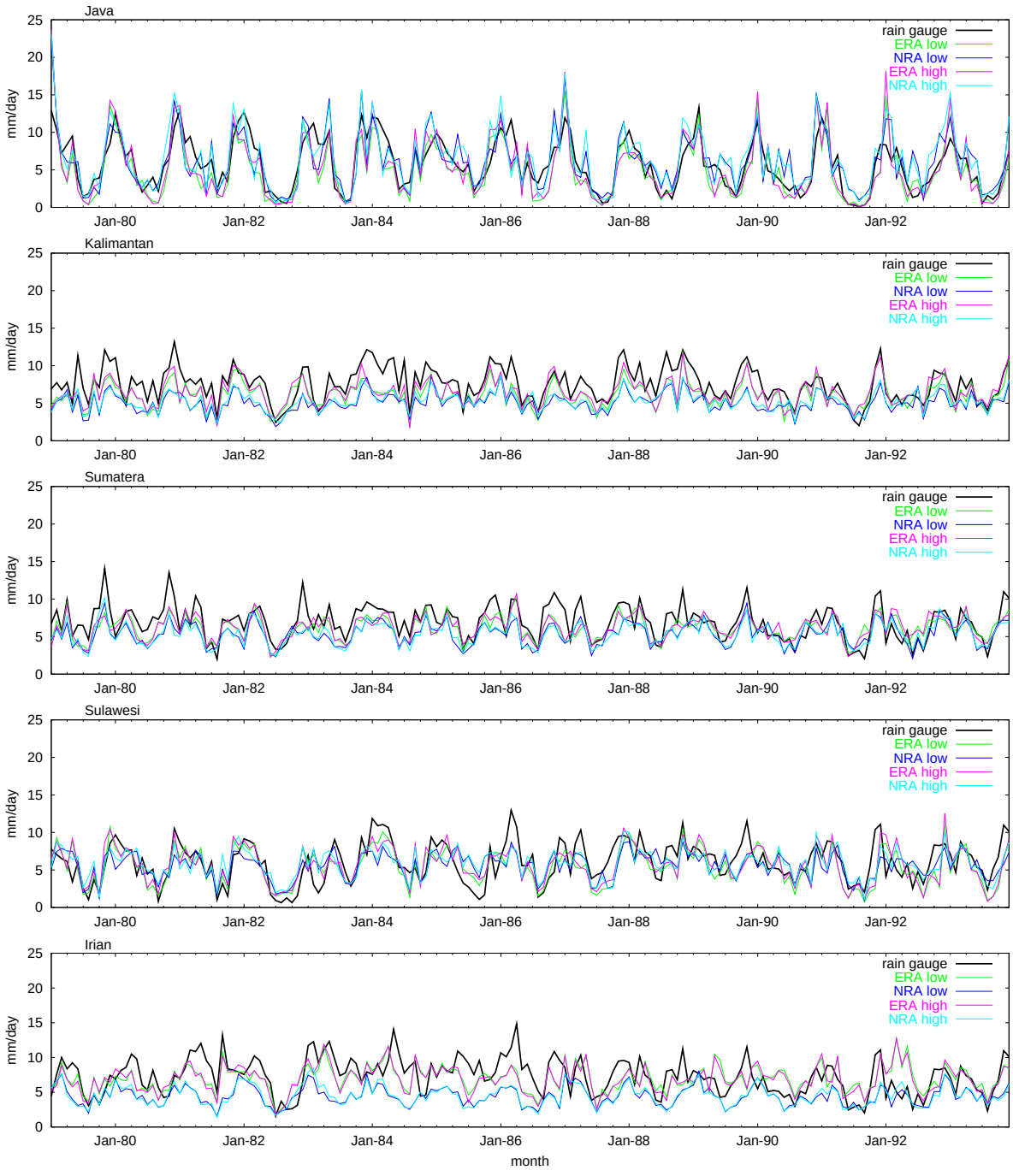

Figure 6.2: Variability of rainfall for the five major islands from the coupled REMO-MPI-OM simulations and their comparison to observation (gauges).

Table 6.1: Correlation between rainfall simulations and observations for reanalyses, uncoupled REMO and two coupled REMO simulations over the five major islands.

NCEP	Java	Kalimantan	Sumatera	Sulawesi	Irian
global reanalysis	0.691	0.761	0.639	0.680	0.443
uncoupled REMO	0.715	0.669	0.691	0.578	0.357
coupled low ocean	0.769	0.734	0.715	0.598	0.385
coupled high ocean	0.780	0.736	0.723	0.576	0.393
ERA	Java	Kalimantan	Sumatera	Sulawesi	Irian
global reanalysis	0.815	0.780	0.764	0.451	0.399
uncoupled REMO	0.798	0.780	0.708	0.645	0.434
coupled low ocean	0.823	0.762	0.691	0.657	0.439
coupled high ocean	0.820	0.749	0.682	0.631	0.463

yses play stronger role here. From that figure, Java seems to have the best performance, where REMO does not produce under- or overestimations as large as on the other islands. There, REMO simulations tend to underestimate and the largest underestimation occurs in Kalimantan and in Irian with the NRA forcing.

The summary of the correlations between original reanalyses or REMO simulations and rainfall observation is given in Table 6.1. For the case of the NCEP analysis in Java, there is about 19% improvement from the original reanalysis to the coupled simulation and about 9% in Sumatera. For other islands, REMO simulations could not produce correlation as high as the original reanalysis. However among the REMO simulations, there is a small improvement by coupled REMO with high resolution ocean model. For the case of ERA reanalysis, improvements occur in Java, Irian and the largest in Sulawesi of about 18%. Among REMO simulations coupling does not always produce a better result. In fact, the improvement by coupling in comparison to the uncoupled model is in general, rather small. For both reanalyses, the best performance is in Java, which has a homogenous climate region (the monsoonal region), while other islands experience a combination between different monsoonal systems. Kalimantan has the second best performance followed by Sumatera and Sulawesi. Irian has the lowest performance in both reanalyses, which is mainly due to boundary zone problem. This island is located in the REMO boundary zone, where the coarse resolution lateral boundary has still some influence. In general, Table 6.1 shows that the quality of the reanalysis largely determines the quality of the REMO result.

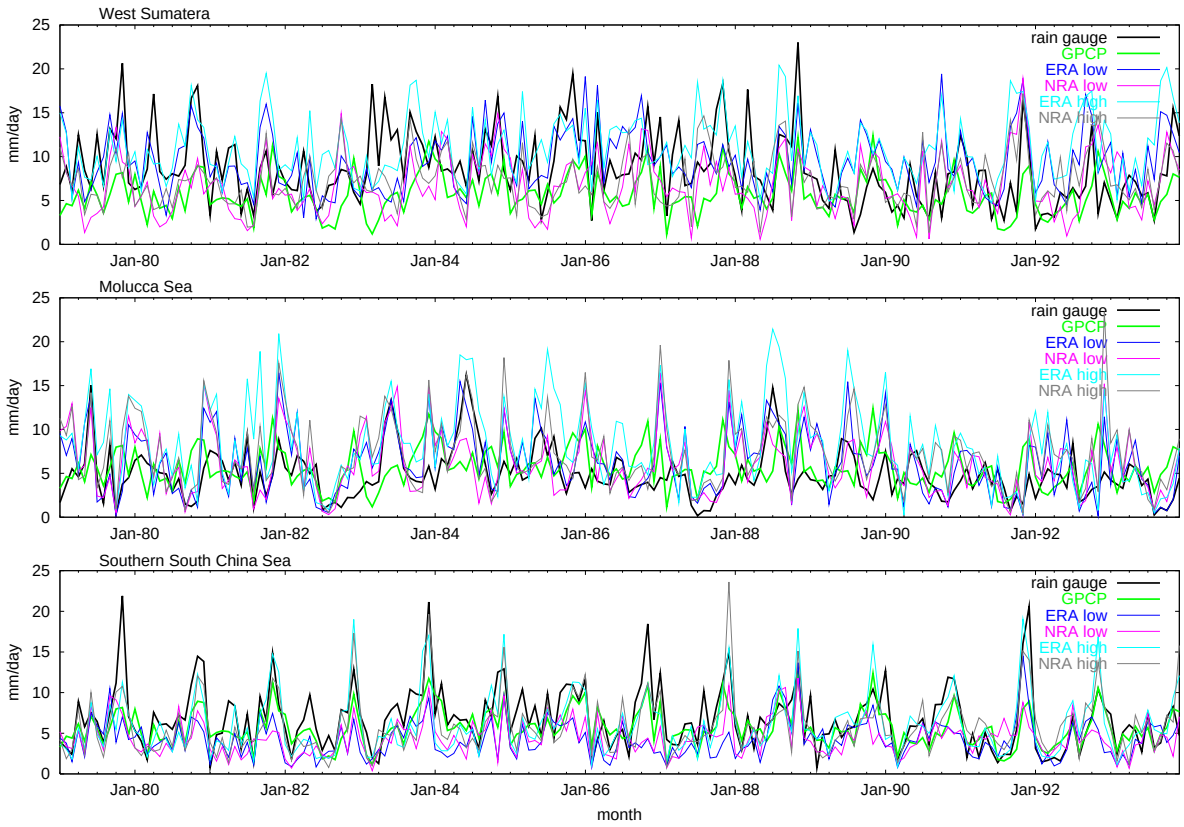

Figure 6.3: Variability of rainfall for the three sea areas from the coupled REMO-MPI-OM simulations and their comparison to observation (gauges).

6.3.2 The three sea regions

The variabilities of REMO simulations for the three sea areas are given in Fig. 6.3. In comparison to Fig. 4.6 there is less overestimation in all three regions. In chapter 4, REMO-ERA gives much too high estimations over the sea, which turns out to be the major problem of REMO simulations in this region. Like in the case of simulations over land, coherence between similar reanalysis for two different ocean model resolutions is high. In other words, the type of reanalysis plays a greater role than the resolution. Over the Molucca Sea, the coherence among all REMO simulations is high, except for some cases with the ERA forcing coupled with the high resolution ocean model. In the Molucca Sea, most REMO simulations overestimate rainfall, while, on the other hand, in the South China Sea, most REMO simulations underestimate. Regardless of these small drawbacks, the too large overestimations over the three sea regions in the uncoupled REMO (Fig. 4.6) have been reduced considerably for the coupled REMO. The simulation in the South China Sea seems to be the best among the three sea regions, followed by the Molucca Sea.

The summary of correlation between reanalysis or model simulations and observation is given in Table 6.2. In most cases, there are some improvements in coupled REMO simulations, espe-

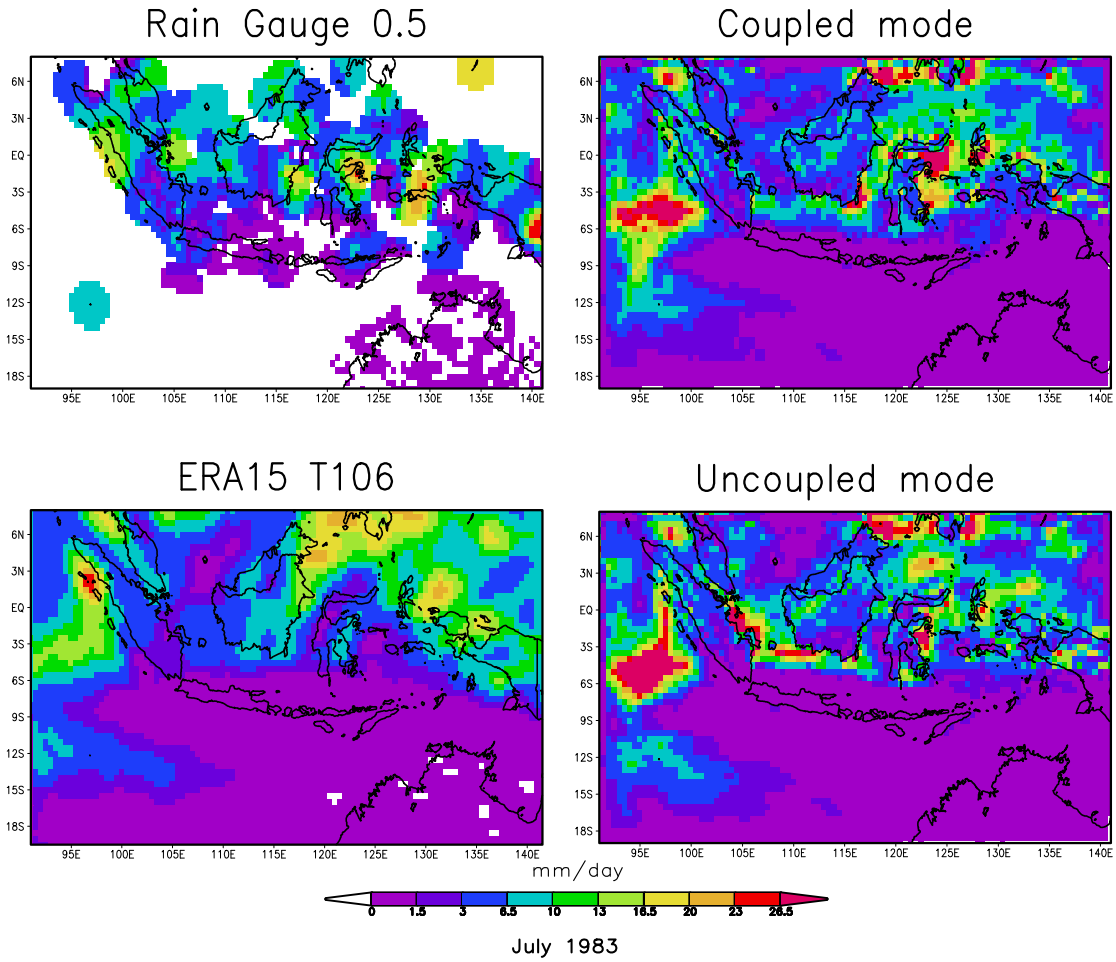

Figure 6.4: Comparison of three rainfall simulations and observation, from land-based rain gauges for July 1983. The coupled mode stands for REMO/MPI-OM with high resolution of the ocean model MPI-OM.

cially over the Molucca Sea from the original ERA reanalysis for about 46%. Among REMO simulations, most have improved from uncoupled to coupled model except for West Sumatera. In fact this region has the lowest correlation in comparison to other regions in different reanalyses. Low correlation in West Sumatera is also due to low quality of observation in the area. The observation data comprises only inland station data and the ocean data have been interpolated.

6.3.3 Precipitation Reduction over the Sea

In Chapter 4, the overestimation of rainfall over the sea is one of the difficult problems faced by REMO. Some sensitivity studies have been performed in order to understand the problem, but none has passed the criterion of lowering the precipitation amount over the sea, while maintaining the accumulated inland precipitation amount. The inland precipitation by REMO has performed well in comparison to the observation. One promising solution from these sensitivity

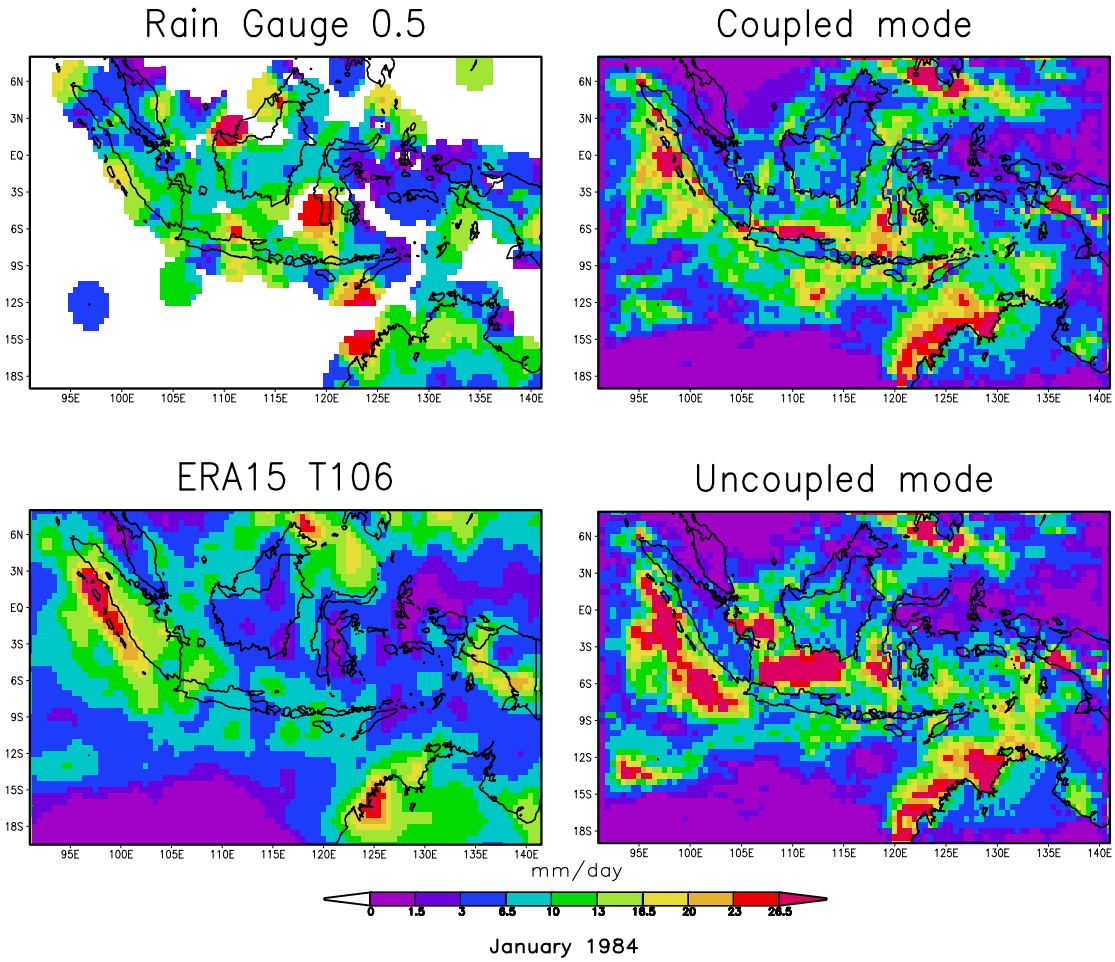

Figure 6.5: As Fig. 6.4, but for January of 1984.

studies is the reduction of SST by 1 °C. The result was a high reduction of precipitation over sea and a small reduction over land. With the coupled model, SST is no longer prescribed but derived from the coupled calculations.

Figures 6.4 and 6.5 illustrate two examples of the coupling effect over the sea by REMO in comparison to the original reanalysis and to the observations. The examples are taken from a non-ENSO year for boreal summer (Fig. 6.4) and boreal winter (Fig. 6.5). The two figures indicate over overestimation of precipitation over the seas by the uncoupled REMO simulations. The over estimations have been reduced in the coupled mode. The boreal winter case illustrates the better example with a strong reduction of overestimations from the uncoupled to the coupled mode. Although correlations between coupled and uncoupled are similar, there is an improvement because of a smaller overestimation of rainfall over the sea.

Table 6.2: Correlation between global reanalyses, uncoupled REMO and two coupled REMO and observations over the three sea areas.

NCEP	WSUM	MALS	SSCS
global reanalysis	0.055	0.517	0.638
Uncoupled	0.198	0.290	0.640
coupled low ocean	0.275	0.468	0.498
coupled high ocean	0.259	0.497	0.688
ERA	WSUM	MALS	SSCS
global reanalysis	0.370	0.222	0.748
Uncoupled	0.390	0.570	0.680
coupled low ocean	0.380	0.639	0.551
coupled high ocean	0.384	0.685	0.723

6.4 Implication for the Ocean

This section presents results from coupled model integrations and their comparisons to the uncoupled MPI-OM model described in Chapter 5. Thus, the stand alone model result will not be described in detail here. We will look at the variabilities of throughflow, SST and thermohaline circulations following what has been described in Chapter 5.

6.4.1 Variability of Throughflow

The coupled model simulations of the variability of two major throughflows (the Makasar and the Halmahera Straits) are given in Fig. 6.6. There is a contrast between the results of uncoupled and coupled models, especially within the Halmahera Strait. The coupled mode throughflow in the Halmahera Strait, in comparison to the uncoupled model, shows more variability and more southward transport. In comparison to the low resolution coupled model (not shown), the high resolution model produces more vigorous flow and more high frequency variability in both straits. In comparison to the observed Makasar strait throughflow (*Gordon et al.*, 1999) in the middle panel, the coupling has damped the variability from September 1997 until February 1998 more than the high resolution uncoupled model. There is more southward transport over that period. This result is unexpected, because in the long simulation of the throughflow in the top panel of Fig. 6.6, the coupled model calculates stronger variability. Thus the uncoupled mode produces a better simulation than the coupled one.

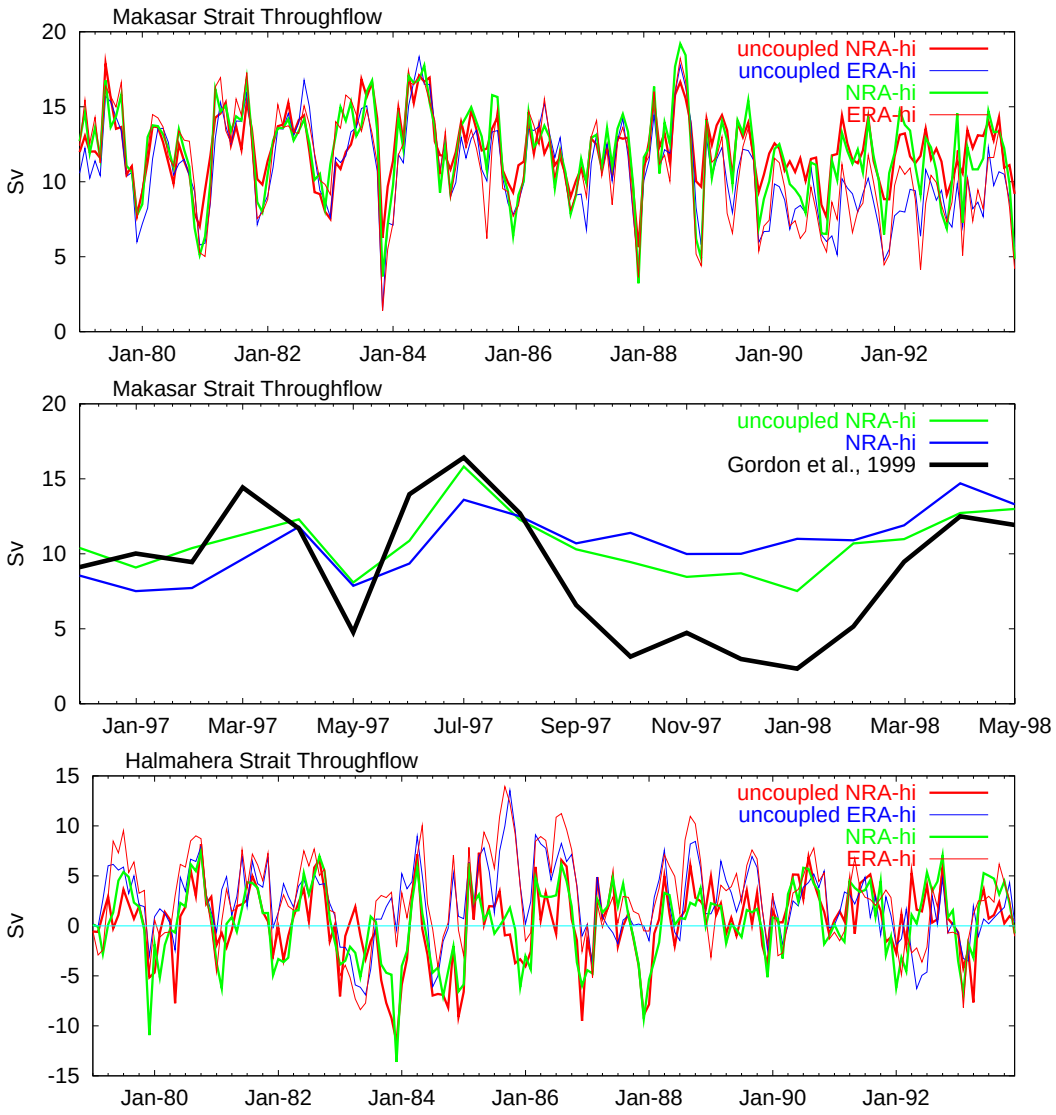

Figure 6.6: Makasar and Halmahera Straits throughflow as simulated by the coupled REMO-MPI-OM and a comparison to observations for Makasar Strait.

6.4.2 SST Variability

The SST variability of the three sea regions from Fig. 6.7 is close to observation (GISST). The coupled model simulates variability better than the uncoupled ocean model, which had an almost 2 °C warm bias all over the place. The results of the coupled ocean are also better than the climatological run with the OMIP forcing at the low resolution uncoupled model. The OMIP forcing simulation has the least biases among the uncoupled model. In most cases, there are large agreements between coupled model results of the same forcing at different resolutions. Between two different forcings, ERA forced simulations produce better SSTs. The significant improvement by the coupled model shows the solution of the warmer biases in the uncoupled model due to bulk formulae. However, the uncoupled model follows the SST variabilities quite

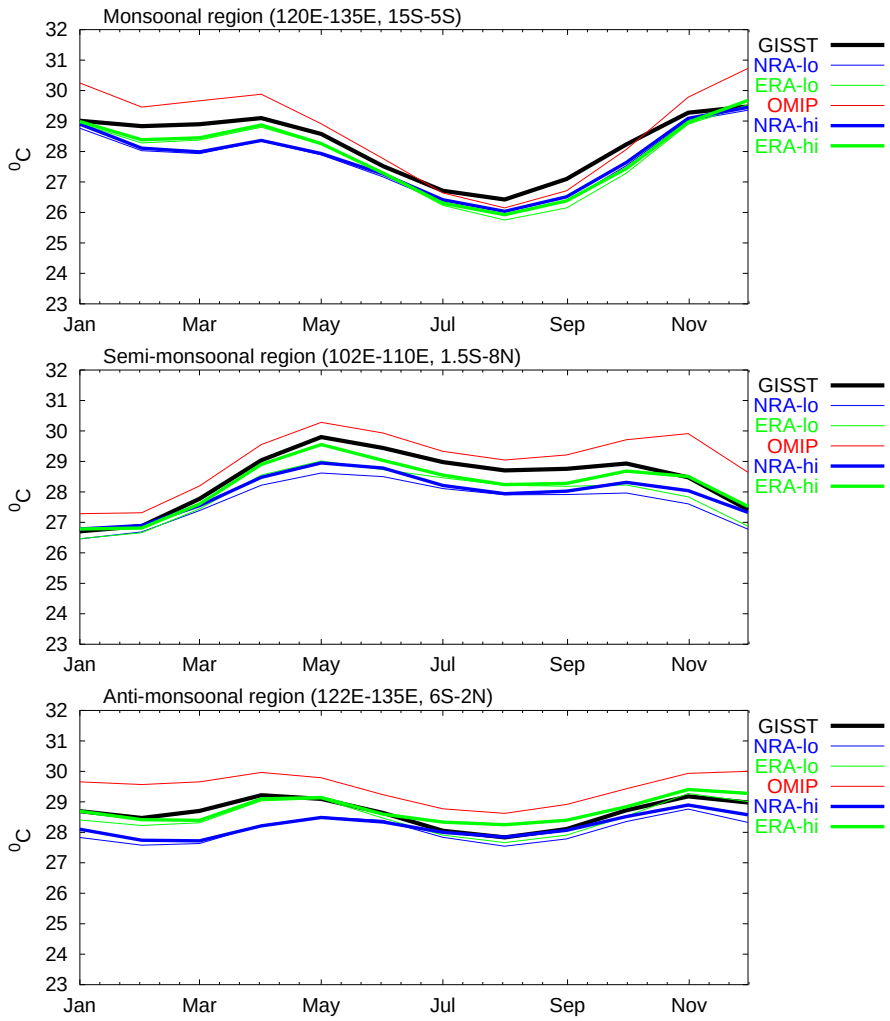

Figure 6.7: SST variability from REMO simulations and comparison to observations as well as simulations within OMIP for the three sea areas.

well but not in the correct magnitude. Inside the limited coupled region, the sea surface atmospheric fluxes are calculated using the dynamic input from the REMO model instead of using the bulk formulae. Besides, the atmospheric regional model works at a higher resolution than the original reanalysis, thus providing better atmospheric fluxes to the ocean.

6.4.3 Mean thermohaline condition

Fig. 6.8 shows the mean difference of the vertical temperature profile in the upper ocean between the coupled and the uncoupled model. Most differences are confirmed to the upper 200 m. In comparison to the uncoupled mode, there is a 2 °C lower surface temperature all over the place and 1 °C higher temperature at around 100 m depth in January in the eastern seas and in July in the South China Sea and the Karimata Strait. The lower surface temperature is associated with the warm bias probably originating from the bulk formulae in the uncoupled model.

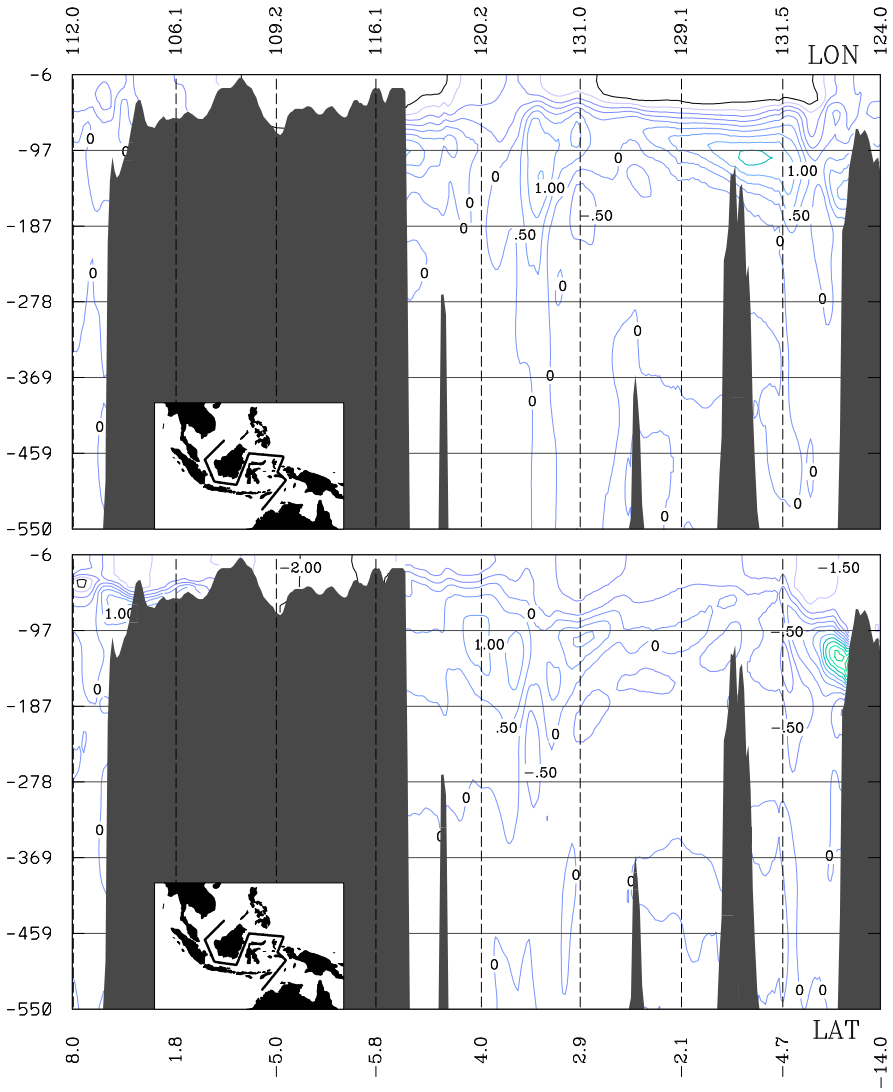

Figure 6.8: Differences of the mean vertical temperature profile in January (above) and July (bottom) for the years 1979-1993 between coupled and uncoupled mode of MPI-OM-NRA in high resolution. Contour interval is 0.5 °C. The inset shows the geographic location of the section following Table 5.2. Labels show depth in m (ordinate), latitude (bottom abscissa) and longitude (top abscissa).

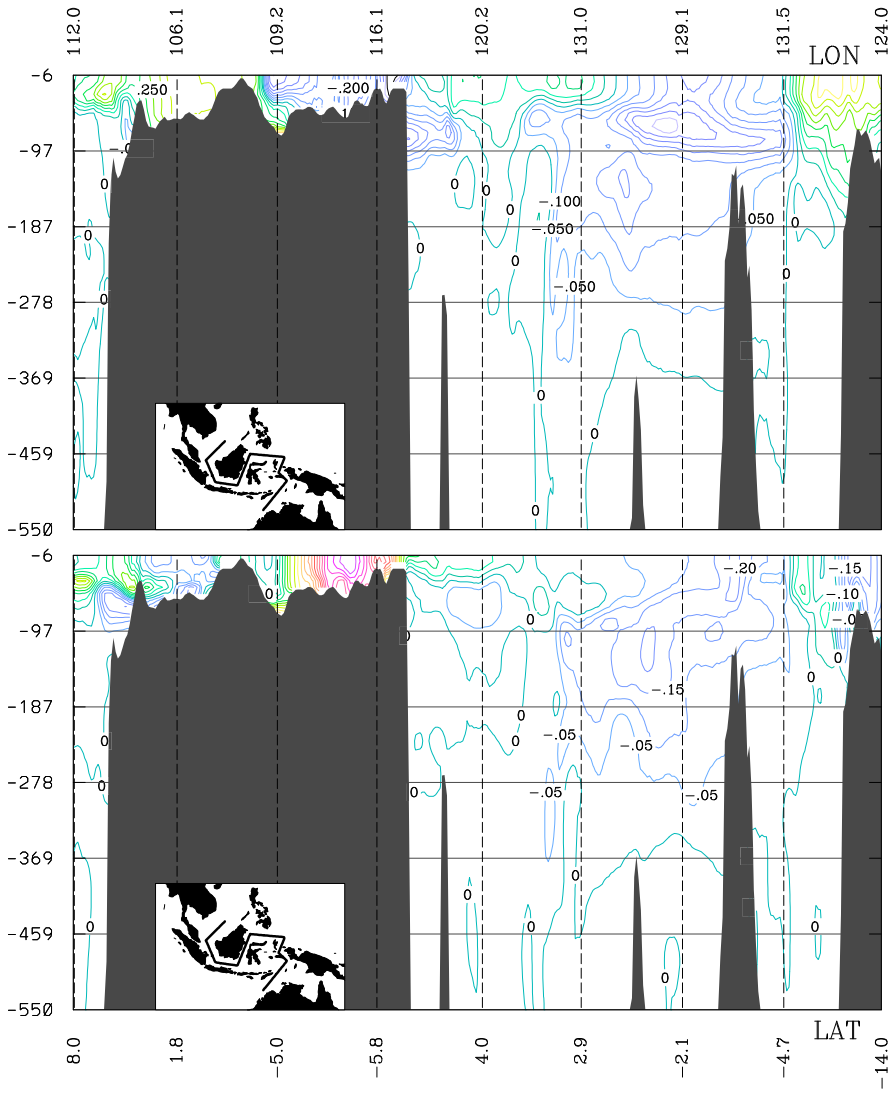

Figure 6.9: As Fig. 8, but for salinity. Contour interval is 0.05 psu.

In the southern edge of the Banda Sea at around 150 m, there is a 4 °C lower temperature in July and 1 °C lower temperature in January. In January in Seram Strait, there is 1.5 °C higher temperature.

The mean salinity difference between the coupled and uncoupled model is given in Fig 6.9. Most differences take place in the upper 100 m and rather in January than in July. Large differences occur in the shallow water regions of the Karimata Strait and the Java Sea. However, the absolute difference between coupled and uncoupled run is small for both months with a maximum difference of 0.25 psu. In January, there is a fresher (less saline) water layer near 70 m depth in Sulawesi Sea and the Halmahera Strait. In January the water is fresher in the coupled model for most of the upper 100 m layer.

6.5 Concluding Remarks

Simulations of the Indonesian climate using a special coupled model setup with a Regional Climate Model, REMO, and an Ocean Global Circulation Model (MPI-OM) with boundary forcings from two reanalyses have been performed. We analyzed the results with the comparison to the uncoupled ocean and atmosphere models. The analysis focuses on the rainfall variability for the atmospheric part and SST and ocean circulation for the oceanic part.

There are only small differences in rainfall variability for two different ocean resolutions and the difference is mainly due to the reanalysis. However in the ocean, different resolutions play a greater role than the atmospheric forcing type. The results also show that the improvement for inland rainfall is very small, but for rainfall over the ocean it is remarkable. Much of the improvements over the sea can be attributed to the reduction of rainfalls overestimation. Thus, large improvement in the atmosphere is due to an introduction of a dynamic change of SST from the uncoupled to the coupled model.

The analyses of the ocean model simulations show the importance of a correct bulk formulae. In the coupled mode, the model simulates the SST variability well. One possible parameter that plays a significant role in the bulk formulae is the cloud cover, which is badly represented in the reanalyses and the global climate model (*Jakob*, 2000). Although the coupling occurs only for a limited domain, the SST variability and ocean circulation has changed drastically compared to the uncoupled mode. With regard to the stratification, the coupling changes the temperature and salinity profiles in the upper 200 m and 100 m, respectively.

In summary the coupling has positive implications for the atmosphere and the ocean. There is less overestimation of rainfall over the sea and a more realistic representation of SST. However, coupling reduces the variability of the throughflow. Both reductions of the rainfall over the sea and the variability of the throughflow show that the coupling damps the atmospheric and ocean circulation. In comparison to previous results from the uncoupled climate model, the rainfall simulation over this region has been simulated best with the high resolution coupled model. This study uses only one spatial resolution in the atmosphere model. It is desirable to extend the work with different atmospheric resolution. The present simulations and analyses are confined to the ERA15 period. It is also desirable to extend the work with the new ERA40 (*Simmons and Gibson*, 2000) and the whole NRA dataset.

Chapter 7

Summary and Concluding Remarks

In this chapter the main results are summarized and the possible extension of future works is discussed.

This thesis introduces three distinct climate regions, the south monsoonal, the northwest semi-monsoonal and the Molucca anti-monsoonal regions. The three regions are characterized by different responses to monsoon and ENSO. The south monsoonal region is the common type, is driven by the ITCZ and covers the largest area. An example of this climate type is the rainfall over Java. The rainfall variability over this island is used as a measure of the model skill to the monsoonal region. The model skills in this region are high from the global to the regional scale due to the model's capability to simulate large scale climate systems such as the ITCZ. In other regions, rainfall variability has more local influences. The SST analyses in Chapter 2, 4 and 5 confirm that the annual pattern of SST in this region agrees with the ITCZ movement, while in Chapter 5, the thermohaline condition in January and July over Java Sea confirms the large scale character of the ITCZ embedded in this region.

With regard to the semi-monsoonal region, Chapter 2 shows no empirical local SST rainfall relationship. In Chapter 4 the SST in this region is the least error prone and REMO has the best results over the sea in this region in comparison to other seas. In Chapter 5, the ocean circulation has stronger lagging correlation to SST than in Molucca. Hence, REMO simulates the rainfall in this region well and the ocean model simulates an ocean circulation consistent with SST, but the SST to rainfall relationship fails in this region, suggesting that it is rather due to atmospheric factors. The cause of the disturbances has not yet been understood.

The anti-monsoonal region is missing in the global model but appears in the results of REMO simulations. Later in Chapter 5, the REMO coupled with an ocean model simulates the region even better. The simulation of the region shows two step-wise improvements: Better representation of topography through the 0.5^0 regional model and a better SST dynamics from the

simulated air-sea interaction. The lagging mechanism confirms the empirical relation between the local SST and rainfall in Chapter 2 and 3 and SST variability in Chapter 5.

From analyses of several models with different resolutions and forcings we conclude that *the rainfall climate of this region is predictable for monthly and seasonal scales but only for a limited and specific period in specific regions.* The best expected seasonal skill exists in JJA followed by SON. The least skill is found in MAM, which may be related to the spring predictability barrier. The skills of the models are improved during strong ENSO years as shown in Chapter 3 and by coherent REMO simulations in Chapter 4. In fact, the interannual signal of the average rainfall of the anti-monsoonal region can be used as an ENSO indicator. In Chapter 3, we find that even the ECHAM4 GCM simulates the rainfall in the monsoonal and anti-monsoonal region well during El Niño years and during JJA and SON, while it fails in other periods.

The problem with the spring barrier was indicated in the remote SST response of the three regions (Chapter 2), the comparison of global model rainfall results and reanalyses with observations in Chapter 3, the ENSO SST impact on rainfall in the same chapter and in the REMO predictability study of Chapter 4. Interestingly, even with the high resolution model the barrier persists or, in other words, does not have a resolution dependence. *The predictability barrier is an intrinsic character of Indonesian rainfall and a challenge to climate modelling in the region because it limits model applications.* Another important property of this barrier is that it exists also in ENSO sensitive regions. Unfortunately the predictability analyses have been made only for the atmosphere. The ocean aspect of this spring barrier has not been explored.

This thesis discusses the ENSO impact on Indonesian rainfall variability in Chapter 2, 3 and 5. There are similarities of the ocean and atmosphere responses to ENSO as revealed from rainfall and SST composites for El Niño, La Niña and normal years. Four circulation characteristics interplay to create an ENSO impact: the wet monsoon, the dry monsoon, ENSO itself and ocean circulation. The monsoon is the major player followed by the ocean circulation. The latter brings an SST change into the archipelago. The ocean circulation in this region is monsoonal and is driven mainly by the surface wind stress. The monsoonal ocean circulation limits the ENSO impact to the region only in the dry monsoon period. Significant rainfall responses to NINO3 SST anomalies only occur from July to November (Chapter 3). Rainfall is reduced during El Niño and increased during La Niña. During the dry season rainfall amount is reduced and during the wet season increased. Hence, the dry season and El Niño are in phase as well as La Niña and the wet season. As the dry season and La Niña are out of phase, there is less impact during La Niña and, as a matter of fact, La Niña has no impact at all at the peak of the dry season. Also the wet season and El Niño are out of phase, thus there is no impact of El Niño during the peak of the wet season on Indonesian rainfall. Moreover, the strength of the monsoon drives the ocean circulation as shown in chapter 5. La Niña is in phase with the wet season, but the ocean circulation does no longer support the mechanism. In conclusion, the monsoonal

ocean circulation is the main factor determining ENSO impact on rainfall in Indonesia.

The discussion on an ENSO impact mechanism highlights the stability of the monsoon through the ocean circulation. It follows that *beside ENSO, important rainfall variability from monthly to interannualy is a stable monsoon system.* The stability of the monsoon in this region has been discussed in many places. In Chapter 2 the monsoonal stability is measured with the regional spectra. The monsoonal character of ocean in Chapter 5 shows the upper ocean monsoonal characters, which in some places explain more than 90% of total variance. What has not been explored by this study are the regional monsoonal indices and the historical trend of the stability of the monsoon. Both are important for the climate change study.

The thesis also explores the influence of model resolution on rainfall simulations. *The Regional Atmospheric Model and the Global Ocean Model are able to produce realistic results.* There is improvement in the global model when increasing resolution from T42 to T106. A remarkable improvement for rainfall in the Molucca or the anti-monsoonal region occurs for the 0.5^0 REMO simulation driven by reanalyses. In many REMO simulations resolution has more influence than the lateral boundary forcing type. Except for the Molucca Sea and its surrounding, the quality of the REMO simulations is tied to the quality of the boundary forcing. The stand alone REMO simulation suffers from overestimations over the sea and a warm bias of SST, probably due to inadequate bulk formulae. The coupled model fixes both problems because of various reasons and in fact the coupled model produces the best inland and sea rainfall variability of all REMO simulations.

When applying a climate model in this region, special care should be given to the ocean surface. In Chapter 2, we found significant teleconnections to remote SST anomalies especially in SON. In Chapter 4, REMO experiments show much larger variances over the sea than over land. Better SSTs due to higher resolution (Chapter 4) and higher dynamic of ocean circulation (Chapter 6) result in a better rainfall simulation in the Molucca region.

The present study explored the potentials and limits of multi-level resolution of climate models. With increasing computer power, climate modelling has reached widespread applications. Using the climate models, we could see underlying and unforeseen processes in a more comprehensive way. This study showed that the state-of-the-art climate models are applicable to the region even for the least predictable model parameter, rainfall.

However, the study leaves some unanswered questions and thus points to possible extensions, such as the comparison with other models. For example, the results of the REMO predictability study in Chapter 4 are only valid for the REMO physics. In order to have a complete picture of the internal rainfall variability of the region, there is a need to extend the predictability study to regional coupled model ensemble simulations. The present study considers only rainfall variability, whereas the whole model data open up chances to explore and analyze other climate

parameters. Our analysis was restricted to the variability from monthly to seasonal, due to the availability of only averaged rainfall data. Higher frequency variability analysis would be the next challenge. Furthermore, the regional model in this study is the non partial model. The non partial REMO allows only one type of surface cover on each grid cell (land, water or ice). There is the possibility to run it in the in the partial version, which allows better soil processes and coastal representation. The latter will provide a better small island representation of the Maritime Continent.

Acknowledgements

I am very grateful to *Prof. Dr. Hartmut Graßl*, my supervisor, for his remarkable suggestions and constant support during this research. I am also thankful to *Dr. Lydia Dümenil Gates*, *Dr. Daniela Jacob* and *Dr. Stephan Bakan* for their guidances through the early years of chaos and confusion and for carefully reviewing the manuscript.

I am grateful to *Prof. Klaus Fraedrich*, *Prof. Kay Christian Emeis* and *Dr. Thomas Pohlmann* for examination of this work.

Working in the pleasant and motivating atmosphere at the Max-Planck-Institut für Meteorologie (MPI) has been an excellent opportunity for me. I greatly appreciate the assistance I received from the staff of the MPI in particular:

Ralf Podzun, *Dr. Tido Semmler*, *Dr. Barbael Langmann* (for their great assistances on REMO), *Dr. Ernst Meier–Reimer*, *Dr. Uwe Mikolajewicz*, *Helmuk Haak*, *Dr. Johan Junclauss* (for their great efforts to setup the BANDA-MPI-OM, many assistances on running MPI-OM and critical review of the MPI-OM related manuscript), *Dr. Dmitry Sein* (for his exceptional expertise on the coupled ocean/atmospheric model), *Astrid Baquero-Bernal* (for her kind friendship), *Uwe Schulzweida*, the IT and the DKRZ staffs (for helping me by various computational assistance).

I had the pleasure of meeting the 'Klimaprozesse' groups especially *Claudia Wunram* (for sharing most of the time in MPI and being patient to me). They are wonderful people and their support makes life in MPI enjoyable. The *Deutscher Akademischer Austauschdienst (DAAD) special Scholarship on Marine Programme*, which was awarded to me for the period 1999–2003, was crucial to the successful completion of this study. All computation were done with the computing facilities from the Deutches KlimaRechenZentrum (DKRZ).

Outside the MPI, special thanks go to *Dr. R. D. Susanto* (for many advices, for working together on a part of the thesis), *Dodo Gunawan* (for the work on REMO 1/6 °), *Tien Sribimawati* (who helped me come to MPI and with many observation data), *Dr. Jun-Ichi Yano* (for many critical discussions), *Prof. Shukla* and *Prof. Khrisnamurti* (for some discussions in ECMWF).

Of course, I am grateful to my parents, my brothers and sister for their patience and great *love*. Without them this work would never have come into existence (literally).

Most of all, I want to thank my wife *Stela* and our children *Mirai* and *Edela* (for their *love*, encouragement, understanding and patience) and Allah SWT for *great love, blessing*, all happiness and luckiness in my life.

Appendix A

Glossary

AGCM	Atmospheric General Circulation Model
AMIP	Atmospheric Model Inter-Comparison Project
ANOVA	Analysis of Variances Method
AR	Auto Regressive Function
BBL	Bottom Boundary Layer
BMG	Badan Meteorologi dan Geofisika, Indonesian Meterology and Geophysics Agency
CCHAR	The Charnock Constant
DCM	The Double Correlation Method
DJF	December/January/February
ECHAM4	ECMWF/Hamburg Atmospheric Model version 4
ECMWF	European Centre for Medium-range Weather Forecast
EM/DM	European Model/Deutsche Model
ENSO	El Niño Southern Oscillation
EOF	Empirical Orthogonal Function
ERA15	15-year ECMWF Re-Analysis
GCM	Global Circulation Model
GHCN	Global Historical Climatology Network
GISST	Global Ice and Sea Surface Temperature
GPCP	Global Precipitation Climatology Project
HOPE	Hamburg Ocean Primitive Equation ocean model
ITCZ	Inter-Tropical Convergence Zone
ITF	Indonesian Throughflow
JAS	July/August/September
JFM	January/February/March
JJ	June/July

JJA	June/July/August
MAM	March/April/May
MJJ	May/June/July
MJJAS	May/June/July/August/September
MOLS	Molucca Sea
MPI	Max Planck Institute for Meteorology
MPI-OM	Max Planck Institute Ocean Model
MSL	Mean Sea Level
NCEP	National Centers for Environmental Prediction
NCEP-NCAR	NCEP- National Center for Atmospheric Research
NDJ	November /December/January
NDJF	November /December/January/February
NDJFM	November /December/January/February/March
NINO3	The NINO3 area (5 °S,5 °N,150 °W-90 °W)
NRA	NCEP/NCAR Re-Analysis
OGCM	Ocean General Circulation Model
OMIP	Ocean Model Inter-Comparison Project
ON	October/November
ONDJ	October/November/December/January
PC	Principal Component of EOF
RCM	Regional Climate Model
REMO	the MPI RCM
RMSE	Root Mean Square Error
SOI	Southern Oscillation Index
SON	September/October/November
SPCZ	Southern Pacific Convergence Zone
SSCS	Southern South China Sea
SST	Sea Surface Temperature
T106	global model resolution, equivalent to 1.125 °at the equator
T30	global model resolution, equivalent to 3.8 °at the equator
T42	global model resolution, equivalent to 2.8125 °at the equator
WCRP	World Climate Research Programme
WMO-NOAA	World Meteorology Organization-National Oceanic Atmospheric Administration
WSUM	West Sumatera
ZL	minimal cloud thickness to precipitate over land
ZO	minimal cloud thickness to precipitate over ocean
ZRTC	minimum humidity level to condensation of a convective cloud
ZRTL	minimum humidity level to condensation of a non-convective cloud

Appendix B

Statistical tools

B.1 The Empirical Orthogonal Function (EOF) Analysis

The Principal Component Analysis (PCA) became popular for analysis of atmospheric data after a paper by *Lorenz* (1956) who called the technique Empirical Orthogonal Function (EOF) analysis. The purpose of the EOF is to reduce a data set containing a large number of variables to a data set with fewer new variables, which can represent a large fraction of the variability of the original data. The technique defines a new coordinate system in which to view the data. This coordinate system is oriented such that each axis is aligned along the direction of the maximum joint variability of the data.

Let consider a geophysical field $f(x,t)$ defined simultaneously at **M** positions denoted as x with **N** observations at times t, An $M \times N$ rectangular matrix, **F**, with M rows (or M series at each station) and N columns (maps). The matrix element f_{mn} represents the observation made at station m at time.

The goal is to find an orthogonal basis in the vector space $\{\mathbf{e}_1, \mathbf{e}_2, \mathbf{e}_3, ...\mathbf{e}_M\}$ such that each vector e_m best represents the original (M X 1) column vector f_n with n=1, ... N. This is equivalent to find a set of M vectors, $\mathbf{e}_m$, whose orientation is such that the sum of the squares of the projections of all the N observation vector $\mathbf{f}_n$ on to each $\mathbf{e}_m$ is maximized sequentially. We assume that the vectors of the set $\{\mathbf{e}\}$ are mutually orthonormal so that by definition of the inner product:

$$\mathbf{e}_m \cdot \mathbf{e}_j = \delta_{m,j} \tag{B.1}$$

where $\delta_{m,j}$ is the Kronecker function. The set of vector $\{\mathbf{e}\}$, which defines this special co-ordinate system, are called the "empirical" Orthogonal functions (EOFs). As we will see the definition of EOFs depends upon the co-variance matrix of the original data set. It follows that

the coordinate system defined by this technique will be different for different data sets. This is the reasonwhy Lorenz called them "Empirical" in contrast to other theoretical functions such as Fourier harmonics.

The expression to maximize is:

$$\frac{1}{N}\sum_{n=1}^{N}[f_n \cdot \mathbf{e}_m]^2 \tag{B.2}$$

for m=1, 2, ... M subject to the conditions of Eq. B.1

Written in matrix form Eq. B.2 becomes:

$$\mathbf{e}_m^T \mathbf{R} \mathbf{e}_m \tag{B.3}$$

where **R** is the (MXM) covariance matrix defined by :

$$\mathbf{R} = \frac{1}{N}\mathbf{F}\mathbf{F}^T \tag{B.4}$$

The maximizing of Eq. B.2 subject to condition of Eq. B.1 leads to an eigenvalue problem.

$$\mathbf{R}\mathbf{e}_m = \lambda_m \mathbf{e}_m \tag{B.5}$$

$$(\mathbf{R} - \lambda\mathbf{I})\mathbf{e}_m = 0 \tag{B.6}$$

where e_m is the eigenvector and λ_m is its corresponding eigenvalue of the matrix **R**, **I** is the unit matrix of order M. The matrix $\mathbf{L} = \lambda\mathbf{I}$ is a diagonal matrix with the eigenvalues λ_m as diagonal elements. The Eq. B.6 leads to an homogeneous system of M linear equations of M unknown which has no trivial solutions if the determinant of the coefficients of the matrix $\mathbf{R} - \lambda\mathbf{I}$ is equal to zero:

$$|\mathbf{R} - \lambda\mathbf{I}| = 0 \tag{B.7}$$

The M solutions $\lambda_1, ...\lambda_M$ are real and positive, because **R** is symmetric and positive definite. Since **R** is symmetric, its trace is invariant under a basis transformation and thus equal to the sum of the eigenvalues, implying that each eigenvalue λ_m explains a fraction of the total explained variance.

$$\sum_{m=1}^{M} r_{mm} = \sum_{m=1}^{M} \lambda_m \tag{B.8}$$

For each value λ_m (m=1, ... M) Eq. B.7 leads to a vector solution $\mathbf{e}_m$ which is the eigenvector associated with λ_m. The eigenvalues are arranged in decreasing order of magnitude so that $\lambda_1 \geq \lambda_2 \geq ... \geq \lambda_m$. Thus, the first mode $\mathbf{e}_1$ associated with λ_1 explains the largest fraction of the total variance of the data.

The set of the M independent and mutually orthogonal eigenvectors, each scaled to have length 1, constitutes the orthonormal basis $\{\mathbf{e}_1, \mathbf{e}_2, \mathbf{e}_3, ...\mathbf{e}_M\}$ in the M-vector space. The coordinate system which axis are defined by this special orthonormal basis provides the optimum representation of the set of the observation data vectors, $\mathbf{f}_n$ Any observation vector $\mathbf{f}_n$ can be expressed as a linear combination of the M eigenvectors $\mathbf{e}_n$:

$$\mathbf{f}_n = \sum_{m=1}^{M} c_{mn}\mathbf{e}_m \tag{B.9}$$

where the coefficients c_{mn} (principal components) are the projections of $\mathbf{f}_n$ on $\mathbf{e}_n$ (m=1, ... M) so that

$$c_{mn} = \mathbf{e}_m^T \mathbf{f}_n \tag{B.10}$$

Because the N observations refer to different times, the element of a row vector $[c_{m1}, c_{m2}, ..., c_{mN}]$ give the values of the coefficients associated with a given eigenvector $\mathbf{e}_m$. It is important to note that the row vectors c_m are also mutually orthogonal.

Equations B.9 and B.10 are formally similar to the corresponding expressions in the fourier analysis, where the $\mathbf{e}_m$ are like sine and cosine functions and the c_{mn} are equivalent to the coefficients of a Fourier expansion.

The present description is based on *Pexioto and Oort* (1991). For an exhaustive description of PCA, oriented specifically towards geophysical data, see *Preseindorfer* (1988).

B.2 The Rotated EOF Analysis

This section describes a class of basis vector "rotation" procedures that is widely used in climate research. The procedures are usually applied to EOFs in the hope that the resulting "rotated EOFs" can be more easily interpreted than the EOFs themselves. The rotated EOF transforms the EOF into a non-orthogonal linear basis. Also, "rotation" can be performed on any linear basis, not just EOFs. The following description is based on *von Storch and Zwiers* (1999).

Rotation consists of the transformation of a set of input vectors $\mathbf{E} = \{\mathbf{e}_1, \mathbf{e}_2, \mathbf{e}_3, ...\mathbf{e}_K\}$ into $\mathbf{Q} =$

$\{\mathbf{q}_1, \mathbf{q}_2, \mathbf{q}_3, ...\mathbf{q}_K\}$ by means of an invertible $K \times K$ matrix $R = (r_{ij})$:

$$Q = PE \tag{B.11}$$

or, for each vector q_i:

$$\mathbf{q}_i = \sum_{j=1}^{K} r_{ij}\mathbf{e}_j \tag{B.12}$$

The matrix R is chosen from a class of matrices, such as orthonormal matrices, subject to the constraint that a functional $V(Q)$ is minimized. Under some conditions, operation of Eq B.11 can be viewed as a rotation of the "input vectors". Since these are often the first K EOFs, the resulting vector $\mathbf{q}_i$ are called "rotated EOFs". When matrix R is orthonormal, the operation is said to be an "orthonormal rotation"; otherwise it is said to be "oblique."

Several arguments are raised in favour of the rotated EOFs:

- The technique produces compact patterns that can be used for "regionalization", that is, to divide an area in a limited number of homogeneous sub-areas.
- Rotated EOFs are less sensitive to the distribution of observing locations than conventional EOFs
- Rotated EOFs are often statistically more stable than conventional EOFs. That is, the sampling variance of rotated EOFs is often less than that of the input vectors.

Appendix C

Determination of the Liquid Water Content

The explanation below is based on *Semmler* (2002). Small-scale condensation processes cannot be solved in REMO explicitly. Therefore a critical humidity is introduced, above which the sub-grid scale condensation is possible. REMO takes this value from the global model ECHAM4 where above approximately 500 hPa the value is 60%. Below this pressure level the value increases exponentially to the lowest model layer to approximately 98%:

$$r_0(p) = r_{0,top} + (r_{0,surf} - r_{0,top}) e^{[1-(p_s/p)^4]} \tag{C.1}$$

where p, p_s, $r_{0,top}$ = 0,6 and $r_{0,surf}$=0.99 are the air pressure, the surface pressure, the critical relative humidity in the upper atmosphere and at the surface, respectively.

Since REMO uses the horizontal resolutions 1/6 ° or 0.5 °, which are much higher than the ECHAM4 resolutions at 1.125 ° or 2.8125 °, the use of the sub-grid scale condensation seems to be reasonable. A weather phenomenon with a horizontal scale of approximately 200 km can explicitly be simulated by REMO, while it must be parameterized in ECHAM4. In one of REMO sensitivity studies of Chapter 4, the $r_{0,top}$ has been changed to 0.8 for convective (ZRTC) and large-scale (ZRTL) cloud systems. Therefore a critical relative humidity 80% ($r_{0,top}$ = 0.8 in Eq. C.1) will increase the critical values above 500 hPa and below this level downward will increase exponentially to approximately 98%. Both profiles of the critical relative humidity are given in Fig. C.1.

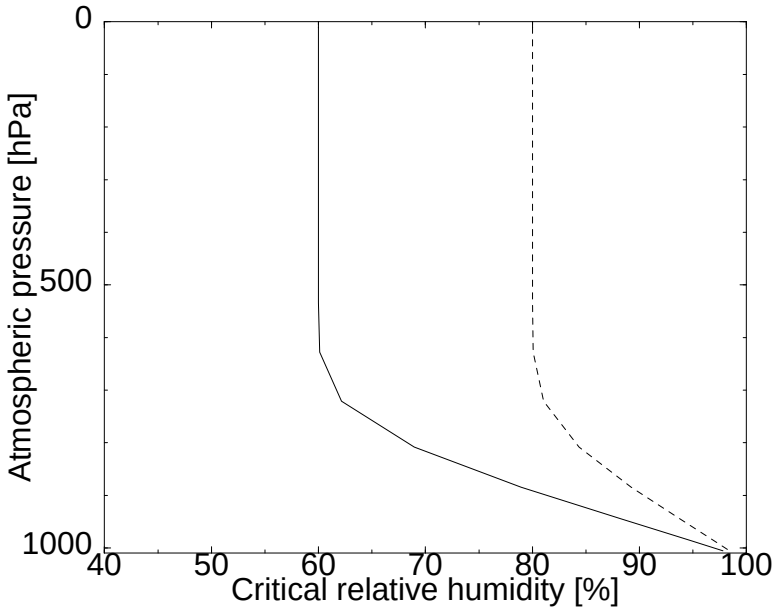

Figure C.1: Vertical profile of the critical relative humidity with $r_{0,top} = 0.6$ (solid line) and $r_{0,top} = 0.8$ (dashed line).

Appendix D

Atmospheric surface fluxes forcing for the ocean model

Simulation with the MPI-OM model requires the specification of heat, freshwater and momentum fluxes at the air/sea interfaces. In this study use is made of a climatological forcing dataset with six-hourly temporal resolution and atmospheric synoptic scale variability. The following describes the formulation of the atmospheric surface fluxes calculation for ocean forcing or the bulk formulae (Eq. D.6 and D.7). The following description is based on *Marsland et al.* (2003).

Introducing Q_{srf} to denote either the open water heat flux (Q_w) or the heat flux over sea ice (Q_i). the surface heat balance is given by

$$Q_{srf} = Q^{se}_{srf} + Q^{la}_{srf} + Q^{lw}_{srf} + Q^{sw}_{srf} \tag{D.1}$$

where Q^{se}_{srf}, Q^{la}_{srf}, Q^{lw}_{srf}, Q^{sw}_{srf} are parameterisations of the sensible, latent, longwave and shortwave heat fluxes, respectively.

Following *Oberhuber* (1993) the turbulent fluxes are parameterised as

$$Q^{se}_{srf} = \rho_a c_a C_H V_{10m}(T_a - T_{srf}) \tag{D.2}$$

$$Q^{la}_{srf} = \rho_a L_{srf} C_L V_{10m}(q_a - q_{srf}) \tag{D.3}$$

Constants ρ_a, c_a and L_{srf} denote the air density, the air specific heat capacity and the latent heat of vaporisation or sublimation as appropriate. The 10 m wind speed V_{10m} and 2 m air temperature T_a are taken as prescribed forcing. Variable coefficients of sensible C_H and latent C_L heat transfer are formulated according to *Large and Pond* (1982). The surface temperature

T_{srf} represents either the ocean model upper layer temperature or the sea ice/snow layer skin temperature as define in the following

$$Q_{cond} = k_i \frac{(T_{freeze} - T_{srf})}{\tilde{h}_i} \tag{D.4}$$

where the conductive heat flux Q_{cond} within the sea ice/snow layer is assumed to be directly proportional to the temperature gradient across the sea ice/snow layer and inversely proportional to the thickness of that layer (i.e. the so-called zero-layer formulation of *Semtner* (1976)).

The specific humidity q is a function of water vapor pressure e (unit of Pascal) and air pressure p (currently approximated by a constant 1000 hPa in MPI-OM).

$$q = (0.623e)/(p - 0.378e) \tag{D.5}$$

At the 2m level (q_a) the water vapor pressure is a function of dew point temperature, while at the surface (q_{srf}) the saturation vapor pressure is a function of the water or ice/snow surface temperature. In both cases the vapor pressure (e) are calculated according to the formulae of *Buck* (1981).

The radiant fluxes are parameterised as

$$Q^{lw}_{srf} = \varepsilon\sigma T_a^4 (0.39 - 0.05\sqrt{e/100})(1 - \chi n^2) + 4\varepsilon\sigma T_a^3 (T_{srf} - T_a) \tag{D.6}$$

$$Q^{sw}_{srf} = (1 - \alpha_{srf}) Q^{incsw} \tag{D.7}$$

The parameterisation of net longwave radiation is based on that of *Berliand and Berliand* (1952), with the fractional cloud cover n is taken as prescribed forcing. The surface thermal emmisivity and Stefan-Boltzmann constant are denoted by ε and σ, respectively. The saturation vapor pressures e depend on water or sea ice/snow conditions and are also calculated according to the formulae of *Buck* (1981). The cloudiness factor χ is a modified form of that proposed by *Budyko* (1974) and is a function of latitude ϕ.

$$\chi = 0.5 + 0.4(min(|\phi|, 60^\circ))/90^\circ \tag{D.8}$$

The incident shortwave radiation Q^{incsw} is provided as part of the forcing data and implicitly modified by cloud cover in the reanalysis model. The surface reflectivity α_{srf} is either that appropriate for open water or takes one of four possible values determined by both the absence or presence of snow and by whether the surface temperature of the sea ice or snow is below $0^\circ C$ (freezing) or equal to $0^\circ C$ (melting). Over open water Q^{sw}_w is allowed to penetrate beyond the upper model layer with an exponential decay profile.

References

Annamalai, H., J. M. Slingo, K. R. Sperber, and K. Hodges, 1999: The Mean evolution and variability of the Asian summer monsoon Comparison of ECMWF and NCEP-NCAR reanalyses. *Monthly Weather Review*, **127**, 1157–1186.

Arakawa, A., and V. R. Lamb, 1977: Computational design of the basic dynamical processes of the UCLA general circulation model. *Methods Comput. Phys.*, **17**, 173–265.

Arpe, K., L. Dümenil, and M. A. Giorgetta, 1998: Variability of the Indian monsoon in the ECHAM3 model: Sensitivity to sea surface temperature, soil moisture, and the stratospheric quasi-biennial oscillation. *Journal of Climate*, **11**, 1837–1858.

Asnani, G. C., 1993: *Tropical Meteorology.*, vol. 1, Asnani, 603 pp.

Balmaseda, M. A., M. K. Davey, and D. L. T. Anderson, 1995: Decadal and seasonal dependence of ENSO prediction skill. *Journal of Climate*, **8**, 2705–2715.

Baquero-Bernal, A., M. Latif, and S. Legutke, 2002: On dipolelike variability of sea surface temperature in the tropical Indian Ocean. *Journal of Climate*, **15**, 1358–1368.

Barnett, T. P., K. Arpe, L. Bengtsson, M. Ji, and A. Kumar, 1997: Potential predictability and AMIP implications of midlatitude climate variability in two general circulation models. *Journal of Climate*, **10**, 2321–2329.

Barnston, A. G., H. M. van den Dool, S. E. Zebiak, T. P. Barnett, M. Ji, D. R. Rodenhuis, M. A. Cane, A. Leetmaa, N. E. Graham, C. R. Ropelewski, V. E. Kousky, E. A. O'Lenic, and R. E. Livezey, 1994: Long-lead seasonal forecasts - Where do we stand? *Bulletin of the American Meteorological Society*, **75**, 2097–2114.

Barnston, A. G., M. H. Glantz, and Y. He, 1999: Predictive skill of statistical and dynamical climate models in forecasts of SST during the 1997-98 El Niño episode and the 1998 La Niña onset. *Bulletin of the American Meteorological Society*, **80**, 217–244.

Berlage, H. P., 1927: East-monsoon forecasting in Java., *Verhandelingen 20*, Koninklijk Magnetisch en Meteorologisch Observatorium te Batavia, Magnetic Meteorology Observation. Batavia, Indonesia, 42 pp.

Berliand, M. E., and T. G. Berliand, 1952: *Determining the net long-wave radiation of the earth with consideration of the effects of cloudiness.*, vol. 1, Isv. Akad. Nauk. SSSR Ser. Geofis., 64-78 pp.

Bhaskaran, B., R. G. Jones, J. M. Murphy, and M. Noguer, 1996: Simulations of the Indian summer monsoon using a nested regional climate model: domain size experiments. *Climate Dynamics*, **12**, 573–587.

Bhowmik, S. K. R., and K. Prasad, 2001: Some characteristics of limited-area model-prescription forecast of Indian monsoon and evaluation of associated flow features. *Meteorology and Atmospheric Physics*, **76**, 223–236.

Blumenthal, M. B., 1991: Predictability of a coupled ocean-atmosphere model. *Journal of Climate*, **4**, 766–784.

Bony, S., K. M. Lau, and Y. C. Sud, 1997a: Sea surface temperature and large-scale circulation influences on tropical greenhouse effect and cloud radiative forcing. *Journal of Climate*, **10**, 2055–2077.

Bony, S., Y. Sud, K. M. Lau, J. Susskind, and S. Saha, 1997b: Comparison and satellite assessment of NASA/DAO and NCEP-NCAR Reanalysis over tropical ocean: Atmospheric hydrology and radiation. *Journal of Climate*, **10**, 1441–1462.

Bougeault, P., 1983: A non-reflective upper boundary condition for limited-height hydrostatic models. *Monthly Weather Review*, **111**, 420–429.

Braak, C., 1919: Atmospheric variations of short and long duration in the Malay Archipelago., *Verhandelingen 5*, Koninklijk Magnetisch en Meteorologisch Observatorium te Batavia, Magnetic Meteorology Observation. Batavia, Indonesia, 57 pp.

Braak, C., 1921: Het Climaat van Nederlandsch Indie., *Verhandelingen 8*, Koninklijk Magnetisch en Meteorologisch Observatorium te Batavia, Magnetic Meteorology Observation. Batavia, Indonesia, 55 pp.

Bray, N. A., S. Hautala, J. Chong, and J. Pariworo, 1996: Large-scale sea level, thermocline, and wind variations in the Indonesian throughflow region. *Journal of Geophysical Research*, **101**, 12,239–12,254.

Buck, A. L., 1981: New equations for computing vapor pressure and enchancement factor. *Journal of Applied Meteorology*, **20**, 1527–1532.

Budyko, M. I., 1974: Climate and life in, *Int. Geophys. Ser.*, Academic Press.

Cheang, B. K., 1987: Short- and long- range monsoon prediction in Southeast Asia. in, *Monsoons.* (Eds.), Fein, J. S., and P. L. Stephens, John Wiley and Sons, Wiley Interscience Publication, 579-606 pp.

Chen, W. Y., and H. M. van den Dool, 1997: Atmospheric predictability of seasonal, annual and decadal climate means and the role of the ENSO cycle: a model study. *Journal of Climate*, **10**, 1236–1254.

Cressman, G. P., 1959: An operational objective analysis scheme. *Monthly Weather Review*, **117**, 765–783.

Cubasch, U., G. A. Meehl, G. J. Boer, R. J. Stouffer, M. Dix, A. Noda, C. A. Senior, S. Raper, and K. S. Yap, 2001: Projections of future climate change. in, *Climate Change 2001: The scientific basis. Report of the Intergovernmental Panel on Climate Change.* (Eds.), Houghton, J. T., Y. Ding, D. J. Griggs, M. Noguer, P. J. van der Linden, X. Dai, K. Maskell, and C. A. Johnson, Cambridge Univ. Press, Cambridge, UK, NY, 881 pp.

Davey, M. K., D. L. T. Anderson, and S. Lawrence, 1996: A simulation of variability in ENSO forecast skill. *Journal of Climate*, **9**, 240–246.

Davidson, N. E., 1984: Short-term fluctuations in the Australian monsoon during winter Monex. *Monthly Weather Review*, **112**, 1697–1708.

Davidson, N. E., J. L. McBride, and B. J. McAvaney, 1984: Divergent circulations during the onset of the 1978-79 Australian monsoon. *Monthly Weather Review*, **112**, 1684–1696.

Davies, H. C., 1976: A lateral boundary formulation for multi-level prediction models. *Quarterly Journal of Royal Meteorological Society*, **102**, 405–418.

Dommenget, D., and M. Latif, 2002: A cautionary note on the interpretation of EOFs. *Journal of Climate*, **15**, 216–225.

Drijfhout, S., C. Heinze, M. Latif, and E. Maier-Reimer, 1996: Mean circulation and internal variability in an ocean primitive equation model. *Journal of Physical Oceanography*, **26**, 559–580.

Dümenil, L., and E. Todini, 1992: A rainfall-runoff scheme for use in the Hamburg climate model. in, *Advance Theoretical Hydrology, vol 1* (Ed.), O'Kane, J. P., vol. 1, European Geoph. Soc. Series on Hydrological Sciences, Elsevier Science Publishers, Amsterdam, 129-157 pp.

Dümenil, L., K. Isele, H. J. Liebscher, U. Schroder, M. Schumaker, and K. Wilke, 1993: Discharge data from 50 selected rivers for GCM validation., *MPI Report 100*, [Available from Max Planck-Institut für Meteorologie, Bundesstr. 55, D-20146, Hamburg, Germany.].

Errico, R. M., and D. P. Baumhefner, 1987: Predictability experiments using a high resolution limited area model. *Monthly Weather Review*, **115**, 488–504.

Ferranti, L., 1997: The Asian summer monsoon and its predictability, Ph.D. thesis, Univ. of Reading, [Available from the European Centre for Medium-range Weather Forecasts, Reading, UK.], 147 pp.

Fieux, M., R. Molcard, and A. G. Ilahude, 1996: Geosttropic transport of the Pacific-Indian Oceans throughflow *Journal of Geophysical Research*, **101**, 12,421–12,432.

Flügel, M., and P. Chang, 1998: Does the predictability of ENSO depend on the seasonal cycle? *Journal of Atmospheric Sciences*, **55**, 3230–3243.

Fouquart, Y., and B. Bonnel, 1980: Computations of solar heating of the Earth's atmosphere: A new parameterization. *Beiträge zur Physik der Atmosphäre*, **53**, 35–62.

Gates, W. L., 1992: AMIP: The Atmospheric Model Intercomparison Project. *Bulletin of the American Meteorological Society*, **73**, 1962–1970.

Gates, W. L., J. S. Boyle, C. Covey, C. G. Dease, C. M. Doutriaux, R. S. Drach, M. Fiorino, P. J. Gleckler, J. J. Hnilo, S. M. Marlais, T. J. Phillips, G. L. Potter, B. D. Santer, K. R. Sperber, K. E. Taylor, and D. N. Williams, 1999: An overview of the results of the Atmospheric Model Intercomparison Project (AMIP I). *Bulletin of the American Meteorological Society*, **80**, 29–56.

Gent, P. R., J. Willebrand, T. McDougall, and J. C. McWilliams, 1995: Parameterizing eddy-induced tracer transports in ocean circulation models. *Journal of Physical Oceanography*, **25**, 463–474.

Gibson, J. K., P. Kallberg, S. Uppala, A. Hernandez, A. Nomura, and E. Serrano, 1997: The ECMWF Re-Analysis (ERA) 1. ERA Description., *ECMWF Reanalysis Project Report Series 1*, ECMWF, [Available from the European Centre for Medium-range Weather Forecasts, Reading, UK.], 71 pp.

Giorgi, F., 1991: Sensitivity of simulated summertime precipitation over the western United States to different physics parameterizations. *Monthly Weather Review*, **119**, 2870–2888.

Goddard, L., S. J. Mason, S. E. Zebiak, C. F. Ropelowski, R. Basher, and M. A. Cane, 2000: Current approaches to seasonal to interannual climate predictions., *(IRI) tech. report 00-01*, International Research Inst., 62 pp.

Godfrey, J. S., 1996: The effect of the Indonesian throughflow on circulation and heat exchange with the atmosphere: A review. *Journal of Geophysical Research*, **101**, 12,217–12,337.

Godfrey, J. S., A. C. Hirst, and J. Wilkin, 1993: Why does the Indonesian throughflow appear to originate from the North Pacific? *Journal of Physical Oceanography*, **23**, 1087–1098.

Gordon, A. L., and R. Fine, 1996: Pathways of water between the Pacific and Indian Oceans in the Indonesian seas. *Nature*, **379**, 146–149.

Gordon, A. L., and J. McClean, 1999: Thermohaline stratification of the Indonesian Seas - model and observations. *Journal of Physical Oceanography*, **29**, 198–216.

Gordon, A. L., and R. D. Susanto, 2001: Banda Sea surface-layer divergence. *Ocean Dynamics*, **52**, 2–10.

Gordon, A. L., R. D. Susanto, and A. Ffield, 1999: Throughflow within Makassar Strait. *Geophysical Research Letters*, **26**, 3325–3328.

Goswami, B., and J. Shukla, 2000: Predictability of a coupled-atmosphere model. *Journal of Climate*, **4**, 3–22.

Griffies, S. M., 1998: The GentMcWilliams skew flux. *Journal of Physical Oceanography*, **28**, 831–841.

Gutman, G., I. Csiszar, and P. Romanov, 2000: Using NOAA/AVHRR products to monitor El Niño impacts: focus on Indonesia in 1997-98. *Bulletin of the American Meteorological Society*, **81**, 1189–1205.

Hackert, E. C., and S. Hastenrath, 1986: Mechanism of Java rainfall anomalies. *Monthly Weather Review*, **114**, 745–757.

Hagemann, S., 2002: An improved land surface parameter dataset for global and regional climate model., *MPI Report 336*, [Available from Max Planck-Institut für Meteorologie, Bundesstr. 55, D-20146, Hamburg, Germany.], 28 pp.

Hagemann, S., M. Botzet, L. Dümenil, and B. Machenhauer, 1999: Derivation of global GCM boundary conditions from 1km land use satellite data., *MPI Report 289*, [Available from Max Planck-Institut für Meteorologie, Bundesstr. 55, D-20146, Hamburg, Germany.], 34 pp.

Halpert, M. S., and C. F. Ropelewski, 1992: Temperature patterns associated with the Southern Oscillation. *Journal of Climate*, **5**, 577–593.

Hamada, J. I., M. D. Yamanaka, J. Matsumoto, S. Fukao, P. A. Winarso, and T. Sribimawati, 2002: Spatial and temporal variations of the rainy season over Indonesia and their link to ENSO. *Journal of the Meteorological Society of Japan*, **80**, 285–310.

Haylock, M., and J. L. McBride, 2001: Spatial coherence and predictability of Indonesian wet season rainfall. *Journal of Climate*, **14**, 3882–3887.

Hirst, A. C., and J. S. Godfrey, 1993: The role of Indonesian throughflow in a global ocean GCM. *Journal of Physical Oceanography*, **23**, 1057–1086.

Huffman, G. J., R. F. Adler, P. Arkin, A. Chang, R. Ferraro, A. Gruber, J. Janowiak, A. McNab, B. Rudolf, and U. Schneider, 1997: The Global Precipitation Climatology Project (GPCP) combined precipitation data set. *Bulletin of the American Meteorological Society*, **78**, 5–20.

Inoue, M., and W. E. Welsh, 1993: Modeling seasonal variability in the wind driven upper-layer circulation in the Indo-Pacific region. *Journal of Physical Oceanography*, **23**, 1411–1436.

Jacob, D., 2001: A note to the simulation of the annual and inter-annual variability of the water budget over the Baltic Sea drainage basin. *Meteorology and Atmospheric Physics*, **77**, 61–73.

Jacob, D., and R. Podzun, 1997: Sensitivity studies with the regional climate model REMO. *Meteorology and Atmospheric Physics*, **63**, 119–129.

Jacob, D., B. J. J. M. V. den Hurk, U. Andræ, G. Elgered, C. Fortelius, L. P. Graham, S. D. Jackson, U. Karstens, C. Köpken, R. Lindau, R. Podzun, B. Roeckel, F. Rubel, B. H. Sass, R. N. B. Smith, and X. Yang, 2001: A comprehensive model inter-comparison study investigation the water budget during the BALTEX-PIDCAP period. *Meteorology and Atmospheric Physics*, **77**, 19–43.

Jakob, C., 2000: The representation of cloud cover in atmospheric general circulation models., Ph.D. thesis, Ludwig-Maximilians- Universitat, Munchen, [Available from the European Centre for Medium-range Weather Forecasts, Reading, UK.], 190 pp.

Janowiak, J., A. Gruber, C. R. Kondragunta, R. E. Livezey, and G. J. Huffman, 1998: A comparison of the NCEP NCAR reanalysis rainfall and the GPCP rain gauge-satellite combined dataset with observational error considerations. *Journal of Climate*, **11**, 2960–2979.

Jha, B., T. N. Khrisnamurti, and Z. Christides, 2000: A Note on horizontal resolution dependence for monsoon rainfall simulations. *Meteorology and Atmospheric Physics*, **74**, 11–17.

Ji, Y., and A. D. Vernekar, 1997: Simulation of the Asian summer monsoons of 1987 and 1988 with a regional model nested in a global GCM. *Journal of Climate*, **10**, 1965–1979.

Jones, R. G., J. M. Murphy, and M. Noguer, 1995: Simulation of climate change over Europe using a nested regional climate model. I: Assesment of control climate, including sensitivity to location of lateral boundaries. *Quarterly Journal of Royal Meteorological Society*, **121**, 1413–1449.

Kaiser, H. F., 1958: The Varimax criterion for analytic rotations in factor analysis. *Psychometrika*, **23**, 187–200.

Kalnay, E., M. Kanamitsu, R. Kistler, W. Collins, D. Deaven, L. Gandin, M. Iredell, S. Saha, G. White, J. Woollen, Y. Zhu, M. Chelliah, W. Ebisuza, W. Higgins, J. Janowiak, K. C. Mo, C. Ropelewski, J. Wang, A. Leetmaa, R.Reynolds, R. Jenne, and D. Joseph, 1996: The

NCEP/NCAR 40-year reanalysis project. *Bulletin of the American Meteorological Society*, **77**, 437 – 471.

Kesler, E., 1969: On the distribution and continuity of water substance in atmospheric circulations., *Meteor. Monogr. 32*, 84 pp.

Kindle, J. C., H. E. Hurlburt, and E. J. Metzger, 1989: On the seasonal and interannual variability of the Pacific-Indian Ocean throughflow. (Eds.), Picaut, J., R. Lukas, and T. Delcroix, Noumea, New Caledonia, 355-366 pp.

Kirono, D. G. C., N. J. Tapper, and J. L. McBride, 1999: Documenting Indonesian rainfall in the 1997/1998 El Niño event. *Physical Geography*, **20**, 422–435.

Klemp, J. B., and D. R. Durran, 1983: An upper boundary condition permitting internal gravity wave radiation in numerical mesoscale models. *Monthly Weather Review*, **111**, 430–444.

Lal, M., U. Cubasch, J. Perlwitz, and J. Waszkewitz, 1997: Simulation of the Indian monsoon climatology in ECHAM3 climate model: sensitivity to horizontal resolution. *International Journal of Climatology*, **17**, 847–858.

Landman, W., and S. J. Mason, 1999: Operational prediction of South African rainfall using canonical correlation analysis. *International Journal of Climatology*, **19**, 1073–1090.

Laprise, R., M. R. Varma, B. Denis, D. Caya, and I. Zawadzki, 2000: Predictability of a nested limited area model. *Monthly Weather Review*, **128**, 4149–4154.

Large, W. G., and S. Pond, 1982: Sensible and latent heat flux measurements over the ocean. *Journal of Physical Oceanography*, **12**, 464–482.

Latif, M., and M. Flügel, 1991: An investigation of shot-range climate predictability in the tropical Pacific. *Journal of Geophysical Research*, **96**, 2661–2673.

Latif, M., and N. E. Graham, 1992: How much predictive skill is contained in the thermal structure of an OGCM? *Journal of Physical Oceanography*, **22**, 951–962.

Latif, M., D. L. T. Anderson, T. P. Barnett, M. A. Cane, R. Kleeman, A. Leetma, J. O'Brien, A. Rosati, and E. Schneider, 1998: A review of the predictability and prediction of ENSO. *Journal of Geophysical Research*, **103**, 14,375–14,393.

Lau, K. M., and H. T. Wu, 1999: Assessment of the impacts of the 1997-98 El Niño on the Asian-Australian monsoon. *Geophysical Research Letter*, **26**, 1747–1750.

Lau, K. M., and H. T. Wu, 2001: Principal modes of rainfall-SST variability of the Asian summer monsoon: A reassessment of the monsoon-ENSO relationship. *Journal of Climate*, **14**, 2880–2895.

Lau, K. M., H. T. Wu, and S. Bony, 1997: The role of large-scale atmospheric circulation in the relationship between tropical convection and sea surface temperature. *Journal of Climate*, **10**, 381–392.

Lau, N. G., and M. J. Nath, 2000: Impact of ENSO on the variability of the Asian-Australian monsoons as simulated in GCM experiments. *Journal of Climate*, **13**, 4287 – 4308.

Legutke, S., and R. Voss, 1999: The Hamburg Atmosphere-Ocean Coupled Circulation Model ECHO-G., *Tech. Rep. 18*, German Climate Computing Center, Hamburg, Germany, 61 pp.

Levitus, S., T. P. Boyer, M. E. Conkright, T. O'Brien, J. Antonov, C. Stephens, L. Stathoplos, D. Johnson, and R. Gelfeld, 1998: World Ocean database 1998. in, *Introduction. NOAA Atlas NESDIS 18, Ocean Climate Laboratory, National Oceanographic Data Center, vol 1*, US Government Printing Office, Washington, DC.

Lorenz, E. N., 1956: Empirical Orthogonal functions and statistical weather prediction., *Sci. Rep. 1. Statistical Forecasting Project (NTIS AD 110268)*, Departement of Meteorology, MIT, 49 pp.

Lorenz, E. N., 1969: The predictability of a flow which possesses many scales of motion. *Tellus*, **21**, 289–307.

Majewski, D., 1991: The Europa Modell of the Deutscher Wetterdienst., ECMWF Seminar Proceedings , ECMWF, Reading, UK, 147-191 pp.

Marsland, S. J., and J. O. Wolff, 1998: East Antartic seasonal sea-ice and ocean stability: A model study. *Ann Glaciol.*, **27**, 477–482.

Marsland, S. J., and J. O. Wolff, 2001: On sensitivity of Southern Ocean sea ice to the surface fresh water flux: A model study. *Journal of Geophysical Research*, **106**, 2723–2741.

Marsland, S. J., H. Haak, J. H. Jungclaus, M. Latif, and F. Röske, 2003: The Max-Planck Institute global ocean/sea ice model with orthogonal curvilinear coordinates. *Ocean Modelling*, **5**, 91–127.

Masumoto, Y., and T. Yamagata, 1993: Simulated seasonal circulation in the Indonesian Seas. *Journal of Geophysical Research*, **98**, 12,501–12,509.

Masumoto, Y., T. Kagimoto, M. Yoshida, M. Fukuda, N. Hirose, and T. Yamagata, 2001: Intraseasonal eddies in the Sulawesi Sea simulated in an Ocean General Circulation Model. *Geophysical Research Letter*, **28**, 1631–1634.

May, W., and E. Roeckner, 2001: A time-slice experiment with the ECHAM4 AGCM at high resolution: the impact of horizontal resolution on annual mean climate change. *Climate Dynamics*, **17**, 407–420.

McBride, J. L., 1999: Indonesia, Papua New Guinea, and tropical Australia: The southern hemisphere monsoon. in, *Meteorology of Southern Hemisphere.* (Eds.), Karoly, D. J., and D. G. Vincent, vol. 49, AMS, Boston, Meteorological Monograph, 89-98 pp.

McGregor, J. L., 1997: Regional climate modeling. *Meteorology and Atmospheric Physics*, **63**, 105–117.

McGregor, J. L., and K. Walsh, 1994: Climate change simulations of Tasmanian precipitation using multiple nesting. *Journal of Geophysical Research*, **99**, 20,889–20,905.

Menendez, C. G., A. C. Saulo, and Z. Li, 2001: Simulation of South American wintertime climate with a nesting system. *Climate Dynamics*, **17**, 219–231.

Mesinger, F., 1997: Dynamics of Limited-area models: formulation and numerical methods. *Meteorology and Atmospheric Physics*, **63**, 3–14.

Meyers, G., 1996: Variation of the Indonesian throughflow and the El Niño-Southern Oscillation. *Journal of Geophysical Research*, **101**, 12,255–12,263.

Moore, A. M., and R. Kleeman, 1996: The dynamics of error growth and predictability in a coupled model of ENSO. *Quarterly Journal of Royal Meteorological Society*, **122**, 1405–1446.

Morcrette, J. J., and Y. Fouquart, 1986: Pressure and temperature dependence of the absorption in longwave radiation parameterizations *Beiträge zur Physik der Atmosphäre*, **59**, 455–469.

Morey, S. L., J. F. Shriver, and J. J. O'Brien, 1999: The effects of Halmahera on the Indonesian throughflow. *Journal of Geophysical Research*, **104**, 23,281–23,296.

Moron, V., A. Navarra, M. N. Ward, and E. Roeckner, 1998: Skill and reproducibility of seasonal rainfall patterns in the tropics in ECHAM-4 GCM simulations with prescribed SST. *Climate Dynamics*, **14**, 83–100.

Newell, R. E., R. Selkirk, and W. Ebisuzaki, 1982: The southern oscillation-sea surface temperature and wind relationships in a 100-year data set. *Journal of Climatology*, **2**, 357–373.

Newman, M., P. D. Sardeshmukh, and J. W. Bergman, 2000: An assessment of the NCEP, NASA, and ECMWF reanalyses over the tropical west Pacific Warm Pool. *Bulletin of the American Meteorological Society*, **81**, 41–48.

Nicholls, N., 1981: Air-sea interaction and the possibility of long-range weather prediction in the Indonesian archipelago. *Monthly Weather Review*, **109**, 2345–2443.

Nicholls, N., 1983: Predicting Indian monsoon rainfall from sea-surface temperature in the Indonesian-north Australia area. *Nature*, **306**, 576–577.

Nicholls, N., 1984: The Southern Oscillation and Indonesia sea surface temperature. *Monthly Weather Review*, **112**, 424–432.

Nicholls, N., 1985: All-India summer monsoon rainfall and sea surface temperature around northern Australia and Indonesia. *Journal of Climate*, **8**, 1463–1467.

Nobre, P., A. D. Moura, and L. Sun, 2001: Dynamical downscaling of seasonal climate prediction over Nordeste Brazil with ECHAM3 and NCEP's regional sprectral model at IRI *Bull. Amer. Meteorol. Soc.*, **82**, 2787–2796.

Nordeng, T. E., 1994: Extended versions of the convective parameterization scheme at ECMWF and their impact on the mean and transient activity of the model in the tropics., *ECMWF Tech. Memo 206*, ECMWF, [Available from the European Centre for Medium-range Weather Forecasts, Reading, UK.].

Nouger, M., R. G. Jones, and J. M. Murphy, 1998: Sources of systematic errors in the climatology of a regional climate model over Europe. *Climate Dynamics*, **14**, 691–712.

Oberhuber, J. M., 1993: Simulation of the Atlantic circulation with a coupled sea ice-mixed layer-isopycnal general circulation model. Part I: Model description. *Journal of Physical Oceanography*, **23**, 808–829.

Paegle, J., Q. Yang, and M. Wang, 1997: Predictability in limited area and global models. *Meteorology and Atmospheric Physics*, **63**, 53–69.

Pexioto, J. P., and A. H. Oort, 1991: *Physics of Climate.*, American Institute of Physics, New York, USA, 513 pp.

Philander, S. G. H., 1983: El Niño southern oscillation phenomena. *Nature*, **302**, 295–301.

Philander, S. G. H., 1989: *El Niño, La Niña, and the Southern Oscillation.*, vol. 46 of *International Geophysical Series*, Academic Press, 289 pp.

Podzun, R., A. Cress, A. Majewski, and V. Renner, 1995: Simulation of European Climate with a limited area model. Part II. AGCM boundary conditions. *Contribution to Atmospheric Physics*, **68**, 205–225.

Potemra, J., R. Lukas, and G. Mitchum, 1997: Large-scale estimation of transport from the Pacific to the Indian Ocean. *Journal of Geophysical Research*, **102**, 27,795–27,812.

Preseindorfer, R. W., 1988: *Principal component analysis in meteorology and oceanography.*, Elsevier, Amsterdam, 425 pp.

Quadfasel, D., and G. R. Cresswell, 1992: A note on the seasonal variability of the south Java current. *Journal of Geophysical Research*, **97**, 3685–3688.

Ramage, C., 1971: *Monsoon Meteorology*, Academic Press, 296 pp.

Rasmusson, E. M., and T. H. Carpenter, 1982: Variations in tropical sea surface temperature and surface wind fields associated with the southern oscillation/El Niño. *Monthly Weather Review*, **110**, 354–384.

Rayner, N. A., E. B. Horton, D. E. Parker, C. K. Folland, and R. B. Hackett, 1996: Version 2.2 of the global sea-ice and sea surface temperature data set, 1903-1994., *Tech. Note CRTN74*, Climate Research, 35 pp.

Reesinck, J. J. M., 1952: Some remarks on monsoon forecasting for Java., *Verhandelingen 44*, Kementrian Perhubungan Lembaga Meteorologi dan Geofisika, Jakarta, Indonesia, 22 pp.

Rodgers, K. B., M. Latif, and S. Legutke, 2000: Sensitivity of equatorial pacific and Indian Ocean watermasses to the position of the Indonesian throughflow. *Geophysical Research Letter*, **27**, 2941–2944.

Roeckner, E., K. Arpe, L. Bengston, M. Christoph, M. Claussen, L. Dumenil, M. Esch, M. Giorgetta, U. Schlese, and U. Schulzweida, 1996a: The atmospheric general circulation model ECHAM-4: Model description and simulation of present-day climate., *MPI Report 218*, [Available from Max Planck-Institut für Meteorologie, Bundesstr. 55, D-20146, Hamburg, Germany.], 90 pp.

Roeckner, E., J. M. Oberhuber, A. Bacher, M. Christoph, and I. Kirchner, 1996b: ENSO variability and atmospheric response in a global coupled atmosphere-ocean GCM. *Climate Dynamics*, **12**, 737–754.

Ropelewski, C., and M. S. Halpert, 1989: Rainfall patterns associated with the high index phase of the Southern Oscillation. *Journal of Climate*, **2**, 268–284.

Ropelewski, C. F., and M. S. Halpert, 1987: Global and regional scale rainfall patterns associated with the El Niño Southern Oscillation (ENSO). *Monthly Weather Review*, **115**, 1606–1626.

Röske, F., 2001: An Atlas of surface fluxes based on the ECMWF Re-Analysis - a climatological dataset to force global ocean general circulation models., *MPI Report 323*, [Available from Max Planck-Institut für Meteorologie, Bundesstr. 55, D-20146, Hamburg, Germany.].

Schell, I. I., 1947: *Dynamic persistence and its applications to long-range forecasting.*, vol. 8, Harvard Meteorological Studies, Blue Hill Observatory, Milton, MA, 80 pp.

Semmler, T., 2002: Der Wasser und Energiehaushalt der arktischen Atmosphäre, Ph.D. thesis, MPI für Meteorologie, [Available from Max Planck-Institut für Meteorologie, Bundesstr. 55, D-20146, Hamburg, Germany.], 105 pp.

Semtner, A. J., 1976: A model for the thermodynamic growth of sea ice in numerical investigations of climate. *Journal of Physical Oceanography*, **6**, 379–389.

Shukla, J., and D. A. Paolino, 1983: The Southern Oscillation and long-range forecasting of the summer monsoon rainfall over India. *Monthly Weather Review*, **111**, 1830–1837.

Simmons, A. J., and D. M. Burridge, 1981: An energy and angular-momentum conserving vertical finite-difference scheme and hybrid vertical coordinates. *Monthly Weather Review*, **109**, 758–766.

Simmons, A. J., and J. K. Gibson, 2000: The ERA-40 Project Plan., *ERA-40 Project Report Series 1*, ECMWF, [Available from the European Centre for Medium-range Weather Forecasts, Reading, UK.], 62 pp.

Staniforth, A., 1997: Regional Modeling: A theoretical discussion. *Meteorology and Atmospheric Physics*, **63**, 15–29.

Stendel, M., and K. Arpe, 1997: Evaluation of the hydrological cycle in reanalyses and observations., *MPI Report 228*, [Available from Max-Planck-Institut für Meteorologie, Bundesstrasse 55, 20146 Hamburg, Germany.], 52 pp.

Stendel, M., and E. Roeckner, 1998: Impacts of horizontal resolution on simulated climate statistics in ECHAM4., *MPI Report 253*, [Available from Max Planck-Institut für Meteorologie, Bundesstr. 55, D-20146, Hamburg, Germany.], 57 pp.

Sukanto, M., 1969: Climate of Indonesia. World Survey of Climatology. in, *Climates of Northern and Eastern Asia* (Ed.), Arakawa, H., vol. 8, Elsevier, 215-229 pp.

Sundqvist, H., 1978: A parameterization scheme for non-convective condensation including prediction of cloud water content. *Quarterly Journal of Royal Meteorological Society*, **104**, 677–690.

Susanto, R. D., A. L. Gordon, and Q. Zheng, 2001: Upwelling along the coasts of Java and Sumatra and its relation to ENSO *Geophysical Research Letter*, **28**, 1599–1602.

Thompson, C. J., and D. S. Battisti, 2001: A linear stochastic dynamical model of ENSO. Part II: Analysis. *Journal of Climate*, **14**, 445–466.

Tiedtke, M., 1989: A comprehensive mass flux scheme for cumulus parameterization in large scale models. *Monthly Weather Review*, **117**, 1779–1800.

Trenberth, K., and J. M. Caron, 2000: The Southern Oscillation revisited: sea level pressure, surface temperature, and precipitation. *Journal of Climate*, **13**, 4358–4365.

Valcke, S., L. Terray, and A. Piacentini, 2000: The OASIS Coupler User's Guide, Version 2.4., *Tech. Rep. TR/CGMC/00-10*, CERFACS, 85 pp.

von Storch, H., and F. W. Zwiers, 1999: *Statistical Analysis in Climate Research.*, 2 ed., Cambridge University Press, Cambridge, UK, 550 pp.

Vose, R. S., R. L. Schmoyer, P. M. Steurer, T. C. Peterson, R. Heim, T. R. Karl, and J. K. Eischeid, 1992: The Global Historical Climatology Network: Long-term monthly temperature, precipitation, sea level pressure, and station pressure data., *ORNL/CDIAC-53 NDP-041*, 325 pp.

Vukicevic, T., and R. M. Errico, 1990: The influence of artificial and physical factors upon predictability estimates using a complex limited area model. *Monthly Weather Review*, **118**, 1460–1482.

Warner, T. T., R. A. Peterson, and R. E. Treadon, 1997: A Tutorial on lateral boundary conditions as a basic and potentially serious limitation to regional numerical weather prediction. *Bulletin of the American Meteorological Society*, **78**, 2599–2617.

WCRP, 1990: Global Rainfall Climatology Project: Implementation and data management plan., *Tech. Rep. WMO/TD-No. 367*, World Climate Research Programme, WMO, Geneva, Switzerland, 47 pp.

WCRP, 1998: CLIVAR initial implementation plan., *WCRP report 103*, World Climate Research Programme, WMO, Geneva, Switzerland, 314 pp.

Webster, P. J., and S. Yang, 1992: Monsoon and ENSO: selectively interactive systems. *Quarterly Journal of Royal Meteorology Society*, **118**, 877–925.

Weiss, J. P., and J. B. Weiss, 1999: Quantifying persistence in ENSO. *Journal of Atmospheric Science*, **56**, 2737–2760.

Wolff, J. O., E. Maier-Reimer, and S. Legutke, 1997: The Hamburg Ocean Primitive Equation Model HOPE., *Technical Report 13*, German Climate Computer Center (DKRZ), Hamburg, Germany, 98 pp.

Wyrtki, K., 1956: The Rainfall over the Indonesian waters., *Verhandelingen 49*, Kementrian Perhubungan Lembaga Meteorologi dan Geofisika, Jakarta, Indonesia, 24 pp.

Wyrtki, K., 1961: Physical Oceanography of the Southeast Asian waters, in Scientific results of Maritime investigations of the South China Sea and Gulf of Thailand 1959-1961., *Naga Report 2*, Univ. of California - Scripps Inst. of Oceanography, 195 pp.

Wyrtki, K., 1973: An equatorial jet in the Indian Ocean. *Science*, **181**, 262–264.

Wyrtki, K., 1987: Indonesian throughflow and the associated pressure gradient. *Journal of Geophysical Research*, **92**, 12,941–12,946.

Yu, Z. P., P. S. Chu, and T. Schroeder, 1997: Predictive skills of seasonal to annual rainfall variations in the US affiliated Pacific Islands: canonical correlation analysis and multivariate principal component regression approaches. *Journal of Climate*, **10**, 2586–2599.

MPI-Examensarbeit-Referenz:

Examensarbeit Nr. 1-79 bei Bedarf bitte Anfragen:
MPI für Meteorologie, Abtlg.: PR, Bundesstr. 55, 20146 Hamburg

Examensarbeit Nr. 80 November 2000	**Vertikalmessungen der Aerosolextinktion und des Ozons mit einem UV-Raman-Lidar** Volker Matthias
Examensarbeit Nr. 81 Dezember 2000	**Photochemical Smog in Berlin-Brandenburg: An Investigation with the Atmosphere-Chemistry Model GESIMA** Susanne E. Bauer
Examensarbeit Nr. 82 Juli 2001	**Komponenten des Wasserkreislaufs in Zyklonen aus Satellitendaten – Niederschlagsfallstudien-** Klepp Christian-Philipp
Examensarbeit Nr. 83 Juli 2001	**Aggregate models of climate change: development and applications** Kurt Georg Hooss
Examensarbeit Nr. 84 Februar 2002	**Ein Heterodyn-DIAL System für die simultane Messung von Wasserdampf und Vertikalwind: Aufbau und Erprobung** Stefan Lehmann
Examensarbeit Nr. 85 April 2002	**Der Wasser- und Energiehaushalt der arktischen Atmosphäre** Tido Semmler
Examensarbeit Nr. 86 April 2002	**Auswirkungen der Assimilation von Meereshöhen-Daten auf Analysen und Vorhersagen von El Niño** Sigrid Schöttle
Examensarbeit Nr. 87 Juni 2002	**Atmospheric Processes in a young Biomass Burning Plume - Radiation and Chemistry** Jörg Trentmann
Examensarbeit Nr. 88 August 2002	**Model Studies of the Tropical 30 to 60 Days Oscillation** **S**tefan Liess
Examensarbeit Nr. 89 Dezember 2002	**Influence of Sub-Grid Scale Variability of Clouds on the Solar Radiative Transfer Computations in the ECHAM5 Climate Model** Georg Bäuml
Examensarbeit Nr.90 Mai 2003	**Model studies on the response of the terrestrial carbon cycle to climate change and variability** Marko Scholze
Examensarbeit Nr.91 Juni 2003	**Integrated Assessment of Climate Change Using Structural Dynamic Models** Volker Barth

ISSN 0938 - 5177